Understanding and optimizing the local catalyst environment in CO_2 reduction electrodes

Thesis by

Alex J. Welch

In Partial Fulfillment of the Requirements for
the degree of
Doctor of Philosophy

Caltech

CALIFORNIA INSTITUTE OF TECHNOLOGY
Pasadena, California

2022
(Defended October 1st, 2021)

Alex J. Welch
ORCID: 0000-0003-2132-9617

ACKNOWLEDGEMENTS

Over the past five years I have grown so much, and this was made possible by an extraordinary group of people: colleagues and mentors who pushed me to explore new scientific territory and believed in my ability to tackle any challenges, friends and family who supported me no matter what and were always down to hang out and laugh. This experience would not have been the same without all of you and I am truly thankful.

First, I would like to thank my advisor, Harry Atwater. I remember trying to decide if I should go to Caltech or stay at Stanford for graduate school, and all of my professors at Stanford kept telling me that I should go to Caltech because of what an amazing mentor Harry is. They could not have been more right. I am constantly inspired by Harry's passion and excitement for science, and no matter how busy Harry is, he always found time to meet with me when I asked. Harry has taught me to always be curious and that no project is impossible.

Next, I would like to thank Giulia Tagliabue and Joe Duchene. I came into graduate school having not taken a chemistry class since high school, and therefore had a lot of questions about what was going on. Both of them took so much time to train me on all of the equipment, explain concepts to me, and answer all of my many questions. I have learned so much from both of them. Particularly, Giulia taught by example to always comes into lab with a smile and to not get discouraged when an experiment doesn't work. Joe taught me how to really think about the purpose of every experiment and to design the most effective studies. After they both became professors, I put a post-it note on my desk saying "What would Giulia/Joe do?" and it helps me get into the right mindset to get through challenges.

I would also like to thank many other members of the Atwater team and other researchers in Jorgensen. I would not have made it nearly as far on all of my projects without all of the brainstorming that I did with people like Aidan, Eowyn, Annette, Lucy, Ian, Ibadillah, CX, Sophia, Matthias, Nick, Artur, and Kate. They were always around the lab and happy to take a look at any experimental problem I was having or help me think of how to design an experiment to probe a particular question. Aidan helped me solve many of the cell design problems I was having with the confocal microscope and it has been great seeing him carry on the work with nanoporous gold. I have had so much fun working with Annette, and it is exciting to see her take over the pH imaging experiments. Ibadillah was a pleasure to work with on techno-economic analysis project. Ian taught me so much about electrochemistry, and I really appreciate how he always puts down what he is doing to answer any question that I have. Eowyn is an amazing friend and encouraged me when experiments were not working. I also want to thank Dagny, Joeson, and Magel for working on the e-beam with me. In particular I would like to thank Joeson for teaching so much about how the e-beam operates, working tirelessly to fix the e-beam after the flood, and for all of our wine nights. There are many more people in the A-team to thank than I have time to here, but you should know that without the community that the A-team provided during my time, Caltech would have been much less fun.

I also want acknowledge my mentors that helped get me to Caltech. First, I want to thank Pat Burchat and Kam Moler for getting me excited about physics and for all of their advice through the years. I also want to thank Mark Brongersma for his help in deciding what classes I should take. I especially want to thank Yi Cui for letting me work in his lab starting freshman fall. Po-Chun was very patient in teaching me how to do all the experiments and Yi always had amazing new ideas for us to try. In my senior year I worked with Jen Dionne on plasmonic upconverters with Guru. Jen's enthusiasm for science is something that I strive for and Guru helped me to believe in my abilities as a scientist.

Now, while all of the scientific mentorship and help was crucial for this thesis, I could not have done it without the support of my friends and family. My first-year roommates Sophia, Sophie, and Sarah helped me find my home in LA. I was lucky enough to get to live with Sophie for the next 3 years; she was always there for me no matter what was going on. I also want to give a shout out to some other Caltech friends from my year: Haley, Cora, Camilla, and Areum. The group that was my anchor through all of Caltech and makes up my LA family is Taco Tuesday. Every other Tuesday, even during the pandemic, we ate tacos, drank margaritas, and laughed. Megan, Kendall, Eowyn, Spencer, Alexander, Alex C., Alex S., Jason, Lauren, Nathan, John, Amy, Sydney, Elyse, Cullen, Sophie, Taylor, Claire, and Jamie: I feel like I could pick up the phone and call any of you right now and you would drop everything to help me. Your friendship means the world to me. I would like say thank you to the skiing crew, those who have not already been listed are Jackie, Eric, Madison, Anna, Clayton, Tarek, and Brian; thank you for all of the adventures. Two friends that I would like to say an extra thank you to are Megan and Kristine, my scuba buddies; whether we are at the cellar or on an adventure there is no one I would rather be with. Kristine, it was so much fun to get to live with you during the pandemic and camp every weekend. Megan, Mondays are now my favorite day of the week because of you. You bring so much happiness to everyone you interact with.

My family has made me who I am today. My dad is always there to share my love for science and building tables. My mom has taught me compassion by always being there and caring for others. John and Tom, you always make me laugh and there is no one who will know me quite like you two. Grandma ,thanks for always being so proud of me.   All of you have given me so much support and love throughout my life. I look forward to many more card games, hikes, and general good times. Thank you for always believing me and helping me become my best self.

And last, and most importantly, thank you Jamie. Thank you for making me smile every day and being my partner in all things. Thank you for letting me epoxy tables in our bathroom and for always being excited about my work. Thank you for everything.

ABSTRACT

Understanding and managing the local microenvironments in carbon dioxide reduction catalysts is crucial for optimizing device performance. In particular a locally high pH can increase catalyst selectivity and activity, as well as indicate which part of the catalyst is most active. In this thesis we begin by studying how nanoporous catalysts can induce this locally high pH in an aqueous system. We observe an increase in both Faradaic efficiency and partial current density for carbon monoxide in the nanoporous system relative to a planar metal film. We then show that this same nanoporous architecture can be used for improved device performance in a gas diffusion electrode configuration. We also perform copper underpotential deposition and secondary ion mass spectroscopy to show that almost half of the catalyst is not in contact with the electrolyte in this configuration. Then we use confocal fluorescent microscopy to image the local pH in a gas diffusion electrode to determine which parts of the electrode are most active. Through a combination of experiment and simulations we find that the catalyst within thin cracks of the microporous layer is most active for carbon dioxide reduction. While the study of local pH and wetting is the main focus of this thesis, we also explore how light can be used to improve selectivity and activity. In particular we study gold nanoparticles on p-type gallium nitride and copper nanoparticles on p-type nickel oxide. Finally, this thesis also explores how carbon dioxide conversion can actually be deployed. We discuss opportunities for combining carbon dioxide capture and conversion, as well as evaluate different pathways for renewable methane generation.

This thesis gives in depth analysis of electrochemical carbon dioxide reduction catalysts as well as putting this research into the larger context of how such devices can be deployed. We hope that by combining systems level thinking and specific device studies better carbon dioxide conversion systems can be realized.

PUBLISHED CONTENT AND CONTRIBUTIONS

***Operando* Local pH Measurement within Gas Diffusion Electrodes Performing Electrochemical Carbon Dioxide Reduction**
Alex J. Welch, Aidan Q. Fenwick, Annette Böhme, Hsiang-Yun Chen, Ian Sullivan, Xueqian Li, Joseph S. Duchene, Chengxiang Xiang, and Harry A. Atwater, *Jour. Phys. Chem. C.* **2021**
DOI: 10.1021/acs.jpcc.1c06265
Contributions: conception and design, fabrication and data collection, data analysis, manuscript writing, and revision

Comparative Techno-Economic Analysis of Renewable Generation of Methane Using Sunlight, Water, and Carbon Dioxide
Alex J. Welch, Ibadillah A Digdaya, Ron Kent, Paul Ghougassian, Harry A. Atwater, and Chengxiang Xiang *ACS Energy Letters* **2021** 6 (4), 1540-1549.
DOI: 10.1021/acsenergylett.1c00174
Contributions: conception, model design, data analysis, manuscript writing, and revision.

Bicarbonate or Carbonate Processes for Coupling Carbon Dioxide Capture and Electrochemical Conversion
Alex J. Welch, Emily Dunn, Joseph S. DuChene, and Harry A. Atwater, *ACS Energy Letters* **2020** *5* (3), 940-945. DOI: 10.1021/acsenergylett.0c00234
Contributions: conception, data collection and analysis, manuscript writing, and revision.

Optical Excitation of a Nanoparticle Cu/p-NiO Photocathode Improves Reaction Selectivity for CO_2 Reduction in Aqueous Electrolytes
Joseph S. DuChene, Giulia Tagliabue, Alex J. Welch, Xueqian Li, Wen-Hui Cheng, Harry A. Atwater, *Nano Letters* **2020** 20 (4), 2348-2358. DOI: 10.1021/acs.nanolett.9b04895
Contributions: device fabrication, characterization, revision.

Nanoporous Gold as a Highly Selective and Active Carbon Dioxide Reduction Catalyst
Alex J. Welch, Joseph S. DuChene, Giulia Tagliabue, Artur Davoyan, Wen-Hui Cheng, and Harry A. Atwater, *ACS Applied Energy Materials* **2019** *2* (1), 164-170.
DOI: 10.1021/acsaem.8b01570
Contributions: fabrication and data collection, data analysis, manuscript writing, and revision

Quantifying the Roles of Surface Plasmon Excitation and Hot Carrier Transport in Plasmonic Devices
Giulia Tagliabue, Adam S. Jermym, Ravishankar Sundararaman, Alex J. Welch, Joseph S. Duchene, Ragip Pala, Artur R. Davoyan, Prineha Narang, and Harry A. Atwater, *Nature Communications* **2018** *9*, 3394.
DOI: 10.1038/s41467-018-05968-x
Contributions: fabrication and characterization, revision

Hot Hole Collection and Photoelectrochemical CO2 Reduction with Plasmonic Au/p-GaN Photocathodes
Joseph S. DuChene, Giulia Tagliabue, Alex J. Welch, Wen-Hui Cheng, and Harry A. Atwater, *Nano Letters* **2018** *18* (4), 2545-2550. DOI: 10.1021/acs.nanolett.8b00241
Contributions: fabrication and characterization, revision

TABLE OF CONTENTS

Chapter VI: Optical excitation of a nanoparticle Cu/p-NiO photocathode improves reaction selectivity for CO_2 reduction in aqueous electrolytes……………….……..98

Chapter VII: Bicarbonate or carbonate processes for coupling carbon Dioxide capture and electrochemical conversion……………………………..………119

Chapter VIII: Comparative techno-economic analysis of renewable Generation of methane using sunlight, water, and CO_2……………………..…………129

LIST OF FIGURES

LIST OF TABLES

Chapter 1

INTRODUTION TO CO_2 REDUCTION

1.1 Role of solar fuels in the mitigation of climate change

Climate change is perhaps the largest threat facing our planet today, due to the catastrophic consequences, and the global coordinated effort it will take to mitigate the problem.[1] For every additional 0.5°C increase in global temperature there will be a discernible increase in heat waves, heavy precipitation, sea level rise, extreme weather events, and drought. In order to mitigate the worst of these effects we must stay below a 1.5°C change in global temperature. Models have shown that this will only be possible if go to negative greenhouse gas emissions by 2050.[2] To achieve this goal, renewable energy needs to become a dominant source of energy globally.[3] Currently, the two largest forms of renewable energy are solar photovoltaics and wind, due to the many options for geographical deployment and the large availability of both resources.[4] However, despite the abundance of these resources, solar and wind energy both experience daily, seasonal, and geographic variation, thus suggesting the need for efficient and inexpensive energy storage to fully replace carbon-based fuels.[5] Batteries, while useful for grid power management and short term storage, are unlikely to be able to provide necessary seasonal storage due to prohibitive costs and charge leakage. Other storage technologies exist – such as pumped hydro, compressed air, and fly wheels – but they also have limitations including scalability, versatility, and storage time.[6,7] In addition to their inability to handle seasonal storage, these technologies are not nearly as energy dense as chemical fuels, and are therefore unlikely to be able to power applications such as intercontinental flights, long-haul shipping, or orbital rockets.[8]

The transformation of renewable energy into chemical bonds can solve both of these challenges because it provides an energy dense and long-term storage solution. In particular the transformation of carbon dioxide (CO_2) serves to store renewable energy as chemical fuels, which are carbon neutral. This is important because there are many industries that are difficult to decarbonize,[3†] such as the production of cement,[9,10] steel,[11] plastic,[12] ammonia,[13] and aluminum,[14,15] which account for 12% of total carbon emissions. By removing CO_2 from the atmosphere we can offset the emissions from these industries. Transforming CO_2 into valuable chemicals allows us to close the carbon cycle and stop the emission of greenhouse gases providing a long term, energy dense storage solution that also removes CO_2 from the atmosphere.

[†] Decarbonization means to remove the emission of greenhouse gases from a process.

The following steps are most commonly followed in order for CO_2 to be captured and transformed: (i) a CO_2 source, (ii) a capture medium, (iii) a process to release CO_2 from the capture medium, (iv) CO_2 compression into a concentrated gas stream, and (v) conversion of CO_2 into fuels, chemicals, and/or materials (e.g., hydrocarbons).[16] In this thesis we focus on the conversion portion (step 5) of this process because this requires the most energy and is least understood. In the final chapters we perform technoeconomic analysis (TEA) on the whole system to see what how a CO_2 capture/conversion system could be deployed.

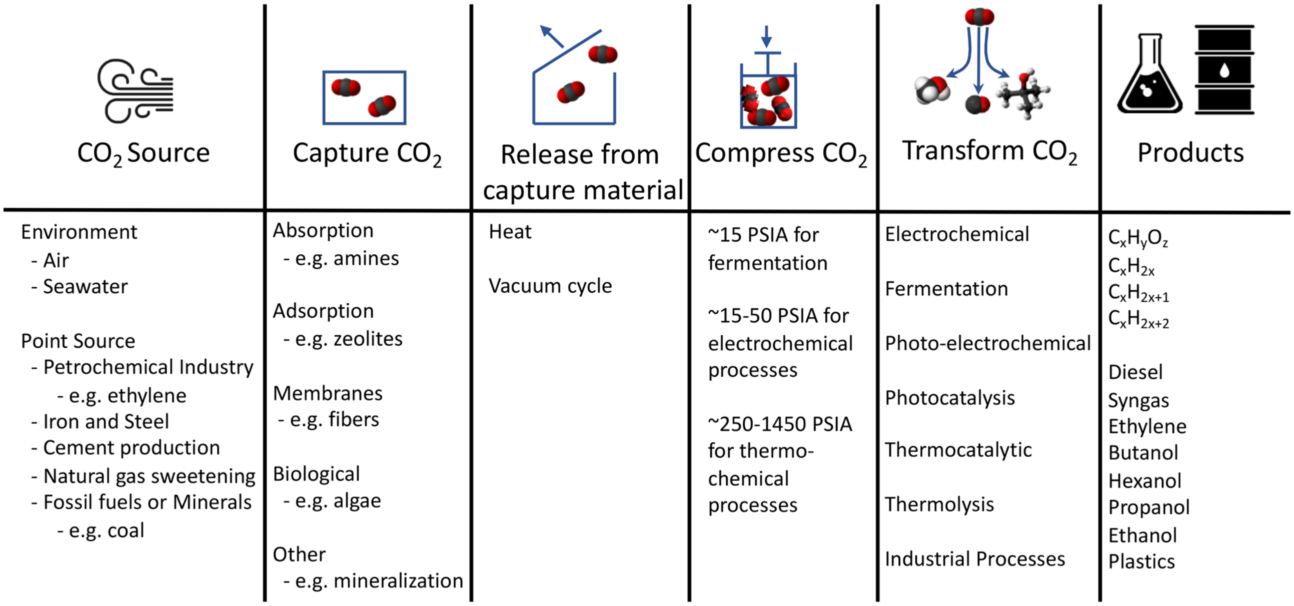

CO_2 Source	Capture CO_2	Release from capture material	Compress CO_2	Transform CO_2	Products
Environment - Air - Seawater Point Source - Petrochemical Industry - e.g. ethylene - Iron and Steel - Cement production - Natural gas sweetening - Fossil fuels or Minerals - e.g. coal	Absorption - e.g. amines Adsorption - e.g. zeolites Membranes - e.g. fibers Biological - e.g. algae Other - e.g. mineralization	Heat Vacuum cycle	~15 PSIA for fermentation ~15-50 PSIA for electrochemical processes ~250-1450 PSIA for thermo-chemical processes	Electrochemical Fermentation Photo-electrochemical Photocatalysis Thermocatalytic Thermolysis Industrial Processes	$C_xH_yO_z$ C_xH_{2x} C_xH_{2x+1} C_xH_{2x+2} Diesel Syngas Ethylene Butanol Hexanol Propanol Ethanol Plastics

Figure 1.1: *Synopsis of various steps involved in capture CO_2 and transforming it into valuable chemicals*[16]

1.2 Fundamentals of electrochemical CO_2 reduction

The cathodic reaction in electrochemical CO_2 reduction (CO_2R) follows this form:

$$xCO_2 + nH^+ + ne^- \rightarrow C_xH_yO_z + mH_2O \qquad (1.1)$$

The anodic reaction is the oxygen evolution reaction (OER) and is as follows:

$$2H_2O \rightarrow O_2 + 4H^+ + 4e^- \qquad (1.2)$$

While other anodic reactions are possible, water is the only viable source of electrons and protons if CO_2R is to be scaled.[17]

Through this section CO_2R reaction will be discussed in terms of thermodynamics. It will also be discussed the cause of the challenges of doing CO_2R instead of the hydrogen evolution reaction (HER). The following chapters will address how the catalyst and local catalyst environments can influence which reaction pathway occurs. The first electrochemical studies of CO_2 reduction began in the early 19th century however the first more systematic study was done by Hori is 1985.[18,19] He explored a variety of different metals, CO_2 pressures, etc. and documented how they effected the onset potential and Faradaic efficiency towards different products. Table 1.1 shows common CO_2R reactions with their equilibrium potentials and names of the products, similar such tables have been shown in many previous CO_2R reviews.[18,20–24] The CO_2R standard potentials are calculated via the Gibbs free energy equation from data provided by NIST.[25] For gas phase products gas-phase thermochemistry data is used while for aqueous products Henry's law data is used. All equilibrium potentials are reported vs the reversible hydrogen electrode (RHE) which is independent of pH. CO_2 is always considered a gas and H_2O a liquid in Table 1.1.

CO_2 Reduction Reactions	**E^0 (V vs RHE)**	**Name of Product**
$CO_2 + 2H^+ + 2e^- \rightarrow HCOOH_{(aq)}$	-0.12	Formic acid
$CO_2 + 2H^+ + 2e^- \rightarrow CO_{(g)} + H_2O$	-0.10	Carbon monoxide
$CO_2 + 6H^+ + 6e^- \rightarrow CH_3OH_{(aq)} + H_2O$	0.03	Methanol, MeOH
$CO_2 + 8H^+ + 8e^- \rightarrow CH_{4(g)} + 2H_2O$	0.17	Methane
$CO_2 + 4H^+ + 4e^- \rightarrow C_{(s)} + 2H_2O$	0.21	Graphite
$2CO_2 + 2H^+ + 2e^- \rightarrow (COOH)_{2(s)}$	-0.47	Oxalic acid
$2CO_2 + 10H^+ + 10e^- \rightarrow CH_3CHO_{(aq)} + 3H_2O$	0.06	Acetaldehyde
$2CO_2 + 12H^+ + 12e^- \rightarrow C_2H_{4(g)} + 4H_2O$	0.08	Ethylene
$2CO_2 + 12H^+ + 12e^- \rightarrow C_2H_5OH_{(aq)} + 3H_2O$	0.09	Ethanol
$2CO_2 + 8H^+ + 8e^- \rightarrow CH_3COOH_{(aq)} + 2H_2O$	0.11	Acetic acid
$2CO_2 + 14H^+ + 14e^- \rightarrow C_2H_{6(g)} + 4H_2O$	0.14	Ethane
$3CO_2 + 16H^+ + 16e^- \rightarrow C_2H_5CHO_{(aq)} + 5H_2O$	0.09	Propionaldehyde
$3CO_2 + 18H^+ + 18e^- \rightarrow C_3H_7OH_{(aq)} + 5H_2O$	0.10	Propanol, PrOH
Other important reactions	**E^0 (V vs RHE)**	**Name of Reaction**
$2H^+ + 2e^- \rightarrow H_2$	0.0	Hydrogen evolution reaction (HER)
$2H_2O \rightarrow O_2 + 4H^+ + 4e^-$	1.23	Oxygen evolution reaction (OER)

***Table 1.1**: list of relevant electrochemical reactions and their corresponding equilibrium potentials.*

From Table 1.1 we are able to see that CO_2R is not only difficult because CO_2 is the most stable form of carbon under environmental conditions, but the variety of reaction pathways and small differences in equilibrium potentials make selectively producing one product challenging. First, the close spacing between many of the equilibrium potentials indicates that merely tuning the applied bias will not be able to easily select for one product. Second, many of the reactions require multiple protons and electrons, and it is difficult to find a single catalyst that can sustain all of the intermediates for a single pathway. In order for a reactant to be reduced, it must bind to the electrode surface so that electrons can be transferred to it. In a reaction pathway with multiple electron transfers each intermediate must also stay bound to the electrode surface, so that all of the electrons can be transferred. If an intermediate does not stay bound to the surface it will float into the electrolyte and the final desired product will not be made. Therefore, the more electrons required for a particular reaction, the more difficult it is to find a catalyst that selectively and actively performs the reaction. Third, the potential of the hydrogen evolution reaction (HER) is right in the middle of the CO_2R reaction potentials. In an aqueous environment, water has a molarity of 55.5M, whereas the maximum CO_2 concentration is 33mM.[26] It is a challenge to selectively to do CO_2R as opposed to HER when there is so much water available, which also can be reduced at a similar potential. In this thesis we explore how through a combination of catalyst engineering and understanding of the local catalyst environment we can overcome these challenges to make highly selective and active CO_2R devices.

1.3 Catalyst compositions

A number of considerations are necessary when choosing a catalyst, the first of which is what products the metal is capable of making. This is largely defined by the adsorption energy of three important intermediates H*, COOH*, CO*.[27‡] An intermediate is any chemical that exists as a reactant is reduced to the final product. As discussed previously, for a reactant to be reduced it must adsorb to the electrode surface, allowing for electrons to transfer. In order for multiple electrons to be transferred each subsequent intermediate must stay adsorbed to the electrode surface.

[‡] The * notation denotes that these chemicals are in the adsorbate form.

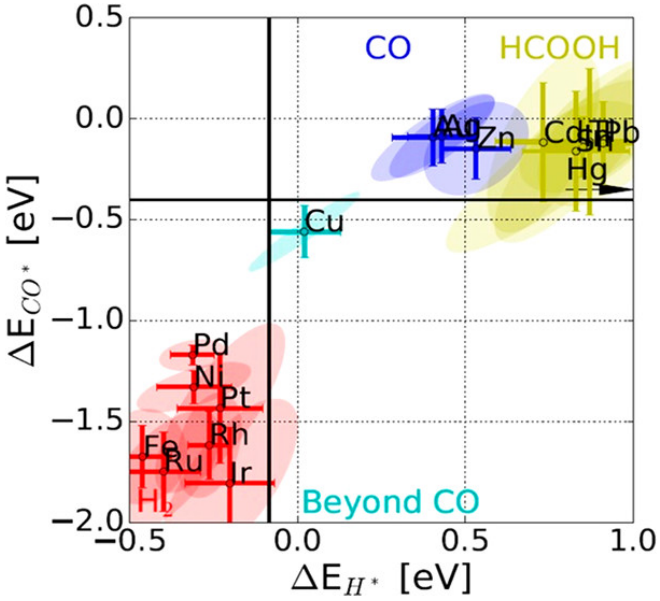

Figure 1.2*: Adsorption energy of CO* vs the adsorption energy of H*. Marks in red are metals that primarily produce* H_2*, teal marks produce products with more than two carbons, blue marks produce mainly CO and yellow marks produce predominantly HCOOH. Reproduced from Bragger et al. Copyright 2017, John Wiley and Sons*[27]

The first adsorption energy to consider is for H* because this defines the metals ability to perform the hydrogen evolution reaction (HER). Most transition metals have a high adsorption energy for H* (red marks in Fig. 1.2) making them very active for HER and therefore not suitable CO_2 reduction catalysts.[19,28] Late transition and p-block metals have much positive binding energy for H* making them much worse HER catalysts[29] (Pd, Cu, Ag, Au, Zn, Cd, Hg, In, Tl, Sn, Pb).

The next consideration is the binding energy for CO*. Metals that bind CO* very strongly (red marks in Fig. 1.2) are poor CO_2R catalysts because their active sites are quickly poisoned.[30] We say the sites are poisoned because the CO occupies the location where the CO_2 needs to bind to in order to be reduced. On the other hand, metals that bind CO* weakly (blue and yellow marks in Fig. 1.2) are unable to make higher order carbon products because the CO is released quickly from the surface. Metals that produce HCOOH as opposed to CO have a very similar adsorption energy of COOH* and H*, while metals that produce CO have a larger difference in the adsorption energy of COOH* and H*. The only metal known to date that can efficiently produce multi-carbon products is Cu (teal mark in Fig 1.2), and this is likely due to the fact that it is has a medium adsorption energy for CO* and a positive adsorption energy for H*.

1.4 Nanostructuring and surface facets of catalyst

After choosing what material to use the next important consideration is how to structure the catalyst. The first consideration is how to structure the catalyst so that the most favorable surface facet is facing the electrolyte. Different surface facets of metals adsorb intermediates differently due to their different electronic structure and number of dangling bonds. Therefore, being able to create devices with specific surface faceting can improve device performance. An important value for understanding and predicting the activity of a particular surface facet is the free energy (ΔG). When intermediates are absorbed onto the surface this changes the ΔG of that surface. The ideal catalyst would have no change in ΔG change throughout a reaction.

In the case of CO_2 reduction to CO, the Au (111) surface shows a change in ΔG double that of the Au (211) surface.[31] This implies that if an electrode is made with only Au (211) it will be highly active for CO. In addition, for Au there is a linear relation between the generalized coordination number of a surface and the overpotential required for CO_2R, with less undercoordinated surfaces requiring lower overpotentials.[32] For Cu the story becomes more complicated due to the number of possible reaction pathways. However, there are still striking differences in products between different facets. With Cu (100) being least active for HER and most active for C_2H_4 production, and Cu (111) being most active for CH_4 production.[33] The ability to structure a catalyst and control the exposed surface facets allows you optimize for different products and make the most efficient devices

Another advantage of nanostructuring the catalyst is that we can increase the activity per gram of material used. In general, undercoordinated sites are more active CO_2R, due to their perturbed electronic structure, which changes ΔG.[34,35] Therefore nanoparticles become an exciting structure for the catalyst because of the high density of undercoordinated sites. In the case of Au[31,32,36] and Cu[35,37–39] it has shown that generally as particles become smaller CO_2R increases.[40] Nanoparticles are not the only way to create a high density of undercoordinated sites, a variety of structures have been explored from nanopores, nanospikes, nanorods, nanofoam, etc. The advantages of these contiguous nanostructured films are that they do not require a conductive support and have more active sites relative to the top-down area as compared to a planar film. The increase in electrochemically active surface area relative to the top-down area allows for increased device performance. Chapter 2 further explores how nanostructuring gold can improve its selectivity and activity.

1.5 Improved CO_2 reduction via plasmonic metal nanoparticle

Light is an additional tool that can be used to enhance the selectively of a catalyst, in particular, plasmonic metal nanoparticles for CO_2 reduction. The given enhancement depends on the specifics of particular system and it requires detailed experiments to determine which mechanism is dominating, as multiple may occur at once. These mechanisms include (1) resonant photon scattering, (2) resonant energy transfer, (3) hot electron transfer, and (4) local photo thermal heating.[41–46]

To understand how light can change the selectivity of a plasmonic metal nanoparticle it is first important to understand the photophysics of how upon resonant optical excitation of plasmonic metal nanoparticle electrons are excited above the Fermi level energy of the metal and then decay back. Before the optical excitation, all electrons are distributed according to the Fermi-Dirac distribution,[47] in which nearly all electrons are restricted to states below Fermi energy and a single temperature (T_F) describes system. Immediately (t = 1-100fs) after optical excitation electrons are promoted above the Fermi level into an electron gas. At this point, these electrons are referred to as 'hot' because their electronic temperature has not equilibrated with the lattice.[41] These hot electrons when they are promoted above the Fermi level leave behind hot holes, deep vacancies in the electronic structure. These hot electrons and hot holes then decay (t = 100 fs -1ps) to a Fermi-Dirac like distribution with a higher electronic temperature than the lattice.[48–50] The hot carriers then continue to decay until they relax to the original electron distribution and the heat is transferred throughout the lattice. The goal of plasmonic photocatalysis is to harness the energy of these carriers before they relax back to the ground state and to use this harvested energy for improved activity and selectivity of the catalyst.

The time scale at which these hot carriers decay is much faster than that of the time scale of chemical reactions, picoseconds vs microseconds, as indicated by the photophysics. It is therefore useful to create a plasmonic metal semiconductor junction to separate hot electrons and hot holes, thereby prolonging their lifetime. Upon optical excitation the plasmonic metal hot electrons are lifted above the Fermi energy. A fraction of the hot carriers moves toward the metal/semiconductor interface. Hot electrons with energy above the valence band of the semiconductor or hot holes with energy below the valence band have a probability of being transferred into the semiconductor (there is still a chance that they be reflected.)[47,50] In the case of CO_2 reduction we usually use a p-type semiconductor so that it can harvest the hot holes out of the plasmonic metal. This leaves behind hot electrons that can then be transferred into the adsorbate. Due to the unique energy of these electrons, it can affect the selectivity of the reaction.[41,50–52] In this thesis we explore how plasmonic Au nanoparticles on p-type GaN[53] and plasmonic Cu nanoparticles on p-type nickel oxide[54] can enhance the CO_2 reduction reaction.

1.6 Local pH effects

Local pH, the measure of the proton concentration, is a critical parameter to device performance, and yet there currently exists minimal experimental understanding. While significant research has been put into the understanding of the catalyst,[18,21,55] there has been less effort to understand the local pH despite its ability to alter reaction selectivity and activity. In this section we will review how pH is influenced by and influences CO_2 concentration, activity of HER and CO_2R, and selectivity of CO_2R. It will also be discussed what techniques can be used to measure the local pH.

1.6.1 Electrolyte concentration and relevant species

There are two different pH values to consider in CO_2 reduction the pH at the catalyst surface and the bulk pH. Before any electrochemical reactions happen the pH locally and in the bulk are the same and defined by the electrolyte concentration and CO_2 saturation. Figure 1.3 shows the concentration of various species in a $KHCO_3/K_2CO_3$ electrolyte as a function of pH. The values for these concentrations can be found by looking at the rate and equilibrium constants for the following chemical reactions relating CO_2, HCO_3^-, CO_3^{2-}, H_2O, H^+, and OH^-. The first species that we consider is CO_2 because its concentration determines whether the electrode will be limited by its own activity or mass transport limitations. The amount of CO_2 dissolved in the electrolyte on pressure, temperature, and salinity of the electrolyte. The equilibrium between the gas and liquid phase of CO_2 is given by Henry's constant (K_0):

$$K_0 = \left(\frac{c_{CO_2}}{f_{CO_2}}\right) \tag{1.3}$$

$$\ln(\mathrm{K_0}) = 93.4517\left(\frac{100}{\mathrm{T}}\right) - 60.2409 + 23.3585\ln\left(\frac{\mathrm{T}}{100}\right) + \mathrm{S}\left(0.023517 - 0.023656\left(\frac{\mathrm{T}}{100}\right) + 0.0047036\left(\frac{\mathrm{T}}{100}\right)^2\right) \tag{1.4}$$

where $c_{CO_2}$is the concentration of dissolved CO_2, $f_{CO_2}$is the gas phase fugacity of CO_2, T is temperature in Kelvin, and S is salinity defined by the amount of salt in grams in 1kg of water (given in parts per thousand). This shows that the concentration of CO_2 decreases with increasing salt concentration.

The dissolved CO_2 dissociates at pH greater that 5 to bicarbonate and carbonate according to (1.5) and 1.6). The forward rate of reaction of (1.5) and (1.6) are $3.71*10^{-2}$ s^{-1} and 59.44 s^{-1} respectively.

$$CO_{2(aq)} + H_2O \rightleftharpoons H^+ + HCO_3^-, \quad pK = 6.37 \tag{1.5}$$

$$HCO_3^- \rightleftharpoons H^+ + CO_3^{2-}, \quad pK = 10.25 \tag{1.6}$$

The final reaction of note is for the dissociation of water. The forward rate of reaction of (1.7) is 2.4*10^{-5} mol/(L*s).

$$H_2O \rightleftharpoons H^+ + OH^-, \quad pK_a = 14 \tag{1.7}$$

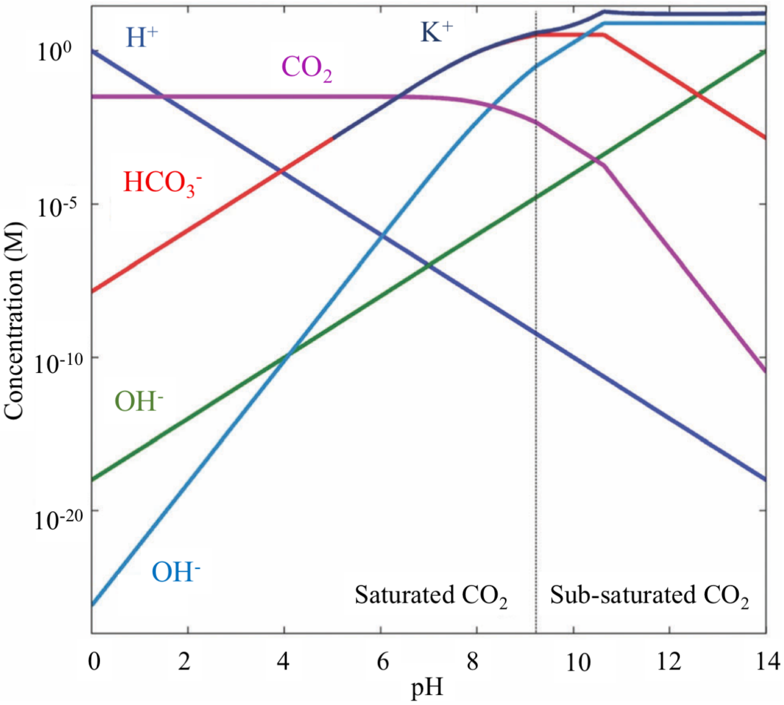

Figure 1.3*: Concentration of carbon dioxide, hydrogen, hydroxyl, bicarbonate, carbonate, and potassium ions as a function of bulk pH in a potassium (bi)carbonate electrolyte at 25°C and a pressure of 1atm. Reproduced from Singh, et al. Copyright 2015, Royal Society of Chemistry.*[26]

Using equations (1.3)-(1.7), Fig. 1.3 shows that to maximize the amount of dissolved CO_2 in an aqueous environment the pH must be kept below 9.2. However, ideally the reaction would occur as close to this pH as possible so that the number of protons can be reduced to suppress HER. We can also see that while the concentration of dissolved CO_2 is maximized below pH 9.2, the concentration never goes above 33mM, showing that in aqueous environments the reaction will be mass transport limited at current densities above roughly 20 mA/cm^2. To overcome this limitation devices have been designed that deliver CO_2 in the gas phase, which is discussed further is section 1.7. This initial look at CO_2, HCO_3^-, CO_3^{2-}, H_2O, H^+, and OH^- in bulk electrolyte is useful, however once the current density is non-zero at the electrode surface H^+, OH^-, and CO_2 begin to be consumed and/or created at the electrode surface. This creates a boundary layer between the electrode surface and the bulk pH. The size of this boundary layer depends on the buffering capability of the electrolyte and the magnitude of the current density. Typical boundary layers for aqueous CO_2 reduction tend to be between 10-

100 μm.[56] This means that the pH at the electrode surface can be quite different than that of the bulk. It is critical that we know what the pH is at the surface of the electrode because that we ultimately affect the reaction. Chapter 3 focuses exclusively on measuring the local pH of a CO_2 reduction electrode.

1.6.2 Dependence of HER and CO_2 reduction on pH

Both the HER and CO_2R require protons to complete the reaction (see Table 1.1). However, there are different mass transport requirements relative to protons for both HER and CO_2R. This has been explored by Hall, et al. on a Au rotating disk electrode.[57] In the experiment a polished polycrystalline is rotated at various speeds, and the rotation speed is proportional to the convective flow of reagents to the electrode surface.[58] As the Au electrode rotation speed is increased from 625 rpm to 3500 rpm, the current density for CO_2R is unchanged but the HER current density increases by ~22%.[57] This shows that CO_2R remains relatively unaffected by limited protons, whereas limited protons significantly suppresses HER. From this it becomes clear that by controlling the pH near the surface of the electrode, HER is suppressed. However, it is important to keep in mind that if the pH is too high that the concentration of CO_2 will decrease (Fig 2.2) and this will limit the current density for CO_2R. That is why it is critical that change in pH only occur locally so that the CO_2 can still be there in high concentration, which is only possible in a non-equilibrium state.

Another important consideration is that while the pH does not affect the total current density for CO_2R, it does impact which reactions occur. There have been numerous reports[59–64] of how the pH impacts what products are made, as will be discussed in later chapters of this thesis. One example shows that as the pH at the surface of the electrode increases the Faradaic efficiency (FE) for HER decreases.[59] They show this in an aqueous system on a Ag foam electrode using in situ Raman spectroscopy. We also see that on microporous Au electrodes that the FE for CO goes up and HER decreases as the pore depth increases.[57] This suggests that as the pores' depth increase, it becomes more difficult for protons to diffuse in, thus allowing for increased pH at the same current density and therefore creating more favorable conditions for CO_2R.

1.6.3 Techniques for the measurement of local pH

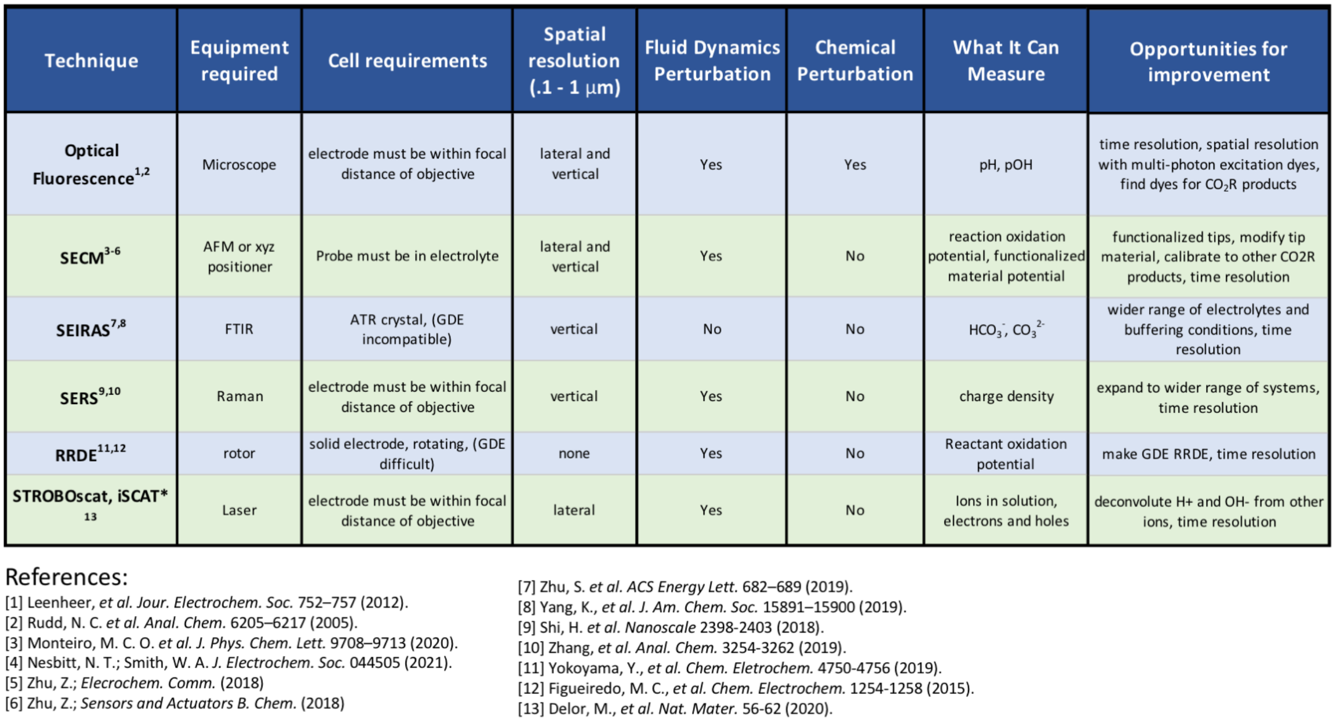

Technique	Equipment required	Cell requirements	Spatial resolution (.1 - 1 μm)	Fluid Dynamics Perturbation	Chemical Perturbation	What It Can Measure	Opportunities for improvement
Optical Fluorescence[1,2]	Microscope	electrode must be within focal distance of objective	lateral and vertical	Yes	Yes	pH, pOH	time resolution, spatial resolution with multi-photon excitation dyes, find dyes for CO_2R products
SECM[3-6]	AFM or xyz positioner	Probe must be in electrolyte	lateral and vertical	Yes	No	reaction oxidation potential, functionalized material potential	functionalized tips, modify tip material, calibrate to other CO2R products, time resolution
SEIRAS[7,8]	FTIR	ATR crystal, (GDE incompatible)	vertical	No	No	HCO_3^-, CO_3^{2-}	wider range of electrolytes and buffering conditions, time resolution
SERS[9,10]	Raman	electrode must be within focal distance of objective	vertical	Yes	No	charge density	expand to wider range of systems, time resolution
RRDE[11,12]	rotor	solid electrode, rotating, (GDE difficult)	none	Yes	No	Reactant oxidation potential	make GDE RRDE, time resolution
STROBOscat, iSCAT*[13]	Laser	electrode must be within focal distance of objective	lateral	Yes	No	Ions in solution, electrons and holes	deconvolute H+ and OH- from other ions, time resolution

References:

[1] Leenheer, *et al. Jour. Electrochem. Soc.* 752–757 (2012).
[2] Rudd, N. C. *et al. Anal. Chem.* 6205–6217 (2005).
[3] Monteiro, M. C. O. *et al. J. Phys. Chem. Lett.* 9708–9713 (2020).
[4] Nesbitt, N. T.; Smith, W. A. *J. Electrochem. Soc.* 044505 (2021).
[5] Zhu, Z.; *Elecrochem. Comm.* (2018)
[6] Zhu, Z.; *Sensors and Actuators B. Chem.* (2018)
[7] Zhu, S. *et al. ACS Energy Lett.* 682–689 (2019).
[8] Yang, K., *et al. J. Am. Chem. Soc.* 15891–15900 (2019).
[9] Shi, H. *et al. Nanoscale* 2398-2403 (2018).
[10] Zhang, *et al. Anal. Chem.* 3254-3262 (2019).
[11] Yokoyama, Y., *et al. Chem. Eletrochem.* 4750-4756 (2019).
[12] Figueiredo, M. C., *et al. Chem. Electrochem.* 1254-1258 (2015).
[13] Delor, M., *et al. Nat. Mater.* 56-62 (2020).

***Table 1.2**: List of techniques for measuring the local pH. The table also shows relevant metrics to compare techniques, such as temporal resolution, spatial resolution, and pH range.*

There are many techniques that can be used to measure the local pH (Table 1.2) each with their own advantages and disadvantages.[65] In this thesis (Chapter 4) we focus on using fluorescent confocal microscopy. This technique was chosen because it is able to provide spatial resolution in x, y and z. It can also be performed in situ with only small perturbations to the electrochemical reaction allowing it to be a platform to study many different catalysts. Finally, it can be used over a wide range of pH values by selecting the appropriate dye. Chapter 3 provides greater detail of the specifics of the device and the pH maps of CO_2 reduction electrodes.

1.7 Device components and CO_2 delivery method

Another consideration for device performance is the design of the device itself. There are many considerations to take into account when designing the device such as distance between electrodes, CO_2 delivery method, membrane, reference electrode, light, etc. While there are generic guidelines for device configuration, much depends on the purpose of the device (e.g., whether the device uses a photoanode or needs to be compatible with a confocal microscope). This section goes through the device components, why different configurations are chosen, and implications of different device design choice. Fig. 1.4 shows a schematic of an electrochemical cell. Electrons flow to the working electrode, cathode, to reduce CO_2 to hydrocarbons. The voltage of the working electrode is measured by a reference electrode, usually a Ag/AgCl, which has a stable and well known electrode potential. It is important that the reference electrode is as close as possible to the working to minimize a solution resistance between the two. The reference electrode is needed because it is not possible to measure the current and voltage between the working and counter electrodes at the same time; introducing a reference electrode solves this challenge.

A membrane is placed between the cathode and anode to prevent any reduced liquid products from being oxidized as well as to stop aqueous O_2 from poisoning the working electrode. There are several types of membranes used, cation exchange membrane (CEM), anion exchange membranes (AEM), and bi-polar membranes (BPM). CEMs allows for cations to flow freely through and AEMs allow for anions to move freely through. BPMs have a CEM and AEM layer, which causes water to dissociate and protons to be on the CEM side and hydroxyls to be on the AEM side. This enables solutions of different pH to be maintained on either side of membrane, however it increases the cell resistance. At the counter electrode, anode, water is oxidized to oxygen, equation (1.2). For all of the experiments performed in this thesis a platinum (Pt) foil or mesh was used for the anode due to its stability and low overpotential. However, Pt is expensive, so in a practical device a nickel (Ni) anode would be a more appropriate choice.

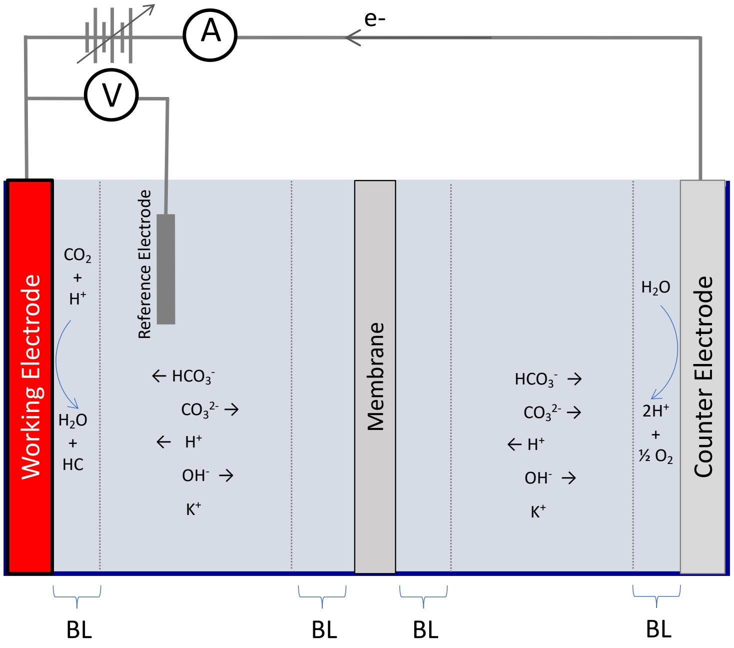

***Figure 1.4**: Schematic of a CO_2 reduction electrochemical cell. Electrons flow to the working electrode, cathode, to reduce CO_2 to hydrocarbons (HC), and electrons are removed from H_2O to create O_2 at the counter electrode, anode. The dotted regions indicate*

boundary layers (BL). Arrows indicate which way different species migrate through the BL. The reference electrode is used to measure the voltage being applied to the working electrode and the current is measured between the cathode and anode.

When combining these various components there are several important factors to consider — minimization of cell resistance, uniformity of voltage across electrodes, and experimental repeatability. Minimization of cell resistance can be accomplished by placing the anode and cathode as close together as possible without running into mass transport limitations. Membrane choice can also impact the cell resistance, with thinner membranes are generally more conductive. It is also important for the voltage across the cathode to be uniform, which can be achieved via a parallel plate configuration.[26] This is not always possible, e.g., when using a photocathode, causing the anode and cathode to be offset.[66] The need for a parallel plate configuration and to have reproducibility between experiments, has led to the use of compression cells.[26] This allows the anode, cathode, and reference electrode to be placed in the exact same position each time and in the optimal configuration. Despite the cost, the best material to make the cell out of is polyether ether ketone (PEEK) due to its hardness and chemical stability. The hardness is crucial so that plastic fittings can be screwed into it without damaging the threads, as well as to prevent the risk of the cell cracking under compression. The chemical stability also means that the cell can be thoroughly cleaned in nitric acid and/or aqua regia thus reducing the risk of contamination between experiments. While many of the considerations listed here may appear obvious, they are critical in being able to obtain consistent results and to be able to reproduce results in literature.

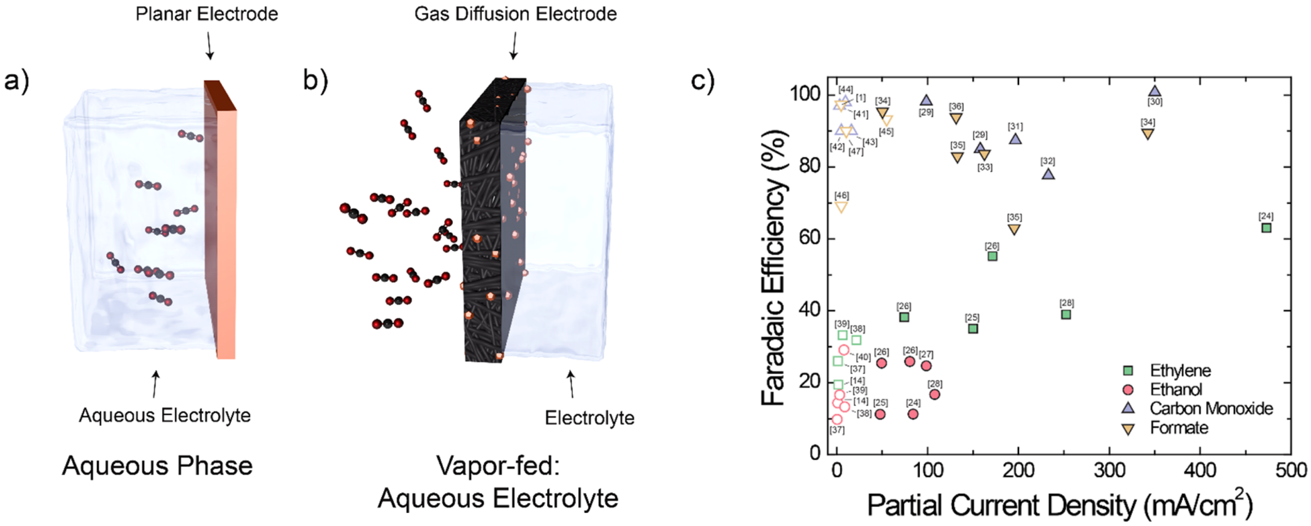

Figure 1.5: *Different electrochemical CO_2 reduction reaction schemes are shown in (a) and (b). (a) shows a schematic of aqueous-phase CO_2 reduction where CO_2 is first dissolved in an aqueous electrolyte then reduced at catalyst surface. (b) shows a vapor fed*

CO_2 reduction system where the CO_2 is delivered in gas phase to catalyst on a gas diffusion electrode; the electrolyte can either be aqueous or polymer. (c) shows a plot of Faradaic efficiency vs. partial current density for different reported devices. Open shapes refer to aqueous-phase CO_2 reduction and filled shapes represent vapor-fed CO_2 reduction devices. The numbers on the plot refer to references from the original paper. Reproduced from Higgins et al. Copyright 2019, American Chemical Society.[67]

The final device consideration which is critical to device performance is the choice of CO_2 delivery method. There are two different options for CO_2 delivery, either the CO_2 can be dissolved into the electrolyte, or the CO_2 can be delivered to the catalyst in the gas phase using a gas diffusion electrode. When scientists first began studying CO_2 reduction aqueous CO_2 systems were predominantly used (Fig. 1.5a).[18,19] This system while complex is simpler to understand relative to a gas fed system. This is due to the fact that when the CO_2 is aqueous the whole system fits into the mold a typical electrochemical reaction, where the reactant is dissolved in the electrolyte, planar metal catalysts can be used, and the anode and cathode are fully wetted and electrically connected via the electrolyte. Despite the advantages of simplicity, it is not possible to run CO_2 reduction at high current densities in aqueous CO_2 fed systems, due to the low solubility of CO_2 in water (33mM).[26,67] In addition the pH of the electrolyte must be kept near neutral to maximize CO_2 solubility, meaning that there is an abundance of protons available creating favorable conditions for HER.[26]

In order to overcome these challenges, researchers have developed porous electrodes where CO_2 can be fed to the catalyst in gas phase, Fig 1.5b.[67] This has allowed for devices to be built that not only had improved current density, but also improved selectivities. We see in Fig 1.5c that the maximum current density observed for an aqueous fed device was around 20 mA/cm^2, but for vapor fed devices we see that many devices reach hundreds of mA/cm^2. We also see an increased Faradaic efficiency for higher order products like ethylene

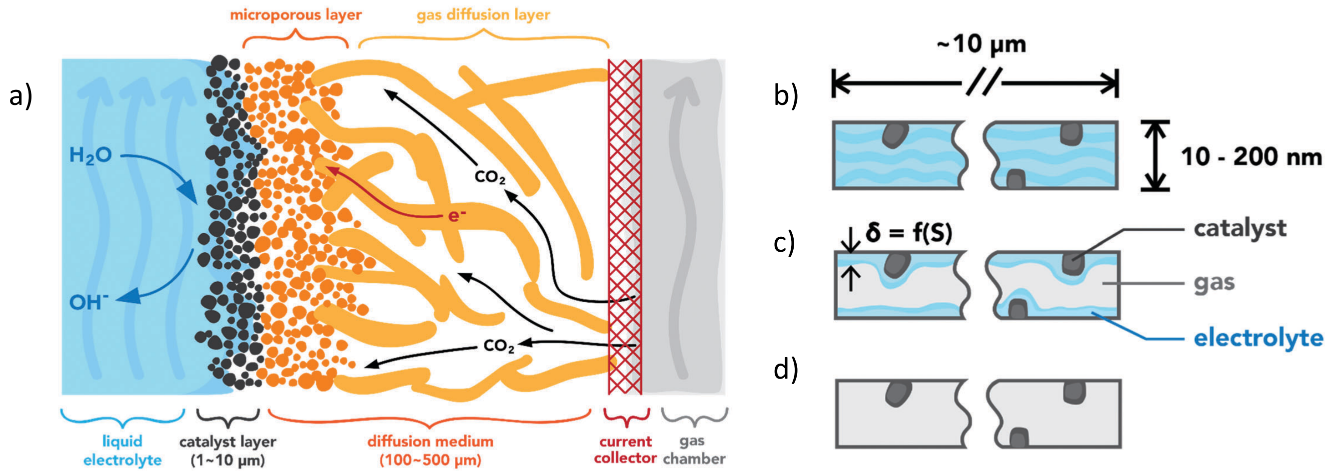

***Figure 1.6**: (a) shows a schematic of gas diffusion CO_2 reduction electrode. The orange lines are carbon fibers, the orange circles are carbon black, and the black circles are catalyst. (b)-(d) show different states that the catalyst can be in; (b) is flooded, (c) is wetted, and (d) is dry. This was reproduced and edited from Weng et al. Copyright 2018, Royal Society of Chemistry.*[68]

These improvements are due to the increased flux of CO_2 to the catalyst which allows for higher current densities. In addition, the electrolyte can have a much higher pH since the CO_2 is being delivered in gas phase, which suppresses HER due to the lack of protons. A typical gas diffusion electrode (GDE) is composed of carbon fiber and carbon black support with catalyst coated on top (Fig. 1.6a). On the backside of the carbon paper is a gas chamber of pure CO_2; the CO_2 diffuses through the network of carbon fibers towards the electrolyte. Coated on the carbon fibers is the microporous layer which is typically composed of carbon black and polytetrafluoroethylene (PTFE). The carbon black provides conductivity and the PTFE is hydrophobic to prevent flooding. On top of the microporous layer the catalyst is coated and in contact with the electrolyte.

Despite the advantages of this new device configuration, it adds new complexity to the system. In the aqueous system all of the catalyst was always in contact with the electrolyte, if the catalyst is not in contact with the electrolyte no reaction can occur since there are no protons for the reaction and the cathode is not electrically connected to the anode. In a vapor fed device there are now three states that the catalyst can be in flooded, wetted, and dry (Fig 1.6b-d). When the catalyst is dry no reaction can occur because it not contacted with the electrolyte. If the catalyst is flooded, the high current densities cannot be achieved due to the low solubility of CO_2 in water which causes mass transport limitations. To create a stable wetted condition the pressure of the CO_2 and electrolyte must be carefully balanced. Catalyst coatings are also often employed to prevent flooding. This device also raises new questions about the physics of the device: (1) how thick is the electrolyte layer, (2) what is the concentration of CO_2, H^+, and OH^- in this layer, and (3) what percentage of the catalyst is in this wetted condition. This thesis seeks to experimentally answers these questions (Chapter 4) and use this knowledge to create an optimized GDE structure (Chapter 3).

1.8 Thesis Outline

This thesis provides deeper understanding to how the local catalyst environment can affect the CO_2R reaction. Chapter 2 focuses on how nanostructured catalysts can induce local pH gradients for improved CO_2 reduction selectivity. Chapter 3 combines nanostructured catalysts and gas diffusion electrodes for improved device performance. Chapter 4 demonstrates a confocal fluorescent microscopy system to measure the local pH in CO_R gas diffusion electrodes. Chapter 5 and 6 shows how light can be used to affect the CO_2R reaction, specifically looking at plasmon-mediated electron transfer in metal/semiconductor heterojunctions. Then in Chapter 6 and 7 the focus shifts to how various CO_2 capture and conversion systems to provide insight on what the optimal systems are to be deployed commercially and provides techno-economic analysis. Finally, Chapter 8 summarizes the main outcomes and contributions of this thesis. Additionally, it provides perspective on future experiments for local pH measurements.

BIBLIOGRAPHY CHAPTER 1

1. Masson-Delmotte, V.; Zhai, P.; Pörtner, H.-O.; Roberts, D.; Skea, J.; Shukla, P. R.; Pirani, A. *IPCC Report: Global Warming of 1.5°C*; 2018.
2. Le Quéré, C.; Andrew, R. M.; Friedlingstein, P.; Sitch, S.; Pongratz, J.; Manning, A. C.; Korsbakken, J. I.; Peters, G. P.; Canadell, J. G.; Jackson, R. B.; Boden, T. A.; Tans, P. P.; Andrews, O. D.; Arora, V. K.; Bakker, D. C. E.; Barbero, L.; Becker, M.; Betts, R. A.; Bopp, L.; Chevallier, F.; Chini, L. P.; Ciais, P.; Cosca, C. E.; Cross, J.; Currie, K.; Gasser, T.; Harris, I.; Hauck, J.; Haverd, V.; Houghton, R. A.; Hunt, C. W.; Hurtt, G.; Ilyina, T.; Jain, A. K.; Kato, E.; Kautz, M.; Keeling, R. F.; Klein Goldewijk, K.; Körtzinger, A.; Landschützer, P.; Lefèvre, N.; Lenton, A.; Lienert, S.; Lima, I.; Lombardozzi, D.; Metzl, N.; Millero, F.; Monteiro, P. M. S.; Munro, D. R.; Nabel, J. E. M. S.; Nakaoka, S.; Nojiri, Y.; Padín, X. A.; Peregon, A.; Pfeil, B.; Pierrot, D.; Poulter, B.; Rehder, G.; Reimer, J.; Rödenbeck, C.; Schwinger, J.; Séférian, R.; Skjelvan, I.; Stocker, B. D.; Tian, H.; Tilbrook, B.; van der Laan-Luijkx, I. T.; van der Werf, G. R.; van Heuven, S.; Viovy, N.; Vuichard, N.; Walker, A. P.; Watson, A. J.; Wiltshire, A. J.; Zaehle, S.; Zhu, D. Global Carbon Budget 2018. *Earth Syst. Sci. Data Discuss.* **2018**.
3. Davis, S. J.; Lewis, N. S.; Shaner, M.; Aggarwal, S.; Arent, D.; Azevedo, I. L.; Benson, S. M.; Bradley, T.; Brouwer, J.; Chiang, Y. M.; Clack, C. T. M.; Cohen, A.; Doig, S.; Edmonds, J.; Fennell, P.; Field, C. B.; Hannegan, B.; Hodge, B. M.; Hoffert, M. I.; Ingersoll, E.; Jaramillo, P.; Lackner, K. S.; Mach, K. J.; Mastrandrea, M.; Ogden, J.; Peterson, P. F.; Sanchez, D. L.; Sperling, D.; Stagner, J.; Trancik, J. E.; Yang, C. J.; Caldeira, K. Net-Zero Emissions Energy Systems. *Science (80-.).* **2018**, *360* (6396).
4. Lewis, N. S. Toward Cost Effective Solar. *Science (80-.).* **2007**, *798* (1), 798–802.
5. Dowling, J. A.; Rinaldi, K. Z.; Ruggles, T. H.; Davis, S. J.; Yuan, M.; Tong, F.; Lewis, N. S.; Caldeira, K. Role of Long-Duration Energy Storage in Variable Renewable Electricity Systems. *Joule* **2020**, *4* (9), 1907–1928.
6. Yang, Z.; Zhang, J.; Kintner-meyer, M. C. W.; Lu, X.; Choi, D.; Lemmon, J. P. Electrochemical Energy Storage for Green Grid: Status and Challenges. *Chem. Rev.* **2011**, *111* (5), 3577–3613.
7. U.S. Department of Energy. *Grid Energy Storage Report*; 2013.

8. Administration, U. S. E. I. Few Transportation Fuels Surpass the Energy Densities of Gasoline and Diesel. *Today In Energy* **2013**, 9991.
9. What is cement? https://www.worldcoal.org/coal/uses-coal/coal-cement (accessed Feb 10, 2020).
10. Andrew, R. M. Global CO_2 Emissions from Cement Production, 1928-2018. *Earth Syst. Sci. Data* **2019**, *11* (4), 1675–1710.
11. World Steel Association. World Steel Figures. *2020 World steel Fig.* **2020**.
12. Geyer, R.; Jambeck, J. R.; Law, K. L. Production, Use, and Fate of All Plastics Ever Made. *Sci. Adv.* **2017**, *3* (7), 25–29.
13. Rissman, J.; Bataille, C.; Masanet, E.; Aden, N.; Morrow, W. R.; Zhou, N.; Elliott, N.; Dell, R.; Heeren, N.; Huckestein, B.; Cresko, J.; Miller, S. A.; Roy, J.; Fennell, P.; Cremmins, B.; Koch Blank, T.; Hone, D.; Williams, E. D.; de la Rue du Can, S.; Sisson, B.; Williams, M.; Katzenberger, J.; Burtraw, D.; Sethi, G.; Ping, H.; Danielson, D.; Lu, H.; Lorber, T.; Dinkel, J.; Helseth, J. Technologies and Policies to Decarbonize Global Industry: Review and Assessment of Mitigation Drivers through 2070. *Appl. Energy* **2020**, *266* (November 2019), 114848.
14. Ore, I.; Pigments, I. O.; Rock, P.; Crystal, Q.; Earths, R.; Ash, S. *Mineral Commodity Summaries 2021*; 2021.
15. Nitopi, S. A. Understanding the Factors That Govern Activity and Selectivity of the Electrochemical Carbon Dioxide Reduction Reaction on Copper Catalysts, Stanford, 2019.
16. Welch, A. J.; Dunn, E.; Duchene, J. S.; Atwater, H. A. Bicarbonate or Carbonate Processes for Coupling Carbon Dioxide Capture and Electrochemical Conversion. *ACS Energy Lett.* **2020**, *5* (3), 940–945.
17. Dau, H.; Limberg, C.; Reier, T.; Risch, M.; Roggan, S.; Strasser, P. The Mechanism of Water Oxidation: From Electrolysis via Homogeneous to Biological Catalysis. *ChemCatChem* **2010**, *2* (7), 724–761. https://doi.org/10.1002/cctc.201000126.
18. Hori, Y.; Vayenas, C. G.; White, R. E.; Gamboa-Aldeco, M. E. Electrochemical CO_2 Reduction on Metal Electrodes. In *Modern Aspects of Electrochemistry*; Springer: New York, 2008; pp 89–189. https://doi.org/https://doi.org/10.1007/978-0-387-49489-0_3.
19. Hori, Yoshio Kikuchi, Katsuhei Suzuki, S. Production of CO and CH_4 in the Electrochemical Reduction of CO_2 at Metal Electrodes in Aqueous Hydrogencarbonate Solution. *Chem. Lett.* **1985**, 1695–1698.
20. Appel, A. M.; Bercaw, J. E.; Bocarsly, A. B.; Dobbek, H.; Dubois, D. L.; Dupuis, M.; Ferry, J. G.; Fujita, E.; Hille, R.; Kenis, P. J. A.; Kerfeld, C. A.; Morris, R. H.; Peden, C. H. F.; Portis, A. R.; Ragsdale, S. W.; Rauchfuss, T. B.; Reek, J. N. H.; Seefeldt, L. C.; Thauer, R. K.; Waldrop, G. L. Frontiers, Opportunities, and Challenges in Biochemical and Chemical Catalysis of CO_2 Fixation. *Chem. Rev.* **2013**, *113* (8), 6621–6658.
21. White, J. L.; Baruch, M. F.; Pander, J. E.; Hu, Y.; Fortmeyer, I. C.; Park, J. E.; Zhang, T.; Liao, K.; Gu, J.; Yan, Y.; Shaw, T. W.; Abelev, E.; Bocarsly, A. B. Light-Driven Heterogeneous Reduction of Carbon Dioxide: Photocatalysts and Photoelectrodes. *Chem.*

Rev. **2015**, *115* (23), 12888–12935.

22. Gattrell, M.; Gupta, N.; Co, A. A Review of the Aqueous Electrochemical Reduction of CO_2 to Hydrocarbons at Copper. *J. Electroanal. Chem.* **2006**, *594* (1), 1–19.
23. Qiao, J.; Liu, Y.; Hong, F.; Zhang, J. *A Review of Catalysts for the Electroreduction of Carbon Dioxide to Produce Low-Carbon Fuels*; 2014; Vol. 43. https://doi.org/10.1039/c3cs60323g.
24. Kortlever, R.; Shen, J.; Schouten, K. J. P.; Calle-Vallejo, F.; Koper, M. T. M. Catalysts and Reaction Pathways for the Electrochemical Reduction of Carbon Dioxide. *J. Phys. Chem. Lett.* **2015**, *6* (20), 4073–4082.
25. Linstrom, P. J.; Mallard, W. G. NIST Chemistry WebBook, NIST Standard Reference Database Number 69. *National Institute of Standards and Technology*. 2014, p 20899.
26. Singh, M. R.; Clark, E. L.; Bell, A. T. Effects of Electrolyte, Catalyst, and Membrane Composition and Operating Conditions on the Performance of Solar-Driven Electrochemical Reduction of Carbon Dioxide. *Phys. Chem. Chem. Phys.* **2015**, *17* (29), 18924–18936.
27. Bagger, A.; Ju, W.; Varela, A. S.; Strasser, P.; Rossmeisl, J. Electrochemical CO_2 Reduction: A Classification Problem. *ChemPhysChem* **2017**, *18* (22), 3266–3273.
28. Noda, H.; Ikeda, S.; Oda, Y.; Imai, K.; Maeda, M.; Ito, K. Electrochemical Reduction of Carbon Dioxide at Various Metal Electrodes in Aqueous Potassium Hydrogen Carbonate Solution. *Chem. Soc. Japan* **1990**, *63* (9), 2459–2462.
29. Nørskov, J. K.; Bligaard, T.; Logadottir, A.; Kitchin, J. R.; Chen, J. G.; Pandelov, S.; Stimming, U. Trends in the Exchange Current for Hydrogen Evolution. *J. Electrochem. Soc.* **2005**, *152* (3), J23.
30. Kuhl, K. P.; Hatsukade, T.; Cave, E. R.; Abram, D. N.; Kibsgaard, J.; Jaramillo, T. F. Electrocatalytic Conversion of Carbon Dioxide to Methane and Methanol on Transition Metal Surfaces. *J. Am. Chem. Soc.* **2014**, *136* (40), 14107–14113.
31. Zhu, W.; Michalsky, R.; Metin, Ö.; Lv, H.; Guo, S.; Wright, C. J.; Sun, X.; Peterson, A. A.; Sun, S. Monodisperse Au Nanoparticles for Selective Electrocatalytic Reduction of CO_2 to CO. *J. Am. Chem. Soc.* **2013**, *135* (45), 16833–16836.
32. Zhang, W.; He, J.; Liu, S.; Niu, W.; Liu, P.; Zhao, Y.; Pang, F.; Xi, W.; Chen, M.; Pang, S. S.; Ding, Y. Atomic Origins of High Electrochemical CO_2 Reduction Efficiency on Nanoporous Gold. *Nanoscale* **2018**, *10* (18), 8372–8376.
33. De Gregorio, G. L.; Burdyny, T.; Loiudice, A.; Iyengar, P.; Smith, W. A.; Buonsanti, R. Facet-Dependent Selectivity of Cu Catalysts in Electrochemical CO_2 Reduction at Commercially Viable Current Densities. *ACS Catal.* **2020**, *10* (9), 4854–4862.
34. Welch, A. J.; Duchene, J. S.; Tagliabue, G.; Davoyan, A.; Cheng, W. H.; Atwater, H. A. Nanoporous Gold as a Highly Selective and Active Carbon Dioxide Reduction Catalyst. *ACS Appl. Energy Mater.* **2019**, *2* (1), 164–170. https://doi.org/10.1021/acsaem.8b01570.
35. Nitopi, S.; Bertheussen, E.; Scott, S. B.; Liu, X.; Engstfeld, A. K.; Horch, S.; Seger, B.; Stephens, I. E. L.; Chan, K.; Hahn, C.; Nørskov, J. K.; Jaramillo, T. F.; Chorkendorff, I. Progress and Perspectives of Electrochemical CO_2 Reduction on Copper in Aqueous Electrolyte. *Chem. Rev.* **2019**, *119* (12), 7610–7672.

36. Mariano, R. G.; McKelvey, K.; White, H. S.; Kanan, M. W. Selective Increase in CO_2 Electroreduction Activity at Grain-Boundary Surface Terminations. *Science (80-.).* **2017**, *358* (6367), 1187–1192.
37. Manthiram, K.; Beberwyck, B. J.; Alivisatos, A. P. Enhanced Electrochemical Methanation of Carbon Dioxide with a Dispersible Nanoscale Copper Catalyst. *J. Am. Chem. Soc.* **2014**, *136* (38), 13319–13325.
38. Loiudice, A.; Lobaccaro, P.; Kamali, E. A.; Thao, T.; Huang, B. H.; Ager, J. W.; Buonsanti, R. Tailoring Copper Nanocrystals towards C2 Products in Electrochemical CO_2 Reduction. *Angew. Chemie - Int. Ed.* **2016**, *55* (19), 5789–5792.
39. Reske, R.; Mistry, H.; Behafarid, F.; Roldan Cuenya, B.; Strasser, P. Particle Size Effects in the Catalytic Electroreduction of CO_2 on Cu Nanoparticles. *J. Am. Chem. Soc.* **2014**, *136* (19), 6978–6986.
40. Hammer, B.; Morikawa, Y.; Nørskov, J. K. CO Chemisorption at Metal Surfaces and Overlayers. *Phys. Rev. Lett.* **1996**, *76* (12), 2141–2144. https://doi.org/10.1103/PhysRevLett.76.2141.
41. Linic, S.; Christopher, P.; Ingram, D. B. Plasmonic-Metal Nanostructures for Efficient Conversion of Solar to Chemical Energy. *Nat. Mater.* **2011**, *10* (12), 911–921.
42. Atwater, H. A.; Polman, A. Plasmonics for Improved Photovoltaic Devices. *Nat. Mater.* **2010**, *9* (3), 205–213.
43. Warren, S. C.; Thimsen, E. Plasmonic Solar Water Splitting. *Energy Environ. Sci.* **2012**, *5* (1), 5133–5146.
44. Hou, W.; Cronin, S. B. A Review of Surface Plasmon Resonance-Enhanced Photocatalysis. *Adv. Funct. Mater.* **2013**, *23* (13), 1612–1619.
45. Linic, S.; Aslam, U.; Boerigter, C.; Morabito, M. Photochemical Transformations on Plasmonic Metal Nanoparticles. **2015**, *14* (June).
46. Linic, S.; Christopher, P.; Xin, H.; Marimuthu, A. Catalytic and Photocatalytic Transformations on Metal Nanoparticles with Targeted Geometric and Plasmonic Properties. *Acc. Chem. Res.* **2013**, *46* (8), 1890–1899.
47. Ashcroft, N. W.; Mermin, N. D. *Solid State Physics*; Hartcourt College: New York, 1976.
48. Link, S.; El-Sayed, M. A. Optical Properties and Ultrafast Dynamics of Metallic Nanocrystals. *Annu. Rev. Phys. Chem.* **2003**, *54*, 331–366.
49. Hartland, G. V. Optical Studies of Dynamics in Noble Metal Nanostructures. *Chem. Rev.* **2011**, *111* (6), 3858–3887.
50. Brongersma, M. L.; Halas, N. J.; Nordlander, P. Plasmon-Induced Hot Carrier Science and Technology. *Nat. Nanotechnol.* **2015**, *10* (1), 25–34.
51. Clavero, C. Plasmon-Induced Hot-Electron Generation at Nanoparticle/Metal-Oxide Interfaces for Photovoltaic and Photocatalytic Devices. *Nat. Photonics* **2014**, *8* (2), 95–103.
52. Christopher, P.; Moskovits, M. Hot Charge Carrier Transmission from Plasmonic Nanostructures. *Annu. Rev. Phys. Chem.* **2017**, *68* (March), 379–398.
53. Duchene, J. S.; Tagliabue, G.; Welch, A. J.; Cheng, W. H.; Atwater, H. A. Hot Hole Collection and Photoelectrochemical CO_2 Reduction with Plasmonic Au/p-GaN

Photocathodes. *Nano Lett.* **2018**, *18* (4), 2545–2550.

54. Duchene, J. S.; Tagliabue, G.; Welch, A. J.; Li, X.; Cheng, W. H.; Atwater, H. A. Optical Excitation of a Nanoparticle Cu/p-NiO Photocathode Improves Reaction Selectivity for CO_2 Reduction in Aqueous Electrolytes. *Nano Lett.* **2020**, *20* (4), 2348–2358.
55. De Luna, P.; Hahn, C.; Higgins, D.; Jaffer, S. A.; Jaramillo, T. F.; Sargent, E. H. What Would It Take for Renewably Powered Electrosynthesis to Displace Petrochemical Processes? *Science (80-.).* **2019**, *364* (6438).
56. Singh, M. R.; Clark, E. L.; Bell, A. T. Effects of Electrolyte, Catalyst, and Membrane Composition and Operating Conditions on the Performance of Solar-Driven Electrochemical Reduction of Carbon Dioxide. *Phys. Chem. Chem. Phys.* **2015**, *17*, 18924–18936.
57. Hall, A. S.; Yoon, Y.; Wuttig, A.; Surendranath, Y. Mesostructure-Induced Selectivity in CO_2 Reduction Catalysis. *J. Am. Chem. Soc.* **2015**, *137* (47), 14834–14837.
58. Bard, A. J.; Faulkner, L. R. *Fundamentals and Applications of Needle Trap Devices*; 2002; Vol. 2.
59. Zhang, Z.; Melo, L.; Jansonius, R. P.; Habibzadeh, F.; Grant, E. R.; Berlinguette, C. P. PH Matters When Reducing CO2in an Electrochemical Flow Cell. *ACS Energy Lett.* **2020**, *5* (10), 3101–3107.
60. Lu, X.; Zhu, C.; Wu, Z.; Xuan, J.; Francisco, J. S.; Wang, H. In Situ Observation of the PH Gradient near the Gas Diffusion Electrode of CO_2 Reduction in Alkaline Electrolyte. *J. Am. Chem. Soc.* **2020**, *142* (36), 15438–15444.
61. Wang, L.; Nitopi, S. A.; Bertheussen, E.; Orazov, M.; Morales-Guio, C. G.; Liu, X.; Higgins, D. C.; Chan, K.; Nørskov, J. K.; Hahn, C.; Jaramillo, T. F. Electrochemical Carbon Monoxide Reduction on Polycrystalline Copper: Effects of Potential, Pressure, and PH on Selectivity toward Multicarbon and Oxygenated Products. *ACS Catal.* **2018**, *8* (8), 7445–7454.
62. Yang, K.; Kas, R.; Smith, W. A. In Situ Infrared Spectroscopy Reveals Persistent Alkalinity near Electrode Surfaces during CO_2 Electroreduction. *J. Am. Chem. Soc.* **2019**, *141* (40).
63. Nesbitt, N.; Smith, W. Water Activity Regulates CO_2 Reduction in Gas-Diffusion Electrodes. *ChemRxiv* **2021**, No. January. https://doi.org/10.26434/chemrxiv.13571141.
64. Nesbitt, N.; Smith, W. A. Operando Topography and Mechanical Property Mappinig of CO_2 Reduction Gas-Diffusion Electrodes Operating at High Currrent Densities. *J. Electrochem. Soc.* **2021**.
65. Monteiro, M. C. O.; Koper, M. T. M. Measuring Local PH in Electrochemistry. *Curr. Opin. Electrochem.* **2021**, *25*, 100649.
66. Corson, E. R.; Creel, E. B.; Kim, Y.; Urban, J. J.; Kostecki, R.; McCloskey, B. D. A Temperature-Controlled Photoelectrochemical Cell for Quantitative Product Analysis. *Rev. Sci. Instrum.* **2018**, *89* (5).
67. Higgins, D.; Hahn, C.; Xiang, C.; Jaramillo, T. F.; Weber, A. Z. Gas-Diffusion Electrodes for Carbon Dioxide Reduction: A New Paradigm. *ACS Energy Lett.* **2019**, *4*, 317–324. https://doi.org/DOI: 10.1021/acsenergylett.8b02035.
68. Weng, L.-C.; Bell, A. T.; Weber, A. Z. Modeling Gas-Diffusion Electrodes for CO_2

Reduction. *Phys. Chem. Chem. Phys.* **2018**, No. 20, 16973–16984.

Chapter 2

NANOPOROUS GOLD AS A HIGHLY SELECTIVE AND ACTIVE CARBON DIOXIDE REDUCTION CATALYST

2.1 Introduction

The ability to reduce CO_2 into useful chemicals or fuels will not only enable clean technology, but it will also close the carbon cycle by recycling CO_2 and preventing its further addition to the atmosphere.[1] The CO_2 reduction products can either be liquid fuels like ethanol or gaseous products like syngas (H_2 and CO), which are feedstocks for thermocatalytic transformations via the Fischer−Tropsch process.[2–5] To date, CO_2 reduction is not a widespread technology because of low energy efficiency associated with high overpotentials, a lack of electrocatalytic stability, and poor selectivity for the CO_2 reduction reaction (CO_2RR) over the H_2 evolution reaction (HER), which results in low partial-current densities for the product of interest.[6]

Various approaches have been explored to improve the activity and selectivity of Au-based electrocatalysts for the CO_2RR, from controlling nanocrystal size to tailoring of the exposed crystal facets, and even surface functionalization with molecular coatings.[7–12] Recently, nanoporous catalytic architectures have shown promise for electrochemical CO_2 reduction due to their large internal surface area and prevalence of stepped sites and grain boundaries inherent in their complex structure of highly-curved metal ligaments.[13–19] This propensity for under-coordinated atomic sites has been suggested to play a pivotal role in improving the selectivity of CO_2 reduction in nanoporous silver (np-Ag) cathodes by stabilizing CO_2^- intermediates involved in the electrochemical conversion of CO_2 to CO.[13] Similar mechanisms have been invoked to explain the electrocatalytic performance of nanoporous gold (np-Au) films.[18,19] While the highly-irregular surface atomic structure of np-Au is well known, relatively less attention has been devoted to exploring how molecular transport into and out of such a tightly-confined catalytic system may also affect the selectivity for CO_2 reduction within the porous network. Mesoporous Au films with controlled pore sizes around 200 nm in diameter have previously been shown to exhibit increased selectivity for CO_2 reduction with increasing film thickness from 0.5 μm up to 2.7 μm.[20] The improved selectivity is attributed to the formation of a pH gradient within the porous network as protons are consumed during electrolysis faster than they can be replenished by the supporting electrolyte; this effect is increased with increasing thickness of the mesoporous metal cathode. Although this study only adjusted the overall film thickness, these observations strongly suggest that fine-tuning the metal porosity by controlling the pore size could offer a simple route to further improving the selectivity of porous cathodes for electrochemical CO_2 reduction in aqueous electrolytes.

Here, we use np-Au films with pore diameters on the order of tens of nanometers to explore the influence of metal porosity on the selectivity for CO_2 reduction in aqueous electrolytes. Due to their small pore diameters, the porous network of metal ligaments is able to sustain pH gradients within np-Au films that are half as thick (~800 nm) as those previously reported in mesoporous Au films (~2 μm).[20] This effect becomes more prominent upon further decreasing the pore diameter from ~30 nm down to ~10 nm, as evidenced by electrochemical studies. We find that np-Au films are highly selective for the conversion of CO_2 to CO with high Faradaic efficiency (FE ~99%) at modest overpotentials (η = 0.40 V), while at the same time delivering large partial current densities for CO (J_{CO} = 6.2 mA cm^{-2}). Finally, we demonstrate that these np-Au films exhibit excellent electrochemical durability and maintain Faradaic efficiency of ~80% for CO production over 4.5 days of continuous electrolysis at an applied potential of E = –0.5 V vs the reversible hydrogen electrode (RHE).

2.2 Fabrication and Characterization of Catalyst

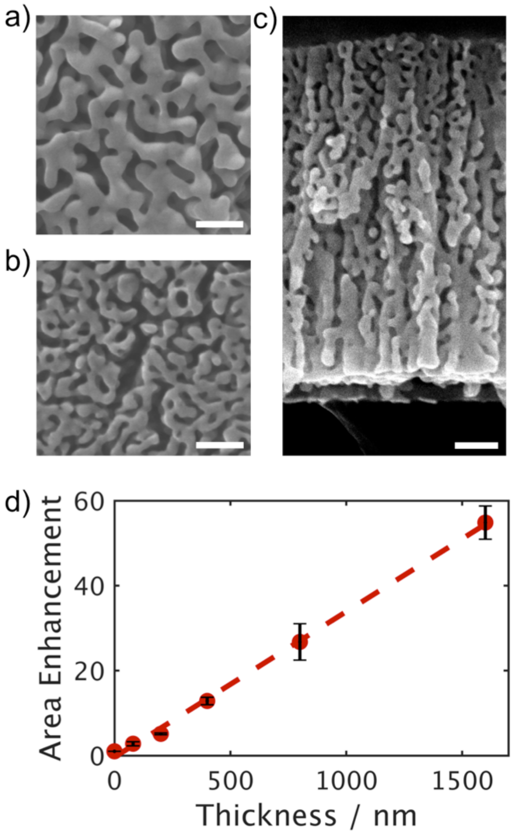

Figure 2.1: *Helium FIB images of (a) top-down view of a nanoporous Au (np-Au) film that was etched at room temperature (RT) and (b) top-down view of a np-Au film that was etched at low temperature (LT). (c) SEM cross-section image of a RT-etched*

np-Au film. All scale bars represent 100 nm. (d) Electrochemical surface area enhancement as a function of film thickness for RT-etched np-Au films as determined by Cu underpotential deposition (UPD) experiments.

The np-Au films were fabricated by electron-beam deposition of Ag and Au alloys onto clean silicon (Si) substrates (Si [p-type, 0-10 Ω cm, (100) orientation, 620 ± 25 μm thick, University Wafers]), followed by selectively etching Ag from the Ag/Au alloy with nitric acid (see Methods). Briefly, An AMOD dual electron beam deposition system (System 02520, Angstrom Engineering) was used to fabricate all samples. First, Si substrates were cleaned by sonicating sequentially in acetone, isopropanol, and deionized water for five minutes each. The samples were then stored in deionized water until they were dried with N_2 prior to being placed in the electron beam deposition chamber. The materials for electron beam deposition were ordered from Plasmaterials. The Au target was 99.99% pure with 3-6 mm random size pieces, Ag was 99.99% pure with 3-6 mm random size pieces, and Ti was 99.995% pure in 0.25" diameter pellets. First, 2 nm of Ti was deposited at a rate of 1 Å/s, then 50 nm of Au was deposited at a rate of 2 Å/s. Next, Au and Ag were co-deposited at a rate of 2Å/s and 6Å/s, respectively, to create a 25% Au and 75% Ag alloy. Over the course of the deposition the partial pressure of the chamber would rise from $\sim 10^{-7}$ torr to $\sim 10^{-6}$ torr and the temperature would rise from 20 °C to 60 °C for a 1μm thick sample. If the samples were then placed in a beaker of 70 wt.% HNO_3 for 10 min to etch out the silver. After this time had elapsed, they were rinsed with deionized water 10 times before being dried with N_2. The room temperature np-Au morphology was obtained by etching the Au/Ag alloy films at room temperature (~22 °C) (denoted RT np-Au), while the low temperature samples were etched at in a freezer (−20°C) (denoted LT np-Au). Secondary ion mass spectrometry (SIMS) indicates that approximately 1.3 at.% of residual Ag remains in the structure after etching, consistent with prior reports.[21]

Figure 2.1 shows helium focused ion beam (He FIB) images of np-Au samples that were etched at room temperature (Figure 2.1a) and at low temperature (Figure 2.1b), displaying an average ligament thickness of 28 ± 8 nm and 10 ± 2 nm, respectively. Chemical etching at low temperatures restricts the surface mobility of the Au atoms during etching and ensures that the ligament diameter is decreased.[22] A scanning electron microscope (SEM) cross-section image of the ~800 nm thick RT etched np-Au film shows that the entirety of the film is porous down to the planar Au base layer (Figure 2.1c). As shown in this cross-sectional image, we routinely observed that the fully etched np-Au films were approximately 20% thinner (~800 nm) than the initial thickness of the Au/Ag alloy (~1 μm). To characterize the electrochemical surface area of the np-Au films, we performed Cu underpotential deposition (UPD) experiments. A Copper(II) sulfate (≥99%, Sigma Aldrich) ($CuSO_4$) solution (0.1 M) in 0.5 M H_2SO_4 was prepared and used as the deposition bath for all Cu UPD experiments. The solution was bubbled with N_2 (Research grade from Airgas) for 30 min to remove dissolved O_2 from the solution prior to starting the experiment. The working electrode was a planar Au film or a np-Au film of various thicknesses with a Pt mesh counter electrode and a Ag/AgCl reference electrode. The potential of the working electrode was swept from 450 mV to 50 mV vs. Ag/AgCl at a scan rate of 5 mV s^{-1}. A total of three to five electrodes were measured at each thickness ranging from 100 nm to 1.6 μm and the electrochemical surface area enhancement was obtained by taking the average surface area of the np-Au film relative to that of a planar Au film of known geometrical surface area. The maximum roughness factor of ~57 for the thickest films was obtained using this method. It is also important to note that the surface area increases linearly with film thickness, indicating that the entire surface area of the np-Au film is electrochemically accessible (Figure 2.1d).

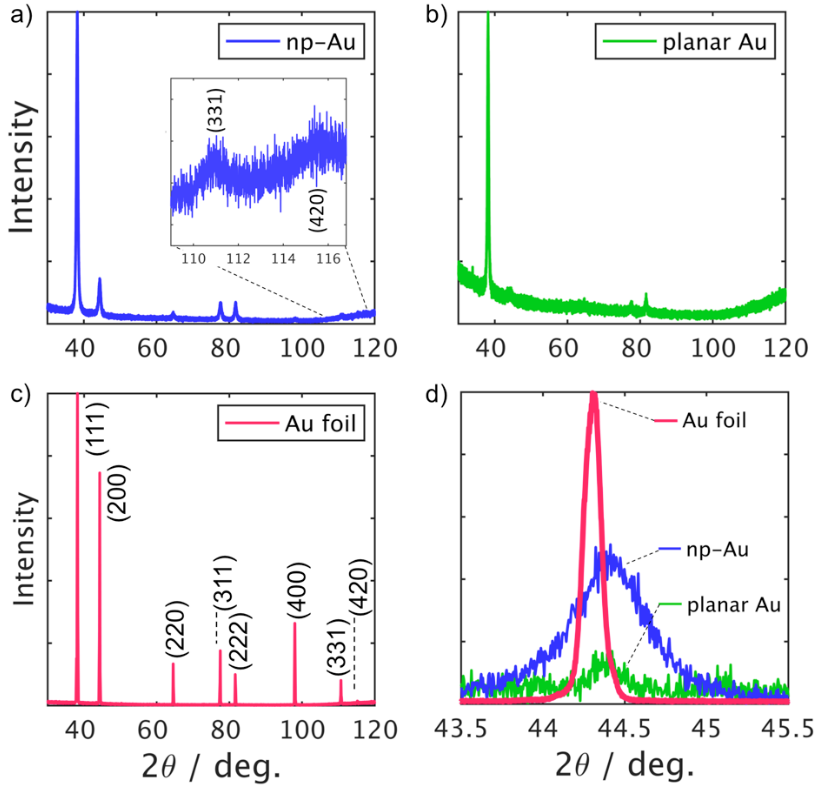

Figure 2.2: *XRD spectra of (a) RT np-Au (~800 nm thick) on a glass substrate, (b) planar Au film on glass, and (c) Au foil after flame annealing. (d) Zoom-in of (200) peak where planar Au and np-Au have been increased by 20x. From the XRD it is evident that the planar Au film is highly oriented in the (111) orientation. The data also shows that the full width half max of the np-Au is much larger than that of the Au foil, indicating that the np-Au has smaller grains.*

To estimate the average grain size of the np-Au films, we performed X-ray diffraction (XRD) on a RT-etched sample of ~800 nm thickness (Figure 2.2a). XRD spectra were taken using an X'PERT-PRO MRD Serial # DY3178 made by PANalytic. The scan went from 30° to 120°. The voltage was 45 kV, current 40 mA and the beam attenuator was Ni 0.125 mm automatic. For comparison, we also examined a 50 nm-thick planar Au base layer, and a commercial Au foil (Alfa Aesar 99.9975%) (Figures 2.2b,c). These data show that the average full-width half maximum of the diffraction peaks from np-Au are larger than the Au foil (Figures 2.1d). According to the Scherrer equation,[23] the np-Au film and Au foil have an average grain size of 20 ± 4 nm and 77 ± 23 nm, respectively. These calculations assume a shape factor of unity and do not take into account the possibility of microstrain.[24] We also performed transmission electron microscopy (TEM) to directly visualize the distribution of grain boundaries within individual ligaments of the np-Au film. Consistent with prior reports,[25–27] we observed many grain boundaries along the surface of the curved Au ligaments (Figure 2.3). Dark-field TEM images were also collected to estimate the average grain size within the np-Au film (Figure 2.4 and Figure 2.5). The average grain size that we observed in TEM (17 ± 4 nm) is very similar with the estimate obtained through analysis of the XRD data. It is known that grain boundaries and under-coordinated sites in Au electrocatalysts serve as the active sites for CO_2 reduction,[28,29] suggesting that these np-Au films should exhibit substantial activity for CO_2 reduction.

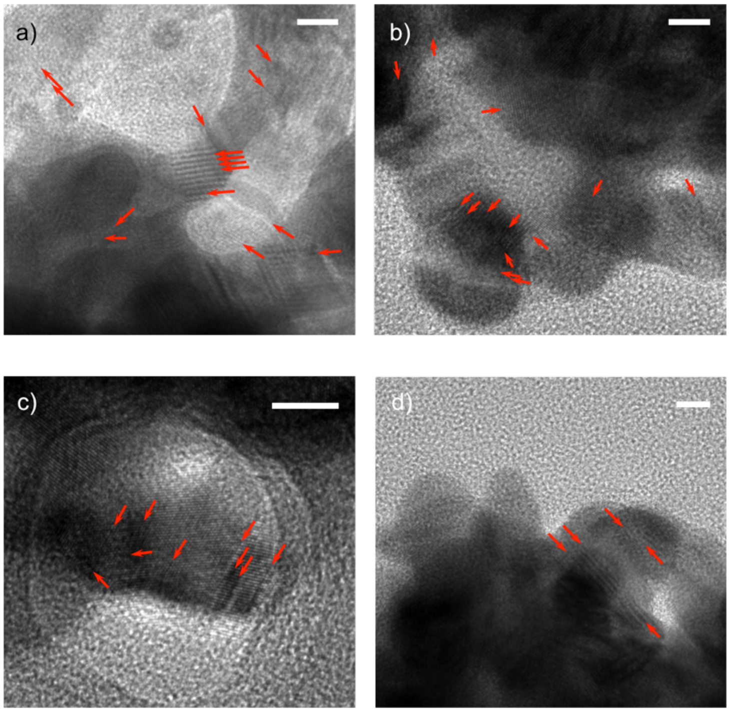

Figure 2.3*: Bright field transmission electron microscopy (TEM) images of RT np-Au film. The red arrows denote grain boundaries. All scale bars represent 5 nm.*

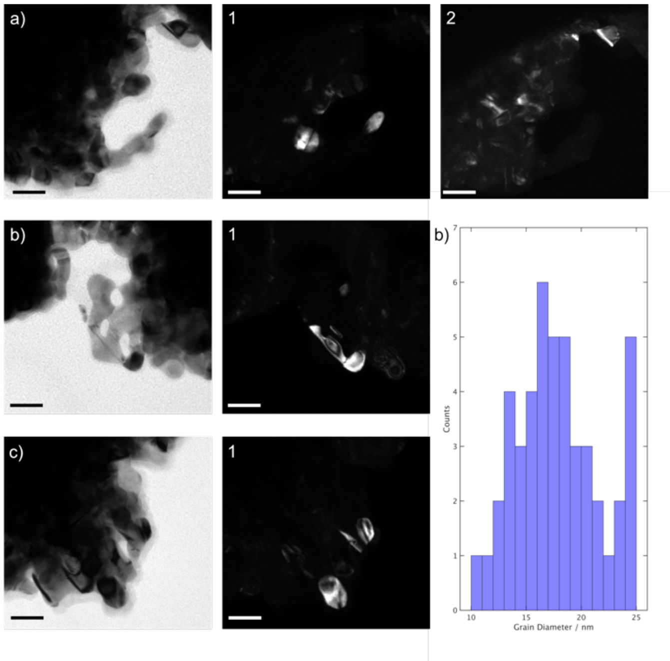

Figure 2.4*: Transmission electron microscopy (TEM) analysis of RT np-Au films. (a) Bright-field TEM of a particular region of the np-Au film along with (b) the corresponding selected area electron diffraction (SAED) pattern. (c1-c7) Dark-field TEM images from the np-Au film obtained from the particular spots numbered in panel b. (d)* Bright-field TEM image of np-Au film along with dark-field TEM images numbered 1-3. *All scale bars in all TEM images represent 20 nm.*

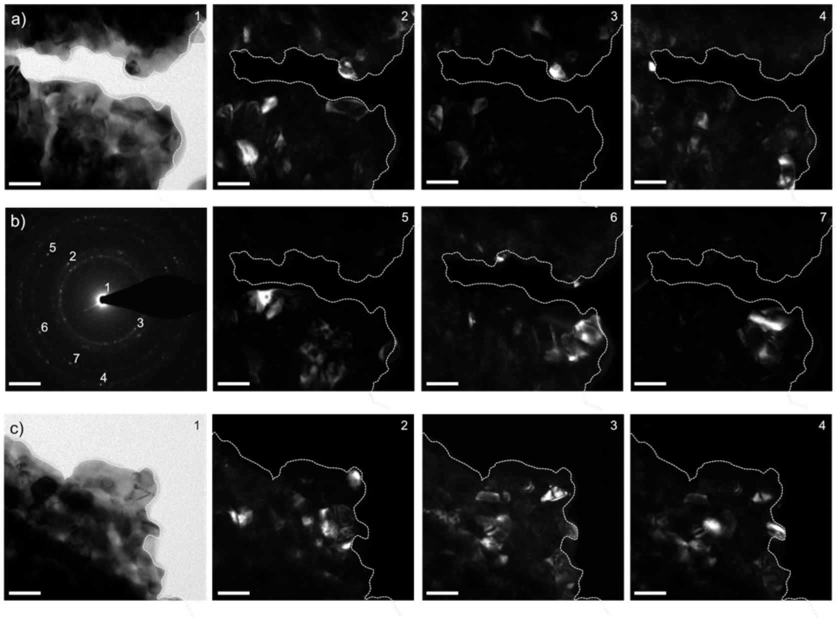

***Figure 2.5**: Transmission electron microscopy (TEM) analysis of RT np-Au films. (a-c) Bright-field TEM of a particular region of the np-Au film along with (d-f) a corresponding dark-field TEM image obtained from that particular region of the np-Au film. All scale bars in all TEM images represent 20 nm.*

2.3 Electrochemical characterization

A two-compartment electrochemical cell made of polyether ether ketone (PEEK) was used to perform CO_2RR experiments on the np-Au films. A volume of 2 mL of 50 mM K_2CO_3 was added to each compartment, which were separated by an anion exchange membrane (AGC, Selemion AMV). The np-Au film served as the working electrode with a Ag/AgCl leakless reference electrode and a Pt foil counter electrode. The Pt foil (99.99% , 0.05 mm thick, Alfa Aesar) was soaked in 10 wt.% HNO_3 for 1 h and then flame annealed to remove contaminants before each experiment. The flame annealing process entails holding a flame to the foil until it glows red then rinsing the foil in water and drying. This process is repeated twice. The same procedure was also applied to the Au foil before testing. CO_2 saturated 50 mM K_2CO_3 (pH 6.8) was prepared by bubbling CO_2 (Research grade from Airgas) into the electrolyte for 30 min prior to experiments. It is known that higher supporting electrolyte concentrations provide higher current densities during electrolysis,[30–32] but we found this concentration sufficient to enable reliable evaluation of our electrodes. Each electrolyte compartment was bubbled with CO_2 at a rate of 5 SCCM through a fine glass dispersion frit to maximize the speed of delivery of CO_2 into solution. The outflowing gas was sent through a flow meter to check that the flow of CO_2 in and out of the cell was the same, ensuring that it was thoroughly sealed against gas leaks. The outflowing gas was sent through a vapor trap to remove all water from the air before it was fed into a (SRI-8610) gas chromatograph.

All experiments were performed at room temperature with a Biologic VSP-300 potentiostat. All potentials were converted to the reversible hydrogen electrode (RHE) scale using the equation: E vs. RHE = E vs. Ag/AgCl + 0.197 V + 0.059 V pH^{-1} × solution pH. Before each experiment, potentiostatic electrochemical impedance spectroscopy (PEIS) was performed to determine the solution resistance of the cell, which was typically between 30 – 60 Ω. The applied electrochemical potential was then compensated by 85% using iR compensation of the potentiostat. The electrochemical cell was dismounted and rinsed multiple times after each experiment and then stored in 10 wt.% HNO_3. Before using the cell for the next experiment, it was sonicated for 10 min in water at least 4 times.

To analyze the chemical products, the electrode was held at the desired potential for at least 2 h allowing for the completion of eight gas chromatography measurements. The gas chromatograph (SRI-8610) used a Hayesep D column and a Molsieve 5A column with N_2 as the carrier gas. The gaseous products were detected using a thermal conductivity detector (TCD) for CO detection and a flame ionization detector (FID) equipped with a methanizer for H_2 detection. Quantitative analysis of gaseous products was based on calibration with several gas standards over many orders of magnitude in concentration. To measure liquid products, the electrolyte on the anode and cathode were sampled at the end of the run and tested with high performance liquid chromatography (HPLC). However, no liquid products were ever observed. Between different potential experiments all of the electrolyte was removed and then the cell was rinsed three times with water before new electrolyte was add and bubbled with CO_2.

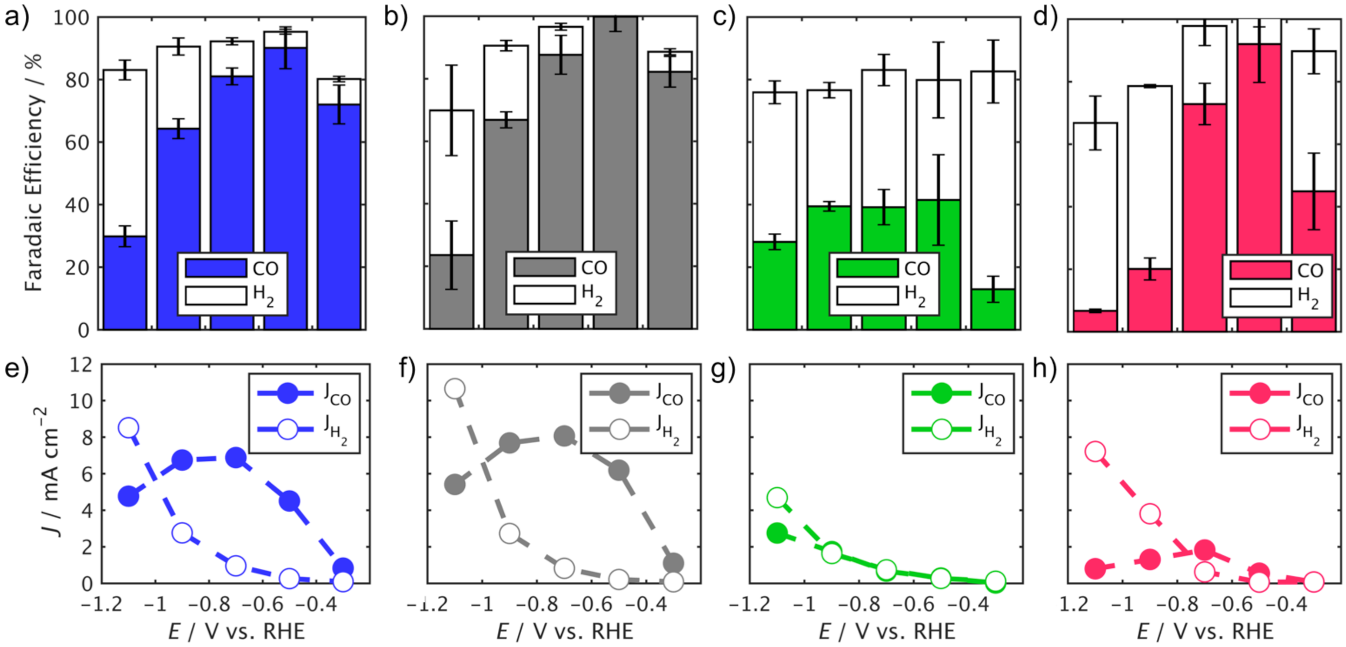

***Figure 2.6**: Electrochemical performance of Au cathodes. Faradaic efficiency (FE) for CO (filled bars) and H_2 (open bars) as a function of applied potential (E) with (a) 661 ± 10 nm thick room temperature etched (RT) np-Au film, (b) 664 ± 5 nm thick low temperature etched (LT) np-Au film, (c) planar Au film, and (d) commercial Au foil. Partial current density (J) for CO (filled circles) and H_2 (open circles) as a function of applied potential for (e) 661 ± 10 nm thick RT np-Au film, (f) 664 ± 5 nm thick LT np-Au film, (g) planar Au film, and (h) commercial Au foil. Each data point represents the average FE for CO or H_2 obtained over 2-3 h of continuous electrolysis at the indicated potential with iR compensation. The partial current densities also represent the average value observed over the same time period. All data was obtained from the same electrode along the potential sweep.*

Figure 2.6a shows the Faradaic efficiency (FE) of a RT np-Au film (661 ± 10 nm thick) for both CO (filled blue bars) or H_2 (white bars) as a function of the applied potential (*E*) from −0.3 V_{RHE} to −1.1 V_{RHE} (V vs. RHE). Each data point shown in Figure 2.6 represents the average FE for CO or H_2 obtained over 2-3 h of continuous electrolysis at the indicated potential with iR compensation. All data was obtained from the same electrode along the potential sweep. The RT np-Au film exhibits a maximum FE for CO of 90% at $E = -0.5$ V_{RHE} with the remainder of the current producing H_2. We note that no liquid products were detected for any of the Au electrodes studied. Notably, the LT np-Au film (664 ± 5 nm thick) obtains a maximum FE for CO (filled grey bars) of 99% at $E = -0.5$ V_{RHE} and maintains at least 80% FE for CO from -0.3 V_{RHE} to -0.7 V_{RHE} before the HER (white bars) begins to account for a larger portion of the products at more negative applied potentials (Figure 2.6b). To examine the influence of the np-Au morphology on CO_2 reduction selectivity, we tested the activity of a 50 nm-thick planar Au film, which is the base Au layer of the np-Au electrodes. As shown in Figure 2.6c, the planar Au film primarily produces H_2 (white bars) across the entire potential window; the FE for CO production (green bars) only reaches ~40% at -0.5 V_{RHE}. We also evaluated the activity of a commercial Au foil (99.9975%, 0.1 mm thick, Alfa Aesar) to confirm that our experimental conditions and cell configuration are capable of adequately reproducing commonly observed activity trends for Au films.[33] As shown in Figure 2.6d, the Au foil obtained a maximum FE for CO of 92% at -0.5 V_{RHE} (filled red bars), consistent with prior reports.[33]

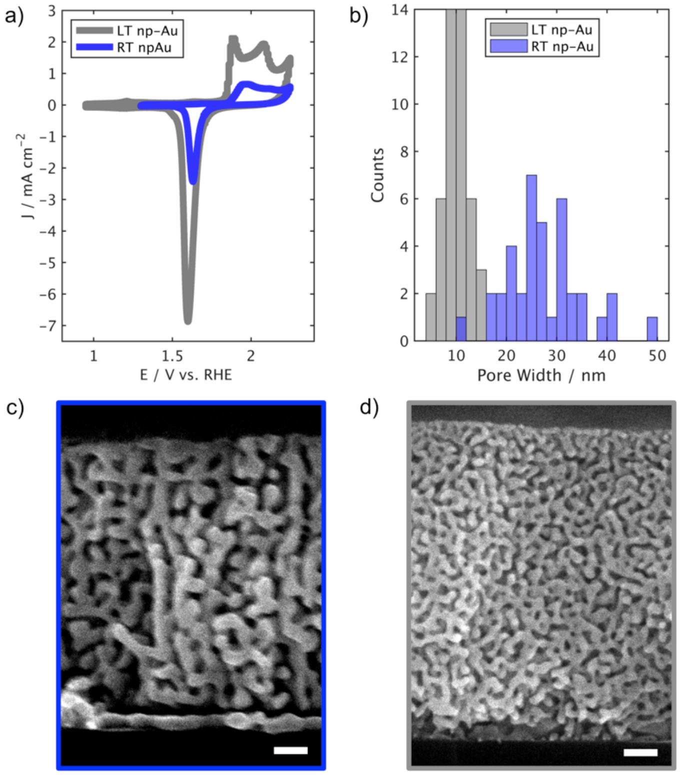

Figure 2.7: *(a) Cyclic voltammetry of LT np-Au (grey curve) and RT np-Au (dark blue curve) in 0.5 M* H_2SO_4 *obtained at a scan rate of 50 mV* s^{-1}*. From these data we can determine that the LT sample has ~3x greater electrochemical surface area as compared to the RT sample. (b) shows a histogram of pore widths measured on these two samples at three different locations on the sample. Representative SEM cross-section images of (c) RT np-Au and (d) LT np-Au films. The scale bars on both images*

correspond to 100 nm. These images correspond to the actual electrodes used for electrochemical tests involving different electrolyte concentrations.

A significant advantage of the np-Au morphology over the planar Au electrodes is illustrated by the high partial current density for CO (J_{CO}) relative to H_2 (Figures 2.6e-h). At an applied potential of −0.7 V_{RHE}, the LT np-Au film exhibits a peak J_{CO} of 8.1 mA cm^{-2} (Figure 2.6f), which is four times higher than the Au foil (Figure 2.6h) and eight times higher than the planar Au film (Figure 2.6g). At the optimum applied potential for CO production (−0.5 V_{RHE}), the LT np-Au film displays J_{CO} of nearly 6.2 mA cm^{-2} while the RT np-Au film J_{CO} is around 4.5 mA cm^{-2}. Interestingly, the LT np-Au film shows only a slight increase in J_{CO} as compared to the RT np-Au despite the ~3 times increase in surface area between the LT and RT np-Au films (Figure 2.7a). This lower than expected J_{CO} from LT np-Au films likely arises due to mass transport limitations, whereby the geometry of the electrochemical cell does not allow for sufficient delivery of CO_2 throughout the porous electrode to keep up with the electrochemically active surface area of the entire film. This hypothesis is confirmed by comparing the FE and J_{CO} for RT-etched samples that were ~800 nm and ~150 nm thick (Figure 2.8). Despite the drastic difference in electrochemical surface area as determined by Cu UPD (Figure 2.1d), the thicker film only showed a ~30% increase in J_{CO} under our experimental conditions (Figure 2.8c). Note that the linear relationship between surface area of the np-Au film and alloy thickness (Figure 2.1d) implies that the entire network is accessible to the electrolyte, suggesting that a large fraction of dissolved CO_2 does not penetrate the entire depth of the film at the current densities studied. These results suggest that to better use the full electrocatalytic surface area of np-Au for CO_2 reduction requires that the geometry of the cell be modified to flow the CO_2 directly through the np-Au film so that CO_2 is efficiently delivered to the catalyst, as opposed to simply flowing the CO_2 past the electrode surface. Indeed, it has recently been shown that such a tactic is highly beneficial for improving the rate of electrochemical CO_2 reduction.[34,35]

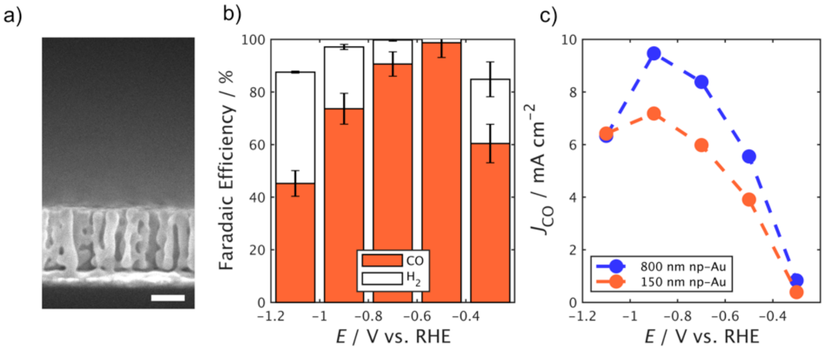

Figure 2.8: *(a) SEM cross-section image of ~150 nm-thick RT np-Au film. The scale bar represents 100 nm. (b) Faradaic efficiency as a function of applied potential (E) for 150 nm-thick RT np-Au film. (c) Partial current density for CO (J_{CO}) from a*

150 nm-thick and ~800 nm-thick RT np-Au sample. Considering the 4x smaller surface area of the thinner film, the relative J_{CO} between the two films is unexpected. We hypothesize that this is due to mass transport limitations.

Both the RT and LT np-Au films exhibit superior FE for CO (Figures 2.6a,b) relative to the planar Au film or Au foil (Figures 2.6c,d) across the entire potential window studied. It has previously been shown that the residual Ag in the np-Au film is not the source of the high FE for CO.[18] We therefore attribute such significant improvements in catalytic selectivity to the prevalence of grain boundaries that exist within the np-Au structure relative to the planar Au film. Another factor that likely contributes to such marked improvements in selectivity is the ability of the np-Au film to support locally-alkaline pH conditions within the porous network as protons are consumed during electrolysis. Such an effect has previously been observed in mesoporous Au electrodes, which serves to suppress the rate of HER while the rate of CO_2 reduction is relatively unaffected.[20]

2.4 Influence of local pH on performance

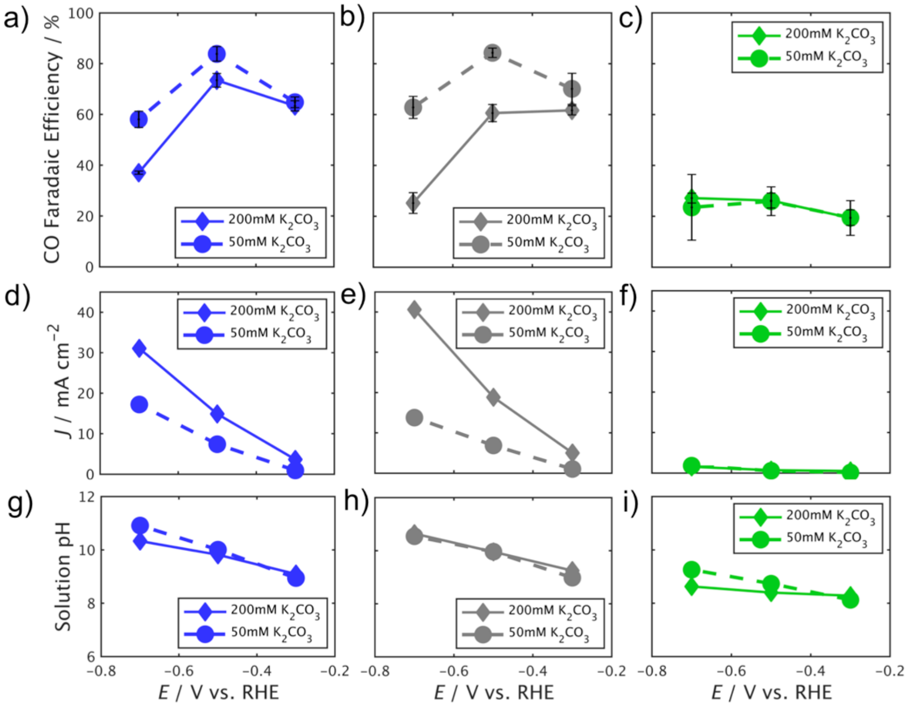

Figure 2.9: *Influence of electrolyte concentration on CO_2 reduction selectivity with Au cathodes. (a-c) The Faradaic efficiency for CO as a function of applied potential (E) obtained at two different electrolyte concentrations (both saturated with CO_2) for (a) 809 ± 15 nm thick room temperature etched (RT) np-Au film, (b) 821 ± 22 nm thick low temperature etched (LT) np-Au film, and (c) 50 nm thick planar Au film. (d-f) The corresponding average current density (J) obtained at the applied potential (E) observed*

at two different electrolyte concentrations for (d) RT np-Au, (e) LT np-Au, and (f) planar Au film. (g-i) Predicted solution pH at the surface of the electrode for (g) RT np-Au, (h) LT np-Au, and (i) planar Au film. A planar electrode geometry is assumed for the simulations.

To examine the influence of local pH gradients within the nanoporous network on the selectivity of np-Au films, we examined the electrochemical activity of a RT and a LT np-Au film (Figures 2.9d, e) at two different electrolyte concentrations (50 mM K_2CO_3 and 200 mM K_2CO_3 – both fully saturated with CO_2). Increasing the electrolyte concentration increases the buffering capacity of the solution,[20,32] which reduces any swings in local pH that are anticipated to form within the pores of the np-Au films as protons are consumed during electrolysis. It was therefore anticipated that the np-Au films would exhibit reduced FE for CO in 200 mM K_2CO_3 electrolyte if an increased solution pH within the porous network was responsible for the high selectivity observed on the np-Au films. As shown in Figure 2.9a and b, the selectivity on both RT np-Au and LT np-Au is essentially unchanged at low applied potentials (-0.3 V_{RHE}), but as the current density increases with increased applied bias (Figures 2.9d,e), any pH gradient that may form within the np-Au film in the 50 mM K_2CO_3 electrolyte (Figures 2.9a,b circles) is diminished by the improved buffering capacity of the 200 mM K_2CO_3 electrolyte (Figures 2.9a,b diamonds). In contrast, no change in FE for CO is observed on a planar Au film at any applied potential (Figure 2.9c), confirming that the change in selectivity observed on the np-Au electrodes is not simply a consequence of the increased electrolyte concentration (Figures 2.9c,f). These results strongly suggest that a pH gradient is forming within the porous network of the Au electrocatalyst and serves an important role in achieving high selectivity of CO_2 reduction in aqueous electrolytes.

Interestingly, the LT np-Au film shows a larger reduction in FE for CO (Figure 2.9a) than the RT np-Au film (Figure 2.9b). Analysis of the pore sizes between these two samples reveals that the LT np-Au film has pores with an average diameter of 10 ± 2 nm while the RT np-Au sample has pores with an average diameter of 28 ± 8 nm (Figure 2.7b). We therefore attribute the improved selectivity of the LT np-Au film relative to the RT np-Au film to the smaller pore size of the former (~10 nm) relative to the latter (~30 nm), which more effectively supports a high local pH within the porous network that improves the selectivity for CO_2RR relative to HER (Figures 2.6a,b). Previous work has shown that increasing the thickness of a mesoporous Au catalyst to ~2 μm helps to achieve a similar effect within ~200 nm pores.[20] Our observations suggest that further reducing the pore volume below 10 nm may enable realizing such an effect within even thinner nanoporous metal films than those studied here.

To further explore whether the pH gradient is developed within the porous Au network or occurs largely in the boundary layer, we simulated the pH profile as a function of distance away from the electrode surface using the model previously reported by Gupta, et al.[30] Briefly, the model assumes a planar electrode geometry, which is a valid assumption for calculating the pH at the outer surface of the electrode because the flux of reactants and products must be the same for either a porous or planar electrocatalyst at this location. The assumption of a planar electrode is clearly incapable of accounting for changes in the transport of reactants and products into and out of the porous film itself, and we therefore interpret any experimental deviations from the model to originate from changes occurring within the porous network of metal ligaments. The inputs into the model are the electrolyte concentration, the total current density, and the Faradaic efficiency for CO and H_2. A 70 μm-thick boundary layer was assumed based on the experimental flow rate of CO_2 of 5 SCCM through the catholyte.[31] As shown in Figures 2.9g-i, these calculations predict very little change in local pH at the electrode surface between the two electrolyte concentrations, albeit small deviations from the bulk electrolyte are predicted for the RT np-Au film and the planar Au electrode (Figures 2.9g,i). While significant reductions in FE for CO were observed on both the RT and LT np-Au films (Figures 2.9a and 2.9b, respectively), no change in FE was observed experimentally on the planar Au film (Figure 2.9c). This obvious contradiction between the results of experiment with those from the model indicates that the local pH changes must be occurring within the porous network itself. Otherwise, we would have observed a similar reduction in FE for CO with the planar electrode at the higher electrolyte concentration. We note that these experimental observations are consistent with a previous report on mesoporous Au films,[20] yet are achieved with much thinner films. Taken together, these results indicate that the pore diameter of porous metal electrocatalysts is a critical parameter for optimizing their selectivity, and suggest that control over the pore size on the nanometer length scale may offer further improvements in electrochemical selectivity.

2.5 Catalyst Stability

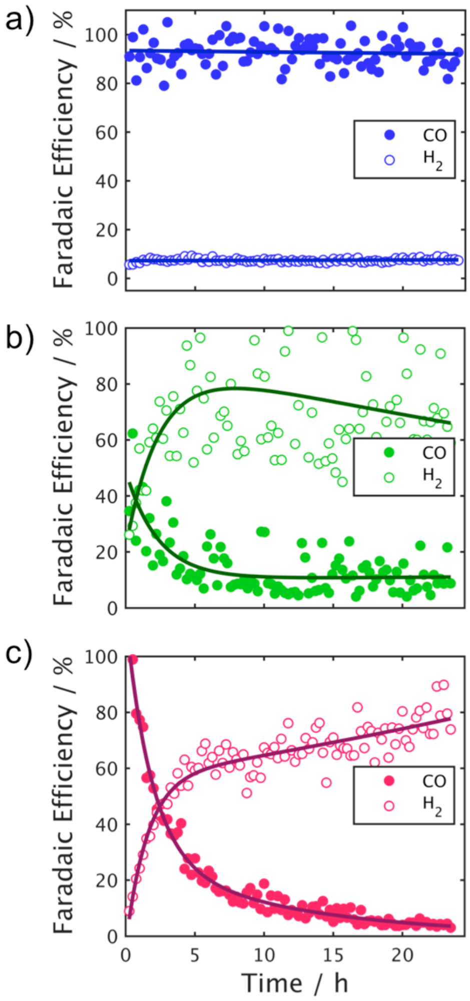

Figure 2.10: *Extended electrochemical stability data for Au cathodes. The Faradaic efficiency for CO (filled circles) and* H_2 *(open circles) was measured every 15 min via gas chromatography over the course of 24 h at an applied potential of* $E = -0.5\ V_{RHE}$ *with iR compensation for (a) room temperature (RT)-etched np-Au, (b) planar Au film, and (c) Au foil.*

We further evaluated the electrocatalytic stability of these Au films for the CO_2RR at an applied potential of $E = -0.5\ V_{RHE}$ (with iR compensation). Significantly, we observed that the np-Au film maintained a high FE for CO (nearly 90%) over the course of 24 h of continuous electrocatalytic testing (Figure 2.10a). In stark contrast, the Au foil and planar Au films exhibit drastic reductions in FE for CO over just one day of testing at the same applied potential (Figures 2.10b,c). Continued testing of a different RT np-Au film for 4.5 days (110 h) showed continued catalytic stability (Figure 2.11). Comparison of the SEM images before and after testing show no significant changes in morphology except that the np-Au ligaments appear to coarsen slightly (Figure 2.12). Analysis of these films by XRD indicates no significant changes in peak width before and after testing, but all films showed a decrease in the overall signal magnitude from diffraction peaks associated with high-index reflections (Figure 2.13). We note that the activity of the Au foil can be recovered if the flame anneal treatment is repeated, but such a process is undesirable as it hinders long-term continual operation under CO_2RR conditions. These observations serve to highlight the benefit of using the nanoporous metal structure to perform CO_2 reduction: the prevalence of grain boundaries offer numerous active sites on the metal ligaments while the porous network is able to support a locally-alkaline pH within the film that helps improve electrocatalytic selectivity for the CO_2RR over the HER.

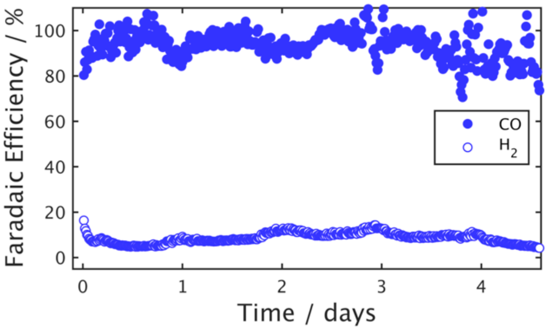

Figure 2.11: *Extended electrochemical stability data for a RT np-Au film (~800 nm thick). The Faradaic efficiency for CO (filled points) and H_2 (open points) was measured every 15 min via gas chromatography over the course of 110 h at an applied potential of E = –0.5 V_{RHE} with iR compensation.*

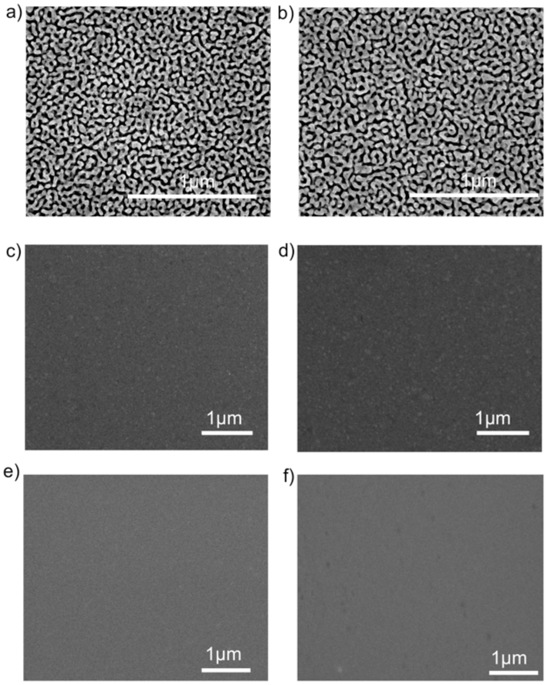

Figure 2.12: *(a,b) SEM images of a ~800 nm thick RT np-Au film (a) before and (b) after testing for 110 h at −0.5 V vs. RHE. (c,d) SEM images of a planar Au film (c) before and (d) after testing for 24 h at −0.5 V vs RHE. (e,f) SEM images of a Au foil (e) before and (f) after testing for 24 h at −0.5 V vs RHE. There is no visible difference between any of the planar*

samples before and after testing. In the np-Au sample there is some minor coarsening of the ligaments, but no significant changes to the film morphology are observed.

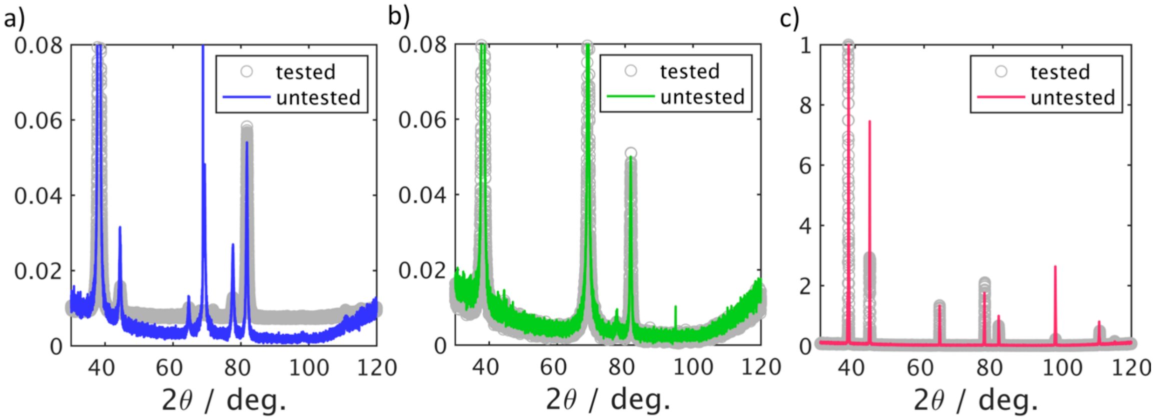

Figure 2.13: *XRD spectra of Au films before and after 24 h of testing for (a) ~800 nm thick RT np-Au film, (b) planar Au film, and (c) Au foil. The peak at 68° in the RT np-Au film and the planar Au film is due to the Si substrate. In Figure 2.2, the XRD patterns were collected from films supported on a glass substrate to avoid the peak from the Si substrate. Negligible differences were observed between Au peaks obtained from on Si vs. glass substrates.*

2.6 Conclusions

In conclusion, we have demonstrated that np-Au films constitute a promising electrocatalytic architecture for CO_2 reduction to yield CO in aqueous electrolytes. The np-Au films exhibit a maximum Faradaic efficiency for CO of 99% at −0.5 V_{RHE} while operating at a partial current density for CO in excess of 6 mA cm^{-2}. We attribute the catalytic performance of np-Au to its high electrochemical surface area possessing a large number of grain boundaries and its ability to support a local depletion of protons within the porous network. Significantly, these np-Au films maintain a Faradaic efficiency of greater than 80% over the course of 110 h of continuous electrolysis at −0.5 V_{RHE}, while the activity and selectivity of both planar Au films and Au foils diminishes significantly over much shorter periods of operation (~4 h). These studies highlight the benefits of nanoporous metal cathodes for CO_2 reduction and indicate that the pore size is an important parameter to control for improving selectivity in these promising electrocatalytic architectures.

BIBLIOGRAPHY CHAPTER 2

1. Jones, J.-P.; Parkash, G. K. S.; Olah, G. A. Electrochemical CO_2 Reduction: Recent Advances and Current Trends. *Isr. J. Chem.* **2014**, *54*, 1451–1466.
2. White, J. L.; Baruch, M. F.; Pander, J. E.; Hu, Y.; Fortmeyer, I. C.; Park, J. E.; Zhang, T.; Liao, K.; Gu, J.; Yan, Y.; Shawn, T. W.; Abelev, E.; Boarsly, A. B. Light-Driven Heterogeneous Reduction of Carbon Dioxide: Photocatalysts and Photoelectrodes. *Chem. Rev.* **2015**, *115*, 12888–12935.
3. Whipple, D.; Kenis, P. Prospects of CO_2 Utilization via Direct Heterogeneous Electrochemical Reduction. *J. Phys. Chem. Lett.* **2010**, *1*, 3451–3458.
4. Kuhl, K. P.; Hatsukade, T.; Cave, E. R.; Abram, D. N.; Kibsgaard, J.; Jaramillo, T. F. Electrocatalytic Conversion of Carbon Dioxide to Methane and Methanol on Transition Metal Surfaces. *J. Am. Chem. Soc.* **2014**, *136*, 14107–14113.
5. Kuhl, K. P.; Cave, E. R.; Abram, D. N.; Jaramillo, T. F. New Insights into the Electrochemical Reduction of Carbon Dioxide on Metallic Copper Surfaces. *Energy Environ. Sci.* **2012**, *5*, 7050–7059.
6. Hori, Y. Electrochemical CO2 Reduction on Metal Electrodes. In *Modern Aspects of Electrochemistry*; Vayenas, C. G., White, R. E., Gamboa-Aldeco, M. E., Eds.; Springer New York: New York, NY, 2008; pp 89–189.
7. Cao, Z.; Kim, D.; Hong, D.; Yu, Y.; Xu, J.; Lin, S.; Wen, X.; Nichols, E. M.; Jeong, K.; Reimer, J. A.; Yang, P.; Chang, C. J. A Molecular Surface Functionalization Approach to Tuning Nanoparticle Electrocatalysts for Carbon Dioxide Reduction. *J. Am. Chem. Soc.* **2016**, *138*, 8120–8125.
8. Fang, Y.; Flake, J. C. Electrochemical Reduction of CO_2 at Functionalized Au Electrodes. *J. Am. Chem. Soc.* **2017**, *139*, 3399–3405.
9. Zhu, W.; Michalsky, R.; Metin, Ö.; Lv, H.; Guo, S.; Wright, C. J.; Sun, X.; Peterson, A. A.; Sun, S. Monodisperse Au Nanoparticles for Selective Electrocatalytic Reduction of CO_2 to CO. *J. Am. Chem. Soc.* **2013**, *135*, 16833–16836.
10. Zhu, W.; Zhang, Y.-J.; Zhang, H.; Lv, H.; Li, Q.; Michalsky, R.; Peterson, A. A.; Sun, S. Active and Selective Conversion of CO_2 to CO on Ultrathin Au Nanowires. *J. Am. Chem. Soc.* **2014**, *136*, 16132–16135.
11. Chen, Y.; Li, C. W.; Kanan, M. W. Aqueous CO_2 Reduction at Very Low Overpotential on Oxide-Derived Au Nanoparticles. *J. Am. Chem. Soc.* **2012**, *134*, 19969–19972.
12. Liu, M.; Pang, Y.; Zhang, B.; De Luna, P.; Voznyy, O.; Xu, J.; Zheng, X.; Dinh, C. T.; Fan, F.; Cao, C.; de Arquer, F. P. G.; Safaei, T. S.; Mepham, A.; Klinkova, A.; Kumacheva, E.; Filleter, T.; Sinton, D.; Kelley, S. O.; Sargent, E. H.Enhanced Electrocatalytic CO_2 Reduction via Field-Induced Reagent Concentration. *Nature* **2016**, *537*, 382.
13. Lu, Q.; Rosen, J.; Zhou, Y.; Hutchings, G. S.; Kimmel, Y. C.; Chen, J. G.; Jiao, F. A Selective and Efficient Electrocatalyst for Carbon Dioxide Reduction. *Nat. Commun.* **2014**, *5*, 3242.
14. Dutta, A.; Morstein, C. E.; Rahaman, M.; Cedeño López, A.; Broekmann, P. Beyond Copper in CO_2 Electrolysis: Effective Hydrocarbon Production on Silver-Nanofoam Catalysts. *ACS Catal.* **2018**, 8357–8368.
15. Sen, S.; Liu, D.; Palmore, G. T. R. Electrochemical Reduction of CO_2 at Copper Nanofoams. *ACS Catal.* **2014**, *4*, 3091–3095.
16. Ma, M.; Trześniewski, B. J.; Xie, J.; Smith, W. A. Selective and Efficient Reduction of Carbon Dioxide to Carbon Monoxide on Oxide-Derived Nanostructured Silver Electrocatalysts. *Angew. Chem. Int. Ed.* **2016**, *55*, 9748–9752.
17. Zhang, Y.; Luc, W.; Hutchings, G. S.; Jiao, F. Photoelectrochemical Carbon Dioxide Reduction Using a Nanoporous Ag Cathode. *ACS Appl. Mater. Interfaces* **2016**, *8*, 24652–24658.

18. Zhang, W.; He, J.; Liu, S.; Niu, W.; Liu, P.; Zhao, Y.; Pang, F.; Xi, W.; Chen, M.; Zhang, W.; et al. Atomic Origins of High Electrochemical CO_2 Reduction Efficiency on Nanoporous Gold. *Nanoscale* **2018**, *10*, 8372–8376.
19. Chen, C.; Zhang, B.; Zhong, J.; Cheng, Z. Selective Electrochemical CO_2 Reduction over Highly Porous Gold Films. *J. Mater. Chem. A* **2017**, *5*, 21955–21964.
20. Hall, A. S.; Yoon, Y.; Wuttig, A.; Surendranath, Y. Mesostructure-Induced Selectivity in CO_2 Reduction Catalysis. *J. Am. Chem. Soc.* **2015**, *137*, 14834–14837.
21. Biener, J.; Biener, M. M.; Madix, R. J.; Friend, C. M. Nanoporous Gold: Understanding the Origin of the Reactivity of a 21st Century Catalyst Made by Pre-Columbian Technology. *ACS Catal.* **2015**, *5*, 6263–6270.
22. Qian, L. H.; Chen, M. W. Ultrafine Nanoporous Gold by Low-Temperature Dealloying and Kinetics of Nanopore Formation. *Appl. Phys. Lett.* **2007**, *91*, 083105.
23. Patterson, A. L. The Scherrer Formula for X-Ray Particle Size Determination. *Phys. Rev.* **1939**, *56*, 978–982.
24. Jiang, H. G.; Rühle, M.; Lavernia, E. J. On the Applicability of the X-Ray Diffraction Line Profile Analysis in Extracting Grain Size and Microstrain in Nanocrystalline Materials. *J. Mater. Res.* **1999**, *14*, 549–559.
25. Hodge, A. M.; Biener, J.; Hsiung, L. L.; Wang, Y. M.; Hamza, A. V.; Satcher, J. H. Monolithic Nanocrystalline Au Fabricated by the Compaction of Nanoscale Foam. *J. Mater. Res.* **2005**, *20*, 554–557.
26. Mathur, A.; Erlebacher, J. Size Dependence of Effective Young's Modulus of Nanoporous Gold. *Appl. Phys. Lett.* **2007**, *90*, 061910.
27. Petegem, S. V.; Brandstetter, S.; Maass, R.; Hodge, A. M.; El-Dasher, B. S.; Biener, J.; Schmitt, B.; Borca, C.; Swygenhoven, H. V. On the Microstructure of Nanoporous Gold: An X-Ray Diffraction Study. *Nano Lett.* **2009**, *9*, 1158–1163.
28. Mariano, R. G.; McKelvey, K.; White, H. S.; Kanan, M. W. Selective Increase in CO_2 Electroreduction Activity at Grain-Boundary Surface Terminations. *Science* **2017**, *358*, 1187.
29. Feng, X.; Jiang, K.; Fan, S.; Kanan, M. W. Grain-Boundary-Dependent CO_2 Electroreduction Activity. *J. Am. Chem. Soc.* **2015**, *137*, 4606–4609.
30. Gupta, N.; Gattrell, M.; MacDougall, B. Calculation for the Cathode Surface Concentrations in the Electrochemical Reduction of CO_2 in $KHCO_3$ Solutions. *J. Appl. Electrochem.* **2006**, *36*, 161–172.
31. Clark, E. L.; Resasco, J.; Landers, A.; Lin, J.; Chung, L.-T.; Walton, A.; Hahn, C.; Jaramillo, T. F.; Bell, A. T. Standards and Protocols for Data Acquisition and Reporting for Studies of the Electrochemical Reduction of Carbon Dioxide. *ACS Catal.* **2018**, *8*, 6560–6570.
32. Singh, M. R.; Clark, E. L.; Bell, A. T. Effects of Electrolyte, Catalyst, and Membrane Composition and Operating Conditions on the Performance of Solar-Driven Electrochemical Reduction of Carbon Dioxide. *Phys. Chem. Chem. Phys.* **2015**, *17*, 18924–18936.
33. Cave, E. R.; Montoya, J. H.; Kuhl, K. P.; Abram, D. N.; Hatsukade, T.; Shi, C.; Hahn, C.; Nørskov, J. K.; Jaramillo, T. F. Electrochemical CO_2 Reduction on Au Surfaces: Mechanistic Aspects Regarding the Formation of Major and Minor Products. *Phys. Chem. Chem. Phys.* **2017**, *19*, 15856–15863.
34. Dinh, C. T.; Burdyny, T.; Kibria, M. G.; Seifitokaldani, A.; Gabardo, C. M.; García de Arquer, F. P.; Kiani, A.; Edwards, J. P.; De Luna, P.; Bushuyev, O. S.; Zou, C.; Quintero-Bermudez, R.; Pang, Y.; Sinton, D.; Sargent, E. H. CO_2 Electroreduction to Ethylene via Hydroxide-Mediated Copper Catalysis at an Abrupt Interface. *Science* **2018**, *360*, 783.
35. Hoang, T. T. H.; Ma, S.; Gold, J. I.; Kenis, P. J. A.; Gewirth, A. A. Nanoporous Copper Films by Additive-Controlled Electrodeposition: CO_2 Reduction Catalysis. *ACS Catal.* **2017**, *7*, 3313–3321.

Chapter 3

OPERANDO DETERMINATION OF CATALYTICALLY-ACTIVE REGIONS IN NANOPOROUS GOLD GAS DIFFUSION ELECTRODES FOR HIGHLY SELECTIVE CARBON DIOXIDE REDUCTION

3.1 Introduction

The electrochemical reduction of carbon dioxide (CO_2R) to value-added commodities represents a promising means to store renewable electricity and create a closed carbon cycle for industrial chemicals.[1–3] CO_2R can produce a wide variety of products based on catalyst choice,[4–6] structuring,[4,7] and treatment.[2,8] Of these products, carbon monoxide (CO) is especially interesting due to its ubiquitous role as a precursor in cornerstone chemical processes such as Fischer-Tropsch reactions,[9–11] hydroformylation of alkenes to aldehydes,[12] methanol production,[10,13] and metal refinement.[14] In addition, CO_2R to CO is a two-electron process which translates to lower energy inputs as compared to other multi-electron products.[10,15] CO production has been demonstrated with high selectivities, with Faradaic efficiencies (FE) for CO reaching >90% in aqueous-based electrolyzers.[7,8] While current densities between -10 mA/cm^2 and -20 mA/cm^2 can be achieved through electrode nano-structuring,[16–20] further improvements in traditional aqueous systems are limited due to low CO_2 solubility and long diffusion lengths.[21,22] In order for electrochemical CO_2R to be economically viable, current densities of greater than −100 mA/cm^2 are required.[23,24]

Gas diffusion electrodes (GDEs) present an alternative electrode design capable of addressing mass transport and CO_2 solubility issues.[25] In a GDE, a blend of CO_2 gas and water vapor is flowed across a porous catalyst layer in contact with a liquid electrolyte.[21,25] High current densities have been achieved by GDEs tuned for high performance in a range of different configurations such as alkaline electrolyzers and membrane electrode assemblies.[26–29]

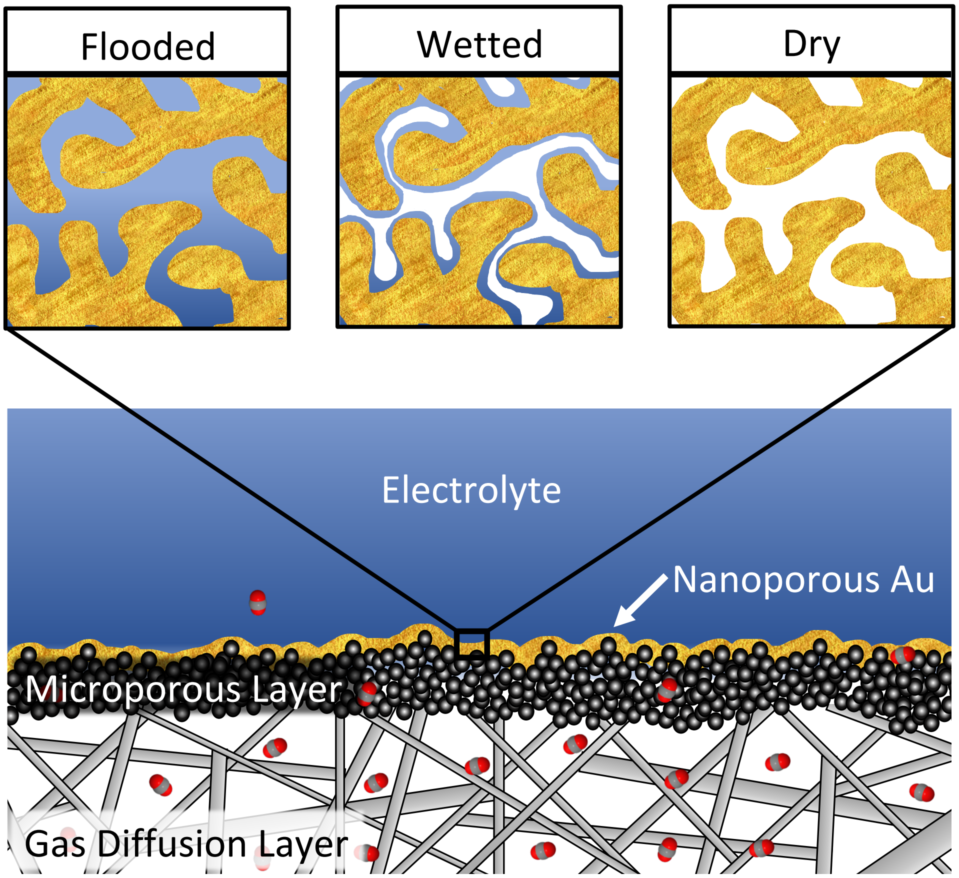

Figure 3.1: *A schematic of the nanoporous gold gas diffusion electrode used in this study in a vapor CO_2 fed device. The bottom image shows the electrode structure. The support consists of a gas diffusion layer composed of carbon fibers, on top of which is coated carbon black and PTFE which makes up the microporous layer. The nanoporous gold is coated on top of this. The top three panels show the different configurations that the nanoporous gold can be in during operation - flooded, wetted, and dry.*

The large disparity in current density between an aqueous electrolyzer and a GDE can be attributed to overcoming the mass transport limits in an aqueous system. In an aqueous electrolyzer, CO_2 must first dissolve into the electrolyte then diffuse to the electrode surface. This process is mass transported limited by the rate at which CO_2 can dissolve into the electrolyte and this precludes the total current density achievable to a regime usually bounded by a performance of less than –20 mA/cm^2. The catalyst in an aqueous electrolyzer can be considered to be fully flooded. The term flooded means that the catalyst is fully submerged in the electrolyte. An idealized GDE, on the other hand, advantageously forms a triple phase boundary in which a meniscus of water wraps the catalyst, and channels of gas flow through the catalyst layer (Figure 3.1). This reduces the diffusion length and substantially increases the CO_2 transport rate to the catalyst surface, thus enabling much higher current densities in the range of -100 of mA/cm^2 to -1000 of mA/cm^2 in ultra high preforming devices. We refer to this GDE state as wetted. There is also the potential that portions of a catalyst in a GDE are dry due to excess gas pressure thus rendering them inactive (Figure 3.1). While in an ideal scenario all of the catalyst in the GDE would be wetted, it likely that a combination of flooded, wetted, and dry conditions exist simultaneously. The interaction between the catalyst and the electrolyte has been probed computationally;[21,25] however, there is little experimental understanding of this layer. Here we seek to understand the relationship between device performance and catalyst wetting.

It has been previously demonstrated that nanoporous gold (np-Au) is a promising CO_2 to CO catalyst.[7] In aqueous CO_2 fed systems, np-Au has shown improved selectivity and catalytic activity relative to planar Au (pl-Au) due to the high density of under-coordinated sites,[30] prevalence of grain boundaries,[30,31] and high surface area.[32,33] Furthermore, pH gradients are built up within the porous structure and this increased pH suppresses the parasitic hydrogen evolution reaction (HER);[34] however, these experiments were only demonstrated in the aqueous CO_2 fed configuration. Here, np-Au GDEs are used as a model catalyst system for a vapor CO_2 fed CO_2R device. We demonstrate that np-Au GDEs achieve >95% selectivity for CO at partial current densities for CO production (J_{CO}) greater than -150 mA/cm^2. One of the outstanding questions in the field of GDEs is understanding what portion of the catalyst layer is meaningfully contributing to active catalysis. We take advantage of the highly porous nature of our electrode to determine via, scanning electron microscopy (SEM), copper under potential deposition (Cu UPD), secondary ion mass spectroscopy (SIMS), and electrochemical product analysis to determine which fraction of the catalyst is flooded/wetted, and dry. We find that only 56% of the available catalyst is active under vapor CO_2 fed conditions and that the bottom 75% of the catalyst layer exhibits the largest difference in wetting between an aqueous CO_2 fed vs vapor CO_2 fed system. These investigations yield improved methods of *in situ* catalyst characterization which can facilitate the optimization and adoption of CO_2R electrolyzers on an industrially-relevant scale.

3.2 Fabrication and characterization of nanoporous gold

The np-Au GDEs used in our studies were fabricated by electron beam co-deposition of Au and Ag targets onto the microporous side of a carbon paper substrate (Sigracet 38BC) to produce a Ag_xAu_{1-x} alloy of uniform distribution. The relative atomic percent of Au relative to Ag is tuned by varying the deposition rates of each metal. The np-Au electrode was produced by soaking the Ag_xAu_{1-x} alloy in concentrated nitric acid (70% weight/volume) for 15 minutes at room temperature. Concentrated nitric acid dealloys the Ag to produce the desired np-Au morphology. (See Figure 5.2 for SEM images of the fabrication process).

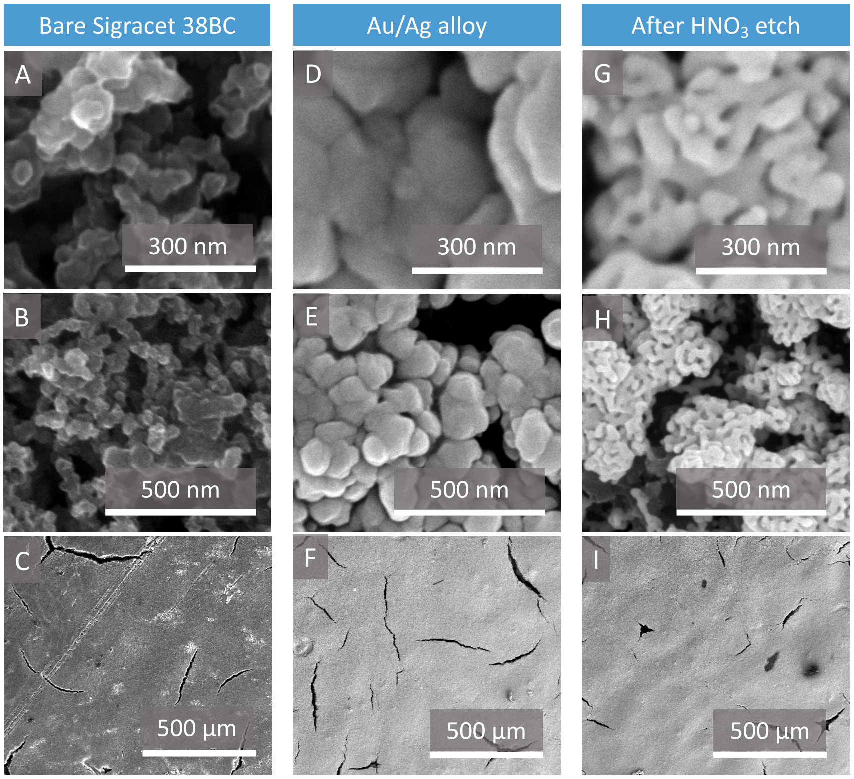

Figure 3.2: *shows SEM images of the electrode at different phases in the fabrication process. (a)-(c) shows images of the bare carbon paper, Sigracet 38BC. (d)-(f) show images of the gold silver alloy on the carbon paper. (g)-(i) show images of the nanoporous gold morphology from a 35% Au alloy that forms after the nitric acid etch.*

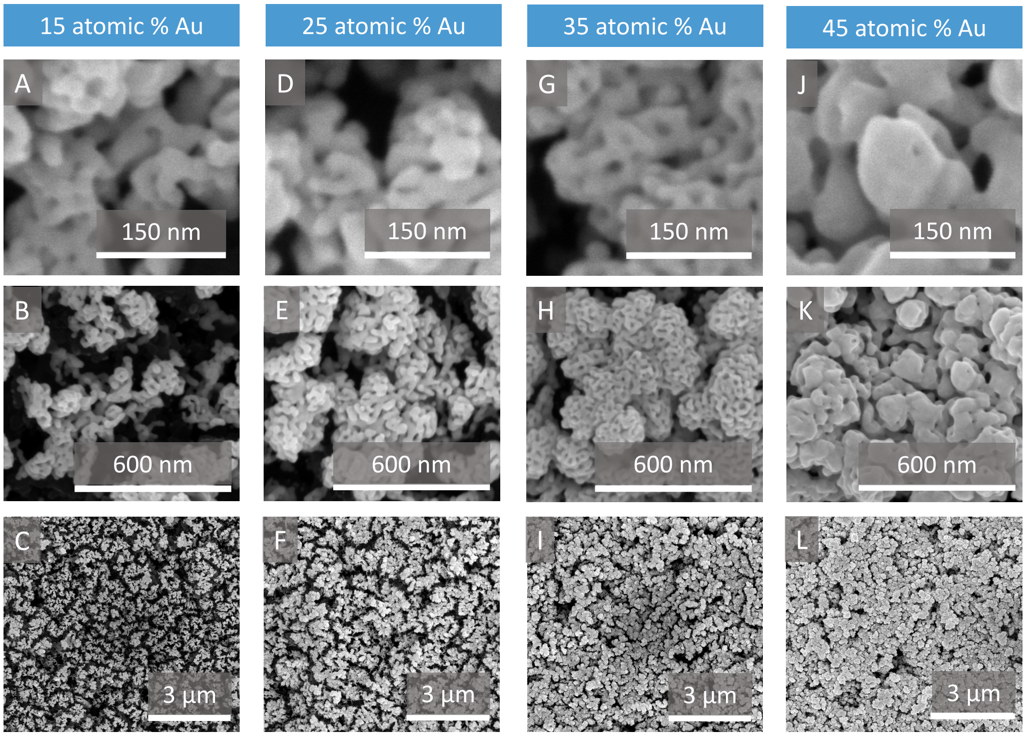

Figure 3.3: *SEM characterization of nanoporous gold (np-Au) electrodes with a varying gold atomic percent ($\%_{Au}$) of 15$\%_{Au}$ (a-c), 25$\%_{Au}$ (d-f), 35$\%_{Au}$ (g-i), and 45$\%_{Au}$ (j-l).*

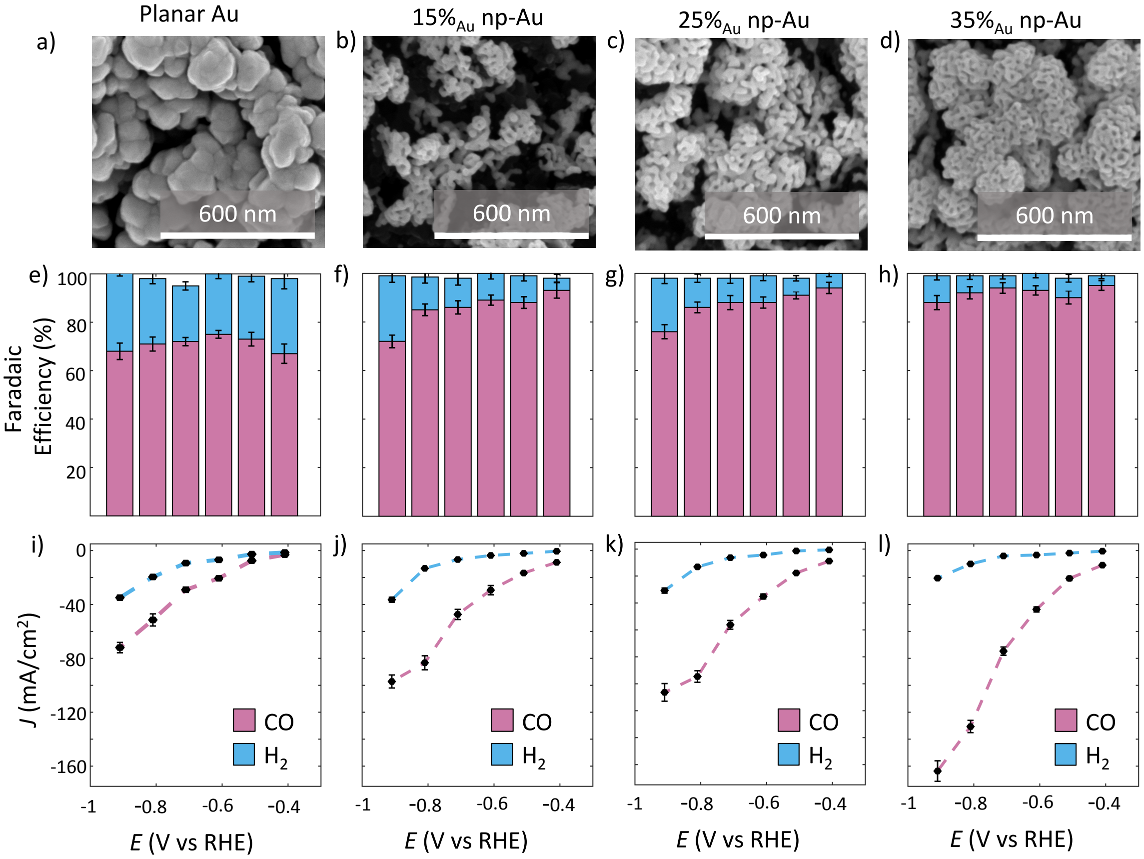

Figure 3.4*: SEM characterization of planar gold (pl-Au) and nanoporous gold (np-Au) electrodes with varying gold atomic percent ($\%_{Au}$) (a-d). CO_2R performance of the pl-Au and np-Au electrodes is shown via Faradaic efficiencies (e-h) and partial current densities (i-l). For all plots, CO is denoted in pink and H_2 by blue. Each data point is the average of three distinct electrodes.*

Representative, top-down SEM images for a range of 300 nm thick np-Au samples of varying gold atomic percent ($\%_{Au}$) from 15$\%_{Au}$ to 35$\%_{Au}$ and a pl-Au control are shown in Figure 3.3 and Figure 3.4a-d. Clear morphological distinctions can be observed between the samples of different $\%_{Au}$. The electrodes consist of a three dimensional network of gold ligaments, pores, and cracks. The cracks in the np-Au morphology are due to the volume contraction (10-30%) that occurs from the removal of Ag.[35] The crack sizes notably increase at $\%_{Au}$ below 25$\%_{Au}$ and yield a discontinuous film at 15$\%_{Au}$, through which the underlying carbon paper substrate is visible (Figure 3.3a-c). The size of the cracks at 35$\%_{Au}$ are greatly diminished as a near continuous network of ligaments is achieved (Figure 3.3g-i). However, the uneven nature of the underlying carbon paper substrate makes this visualization difficult. To better understand the morphology changes, np-Au was deposited on Si substrates as shown in Figure 3.5. A nanoporous morphology is no longer observed above 45$\%_{Au}$ due to the lack of continuous channels of Ag present in the base alloy (Figure 3.3j-l). At these atomic ratios, Au forms a protective barrier that prevents the nitric acid from penetrating deeper into the alloy to remove the residual Ag.[35] The coarseness of the nanoporous ligaments and pores are modestly reduced as the $\%_{Au}$ is increased. Cross sectional SEM demonstrates that the nanoporous ligaments are consistently distributed throughout the entire volume of the film after dealloying (Figure 3.6). Figure 3.2 shows SEM images of the bare carbon paper substrate, the Ag_xAu_{1-x} base alloy before the nitric acid etch, and after the etch.

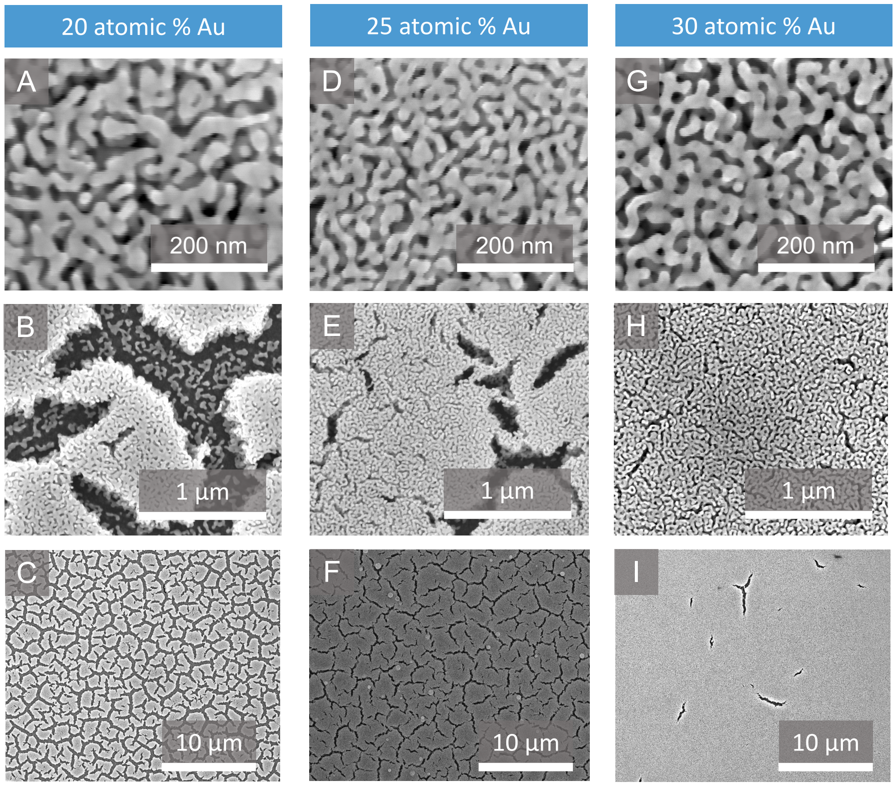

Figure 3.5: *SEM characterization of nanoporous gold (np-Au) electrodes with a varying gold atomic percent ($\%_{Au}$) on silicon. $20\%_{Au}$ (a-c), $25\%_{Au}$ (d-f), and $30\%_{Au}$ (g-i).*

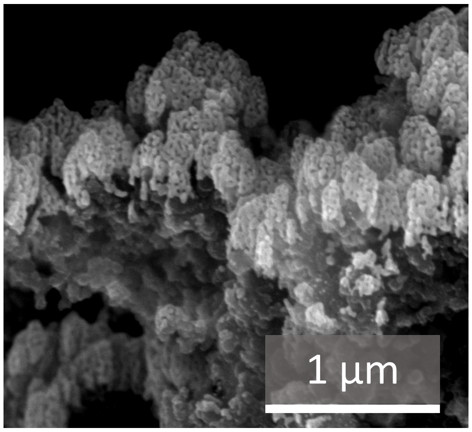

***Figure 3.6**: cross sectional SEM of a 300 nm thick 35% gold nanoporous gold electrode on carbon paper. From this image we can see how uneven the carbon paper substrate is and that the nanoporous gold has a homogenous pore structure through the entire thickness.*

3.3 Electrochemical characterization of nanoporous gold

CO_2R performance for each electrode was evaluated in a two-compartment flow cell. A Selemion anion exchange membrane was used to separate the Pt mesh anode from the np-Au cathode. A 1M $KHCO_3$ electrolyte saturated with CO_2 electrolyte was independently recirculated through the anode and cathode chambers. Despite the fact that the increased alkalinity of KOH electrolytes has been shown to improve CO_2R selectivity,[28,29,36] KOH is considered to be a sacrificial medium because the hydroxide anions are converted into bicarbonate and carbonate upon contact with any unreacted CO_2 gas.[37] The carbonate salts are then known to precipitate out of solution and potentially clog the pores of the anion exchange membrane,[38] which necessitates that the KOH electrolyte be continuously replaced throughout the electrolysis.[39,40] The $KHCO_3$ electrolyte thereby offers a sustainable alternative, albeit often at the expense of CO_2R selectivity. The CO_2 gas was delivered through a serpentine channel located behind the GDE at a constant flow rate of 50 standard cubic centimeters per minute (SCCM) unless otherwise noted. A leakless Ag/AgCl electrode was used as the reference electrode. A gas chromatograph was used to quantify the concentration of product gasses in the effluent stream and a potentiostat was used to control the applied electrochemical potential. All electrode potentials (E) are reported relative to the reversible hydrogen electrode (RHE) scale (V_{RHE}).

Figure 3.4e-h shows the FE of a pl-Au and np-Au GDEs (300 nm thick) for both CO and H_2 and Figure 3e shows the corresponding partial current densities (Figure 1i-l) as a function of applied potential between the range of $-0.42\ V_{RHE}$ to $-0.92\ V_{RHE}$ in a vapor CO_2 fed configuration. Each measurement represents the averaged result of three distinct electrodes. The pl-Au GDE has a maximum current density (J) of -106 mA/cm^2 at $-0.92\ V_{RHE}$ and a maximum FE for CO of 82% at $-0.82\ V_{RHE}$. After benchmarking the performance of the pl-Au film as a reference, we then tested a series of np-Au electrodes to evaluate the performance over a range of varying $\%_{Au}$. Both the $15\%_{Au}$ and $25\%_{Au}$ electrodes demonstrate a notable improvement on the pl-Au electrode in terms of current density (J) and FE across the entire potential range. At $15\%_{Au}$ and $25\%_{Au}$ the performance of the GDEs is relatively similar with the $25\%_{Au}$ electrode offering a slightly higher performance. The $25\%_{Au}$ np-Au has a J_{CO} that is 1.48X that of the planar Au film at $-0.92\ V_{RHE}$ and 2.92x improvement over the pl-Au with a peak FE for CO of 93% at $-0.42\ V_{RHE}$. The $35\%_{Au}$ electrode significantly outperforms the pl-Au across the entire potential range with a minimum enhancement in J_{CO} of over 2x. At $-0.92\ V_{RHE}$ the J_{CO} is -164 mA/cm^2

with an FE for CO of 88%. At lower potentials the FE for CO remains above 90% with a peak of 95% at −0.42 V_{RHE}. Additionally, the J_{CO} of the $35\%_{Au}$ electrodes at −0.82 V_{RHE} is higher at −130 mA/cm^2 than the −0.92 V_{RHE} data points for all other systems. We hypothesize that the enhanced performance of the $35\%_{Au}$ electrode is due to the near continuous ligament coverage across the electrode surface that may improve electrolyte wetting, decrease the potential for flooding and increase the residency of CO_2 in the catalyst layer by reducing the distribution of cracks that would otherwise allow the gas to circumvent the catalyst regions.

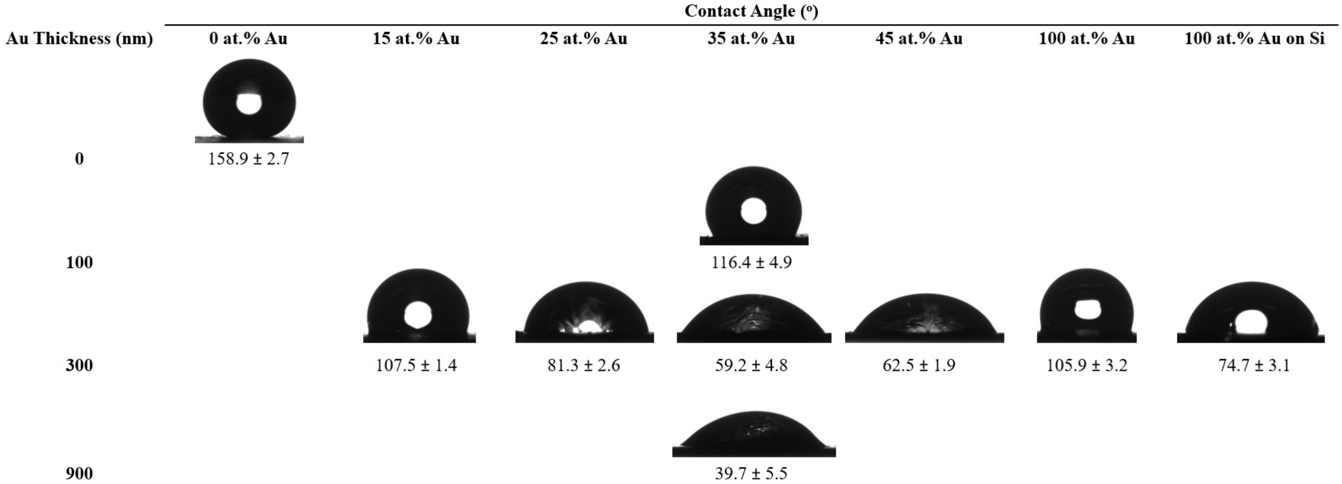

Figure 3.7*: Contact angle measurements of nanoporous gold electrodes with varying atomic gold percentages. 0 atomic percent Au indicates that there is no catalyst layer and 100 atomic percent Au indicates that there was a solid gold film deposited. All samples were deposited on Sigracet 38BC unless otherwise noted.*

We sought to better understand the difference in performance between the np-Au catalysts of varying $\%_{Au}$ by understanding how the electrolyte interacts with each system. Catalyst wetting is a critical component of device performance and we therefore carried out contact angle analysis of each of the electrodes to understand the macroscopic wetting properties. Figure 3.7 shows the contact angle of a variety of samples including the base carbon paper, 300 nm thick Au on Si substrate, pl-Au on carbon paper, and np-Au on carbon paper. The carbon paper itself is hydrophobic since it contains a fluorinated microporous layer and thus exhibits a contact angle of 159° whereas the 300 nm thick pl-Au GDE has a contact angle of 106°. The $15\%_{Au}$ GDE sample has a similar hydrophobicity to the pl-Au reference with a contact angle of 108°. Interestingly, the $35\%_{Au}$ was found to be the most hydrophilic with a contact angle of 59°. We attribute the higher hydrophobicity of lower $\%_{Au}$ samples to the large cracks in the catalyst layer that penetrate through to the hydrophobic microporous layer, which allows the water droplet to come into contact with the fluorinated microporous layer. The $35\%_{Au}$ has a more complete metal coverage, which minimizes contact with the microporous layer. Therefore, the hydrophilic network of pores is able to wick water into its structure and lower the contact angle. While this provides correlation between wetting and device performance this does not explain the improvement in CO_2R performance as catalyst hydrophobicity has been demonstrated in literature to improve CO_2R this trend was not observed in our system. To better understand our system, we must therefore consider wetting on the nanoscale as distinct from the bulk properties highlighted by contact angle analysis.

3.4 Copper underpotential deposition characterization

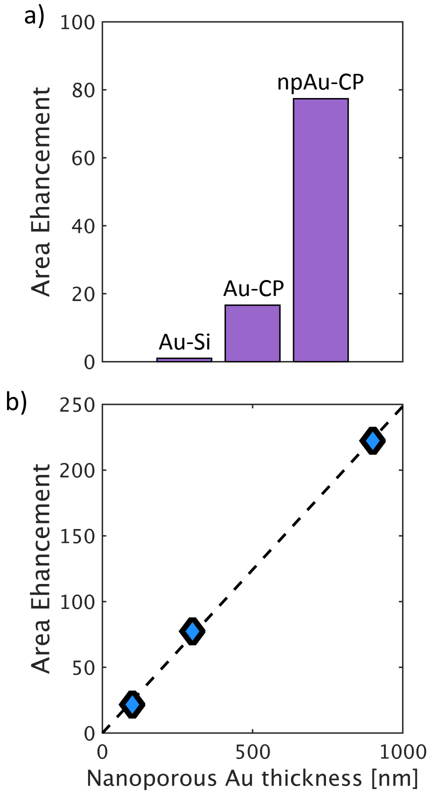

Figure 3.8: *(a) relative surface area enhancements of a 300 nm thick Au electrode and 300 nm thick 35 $\%_{Au}$ np-Au normalized to the Au on Si sample as calculated by Cu UPD. (b), Surface area enhancement of 100 nm, 300 nm, and 900 nm thick 35$\%_{Au}$ electrodes. The dashed line shows a linear fit with an* R^2 *= 1.00.*

Cu UPD allows us to further probe wetting on the nanoscale by evaluating where electrolyte is present. The Cu UPD process electroplates a monolayer of Cu onto any Au surface exposed to the electrolyte solution. It is then possible to integrate the cyclic voltammogram to determine how much charge was passed, which is proportional to the surface area.[7,41,42] We are therefore able to determine the surface area of the catalyst that is in contact with the electrolyte. We first measured the surface area of 300 nm of Au deposited onto a silicon wafer (Au-Si) as a baseline and normalized all further Cu UPD measurements to this value (Figure

3.8a). A 300 nm thick film of Au deposited onto carbon paper (pl-Au) exhibited a 15x area enhancement compared to the Au-Si. This enhancement indicated that the irregular carbon paper base substrate increases the rugosity and subsequently the surface area of the pl-Au electrode. In comparison a 300 nm thick 35%$_{Au}$ np-Au electrode on carbon paper has a 78x increase in surface area compared to the Au-Si and a 5x increase in surface area compared to the pl-Au electrode. This significant increase in surface area demonstrated that the nanotexturing method greatly enhanced the available surface area of a np-Au electrode relative to a pl-Au electrode. While cross-sectional SEM demonstrated a cross-sectionally consistent np-Au morphology (Figure S4), we sought to verify this interpretation with Cu UPD experiments. To achieve this, three distinct, 35%$_{Au}$ electrodes with a catalyst layer thickness of 100 nm, 300 nm, and 900 nm were fabricated and intentionally flooded by soaking them in an aqueous CO_2 fed electrochemical cell to ensure that the entire surface area of the catalyst layer was electrochemically accessible (Figure 3.8b). We found that the surface area as measured by Cu UPD increased linearly with the thickness of the catalyst. The linear increase in surface area with film thickness confirmed that our electrodes are indeed cross sectionally consistent and that the Cu^{2+} ions in solution penetrate into the entire depth of the catalyst layer in the aqueous CO_2 fed configuration. If this were not the case, we would have observed that the surface area enhancement measured by Cu UPD would taper off with increasing np-Au film thickness. This effect would result from the Cu^{2+} ions inability to diffuse throughout the extend of the np-Au network.

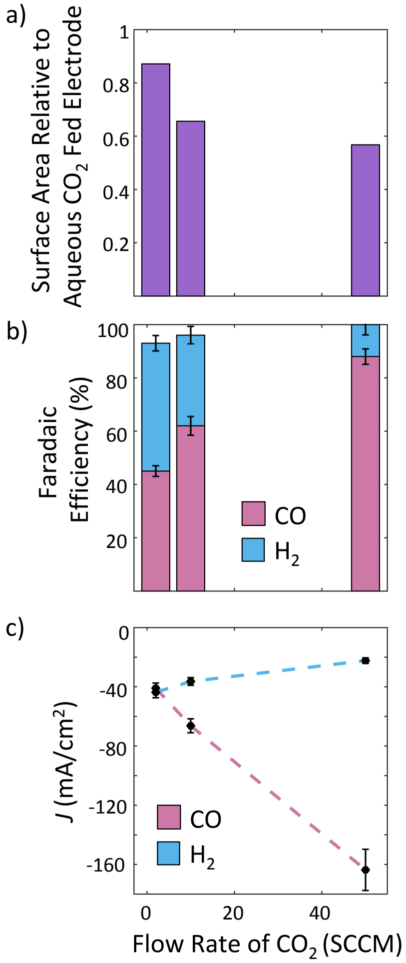

Figure 3.9: *(a) relative surface area of three identical 300 nm thick, 35%*$_{Au}$ *np-Au electrodes under different* CO_2 *flow rates normalized to the surface area of the same electrode in an aqueous* CO_2 *fed system. (b) Faradaic efficiencies of the electrodes at different* CO_2 *flow rates. (c) Partial current densities of the electrodes at different* CO_2 *flow rates. All experiments for (b) and (c) were carried out at -0.92* V_{RHE}.

Interestingly, we observed a 5x increase in surface area for the 35%$_{Au}$ sample compared to the pl-Au, with only a 2–3.5x increase in *J*. To understand the discrepancy between surface area and *J* we carried out a set of Cu UPD experiments under vapor CO_2 fed conditions (Figure 3.9a). We hypothesized that the surface area calculated by Cu UPD from an electrode in an aqueous CO_2 fed system represents the true surface area of the of the np-Au catalyst layer as the entirety of the Au is in contact with the electrolyte, i.e. flooded. The surface area of a fully flooded np-Au electrode is normalized to one and any deviation from this value by a vapor CO_2 fed electrode can be attributed to a percentage of the catalyst layer being inaccessible to the electrolyte. At a flow rate of 50 SCCM the measured surface area of a 35%$_{Au}$ electrode decreased to 57% of its maximum value, indicating that only ~½ the electrode is in contact with the electrolyte. As the flow rate was reduced to 10 SCCM and 2 SCCM the accessible surface area increased to 66% and 87% of the total available surface area respectively. We attribute this effect to an increase of flooded pores in the np-Au catalyst layer due to the pressure drop as a result of the reduced flow rate. To evaluate this, we performed a series of CO_2R experiments on 300 nm thick, $35\%_{Au}$ np-Au electrodes at 50 SCCM, 10 SCCM and 2 SCCM at $-0.92\ V_{RHE}$. We found that the current density decreased from -190 mA/cm^2 for the 50 SCCM sample to -107 mA/cm^2 for the 10 SCCM sample and further to -91 mA/cm^2 for the 2 SCCM sample (Figure 3c). This drop in current density indicates that the catalyst layer is flooding as the flow rate of CO_2 is reduced and that the flooded sections of the electrode have regions more similar to the mass transport limited, aqueous CO_2 fed system rather than the vapor CO_2 fed system. To further verify this, we tracked the FE for H_2 of each electrode and found it to increase from 12% for the 50 SCCM sample to 34% for the 10 SCCM sample and to 48% for the 2 SCCM sample (Figure 3.9b). This increase in HER indicates that the catalyst cannot carry out CO_2R and instead, increasingly engages in parasitic HER in the flooded pores. This result indicates that the catalyst layer exists in as a combination of three distinct states (Figure 3.1). State one is the fully flooded state that aqueous CO_2 fed systems exists in. This state of operation heavily suppresses current density due the mass transport limitations caused by the longer diffusion lengths that CO_2 must travel through the electrolyte to reach the catalyst surface. State two is the vapor CO_2 fed, GDE configuration in which thin layers of electrolyte wet the catalyst surface and gaseous pores effectively deliver CO_2 throughout the catalyst layer. In this state, the much smaller diffusion length allows high current densities to be achieved. It should be noted that these two states are indistinguishable by Cu UPD but that an increase in flooding is apparent as current density is reduced and HER is increased. In state three, the catalyst is completely dry and unavailable for catalysis.

3.5 Secondary ion mass spectroscopy characterization

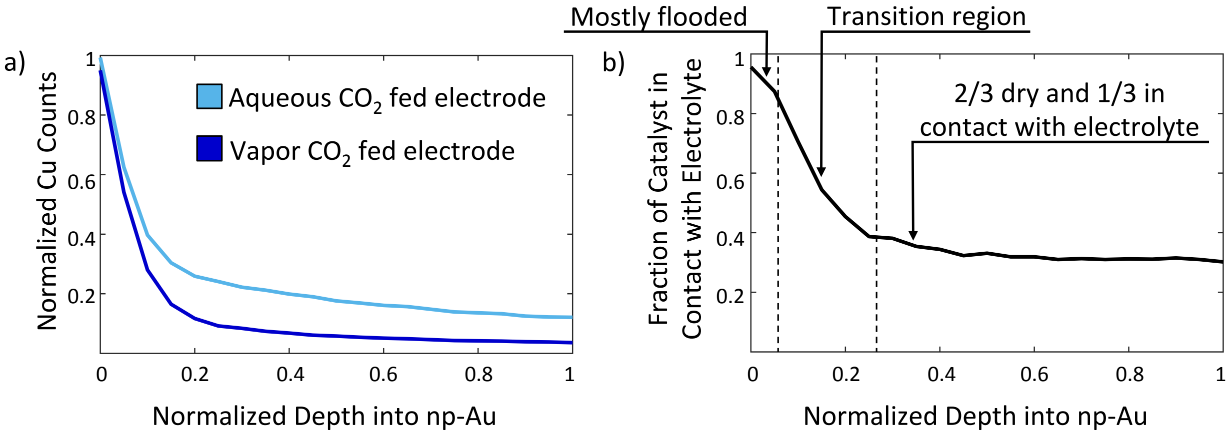

Figure 3.10: *Secondary ion mass spectroscopy data summary. (a) shows normalized Cu counts relative to normalized depth into the np-Au electrode with 0 as the surface of the np-Au electrode in contact with the electrolyte and 1 as the np-Au electrode in contact*

with the microporous layer. (b) is the ratio of the of the vapor CO_2 fed counts to the aqueous CO_2 fed counts in (a) and represent the portion of the catalyst that is in contact with the electrolyte as a function of depth.

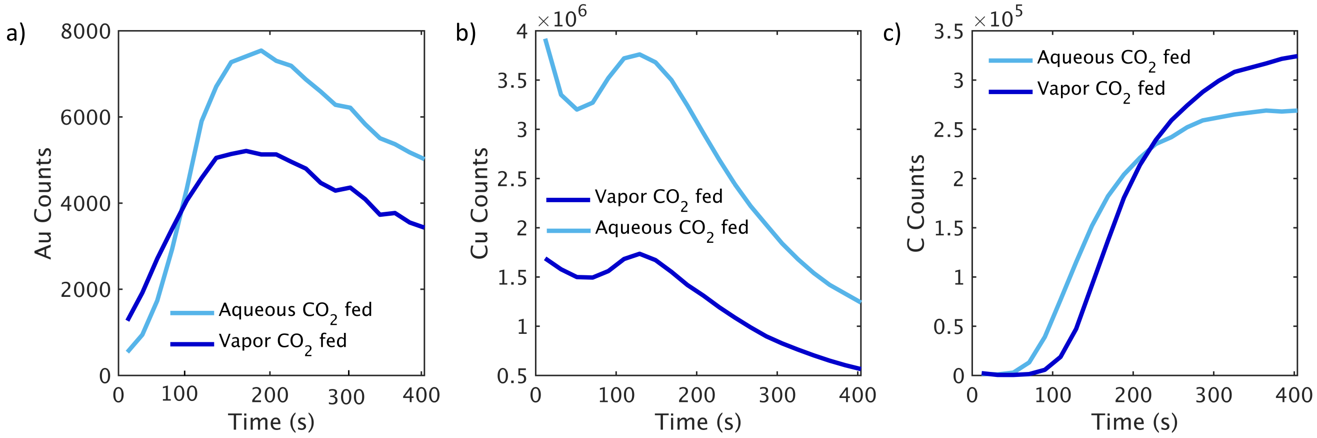

***Figure 3.11**: Secondary ion mass spectroscopy raw data for aqueous CO_2 fed system and vapor CO_2 fed system. (a) shows the gold counts, (b) the copper counts, and (c) the carbon counts.*

In order to verify that these Cu UPD results indicate that a certain fraction of the catalyst is unwetted, we electroplated Cu onto a flooded and operando electrode. This should yield an electrode with copper metal plated onto the regions that were in contact with electrolyte and an absence of copper where the electrode is dry. Therefore, the presence of Cu is a proxy for wetting and will be referred to as such from now on. Secondary Ion Mass Spectroscopy (SIMS) was carried out on an aqueous CO_2 fed electrode and a vapor CO_2 fed electrode to elucidate where the Cu was spatially deposited (Figure 3.10a and Figure 3.11). We make the assumption that the np-Au electrodes of each sample are near identical and then compare the Cu/Au ratio of each distinct electrode. We find that the total integrated Cu/Au count of the vapor CO_2 fed electrode is 57% that of the aqueous CO_2 fed electrode (Figure 3.10a). This result is in close agreement with our Cu UPD finding that the vapor CO_2 fed electrode has 56% the surface area of the aqueous CO_2 fed one. Next, we took the ratio of these results to determine the percentage of the vapor CO_2 fed electrode that is in contact with the electrolyte as a function of depth (Figure 3.10b). We define 0 as the surface of the np-Au electrode in contact with the electrolyte and 1 as the np-Au electrode in contact with the microporous layer. If the vapor fed/aqueous fed ratio is equal to 1, the wetting of the electrodes are equivalent whereas fractional deviations indicate that the aqueous CO_2 fed electrode has more gold in contact with the electrolyte. We find that the vapor fed/aqueous fed depth profile can be separated into three distinct regions. In region 1 (the top 10% of the catalyst) both electrodes have a comparable wetting which indicates that the vapor CO_2 fed electrode is likely highly flooded this region. Region 2 is a transition zone where the wetting in the catalyst layer of the vapor CO_2 fed is increasingly reduced compared to the aqueous CO_2 fed electrode. Region 3 consists of the bottom 75% of the catalyst layer and here the vapor CO_2 fed electrode has 2/3 less wetting than the aqueous CO_2 fed electrode. This finding shows that a significant fraction of the catalyst layer of the vapor CO_2 fed electrode is not in contact with the electrolyte and therefore does not contribute to CO_2R. These previously unknown results allow us to determine the percentage of the catalyst that contributes towards CO_2R. We anticipate that these results will allow for improved GDE designs that are capable of harnessing all of the available electrode surface area to drive electrocatalytic CO_2R.

3.6 Conclusion

In this work we provide a new method for how to evaluate the active regions of GDEs for CO_2R. Through a combination of Cu UPD and SIMS we were able to show that under operating conditions for a vapor CO_2 fed device that the top 10% of the nanoporous gold layer is fully flooded, while the rest of the catalyst layer exists as combination of the flooded/wetted and dry. Strikingly, 43% of the catalyst is not in contact with the electrolyte at all. In addition to providing this new insight into the active regions of the catalyst we also demonstrate a highly active CO_2R device. The np-Au GDEs are capable of attaining an FE for CO of up to 95% and a J_{CO} of -168 mA/cm^2. We hope that our analysis will enable our colleagues in the field to better understand and maximize the amount of catalyst that contributes towards CO_2R.

BIBLIOGRAPHY CHAPTER 3

1. Garg, S.; Li, M.; Weber, A. Z.; Ge, L.; Li, L.; Rudolph, V.; Wang, G.; Rufford, T. E. Advances and Challenges in Electrochemical CO_2 Reduction Processes: An Engineering and Design Perspective Looking beyond New Catalyst Materials. *J. Mater. Chem. A* **2020**, *8* (4), 1511–1544.
2. Schreier, M.; Héroguel, F.; Steier, L.; Ahmad, S.; Luterbacher, J. S.; Mayer, M. T.; Luo, J.; Grätzel, M. Solar Conversion of CO_2 to CO Using Earth-Abundant Electrocatalysts Prepared by Atomic Layer Modification of CuO. *Nat. Energy* **2017**, *2* (7).
3. Lin, S.; Diercks, C. S.; Zhang, Y. B.; Kornienko, N.; Nichols, E. M.; Zhao, Y.; Paris, A. R.; Kim, D.; Yang, P.; Yaghi, O. M.; Chang, C. J. Covalent Organic Frameworks Comprising Cobalt Porphyrins for Catalytic CO_2 Reduction in Water. *Science (80-.).* **2015**, *349* (6253), 1208–1213.
4. Kuhl, K. P.; Cave, E. R.; Abram, D. N.; Jaramillo, T. F. New Insights into the Electrochemical Reduction of Carbon Dioxide on Metallic Copper Surfaces. *Energy Environ. Sci.* **2012**, *5* (5), 7050–7059.
5. Kuhl, K. P.; Hatsukade, T.; Cave, E. R.; Abram, D. N.; Kibsgaard, J.; Jaramillo, T. F. Electrocatalytic Conversion of Carbon Dioxide to Methane and Methanol on Transition Metal Surfaces. *J. Am. Chem. Soc.* **2014**, *136* (40), 14107–14113.
6. Hatsukade, T.; Kuhl, K. P.; Cave, E. R.; Abram, D. N.; Jaramillo, T. F. Insights into the Electrocatalytic Reduction of CO_2 on Metallic Silver Surfaces. *Phys. Chem. Chem. Phys.* **2014**, *16* (27), 13814–13819.

7. Welch, A. J.; Duchene, J. S.; Tagliabue, G.; Davoyan, A.; Cheng, W. H.; Atwater, H. A. Nanoporous Gold as a Highly Selective and Active Carbon Dioxide Reduction Catalyst. *ACS Appl. Energy Mater.* **2019**, *2* (1), 164–170.
8. Rosen, B. A.; Salehi-khojin, A.; Thorson, M. R.; Zhu, W.; Whipple, D. T.; Kenis, P. J. A.; Masel, R. I. Ionic Liquid – Mediated Selective. *Science (80-.).* **2011**, *334* (November), 643–645.
9. Yang, J.; Ma, W.; Chen, D.; Holmen, A.; Davis, B. H. Fischer-Tropsch Synthesis: A Review of the Effect of CO Conversion on Methane Selectivity. *Appl. Catal. A Gen.* **2014**, *470*, 250–260.
10. Verma, S.; Kim, B.; Jhong, H. R. M.; Ma, S.; Kenis, P. J. A. A Gross-Margin Model for Defining Technoeconomic Benchmarks in the Electroreduction of CO_2. *ChemSusChem* **2016**, *9* (15), 1972–1979.
11. Hernández, S.; Farkhondehfal, M. A.; Sastre, F.; Makkee, M.; Saracco, G.; Russo, N. Syngas Production from Electrochemical Reduction of CO_2: Current Status and Prospective Implementation. *Green Chem.* **2017**, *19* (10), 2326–2346.
12. Pruett, R. L.; Smith, J. A. A Low-Pressure System for Producing Normal Aldehydes by Hydroformylation of α Olefins. *J. Org. Chem.* **1969**, *34* (2), 327–330.
13. Jhong, H. R. M.; Ma, S.; Kenis, P. J. Electrochemical Conversion of CO_2 to Useful Chemicals: Current Status, Remaining Challenges, and Future Opportunities. *Curr. Opin. Chem. Eng.* **2013**, *2* (2), 191–199.
14. Bloemacher, D. Carbonyl Iron Powders: Its Production and New Developments. *Met. Powder Rep.* **1990**, *45* (2), 117–119.
15. Bushuyev, O. S.; De Luna, P.; Dinh, C. T.; Tao, L.; Saur, G.; van de Lagemaat, J.; Kelley, S. O.; Sargent, E. H. What Should We Make with CO_2 and How Can We Make It? *Joule* **2018**, *2* (5), 825–832.
16. Nitopi, S.; Bertheussen, E.; Scott, S. B.; Liu, X.; Engstfeld, A. K.; Horch, S.; Seger, B.; Stephens, I. E. L.; Chan, K.; Hahn, C.; Nørskov, J. K.; Jaramillo, T. F.; Chorkendorff, I. Progress and Perspectives of Electrochemical CO2 Reduction on Copper in Aqueous Electrolyte. *Chem. Rev.* **2019**, *119* (12), 7610–7672.
17. Lu, Q.; Rosen, J.; Zhou, Y.; Hutchings, G. S.; Kimmel, Y. C.; Chen, J. G.; Jiao, F. A Selective and Efficient Electrocatalyst for Carbon Dioxide Reduction. *Nat. Commun.* **2014**, *5*, 1–6.
18. Asadi, M.; Kim, K.; Liu, C.; Addepalli, A. V.; Abbasi, P.; Yasaei, P.; Phillips, P.; Behranginia, A.; Cerrato, J. M.; Haasch, R.; Zapol, P.; Kumar, B.; Klie, R. F.; Abiade, J.; Curtiss, L. A.; Salehi-Khojin, A. Nanostructured Transition Metal Dichalcogenide Electrocatalysts for CO_2 Reduction in Ionic Liquid. *Science (80-.).* **2016**, *353* (6298), 467–470.
19. Gao, D.; Zhou, H.; Wang, J.; Miao, S.; Yang, F.; Wang, G.; Wang, J.; Bao, X. Size-Dependent Electrocatalytic Reduction of CO_2 over Pd Nanoparticles. *J. Am. Chem. Soc.* **2015**, *137* (13), 4288–4291.
20. Chen, Y.; Li, C. W.; Kanan, M. W. Aqueous CO_2 Reduction at Very Low Overpotential on Oxide-Derived Au Nanoparticles. *J. Am. Chem. Soc.* **2012**, *134* (49), 19969–19972.
21. Weng, L. C.; Bell, A. T.; Weber, A. Z. Modeling Gas-Diffusion Electrodes for CO_2 Reduction. *Phys. Chem. Chem. Phys.* **2018**, *20* (25), 16973–16984.
22. Ma, M.; Clark, E. L.; Therkildsen, K. T.; Dalsgaard, S.; Chorkendorff, I.; Seger, B. Insights into the Carbon Balance for CO_2 Electroreduction on Cu Using Gas Diffusion Electrode Reactor Designs. *Energy Environ. Sci.* **2020**, *13* (3), 977–985.
23. Singh, M. R.; Goodpaster, J. D.; Weber, A. Z.; Head-Gordon, M.; Bell, A. T. Mechanistic Insights into Electrochemical Reduction of CO_2 over Ag Using Density Functional Theory and Transport Models. *Proc. Natl. Acad. Sci. U. S. A.* **2017**, *114* (42), E8812–E8821.
24. Weekes, D. M.; Salvatore, D. A.; Reyes, A.; Huang, A.; Berlinguette, C. P. Electrolytic CO_2 Reduction in a Flow Cell. *Acc. Chem. Res.* **2018**, *51* (4), 910–918.
25. Higgins, D.; Hahn, C.; Xiang, C.; Jaramillo, T. F.; Weber, A. Z. Gas-Diffusion Electrodes for Carbon Dioxide Reduction: A New Paradigm. *ACS Energy Lett.* **2019**, *4* (1), 317–324.
26. García de Arquer, F. P.; Dinh, C. T.; Ozden, A.; Wicks, J.; McCallum, C.; Kirmani, A. R.; Nam, D. H.; Gabardo, C.; Seifitokaldani, A.; Wang, X.; Li, Y. C.; Li, F.; Edwards, J.; Richter, L. J.; Thorpe, S. J.;

Sinton, D.; Sargent, E. H. CO_2 Electrolysis to Multicarbon Products at Activities Greater than 1 A Cm−2. *Science (80-.).* **2020**, *367* (6478), 661–666.

27. Grigioni, I.; Sagar, L. K.; Li, Y. C.; Lee, G.; Yan, Y.; Bertens, K.; Miao, R. K.; Wang, X.; Abed, J.; Won, D. H.; Garciá De Arquer, F. P.; Ip, A. H.; Sinton, D.; Sargent, E. H. CO_2 Electroreduction to Formate at a Partial Current Density of 930 MA Cm-2 with InP Colloidal Quantum Dot Derived Catalysts. *ACS Energy Lett.* **2021**, *6* (1), 79–84.
28. Dinh, C. T.; García De Arquer, F. P.; Sinton, D.; Sargent, E. H. High Rate, Selective, and Stable Electroreduction of CO_2 to CO in Basic and Neutral Media. *ACS Energy Lett.* **2018**, *3* (11), 2835–2840.
29. Verma, S.; Hamasaki, Y.; Kim, C.; Huang, W.; Lu, S.; Jhong, H. R. M.; Gewirth, A. A.; Fujigaya, T.; Nakashima, N.; Kenis, P. J. A. Insights into the Low Overpotential Electroreduction of CO_2 to CO on a Supported Gold Catalyst in an Alkaline Flow Electrolyzer. *ACS Energy Lett.* **2018**, *3* (1), 193–198.
30. Zhang, W.; He, J.; Liu, S.; Niu, W.; Liu, P.; Zhao, Y.; Pang, F.; Xi, W.; Chen, M.; Pang, S. S.; Ding, Y. Atomic Origins of High Electrochemical CO_2 Reduction Efficiency on Nanoporous Gold. *Nanoscale* **2018**, *10* (18), 8372–8376.
31. Chen, C.; Zhang, B.; Zhong, J.; Cheng, Z. Selective Electrochemical CO_2 Reduction over Highly Porous Gold Films. *J. Mater. Chem. A* **2017**, *5* (41), 21955–21964.
32. Wang, R.; Wang, C.; Cai, W. Bin; Ding, Y. Ultralow-Platinum-Loading High-Performance Nanoporous Electrocatalysts with Nanoengineered Surface Structures. *Adv. Mater.* **2010**, *22* (16), 1845–1848.
33. Sukeri, A.; Saravia, L. P. H.; Bertotti, M. A Facile Electrochemical Approach to Fabricate a Nanoporous Gold Film Electrode and Its Electrocatalytic Activity towards Dissolved Oxygen Reduction. *Phys. Chem. Chem. Phys.* **2015**, *17* (43), 28510–28514.
34. Hall, A. S.; Yoon, Y.; Wuttig, A.; Surendranath, Y. Mesostructure-Induced Selectivity in CO_2 Reduction Catalysis. *J. Am. Chem. Soc.* **2015**, *137* (47), 14834–14837.
35. Biener, J.; Biener, M. M.; Madix, R. J.; Friend, C. M. Nanoporous Gold: Understanding the Origin of the Reactivity of a 21st Century Catalyst Made by Pre-Columbian Technology. *ACS Catal.* **2015**, *5* (11), 6263–6270.
36. Verma, S.; Lu, X.; Ma, S.; Masel, R. I.; Kenis, P. J. A. The Effect of Electrolyte Composition on the Electroreduction of CO_2 to CO on Ag Based Gas Diffusion Electrodes. *Phys. Chem. Chem. Phys.* **2016**, *18* (10), 7075–7084.
37. Winter, M.; Brodd, R. J. What Are Batteries, Fuel Cells, and Supercapacitors? *Chem. Rev.* **2004**, *104* (10), 4245–4269.
38. Gülzow, E.; Schulze, M. Long-Term Operation of AFC Electrodes with CO_2 Containing Gases. *J. Power Sources* **2004**, *127* (1–2), 243–251. https://doi.org/10.1016/j.jpowsour.2003.09.020.
39. Gülzow, E. Alkaline Fuel Cells: A Critical View. *J. Power Sources* **1996**, *61* (1–2), 99–104.
40. Gouérec, P.; Poletto, L.; Denizot, J.; Sanchez-Cortezon, E.; Miners, J. H. The Evolution of the Performance of Alkaline Fuel Cells with Circulating Electrolyte. *J. Power Sources* **2004**, *129* (2), 193–204.
41. Zhang, B. A.; Ozel, T.; Elias, J. S.; Costentin, C.; Nocera, D. G. Interplay of Homogeneous Reactions, Mass Transport, and Kinetics in Determining Selectivity of the Reduction of CO_2 on Gold Electrodes. *ACS Cent. Sci.* **2019**, *5* (6), 1097–1105.
42. Ross, M. B.; Dinh, C. T.; Li, Y.; Kim, D.; De Luna, P.; Sargent, E. H.; Yang, P. Tunable Cu Enrichment Enables Designer Syngas Electrosynthesis from CO_2. *J. Am. Chem. Soc.* **2017**, *139* (27), 9359–9363.

Chapter 4

OPERANDO LOCAL pH MEASUREMENT WITHIN GAS DIFFUSION ELECTRODES PERFORMING ELECTROCHEMICAL CARBON DIOXIDE REDUCTION

4.1 Introduction

While the cost of renewable electricity has declined markedly, selective, energy-efficient synthesis of storable chemical fuels is necessary to enable widespread adoption of sustainable energy. One approach is to transform solar energy into chemical fuels and fuel precursors via artificial photosynthesis. Recently, significant advances have been made in the design of gas diffusion electrodes (GDEs) for electrochemical carbon dioxide (CO_2) reduction at high current densities. While promising, GDEs have not yet achieved their full potential for product selectivity and energy efficiency due to the complexity of the electrocatalytic reactions involved in making fuels from CO_2 reduction.

Many parameters may influence the selectivity and activity of the CO_2 reduction reaction, the most obvious of which are the catalyst[1–3] and applied potential.[4,5] Aside from these two critical parameters, GDE system configurations (flow through vs. flow by),[6] local electrolyte viscosity,[7] concentration and identity of cations in the electrolyte,[8] salt deposition on the GDE,[9] membrane structure and composition,[10] bicarbonate and carbonate formation in the electrolyte,[11] hydrophobicity of thee GDE,[12] and other factors can have a significant influence on device performance.

Of particular interest in this work is the local pH established at the electrode surface during fuel synthesis. Electrochemical solar fuel-forming reactions create hydroxide ions (OH^-) at the catalyst surface during the reaction when in alkaline electrolyte which alters the local pH near the cathode,[13,14] thus strongly impacting both product selectivity and activity.[15–18] Therefore, it is important to distinguish the local pH near the electrode surface from the pH in the bulk electrolyte. Although challenging to determine experimentally, the local pH near the electrode surface should be measured under operating conditions to provide the necessary insight required to further improve the activity, selectivity, and stability of these fuel-forming devices.

In this study, we focus on understanding the pH in GDEs because this device architecture has increased the performance of CO_2 reduction electrodes by an order of magnitude due to their ability to deliver CO_2 in the gas phase, thereby overcoming the mass transport limitations encountered in more traditional electrocatalytic devices.[19] Not only does this architecture allow for higher current densities, but also improved product selectivity in CO_2 reduction.[19–21] In CO_2 reduction devices where the CO_2 is dissolved directly into the electrolyte, the maximum current density is less than –30 mA/cm^2 due to low CO_2 solubility in aqueous electrolytes (around [34 mM] at maximum).[22] The main challenge of the GDE architecture is in developing the appropriate device structure to maintain what is referred to as a "wetted" condition. Here, a thin layer of electrolyte coats the catalyst to provide water molecules while simultaneously allowing for rapid dissolution of CO_2 through the electrolyte to avoid mass-transport limitations. If the water layer coating the catalyst is too thick, the catalyst becomes flooded and its operation is more similar to a bulk aqueous electrolyte CO_2 reduction device.[23] Alternatively, if there is no electrolyte, the catalyst has no access to water molecules and no reaction can occur. To achieve this wetted condition the GDE is composed of a gas diffusion layer, microporous layer, and catalyst layer (Figure 4.1). The microporous layer is perhaps the most critical because the concentration of polytetrafluoroethylene (PTFE) allows the wetting to be tuned.[12,23] Tailored GDE architectures have demonstrated current densities greater than 1 A/cm^2 for multi-carbon products.[24]

It is vital to understand the local pH within GDEs due to the high CO_2 flow rates and high current densities at which these devices operate. Interestingly, these two characteristics have opposing effects on the local pH near the electrode surface. High current densities result in the creation of multiple hydroxide ions per unit time, thus rapidly increasing the pH, while any unreacted CO_2 will acidify the electrolyte via reaction with OH^- to form HCO_3^- and H^+ ions. If the pH is increased locally, the activity of the hydrogen evolution reaction (HER) decreases substantially, while the CO_2 reduction reaction becomes relatively more favorable.[17,18] While both reactions consume water molecules, the rate of H_2 evolution has been shown to be far more dependent on the local pH than the rate of CO_2 reduction.[17,25] In addition to suppressing HER, the local pH also influences which CO_2 reduction pathways are most energetically favorable.[16,18,26] Alkaline conditions in particular promote the formation of multi-carbon products (C_{2+}) such as ethanol, propanol, acetate, etc.[16,25,26] Theoretical models have been developed to simulate the local pH near operating CO_2 reduction GDEs,[23,27,28] however it is difficult to accurately represent the complex electrochemical environment created by the triple phase boundary at the catalyst surface. We therefore seek to directly measure the local pH near an operating GDE and experimentally validate the results of these prior simulations.

There are various techniques that can be used to probe the local pH, such as fluorescence microscopy,[15,29–34] scanning electrochemical cell microscopy (SECM),[35–37] surface enhanced Raman spectroscopy (SERS),[38] and surface-enhanced infrared absorption spectroscopy (SEIRAS).[39] Previously, SERS has been used to measure the local pH in a CO_2 reduction GDE with a 1 M KOH electrolyte (pH 14). It was found that the local pH was near 7 in the absence of any current flow, and as the current density increased to 100 mA/cm^2, the local pH increased to 10. It is interesting to note that even with an electrolyte with a bulk pH of 14, the electrode surface remained in the range pH range of 7-10 for a wide range of current densities. However, this measurement did not provide any resolution along the plane of the electrode surface. SECM studies confirm that the local pH increases during device operation. [35–37] While SECM allows for better spatial resolution than confocal fluorescent microscopy, it is unable to probe the pH within the trenches of the GDE, Figure 4.1e, f. Our study builds on previous work by mapping the pH both on the surface and within the heterogeneous reaction environments encountered in GDEs. This experimental approach therefore allows us to correlate the width of trenches in GDEs to the local pH.

Here, we use confocal microscopy and a pH-sensitive two-color fluorescent dye to probe the *operando* local pH of a copper (Cu) GDE under CO_2 reduction conditions with micron-scale resolution in all three spatial dimensions [within the plane of the electrode (x, y) and perpendicular to its surface (z)]. This approach offers new insight into how CO_2 reduction affects the local electrolyte pH near the Cu catalyst. Interestingly, our study indicates that at low overpotentials, the pH varies widely across the electrode surface. Specifically, in narrow trenches throughout the electrode, the pH is significantly elevated compared to the surroundings. Our findings highlight the electrocatalytic heterogeneity in GDEs and strongly suggest that these regions of locally-high pH are the most active parts of the electrode for CO_2 reduction.

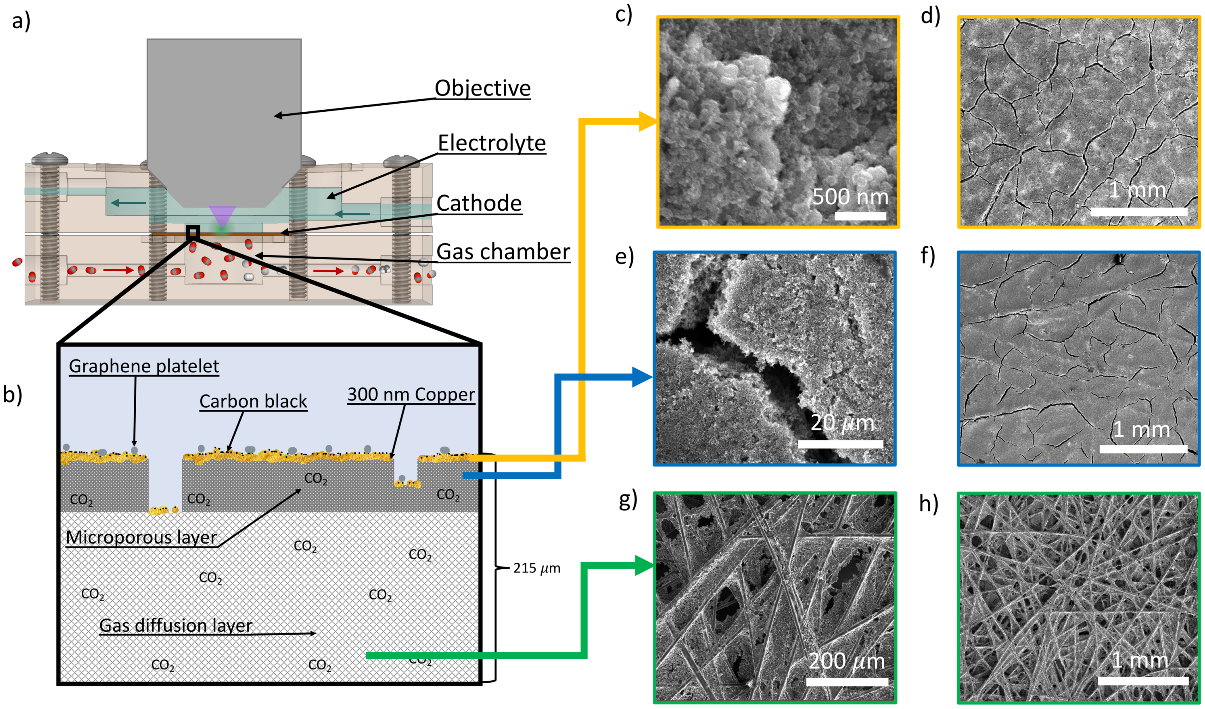

Figure 4.1: *Overview of a Cu gas diffusion electrode (GDE) for CO_2 reduction studies. (a) Cross-sectional diagram of the custom electrochemical cell designed to enable in situ confocal fluorescent microscopy experiments. (b) Schematic of a typical Cu GDE, not to*

scale. (c), (d) Scanning electron microscope (SEM) images of a Cu GDE. (e), (f) SEM images of an uncoated microporous layer. (g), (h) SEM images of the gas diffusion layer.

A Cu-based GDE was investigated owing to the unique ability of Cu to produce C_{2+} products (e.g. ethanol).[3,40] Figure 4.1 shows a schematic of the GDE and experimental setup used, as well as scanning electron microscopy (SEM), and optical bright-field microscopy images of different layers of the device. The GDE used here and in many other devices[19,25,41,42] is composed of three layers: (1) a gas diffusion layer, (2) a microporous layer, and (3) a catalyst layer (Figure 4.1b). The CO_2 first diffuses through the gas diffusion layer, composed of carbon fibers (Figure 4.1 g, h), and then through the microporous layer, which is made of carbon black coated in hydrophobic PTFE to regulate local electrolyte availability (Figure 4.1e, f). After diffusion through the microporous layer, the CO_2 comes into contact with the electrolyte at the catalyst layer (Figure 4.1c, d) where it can then undergo reduction to yield a variety of chemical products.

Some CO_2 reacts at the catalyst surface into products such as CO, HCOOH, or CH_4. The remaining unreacted portion of the CO_2 then passes into the electrolyte and increases its acidity.[43] While several reports quantified the one pass CO_2 utilization efficiency,[44] the vast majority of the CO_2 reduction experiments did not seek to optimize the utilization of CO_2. The competition between these two processes – CO_2 acidification and hydroxide ion generation – can be investigated *via* measurement of the local pH at the catalyst-electrolyte interface.

4.2 Experimental set up and characterization

We used confocal fluorescent microscopy to measure the local pH due to its high spatial resolution relative to the dimensions of interest in the system. Figure 4.1a shows a schematic of the experimental set up and Figure 4.2 shows a more detailed schematic, as well as photos of the cell. The technical resolution of this system is 280 nm in x-y and 560 nm in z. However due to noise from the electrolyte pump and diffusion, the resolution is on the order of a micron under our conditions. A laser is used to excite a ratiometric two-color pH sensitive fluorescent dye, 6,8-dihydroxy-1,3-pyrenedisulfonic acid (DHPDS) in the electrolyte.[45] This approach ensures that the pH is independent of the concentration of DHPDS in the solution.[15] Figure 4.3 shows the absorbance vs. wavelength of DHPDS in different standard solutions of known pH. At the most acidic pH of 4.6, the peak absorbance is centered at ~400 nm, at pH 8.5 the peak absorbance is at ~455 nm, and at pH 11.7 the peak absorbance shifts toward ~480 nm. We focused our studies on near-neutral to basic pH conditions based on the results of previous work,[22,25] which reported that these conditions are most favorable for CO_2

reduction. We therefore sequentially excite the dye line by line with a 458 nm (λ_{ex1}) and 488 nm (λ_{ex2}) laser in order to achieve the resolution over the widest range of relevant pH values.

DHPDS was calibrated by collecting the fluorescence from two different wavelength excitations (458 nm and 488 nm) for a range of pH solutions. The solutions were made by mixing KOH, bicarbonate, water and standard buffer solutions. The pH of these solutions was measured by a Denver Instruments Ultra Basic pH meter and results were confirmed with color changing pH strips. The pH meter was calibrated with buffer solutions at pH 4, pH 7, and pH 10 before every set of measurements. The solution was then placed under the microscope and the water immersion objective was immersed in it. The objective was then focused on a point in the middle of the solution. Three images were then taken here with sequential line by line excitation of 458 nm and 488 nm. The fluorescence intensity signal was gathered from 515 – 700 nm. The ratio of the fluorescence from these two excitations was then plotted vs. pH to generate Figure 4.3b. The pH was measured again after the image was taken to make sure the pH reading is accurate. After acquiring all of the data, we fit the pH data to the function, $y = -a / (1 + \exp(-b * (x - c))) + d$. We found that coefficients to be $a = -33.72$, $b = 1.413$, $c = 8.083$, and $d = 5.571$ for a 95% confidence bounds. We therefore have an error of 0.3 pH units.

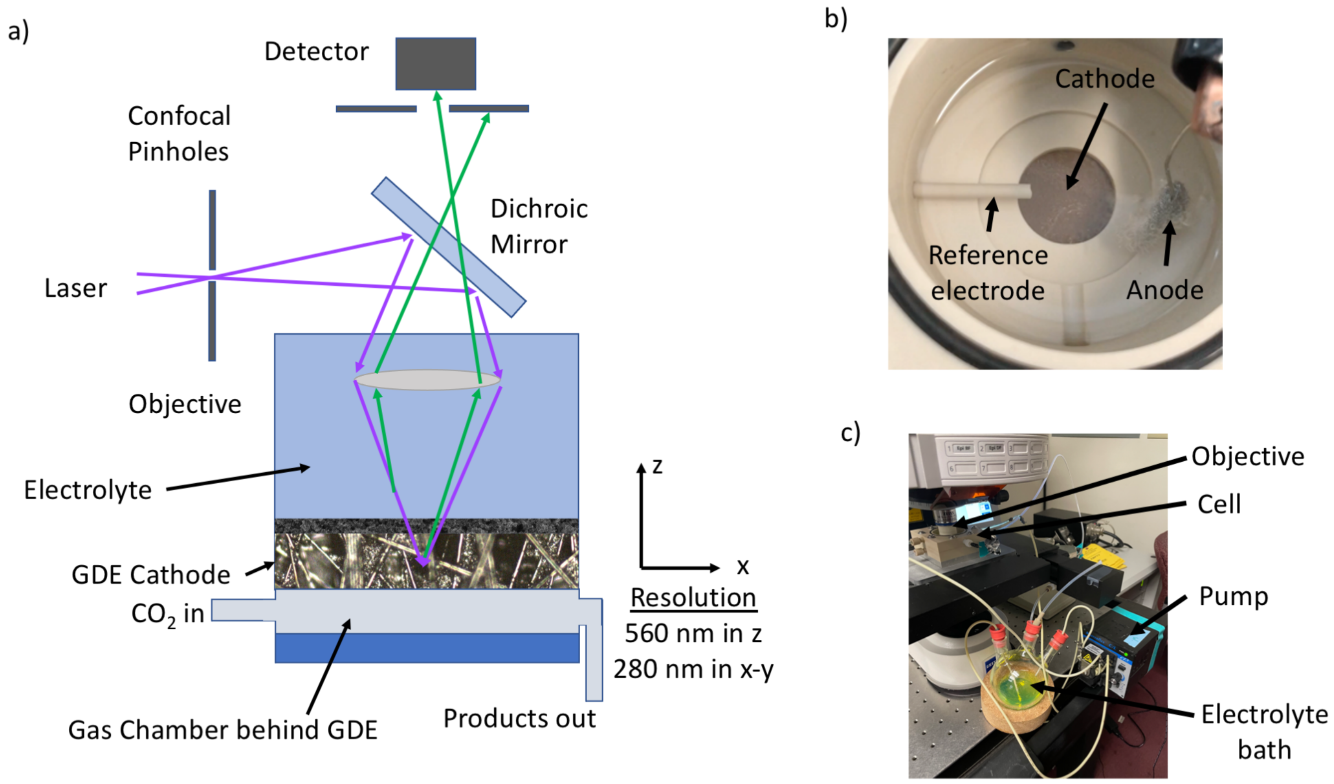

***Figure 4.2**: (a) shows a schematic of the electrochemical cell used for imaging the pH via confocal fluorescent microscopy. The bottom plate is the gas chamber and the top plate holds the electrolyte. This setup has no membrane and the electrolyte is constantly being*

flowed across the active catalyst layer. (b) shows a top-down photo of the electrochemical cell without the microscope objective. (c) shows a photo of the entire experimental setup with the objective in the cell, the electrolyte bath, and the pump to circulate the electrolyte through the electrochemical cell.

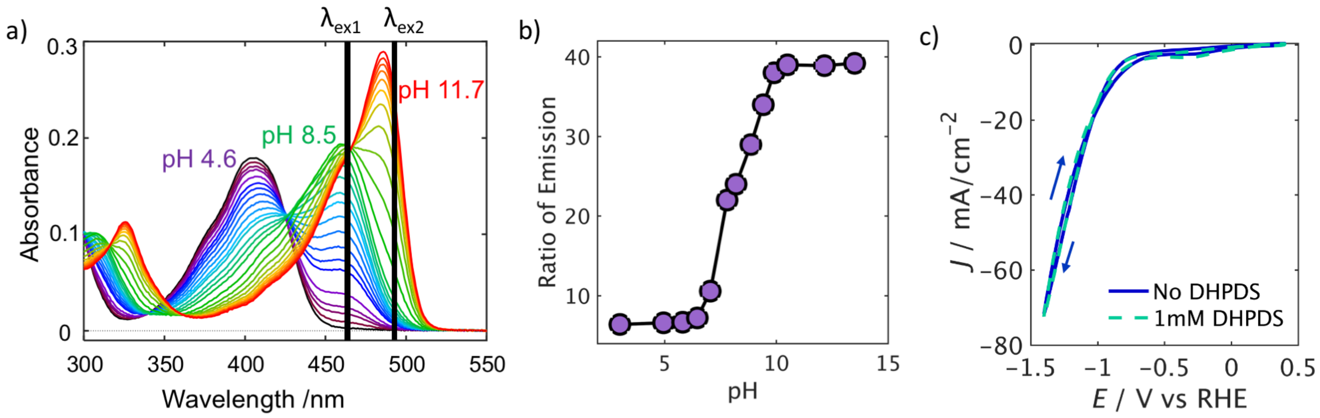

Figure 4.3: *Characterization of the pH-sensitive DHPDS fluorescent dye. (a) shows the absorbance of DHPDS for different pH solutions. vertical black lines denote the two different excitation wavelengths (λ_{ex1} = 458 nm) and (λ_{ex2} = 458 nm) used for the study. (b) shows the ratio of fluorescence emission from a 458 nm and 488 nm excitation wavelength as a function of solution pH. After acquiring all of the data, we fit the pH data to the function, $y = -a/(1+exp(-b*(x-c)))+d$. We found the coefficients to be a = –33.72, b = 1.413, c = 8.083, and d = 5.571 for 95% confidence bounds. We therefore have an error of 0.3 pH units. (c) shows the current (J) vs applied electrode potential (E) for a CO_2 reduction electrode with (dashed line) and without (solid line) DHPDS dye in the electrolyte.*

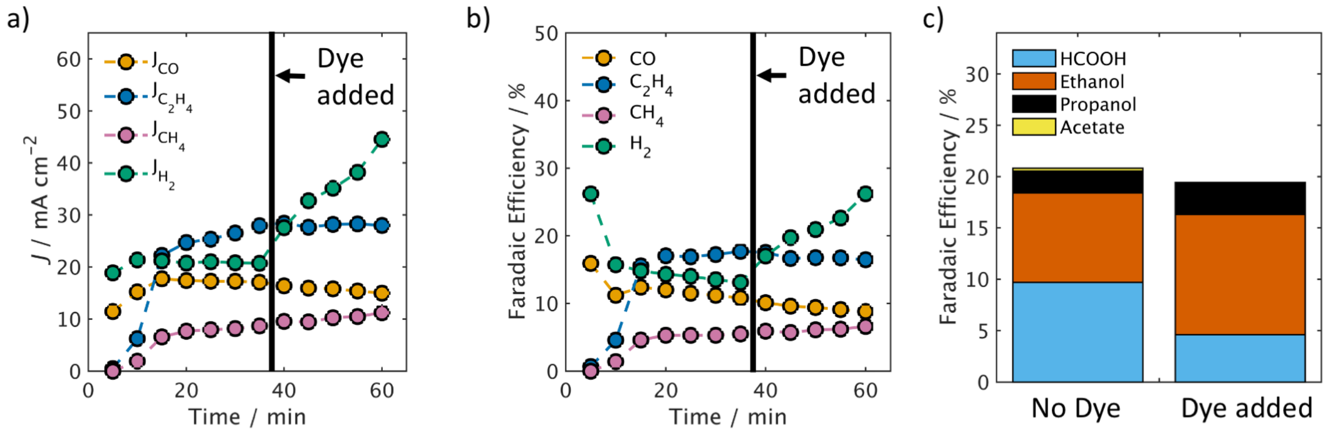

Figure 4.4: *Characterization of how the pH-sensitive DHPDS fluorescent dye affects the activity and selectivity of the copper GDE. (a) shows the current density (J) vs time before the dye is added (0 to 34 minutes) and after the dye is added to the electrolyte at 35 minutes. The partial current density for HER increases but the CO_2 reduction partial current densities remain*

stable. (b) shows the Faradaic efficiency for gas products vs time. The dye is added to the electrolyte at 35 minutes. The Faradaic efficiency for HER increases but the CO_2 reduction Faradaic efficiency remains stable. (c) shows the Faradaic efficiency for liquid products before and after the dye was added. The Faradaic efficiency for the CO_2 reduction reactions remain similar before and after the addition of the dye, albeit with slight increase in ethanol (orange) and decrease in formic acid (blue).

A CO_2-saturated solution of 100 mM $KHCO_3$ with a bulk pH of 6.8 was used as the electrolyte in our experiments, ensuring that the bulk pH will be at the lower sensitivity limit of the DHPDS. The DHPDS dye is electrochemically stable under CO_2 reduction reaction conditions (Figure 4.3c and Figure 4.4). In Figure 4.3c, the current-voltage characteristics of the electrode are nearly identical with or without the ratiometric dye. Upon addition of the dye, HER activity slightly increased but left the CO_2 reduction reaction activity remains largely unchanged (Figure 4.4). Based on these control experiments, the DHPDS dye is relatively inert with regards to GDE operating conditions.

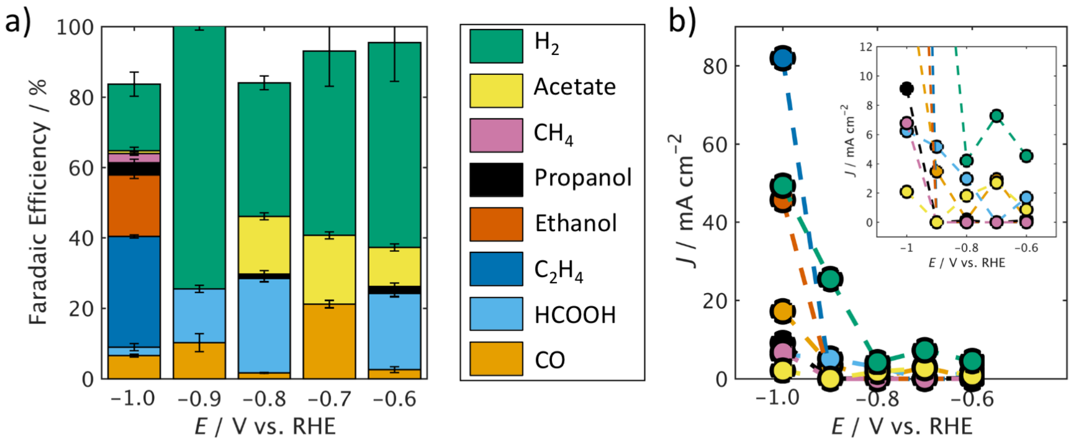

Figure 4.5: *Electrocatalytic characterization of a GDE composed of carbon paper coated with 300 nm of Cu on top of the microporous layer. (a) Faradaic Efficiency and (b) partial current density, J, for each product as a function of electrode potential, E. The figure legend applies to both panels (a) and (b).*

We first characterized the electrochemical performance of our Cu-based GDE prior to imaging the local solution pH. An AMOD dual electron beam deposition system (System 02520, Angstrom Engineering) was used to fabricate all samples. 300 nm of Cu was deposited onto the microporous layer of the gas diffusion electrode (GDE) at a rate of 2 A°/s. The substrate holder was rotating for all depositions. Over the course of the deposition the partial pressure of the chamber would rise from ~10-7 torr to ~10-6 torr and the temperature would rise from 20 °C to 30 °C for a 300 nm thick sample. For samples that were used for confocal fluorescent microscopy, an aluminum foil shadow mask with 3 mm diameter holes was used. For electrodes used for product detection, no shadow mask was used. After deposition, the samples were first spray coated with a solution of carbon black and Nafion. The solution is one-part DI water and one-part isopropyl alcohol with 2.5 mg of carbon black per ml of solution and 50 ml of 5 weight % Nafion per ml of solution. For both coatings the solution was sprayed from a distance of 3 inches for 1 second per square inch of electrode. After the samples were coated, they were dried under vacuum overnight.

Chronoamperometry experiments were performed across a range of applied potentials and the products were measured via gas chromatography and high-performance liquid chromatography (Figure 4.5). All applied potentials (E) are reported vs. the Reversible Hydrogen Electrode (E vs. RHE). As shown in Figure 4.5a, at potentials more positive than –1.0 V vs. RHE, the Cu GDE produced primarily H_2 with some C_1 and C_2 products. Consistent with prior observations from Cu GDEs, H_2 is the dominant product at low overpotentials, while higher overpotentials favor CO_2 reduction.[4,46] Cu requires higher overpotentials to perform the C-C coupling reactions necessary to synthesize C_2 products.[21] At –1.0 V vs. RHE, we begin to observe many CO_2 reduction products, with the largest fraction consisting of C_2 products, ethylene and ethanol. Higher overpotentials were not evaluated because the limited pH sensitivity range of the DHPDS dye is not suited for higher current densities. We therefore restricted our electrocatalytic characterization to those conditions that could be directly examined with confocal microscopy.

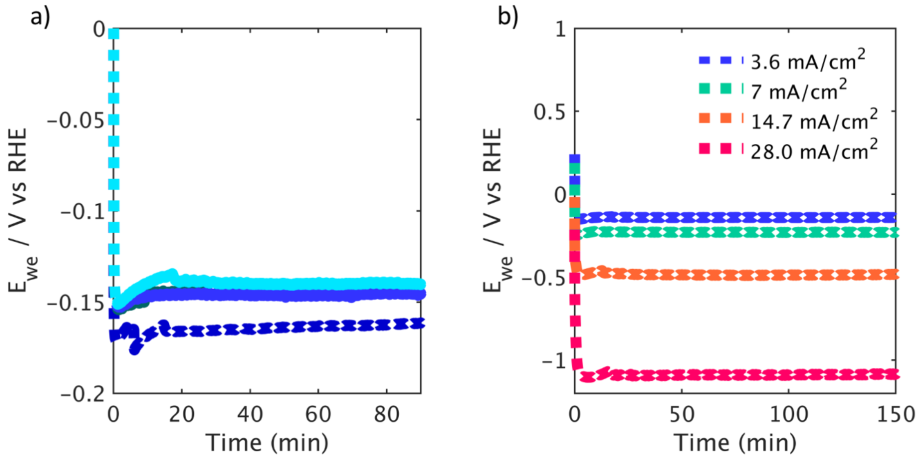

Figure 4.6: *Stability of the Cu GDE working electrode potential (E_{we}) over time. (a) shows four different electrochemical tests where the current density is set to -3.4 mA/cm^2. From this we can see that there are only very small changes in potential of the working electrode between tests. (b) shows electrochemical tests with varying current density. We note that the potential of the working electrode is very stable after the first 5 minutes indicating that electrode is stable throughout the run.*

For the confocal microscopy experiments, an electrochemical compression cell similar to the one used for the electrocatalytic characterization (Figure 4.1a and Figure 4.2) was employed. We note that the cell membrane was removed to accommodate the short focal length (1.7 mm) of the objective so that it could be positioned close to the cathode. Additionally, the cell was rotated 90° to accommodate the geometry of the confocal microscope. The choice and design of the electrochemical cell is further discussed in the Supplementary Information. The DHPDS dye (100 μM) was dissolved in the electrolyte and the electrolyte was replaced between every experiment to ensure that the initial conditions were standardized to keep the flux of hydroxide ions constant between experiments. The electrode was stable between experiments with minimal changes in the potential of the working electrode after 5 minutes (Figure 4.6). For each current density that was tested, a series of images were taken 3 μm apart in the z-direction (perpendicular to the electrode surface). Figure 4.7 shows two-dimensional (x,y) maps of solution pH obtained from a single location on the cathode surface at varying distances from the electrode surface (within a column) and at different current densities (along a row). The color scale in each map from blue to yellow denotes the local solution pH from pH = 7 to 10.

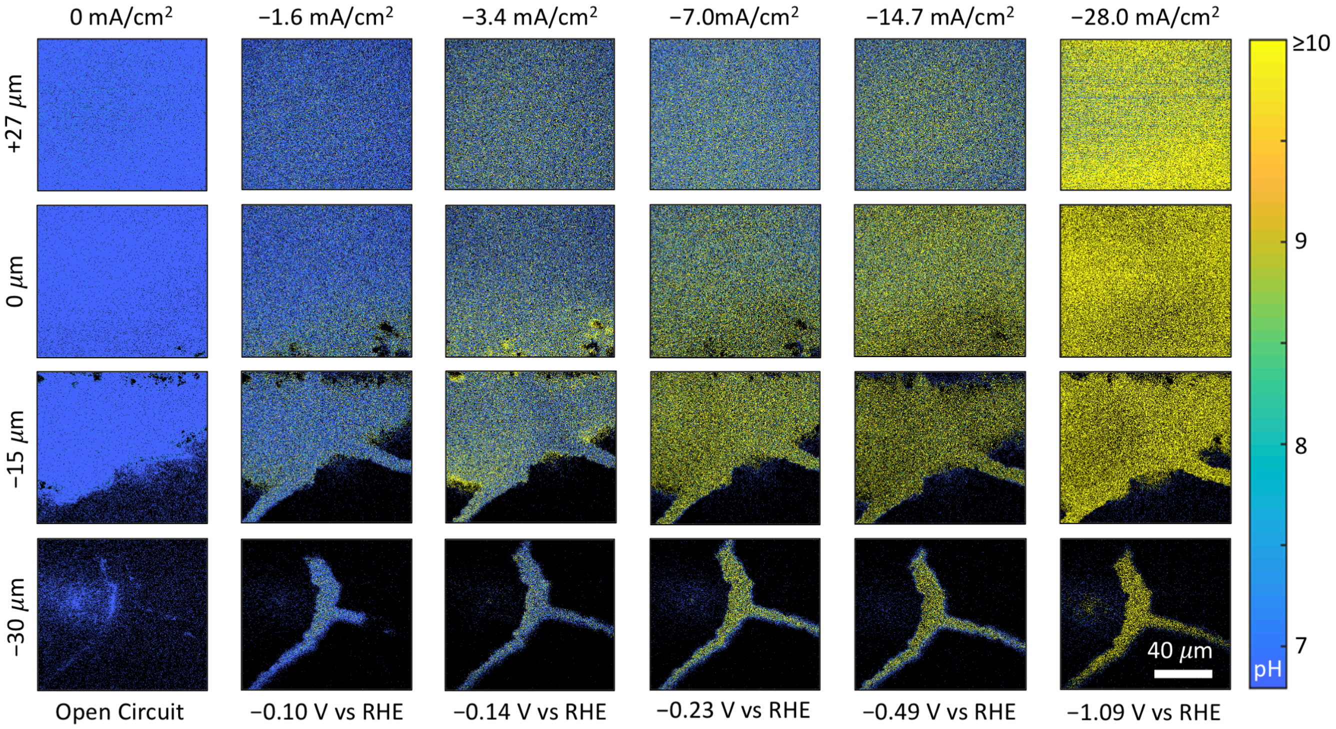

Figure 4.7: *Operando mapping of solution pH in three dimensions over a Cu GDE. Maps are obtained at the same location on the electrode at different heights above the electrode surface and at different current densities. From top to bottom, each row of maps corresponds to 27 μm above, 0 μm (at the surface), 15 μm below, and 30 μm below the electrocatalyst surface. From left to right, each column of maps were obtained at 0 mA/cm² (no reaction under open circuit conditions), –1.6 mA/cm², –3.4 mA/cm², –14.7 mA/cm², and –28.0 mA/cm². The pH color scale and the scale bar in the bottom right-hand corner apply to all images.*

4.3 Results and discussion

In the first column of Figure 4.7, at 0 mA/cm^2, the solution pH is uniform throughout the z-direction. The second row of pH maps at 0 μm defines the surface of the electrode; as the electrode is not flat, the highest point of the electrode in the image area was chosen as the 0 μm height. Black regions in the pH map indicate areas where no fluorescence was observed and therefore no electrolyte was present. The bottom row of pH maps in Fig. 4.7 shows the solution pH within a trench in the microporous layer. As the current density increases from left to right along a row, the local solution pH increases both within the trench of the microporous layer and above the electrode surface. It is particularly interesting to note that the pH is not completely uniform over the electrode surface, which can be most easily seen in the 0 μm and –15 μm height maps at a current density of –3.4 mA/cm^2. We are only able to observe this inhomogeneity at low current density where the pH gradient built up is not large. As the current density is further increased and all catalyst particles become electrochemically active we are no longer able to disentangle the pH gradient creation from individual locations along the catalyst. This effect was repeatedly observed at multiple locations across the electrode surface, as shown in Figure 4.8. We observe much smaller local variations at –1.6 mA/cm^2 because the applied bias is smaller.

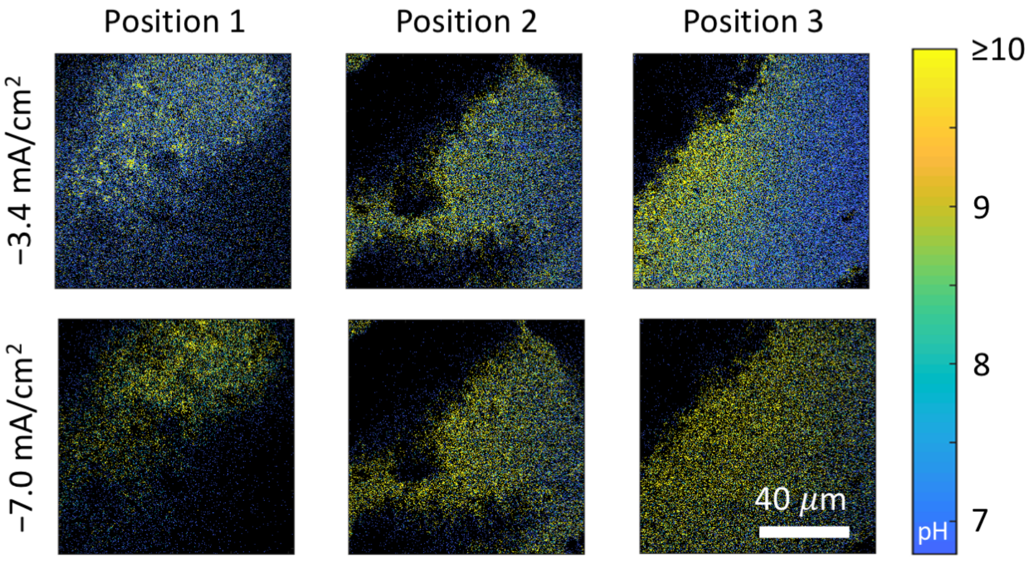

Figure 4.8: *pH maps at three different locations along the electrode surface. Position 1 is off to the side of the electrolyte inlet, position 2 is near the electrolyte inlet, and position 3 is near the electrolyte outlet. The first row shows pH maps all taken at –3.4 mA/cm^2 and the second row shows pH maps all taken at –7.0 mA/cm^2. We observe the hot spots for all 3 positions at -3.4 mA/cm^2 and we do not observe the hot spots at –7.0 mA/cm^2.*

We can use pH as a proxy for the total current density, as each electron catalyzing either the HER or the CO_2 reduction reaction corresponds to the creation of one hydroxide ion in the electrolyte. Hence, higher pH regions are indictive of higher activity. As the current density was further increased, the fluorescent signal from the dye eventually saturates. To confirm that only electrochemically-active areas of the electrode were responsible for locally increasing the solution pH, a map was obtained 9 μm above the electrode surface over a region that was only partially covered with Cu (Figure 4.9). The electrolyte flowed left to right across the electrode and the current density was set at –14.7 mA/cm^2. As shown in Figure 4.9a, the left side of map has a pH ~7, which was obtained above a region of the catalyst without Cu, while the right side of the map has a pH ~ 9, which was taken from above a region coated in Cu. It is clear from this map that regions of locally-high pH only occur near regions of the electrode where hydroxide ions are being created via electrocatalysis. In addition, we measured the pH under the same conditions as the back edge of the electrolyte (Figure 4.9b).

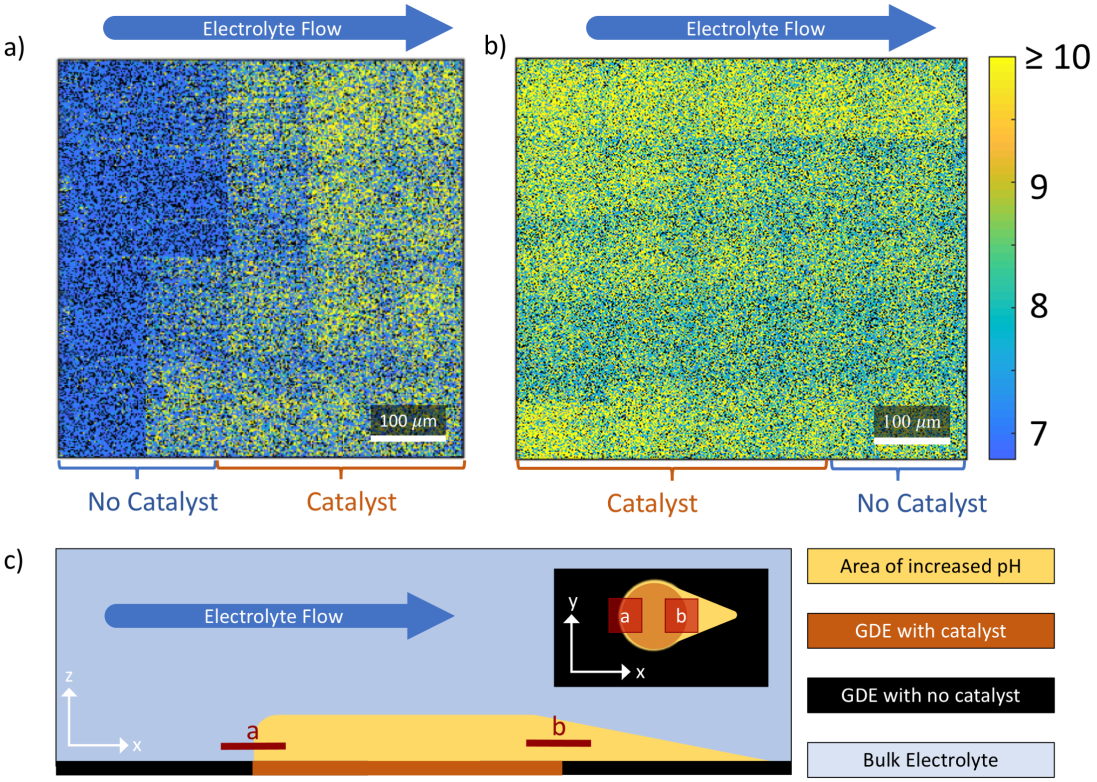

Figure 4.9: *Influence of electrolyte flow on the spatial resolution of pH maps. (a) and (b) are pH maps stitched together, taken at 9 μm above the surface of the electrode and at a current density of –14.7 mA/cm^2. In (a) the left half of the image has no Cu while the right half has Cu catalyst. The electrolyte is flowing from left to right across the surface of the electrode. In (a) the left half of the image is coated with Cu while the right half has no Cu catalyst. The electrolyte is flowing from left to right across the surface. (c) shows a schematic that is not to scale of what the pH gradient looks like in both x-y and x-z planes. The area within the*

orange circle in the x-y plane indicates where the Cu catalyst is located on the GDE. The position where image (a) was taken is indicated in panel (c) by the red square and the red line labeled 'a'. The position where image (b) was taken is indicated in panel (c) by the red square and the red line labeled 'b'.

When the average pH at the surface of the electrode is below pH 9.5 ($J < –14.7$ mA/cm^2, or applied potentials less negative than –0.7 V vs. RHE) the electrode mostly produces C$_1$ products and H$_2$. In contrast, many C$_2$ products were observed when the solution pH at the surface of the electrode was above pH 10 ($J > –28.0$ mA/cm^2, or at –1.0 V vs RHE). Potentials greater than –0.9 V vs RHE are required to produce these higher current densities and C$_2$ products, but the local pH also plays a role in suppressing the HER and promoting CO$_2$ reduction.[17,39] The activity of CO$_2$ reduction is independent, whereas the HER activity is greatly dependent on the hydroxide ion concentration.[17] For CO reduction on Cu, locally high pH conditions reduce the free energy required for important steps along the reaction pathway to yield C$_2$ products such as ethanol.[16] Areas of locally high pH may also reduce the free energy for CO$_2$ reduction pathways. Thus, our results indicate that a highly-alkaline local pH increases the selectivity towards C$_2$ products while decreasing the selectivity towards the HER.

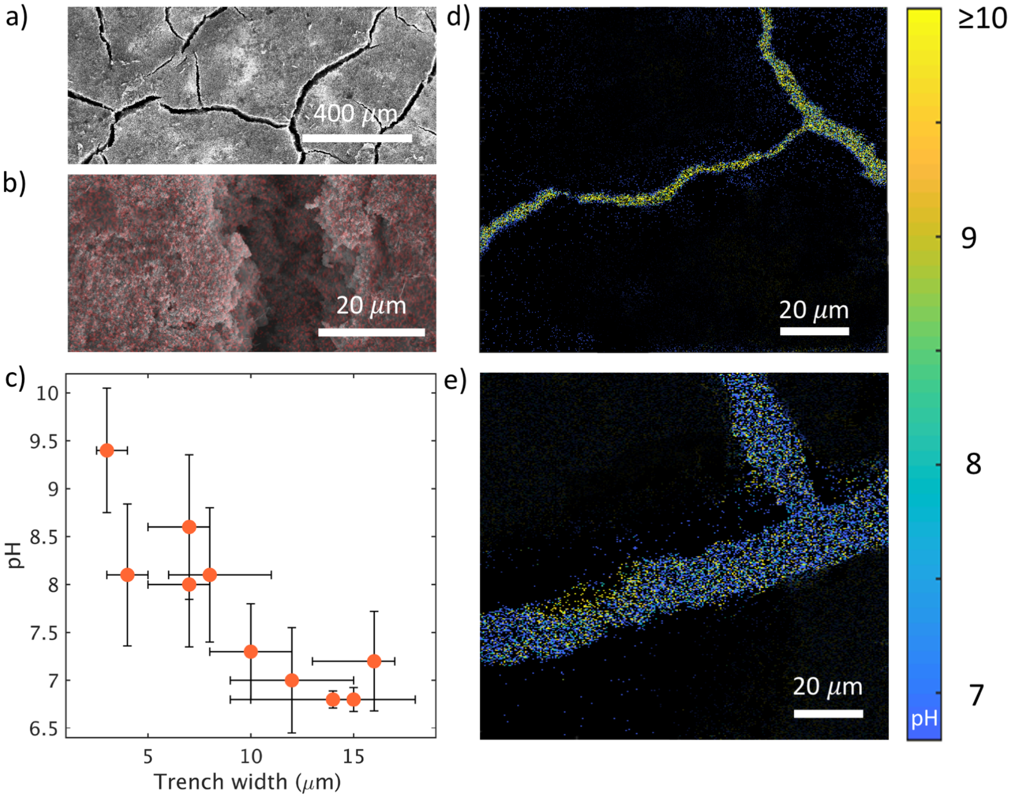

Figure 4.10: *Influence of physical confinement on CO_2 reduction performance. (a) Low-magnification SEM image of a Cu gas diffusion electrode; (b) High-magnification SEM image of a Cu gas diffusion electrode with an overlay of the Cu signal obtained from an EDS map, red shading indicates Cu covered regions. (c) Measured pH as a function of trench width. The orange data points denote the average trench width. The error bars in the abscissa axis indicate the variation in trench width with the smallest and largest end points denoting the thinnest and the widest point along the trench. The error bars in the ordinate axis represent the standard deviation of pH values within the trench. (d) and (e) pH maps obtained from two representative trenches with different widths located at different regions on the electrode at a distance of 8 μm below the electrode surface while operating at a current density of –3.4 mA/cm^2.*

Finally, we explore the local pH within trenches in the microporous layer, as shown in Figure 4.10. The trenches are randomly distributed throughout the electrode and have an average of width of 18.8 μm ± 8 μm (Figure 4.10a). Figure 4.10b shows a higher-magnification SEM image of a crack, with an overlay of an energy dispersive spectroscopy (EDS) map indicating regions that contain Cu (red shading). Figures 4.11 and 4.12 show more EDS maps of Cu, F, and C from different trenches. From this data we found that Cu is not only coated on top of the microporous layer, but also at the bottom and on the sides of the trenches, suggesting that CO_2 reduction can be performed within these confined regions of the electrode. These trenches within the microporous layer offer an interesting opportunity for studying the influence of physical confinement on the CO_2 reduction process in a GDE device. Accordingly, we employed our pH mapping techniques to these regions of the electrode to see how the reduced dimensions of the device influence the local solution pH near the active Cu electrocatalyst. At a current density of –3.4 mA/cm^2, we found that the solution pH within a narrow trench (~3.2 μm wide) was pH 9.5. We emphasize that this local pH was much higher than the pH of 7.3 within a comparatively wider trench (~16.2 μm wide). Interestingly, even at this relatively low current density (–3.4 mA/cm^2), the more confined electrochemically-active region produces a higher local pH than more open regions, which serves to suppress HER without substantially impeding CO_2 reduction.[47,48] We also note that the pH within a narrow trench is higher than the surrounding surface of the electrode (Figure 4.13). We proceeded to map to elucidate the trend of local pH vs. trench width, as shown in Figure 4.10c. While we find that the electrolyte flow is very small between the objective and the catalyst in our COMSOL flow model (Figure 4.14), we only measured the pH within trenches that were perpendicular to the electrolyte flow to ensure that the flow dynamics are as comparable as possible. We observed that as the trench width decreased, the local solution pH within the trench increased. This observation is consistent with prior electrochemical studies,[17,47] and has important implications for the design of more active GDEs capable of performing selective CO_2 reduction at lower overpotentials with improved energy efficiency.

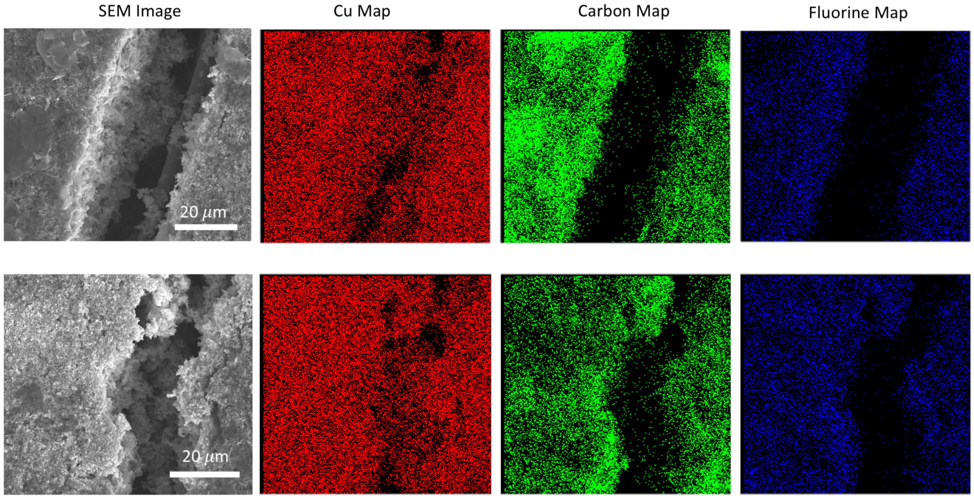

Figure 4.11: *SEM and EDS maps of two locations on a GDE with 300 nm Cu. The SEM images at the left show the location for all EDS maps in the corresponding row. From the EDS maps we can see that at the bottom of the cracks, there is Cu while less carbon and PTFE (Fluorine signal) is present.*

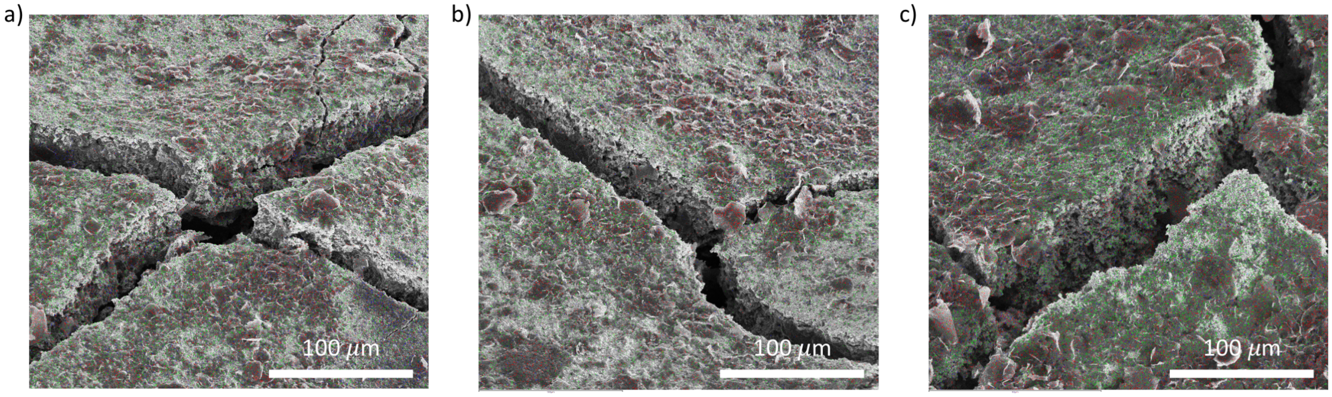

Figure 4.12: *SEM and EDS maps of three locations on a GDE with 300 nm Cu. Red shading denotes carbon, green shading denotes Cu, and blue indicates fluorine. From the EDS maps we can see that there is Cu deposited on the side walls of the trenches.*

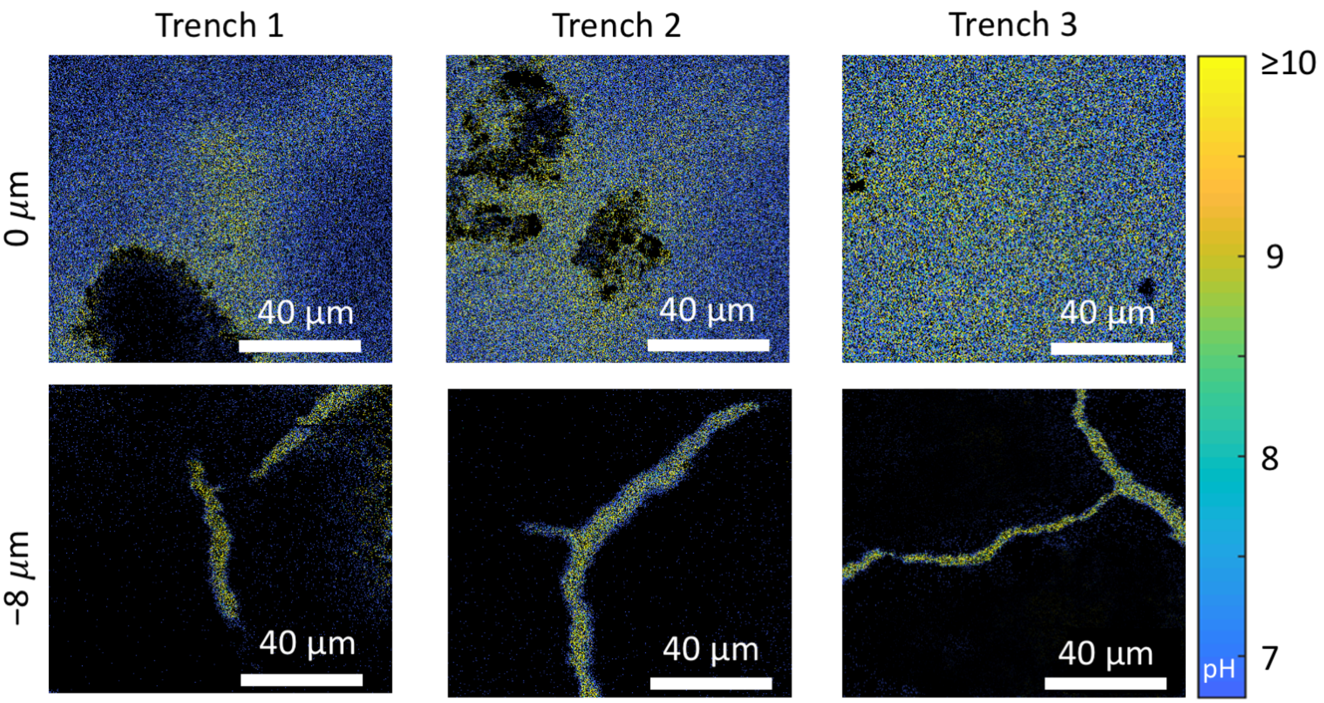

Figure 4.13*: pH maps at three different locations along the electrode surface. All measurements were taken at –3.4 mA/cm^2. The image in the first row is taken at the surface of the electrode and the second row is at 8 µm below the surface (0 µm). We observe that for all cases the pH within the narrow trench is higher than it is at the surface of the GDE.*

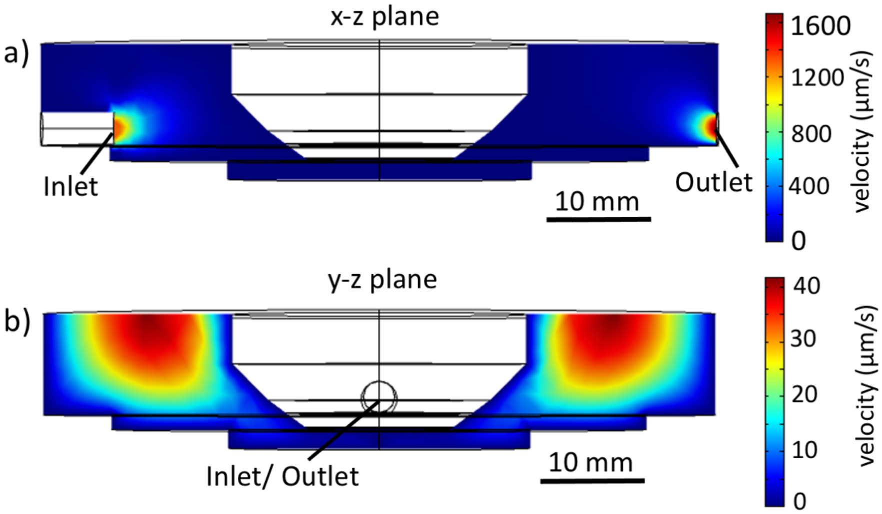

Figure 4.14*: shows a COMSOL simulation of the velocity of the electrolyte in the electrochemical cell with the objective submerged in the electrolyte. (a) shows the velocity in the x-z plane with the inlet on the left and outlet on the right. (b) shows the velocity in the y-z plane with the electrolyte flowing into the page. From these simulations it is clear that the velocity underneath the objective is small.*

We additionally confirm the experimentally-measured pH within the trenches for various widths and current densities by simulating the solution pH using the charge transfer and bulk reactions in a two-dimensional COMSOL model (Figure 4.15).[49] Simulations were performed with a stationary COMSOL Multiphysics 5.5 model with a combination of the Laminar Flow Module and the Transport of Diluted Species Module. To estimate the appropriate flow velocity close to the electrode surface, a three-dimensional COMSOL model with the Laminar Flow Module simulating the electrolyte flow in the electrochemical cell and around the immersion objective used for experiments was set up, see Fig. 4.14. The velocity at the inlet of the cell was experimentally determined to be 1.3 mm/s. As expected, the flow velocity underneath the objective is found to be much lower than around it. The average flow velocity 30 μm above the electrode surface was determined to be 0.14 μm/s. This value was used as an input for the two-dimensional model of pH around a trench.

The geometry of the two-dimensional model of the pH is depicted in Fig 4.15d. At the inlet (left), we assume a flow velocity of 0.14 μm/s, at the outlet (right) a zero-pressure condition is applied. On the electrode surface as well as on the trench walls and at the bottom of the trench we apply no-slip boundary conditions. Both convection and diffusion are taken into consideration for the transport properties. The inputs here are the velocity field calculated with the laminar flow module and the diffusion coefficients of all species (see Table 4.1). We assume a boundary layer thickness of 60 μm where we apply concentration boundary conditions as expected for a CO_2-saturated 100 mM $KHCO_3$ electrolyte in equilibrium (see Table 4.1). The same concentrations are used as inflow concentrations at the inlet.

On the surface of the electrode as well as at the bottom and the side wall of the trench we assume a CO2 flux of $1\ \frac{\mu mol}{cm^2 \cdot s}$. This value was determined experimentally by measuring the difference in the CO_2 flow rate with a flow meter before and after passing the GDE in the electrochemical cell. Note that this method only provides an estimate as the CO_2 flux though the GDE is not homogeneous. Also on the electrode surface, the trench bottom and walls we assume that there is catalytic activity. The charge-transfer reactions considered on these walls are

$$CO_2\,(aq) + H_2O + 2e^- \rightarrow CO + 2OH^-$$
$$2H^+ + 2e^- \rightarrow H_2$$
$$2H_2O + 2e^- \rightarrow H_2 + 2OH^-$$

The source terms are determined with

$$R_n = -\sum \frac{s_j \cdot J \cdot FE_n}{n_j \cdot F}$$

with s_j the stoichiometric coefficient of equation j, J the current density, FE_n the Faradaic efficiency of species n determined experimentally (see Fig 4.5, the Faradaic efficiency for CO is assumed to be the sum of the Faradaic Efficiency of all carbon products), n_j the number of transferred electrons, and F Faraday's constant.

Furthermore, bulk carbonate reactions are assumed to take place in the whole electrolyte body:

$$CO_2(aq)+H_2O \rightarrow H^++HCO_3^-$$
$$HCO_3^- \rightarrow H^++CO_3^{2-}$$
$$CO_2(aq)+OH^- \rightarrow HCO_3^-$$
$$HCO_3^-+OH^- \rightarrow H_2O+CO_3^{2-}$$
$$H_2O \rightarrow H^++OH^-$$

The source terms are calculated with

$$R_n = \sum_j s_j \cdot (k_j \prod_{s_j<0} c_n - k_{-j} \prod_{s_j>0} c_n)$$

where s_j is the stoichiometric coefficient of reaction j, k_j the forward rate constant, k_{-j} the reverse reaction rate constant, and $k_{-j} = \frac{k_j}{K_j}$ with the equilibrium constant K_j (see Table 4.1). c_n is the concentration of species n.

***Table 4.1**: Model parameters*

Diffusion Coefficients (Weng et al, Phys. Chem. Chem. Phys., 2018, 20, 16973-16984)	
Species	**Value**
K^+	$1.957 \cdot 10^{-5} \frac{cm^2}{s}$
H^+	$9.311 \cdot 10^{-5} \frac{cm^2}{s}$
OH^-	$5.293 \cdot 10^{-5} \frac{cm^2}{s}$
CO_2	$1.91 \cdot 10^{-5} \frac{cm^2}{s}$
HCO_3^-	$1.185 \cdot 10^{-5} \frac{cm^2}{s}$
CO_3^{2-}	$0.91 \cdot 10^{-5} \frac{cm^2}{s}$
Equilibrium Concentrations	
Species	**Value**
K^+	$100 \frac{mol}{m^3}$
H^+	$1.58 \cdot 10^{-4} \frac{mol}{m^3}$
OH^-	$6.31 \cdot 10^{-5} \frac{mol}{m^3}$
CO_2	$37.13 \frac{mol}{m^3}$

HCO_3^-	$99.94 \frac{mol}{m^3}$
CO_3^{2-}	$3.02 \cdot 10^{-2} \frac{mol}{m^3}$
Forward Rate Constants (Schulz et al, Mar. Chem., 2006,100,53-65)	
k_1	$3.71 \cdot 10^{-2} \frac{1}{s}$
k_2	$59.44 \frac{1}{s}$
k_3	$2.23 \cdot 10^{3} \frac{L}{mol \cdot s}$
k_4	$6 \cdot 10^{9} \frac{L}{mol \cdot s}$
k_w	$1.4 \cdot 10^{-3} \frac{mol}{L \cdot s}$
Equilibrium Constants (Schulz et al, Mar. Chem., 2006,100,53-65)	
K_1	$10^{-6.37} \frac{mol}{L}$
K_2	$10^{-10.32} \frac{mol}{L}$
K_3	$\frac{K_1}{K_w}$
K_4	$\frac{K_2}{K_w}$
K_w	$10^{-14} \frac{mol^2}{L^2}$

For the model (Figure 4.15a), we assumed a constant flux of CO_2 of 1 μmol cm^{-2} s^{-1} through the planar electrode surface, the trench walls and trench bottom (see SI for details). We used the experimental current density of –3.4 mA/cm^2 at the same boundaries because SEM and EDS images of our samples show that copper coats the surface, trench side walls and trench bottom (see Figures 4.11 and 4.12). We assume a boundary layer thickness of 60 μm where a concentration boundary condition matching the concentration of CO_2-saturated 100 mM $KHCO_3$ electrolyte was applied. The electrolyte flow from left to right was also taken into consideration in the model. The appropriate flow velocity is determined with a three-dimensional COMSOL model of the flow in the electrochemical cell (Figure 4.14).

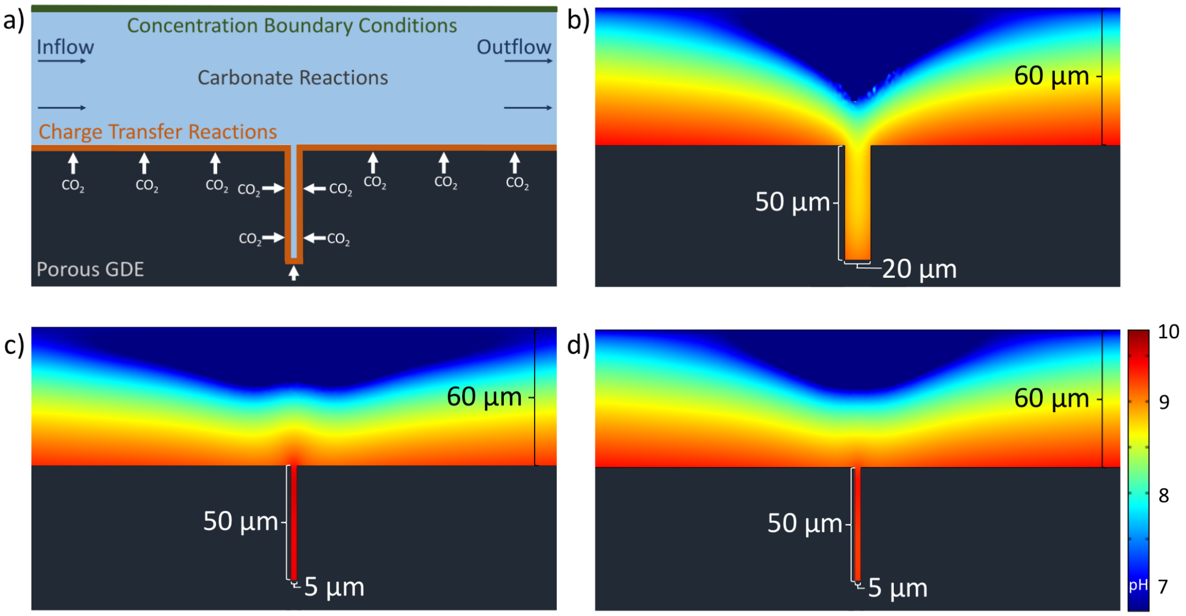

Figure 4.15: *Simulations of local pH within and around trenches of various dimensions in the GDE. (a) Schematic of the model used for simulations indicating regions of CO_2 flux (white), current density (orange), concentration boundary conditions (green), and electrolyte flow (blue). pH map in the x-z plane at a uniform current density of –3.4 mA/cm^2 for a trench with a depth of 50 μm deep and a width of (b) 20μm and (d) 5 μm. (c) pH map in the x-z plane for a trench [50 deep x 5μm wide] with an average current density of –3.4 mA/cm^2 where the current density in the trench is twice as high as the current density on the surface. The CO_2 flux is constant through all surfaces and boundary conditions are kept the same for all simulations. The pH scale bar applies to all pH profiles (b)-(d).*

As we expected, the pH was increased close to the electrode surface and inside the trench due to charge transfer reactions locally creating hydroxide ions. The pH decreased further away from the electrode surface due to convection and diffusion within the bulk electrolyte. There was a dip in the pH profile above the trench because more CO_2 comes through the electrode at this point and acidifies the electrolyte close to the trench. Additionally, there is increased CO_2 flux here because CO_2 is able to diffuse not only through the bottom of the trench but also through the sidewalls. This feature was also observed experimentally, as shown in the pH map in Figure 4.7 for –3.4 mA/cm^2 at –15 μm. We note that the pH gradient is nearly symmetric above the crack because the electrolyte velocity is low. At higher current densities we observed that pH increases in the trench and on the surface of the electrode as expected (Figure 4.16).

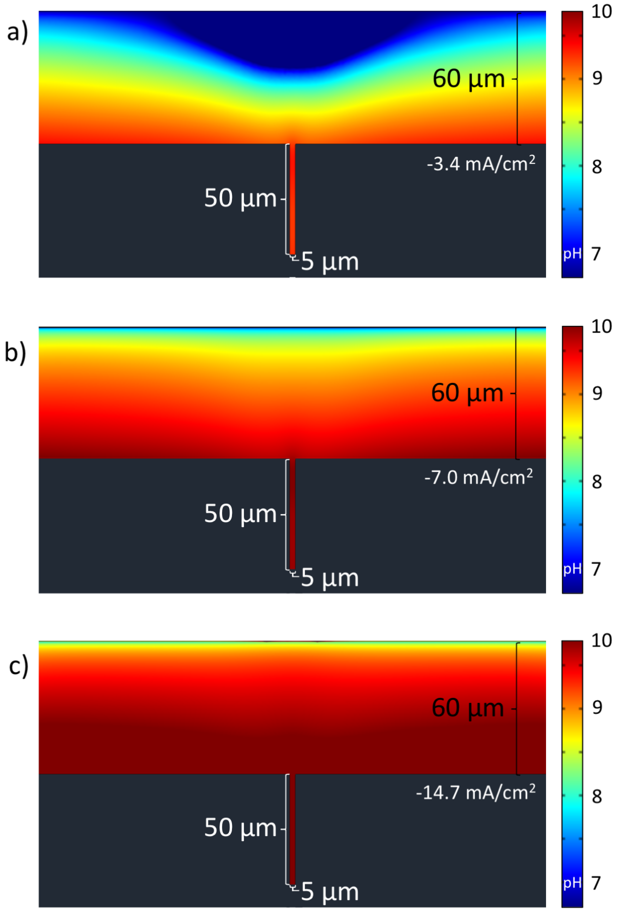

Figure 4.16: *shows COMSOL simulations of the pH profile in a trench that is 5μm wide and 50 μm deep at different current densities. The current density is constant over all surfaces. (a) shows the pH profile at –3.4* mA/cm^2*, (b) shows the pH profile at –7.0* mA/cm^2*, and (c) shows the pH profile at –14.7* mA/cm^2*. From these simulations we observe that the pH near the catalyst layer increases as the current density increases.*

Comparing Figure 4.17b and Figure 4.17d it is clear that the pH is considerably lower in the wider trenches than the narrower trenches which is in agreement with experimental results (Fig 4.10c). In Figure 4.17c, we simulated a trench with the same dimensions as the trench shown in Figure 4.17d. However, we modeled a non-uniform catalyst activity where the activity in the trench is twice as high as it is on the electrode surface, while maintaining the same average current density over the whole electrode. We observed that in this case, the pH within the trench is higher than the pH above the surface of the electrode which we did not observe in experiment (see Figure 4.13). This discrepancy leads to the conclusion that the experimentally observed higher pH in narrow trenches cannot only be explained by the confinement of the trench, but must also be due to increased catalytic activity within the trench.

4.4 Conclusion

We have employed confocal fluorescent microscopy to elucidate how the *operando* local pH changes with current density as a function of distance above and below the surface of a Cu-based GDE. It is clear from the experimentally obtained pH maps that there are non-uniform hotspots of locally high pH across the catalyst even at relatively low overpotentials. Through experimental results confirmed by simulations, we show that the catalyst within narrow trenches is more active than catalyst at the surface of the electrode. We also observed that the pH was higher in narrow trenches as opposed to wider trenches, and we confirmed this result with COMSOL simulations. Further work must be done to understand why catalyst in narrow trenches performs better than catalyst in wider trenches, and this will be the subject of ongoing studies. Nevertheless, the ability to locally image the solution pH in three dimensions (x, y, and z) with micron spatial resolution is an important tool for understanding and identifying which part of the catalyst is most productive under real operating conditions. Our results have therefore demonstrated that the overpotential required to perform selective CO_2 reduction can be reduced within narrow trenches. We anticipate that this knowledge will help inform the design and construction of more efficient CO_2 reduction devices.

BIBLIOGRAPHY CHAPTER 4

1. Hori, Yoshio Kikuchi, Katsuhei Suzuki, S. Production of CO and CH_4 in the Electrochemical Reduction of CO_2 at Metal Electrodes in Aqueous Hydrogencarbonate Solution. *Chem. Lett.* **1985**, 1695–1698.
2. Kortlever, R.; Shen, J.; Schouten, K. J. P.; Calle-Vallejo, F.; Koper, M. T. M. Catalysts and Reaction Pathways for the Electrochemical Reduction of Carbon Dioxide. *J. Phys. Chem. Lett.* **2015**, *6* (20), 4073–4082.
3. Bagger, A.; Ju, W.; Varela, A. S.; Strasser, P.; Rossmeisl, J. Electrochemical CO_2 Reduction: A Classification Problem. *ChemPhysChem* **2017**, *18* (22), 3266–3273.
4. Kuhl, K.; Jaramillo, T. F. New Insights into the Electrochemical Reduction of Carbon Dioxide on Metallic Copper Surfaces. **2012**, 7050–7059.
5. Cave, E. R.; Montoya, J. H.; Kuhl, K. P.; Abram, D. N.; Hatsukade, T.; Shi, C.; Hahn, C.; Nørskov, J. K.; Jaramillo, T. F. Electrochemical CO_2 Reduction on Au Surfaces: Mechanistic Aspects Regarding the Formation of Major and Minor Products. *Phys. Chem. Chem. Phys.* **2017**, *19* (24), 15856–15863.
6. Endrődi, B.; Bencsik, G.; Darvas, F.; Jones, R.; Rajeshwar, K.; Janáky, C. Continuous-Flow Electroreduction of Carbon Dioxide. *Prog. Energy Combust. Sci.* **2017**, *62*, 133–154.
7. Bohlen, B.; Wastl, D.; Radomski, J.; Sieber, V.; Vieira, L. Electrochemical CO_2 Reduction to Formate on Indium Catalysts Prepared by Electrodeposition in Deep Eutectic Solvents. *Electrochem. commun.* **2020**,

110 (October 2019), 106597.

8. Singh, M. R.; Kwon, Y.; Lum, Y.; Ager, J. W.; Bell, A. T. Hydrolysis of Electrolyte Cations Enhances the Electrochemical Reduction of CO_2 over Ag and Cu. *J. Am. Chem. Soc.* **2016**, *138* (39), 13006–13012.
9. Jeanty, P.; Scherer, C.; Magori, E.; Wiesner-Fleischer, K.; Hinrichsen, O.; Fleischer, M. Upscaling and Continuous Operation of Electrochemical CO_2 to CO Conversion in Aqueous Solutions on Silver Gas Diffusion Electrodes. *J. CO_2 Util.* **2018**, *24* (January), 454–462.
10. Weekes, D. M.; Salvatore, D. A.; Reyes, A.; Huang, A.; Berlinguette, C. P. Electrolytic CO_2 Reduction in a Flow Cell. **2018**.
11. Rabinowitz, J. A.; Kanan, M. W. The Future of Low-Temperature Carbon Dioxide Electrolysis Depends on Solving One Basic Problem. *Nat. Commun.* **2020**, *11* (1), 10–12.
12. Kim, B.; Hillman, F.; Ariyoshi, M.; Fujikawa, S.; Kenis, P. J. A. Effects of Composition of the Microporous Layer and the Substrate on Performance in the Electrochemical Reduction of CO_2 to CO. *J. Power Sources* **2016**, *312*, 192–198.
13. Davis, S. J.; Lewis, N. S.; Shaner, M.; Aggarwal, S.; Arent, D.; Azevedo, I. L.; Benson, S. M.; Bradley, T.; Brouwer, J.; Chiang, Y.; et al. Net-Zero Emissions Energy Systems. **2018**, *9793*.
14. Birdja, Y. Y.; Pérez-Gallent, E.; Figueiredo, M. C.; Göttle, A. J.; Calle-Vallejo, F.; Koper, M. T. M. Advances and Challenges in Understanding the Electrocatalytic Conversion of Carbon Dioxide to Fuels. *Nat. Energy* **2019**, *4* (9), 732–745.
15. Leenheer, A. J.; Atwater, H. A. Imaging Water-Splitting Electrocatalysts with PH-Sensing Confocal Fluorescence Microscopy. *J. Electrochem. Soc.* **2012**, *159* (9), H752–H757.
16. Liu, X.; Schlexer, P.; Xiao, J.; Ji, Y.; Wang, L.; Sandberg, R. B.; Tang, M.; Brown, K. S.; Peng, H.; Ringe, S.; et al. pH Effects on the Electrochemical Reduction of CO_2 towards C2 Products on Stepped Copper. *Nat. Commun.* **2019**, *10* (1).
17. Hall, A. S.; Yoon, Y.; Wuttig, A.; Surendranath, Y. Mesostructure-Induced Selectivity in CO_2 Reduction Catalysis. *J. Am. Chem. Soc.* **2015**, *137* (47), 14834–14837.
18. Zhang, Z.; Melo, L.; Jansonius, R. P.; Habibzadeh, F.; Grant, E. R.; Berlinguette, C. P. PH Matters When Reducing CO_2 in an Electrochemical Flow Cell. *ACS Energy Lett.* **2020**, *5* (10), 3101–3107.
19. Higgins, Drew Hahn, Christopher Chengxiang, Xiang Jaramillo, Thomas F. Weber, A. Z. Gas-Diffusion Electrodes for Carbon Dioxide Reduction: A New Paradigm. *ACS Energy Lett.* **2019**, *4*, 317–324.
20. Inaba, M.; Jensen, A. W.; Sievers, G. W.; Escudero-Escribano, M.; Zana, A.; Arenz, M. Benchmarking High Surface Area Electrocatalysts in a Gas Diffusion Electrode: Measurement of Oxygen Reduction Activities under Realistic Conditions. *Energy Environ. Sci.* **2018**, *11* (4), 988–994.
21. Nitopi, S.; Bertheussen, E.; Scott, S. B.; Liu, X.; Engstfeld, A. K.; Horch, S.; Seger, B.; Stephens, I. E. L.; Chan, K.; Hahn, C.; et al. Progress and Perspectives of Electrochemical CO_2 Reduction on Copper in Aqueous Electrolyte. *Chem. Rev.* **2019**, *119* (12), 7610–7672.
22. Singh, M. R.; Clark, E. L.; Bell, A. T. Effects of Electrolyte, Catalyst, and Membrane Composition and Operating Conditions on the Performance of Solar-Driven Electrochemical Reduction of Carbon Dioxide. *Phys. Chem. Chem. Phys.* **2015**, *17*, 18924–18936.
23. Weng, L.-C.; Bell, A. T.; Weber, A. Z. Modeling Gas-Diffusion Electrodes for CO_2 Reduction. *Phys. Chem. Chem. Phys.* **2018**, No. 20, 16973–16984.
24. García de Arquer, F. P.; Dinh, C. T.; Ozden, A.; Wicks, J.; McCallum, C.; Kirmani, A. R.; Nam, D. H.; Gabardo, C.; Seifitokaldani, A.; Wang, X.; et al. CO_2 Electrolysis to Multicarbon Products at Activities Greater than 1 A Cm−2. *Science (80-.).* **2020**, *367* (6478), 661–666.
25. Dinh, C.; Burdyny, T.; Kibria, G.; Seifitokaldani, A.; Gabardo, C. M.; Arquer, F. P. G. De; Kiani, A.; Edwards, J. P.; Luna, P. De; Bushuyev, O. S.; et al. CO_2 Electroreduction to Ethylene via Hydroxide-Mediated Copper Catalysis at an Abrupt Interface. *Science (80-.).* **2018**, *360*, 783–787.
26. Wang, L.; Nitopi, S. A.; Bertheussen, E.; Orazov, M.; Morales-Guio, C. G.; Liu, X.; Higgins, D. C.; Chan, K.; Nørskov, J. K.; Hahn, C.; Jaramillo, T. F. Electrochemical Carbon Monoxide Reduction on

Polycrystalline Copper: Effects of Potential, Pressure, and PH on Selectivity toward Multicarbon and Oxygenated Products. *ACS Catal.* **2018**, *8* (8), 7445–7454.

27. Nesbitt, N.; Smith, W. Water Activity Regulates CO_2 Reduction in Gas-Diffusion Electrodes. *ChemRxiv* **2021**, No. January.
28. Suter, S.; Haussener, S. Optimizing Mesostructured Silver Catalysts for Selective Carbon Dioxide Conversion into Fuels. *Energy Environ. Sci.* **2019**, *12* (5), 1668–1678.
29. Monteiro, M. C. O.; Koper, M. T. M. Measuring Local PH in Electrochemistry. *Curr. Opin. Electrochem.* **2021**, *25*, 100649.
30. Rudd, N. C.; Cannan, S.; Bitziou, E.; Ciani, I.; Whitworth, A.; Unwin, P. R. Fluorescence Confocal Laser Scanning Microscopy as a Probe of PH Gradients in Electrode Reactions and Surface Activity Nicola. *Anal. Chem.* **2005**, *77*, 6205–6217.
31. Bouffier, L.; Doneux, T. Coupling Electrochemistry with in Situ Fluorescence (Confocal) Microscopy. *Curr. Opin. Electrochem.* **2017**, *6* (1), 31–37.
32. Pande, N.; Chandrasekar, S. K.; Lohse, D.; Mul, G.; Wood, J. A.; Mei, B. T.; Krug, D. Electrochemically Induced PH Change: Time-Resolved Confocal Fluorescence Microscopy Measurements and Comparison with Numerical Model. *J. Phys. Chem. Lett.* **2020**, *11* (17), 7042–7048.
33. Vitt, J. E.; Engstrom, R. C. Imaging of Oxygen Evolution and Oxide Formation Using Quinine Fluorescence. *Anal. Chem.* **1997**, *69* (6), 1070–1076.
34. Bowyer, W. J.; Xie, J.; Engstrom, R. C. Fluorescence Imaging of the Heterogeneous Reduction of Oxygen. *Anal. Chem.* **1996**, *68* (13), 2005–2009.
35. Nesbitt, N.; Smith, W. A. Operando Topography and Mechanical Property Mappinig of CO_2 Reduction Gas-Diffusion Electrodes Operating at High Currrent Densities. *J. Electrochem. Soc.* **2021**.
36. Botz, A.; Clausmeyer, J.; Öhl, D.; Tarnev, T.; Franzen, D.; Turek, T.; Schuhmann, W. Local Activities of Hydroxide and Water Determine the Operation of Silver-Based Oxygen Depolarized Cathodes. *Angew. Chemie - Int. Ed.* **2018**, *57* (38), 12285–12289.
37. Dieckhöfer, S.; Öhl, D.; Junqueira, J. R. C.; Quast, T.; Turek, T.; Schuhmann, W. Probing the Local Reaction Environment During High Turnover Carbon Dioxide Reduction with Ag-Based Gas Diffusion Electrodes. *Chem. - A Eur. J.* **2021**, *27* (19), 5906–5912.
38. Lu, X.; Zhu, C.; Wu, Z.; Xuan, J.; Francisco, J. S.; Wang, H. In Situ Observation of the PH Gradient near the Gas Diffusion Electrode of CO_2 Reduction in Alkaline Electrolyte. *J. Am. Chem. Soc.* **2020**, *142* (36), 15438–15444.
39. Yang, K.; Kas, R.; Smith, W. A. In Situ Infrared Spectroscopy Reveals Persistent Alkalinity near Electrode Surfaces during CO_2 Electroreduction. *J. Am. Chem. Soc.* **2019**, *141* (40).
40. Nitopi, S.; Bertheussen, E.; Scott, S. B.; Liu, X.; Engstfeld, A. K.; Horch, S.; Seger, B.; Stephens, I. E. L.; Chan, K.; Hahn, C.; et al. Progress and Perspectives of Electrochemical CO_2 Reduction on Copper in Aqueous Electrolyte. **2019**.
41. Wang, Y.; Shen, H.; Livi, K. J. T.; Raciti, D.; Zong, H.; Gregg, J.; Onadeko, M.; Wan, Y.; Watson, A.; Wang, C. Copper Nanocubes for CO_2 Reduction in Gas Diffusion Electrodes. *Nano Lett.* **2019**.
42. Nguyen, T. N.; Dinh, C. T. Gas Diffusion Electrode Design for Electrochemical Carbon Dioxide Reduction. *Chem. Soc. Rev.* **2020**, *49* (21), 7488–7504.
43. Ripatti, D. S.; Veltman, T. R.; Kanan, M. W. Carbon Monoxide Gas Diffusion Electrolysis That Produces Concentrated C2 Products with High Single-Pass Conversion. *Joule* **2019**, *3* (1), 240–256.
44. Welch, A. J.; Dunn, E.; Duchene, J. S.; Atwater, H. A. Bicarbonate or Carbonate Processes for Coupling Carbon Dioxide Capture and Electrochemical Conversion. *ACS Energy Lett.* **2020**, *5* (3), 940–945.
45. Hakonen, A.; Hulth, S. A High-Performance Fluorosensor for PH Measurements between 6 and 9. *Talanta* **2010**, *80* (5), 1964–1969.
46. Hori, Y. Electrochemical CO 2 Reduction on Metal Electrodes. *Mod. Asp. Electrochem.* **2008**, No. 42, 89–189.

47. Welch, A. J.; Duchene, J. S.; Tagliabue, G.; Davoyan, A.; Cheng, W. H.; Atwater, H. A. Nanoporous Gold as a Highly Selective and Active Carbon Dioxide Reduction Catalyst. *ACS Appl. Energy Mater.* **2019**, *2* (1), 164–170.
48. Hall, A. S.; Yoon, Y.; Wuttig, A.; Surendranath, Y. Mesostructure-Induced Selectivity in CO_2 Reduction Catalysis. *J. Am. Chem. Soc.* **2015**, *137* (47), 14834–14837.
49. Schulz, K. G.; Riebesell, U.; Rost, B.; Thoms, S.; Zeebe, R. E. Determination of the Rate Constants for the Carbon Dioxide to Bicarbonate Inter-Conversion in PH-Buffered Seawater Systems. *Mar. Chem.* **2006**, *100* (1–2), 53–65.

Chapter 5

HOT HOLE COLLECTION AND PHOTOELECTROCHEMICAL CO_2 REDUCTON WITH PLASMONC Au/p-GaN PHOTOCATHODES

5.1 Introduction

Harvesting non-equilibrium hot carriers from plasmonic-metal nanostructures offers unique opportunities for driving photochemical reactions at the nanoscale. Despite numerous examples of hot electron-driven processes, the realization of plasmonic systems capable of harvesting hot holes from metal nanostructures has eluded the nascent field of plasmonic photocatalysis. Here, we fabricate gold/p-type gallium nitride (Au/p-GaN) Schottky junctions tailored for photoelectrochemical studies of plasmon-induced hot-hole capture and conversion. Despite the presence of an interfacial Schottky barrier to hot-hole injection of more than 1 eV across the Au/p-GaN heterojunction, plasmonic Au/p-GaN photocathodes exhibit photoelectrochemical properties consistent with the injection of hot holes from Au nanoparticles into p-GaN upon plasmon excitation. The photocurrent action spectrum of the plasmonic photocathodes faithfully follows the surface plasmon resonance absorption spectrum of the Au nanoparticles and open-circuit voltage studies demonstrate a sustained photovoltage during plasmon excitation. Comparison with Ohmic Au/p-NiO heterojunctions confirms that the vast majority of hot holes generated via interband transitions in Au are sufficiently hot to inject above the 1.1 eV interfacial Schottky barrier at the Au/p-GaN heterojunction. We further investigated plasmon-driven photoelectrochemical CO_2 reduction with the Au/p-GaN photocathodes, and observed improved selectivity for CO production over H_2 evolution in aqueous electrolytes. Taken together, our results offer experimental validation of photoexcited hot holes more than 1 eV below the Au Fermi level and demonstrate a photoelectrochemical platform for harvesting hot carriers to drive solar-to-fuel energy conversion.

The generation of non-equilibrium "hot" electron-hole pairs via surface plasmon decay within metal nanostructures holds great promise for initiating and controlling chemical reactions at the nanoscale.[1-6] However the capture and conversion of photoexcited hot carriers presents challenges, given their very short mean-free paths (l_{mfp} ~2–20 nm) and excited-state lifetimes (t ~fs–ps).[7-15] Hot carrier collection schemes typically involve the formation of an interfacial Schottky barrier (Φ_B) between plasmonic metals (e.g. Au) and wide band gap semiconductors (e.g. n-type TiO_2) to quickly capture hot electrons in a plasmonic photosensitization strategy similar to that employed in dye-sensitized solar cells (Figure 5.1a). Although numerous optoelectronic systems have been devised to harness plasmonic hot electrons for sub-band gap photodetection[16-21] and plasmon-driven photocatalysis,[22-32] little is known about hot holes derived from surface plasmon decay. Recent theoretical calculations have predicted an asymmetry in the energy distributions between hot electrons and hot holes relative to the metal Fermi level (E_F) in common plasmonic metals like Au and Cu.[8-12] Due to the high density of electronic d-band states, photoexcitation above the interband threshold of the metal (d-band to sp-band transition) can generate hot holes that are much "hotter" (further away from the Fermi level) than hot electrons (Figure 5.1b).[8-12] In Au nanostructures, an imbalance in hot carrier distributions would be expected to occur for photon energies $h\nu > 1.8$ eV.[8] Resonant optical excitation of the dipole plasmon mode in spherical Au nanoparticles ($h\nu$ ~2.4 eV) should therefore preferentially produce hot holes within the Au d-band that reside far below the Au Fermi level.[8-12,33] This substantial asymmetry between the energy distributions of hot carriers implies a greater collection efficiency of hot holes relative to hot electrons for a comparable Schottky barrier height. The strong oxidizing power of these hot d-band holes also offers the potential for driving various oxidation reactions if they could be transferred to an appropriate catalyst. Indeed, photo-oxidation of adsorbed citrate molecules in the plasmon-driven synthesis of colloidal Ag and Au nanoprisms is known to proceed more efficiently via "hot" d-band holes as compared to "warm" sp-band holes.[34-39] Strategies that can efficiently and selectively harvest hot holes from metal nanostructures would therefore offer significant benefits for plasmonic photochemistry.[40-42]

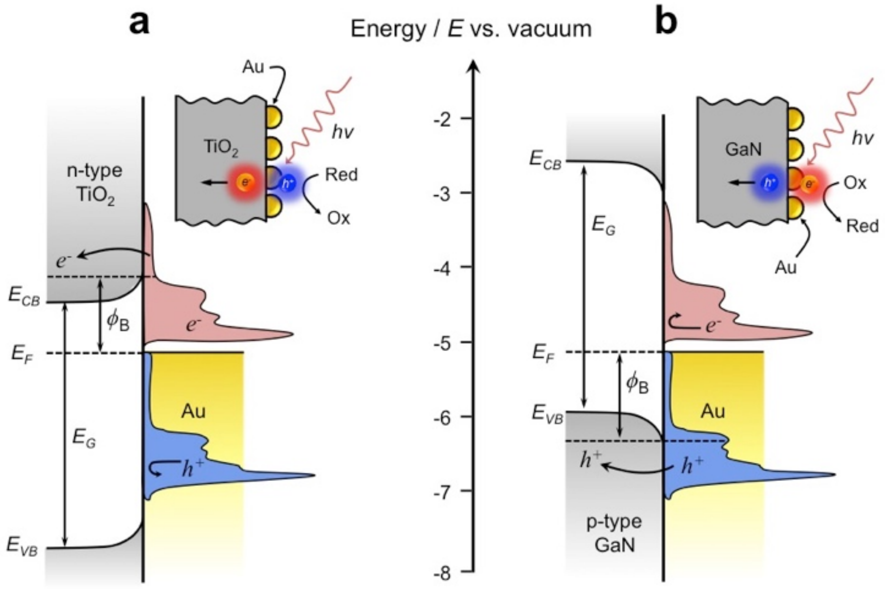

Figure 5.1: *Hot carrier collection across an interfacial Schottky barrier at metal/semiconductor heterojunctions. (a) Qualitative energy band diagram of a plasmonic metal (e.g. Au) in physical contact with an n-type semiconductor (e.g.* TiO_2*), depicting the conduction band edge (*E_{CB}*), valence band edge (*E_{VB}*), band gap (*E_G*), Fermi level (*E_F*), and the interfacial Schottky barrier*

(Φ_B). Plasmon excitation creates hot electrons (red) and hot holes (blue) above and below the E_F of Au, respectively, with a distribution of energies governed by the metal band structure and the incident photon energy (hv = 2.4 eV). Only those hot electrons with sufficient energies above Φ_B (indicated by dashed line) can surmount the interfacial barrier and populate available CB levels of the n-type semiconductor support. (b) Qualitative energy band diagram of a plasmonic metal (e.g. Au) in physical contact with a p-type semiconductor (e.g. p-GaN), depicting E_{CB}, E_{VB}, E_G, E_F, and Φ_B. Plasmon excitation creates hot electrons (red) and hot holes (blue) above and below the E_F of Au, respectively. Only those hot holes with sufficient energies below Φ_B (indicated by dashed line) can surmount the interfacial barrier and populate available VB levels of the p-type semiconductor support.

To date, however, nearly all studies of hot carrier collection have focused on the capture and conversion of hot electrons with n-type semiconductors (Figure 5.1a). Comparatively fewer studies have examined the sensitization of wide band gap p-type semiconductors, in which the plasmonic metal injects hot holes directly into the valence band of an adjoining p-type semiconductor support (Figure 5.1b). Such a plasmonic photosensitization scheme would enable adsorbed molecules to harvest hot electrons directly from metal nanostructures while obviating the need for sacrificial reagents that are often used to facilitate charge separation. Despite much promise, harvesting hot holes from metal nanostructures is more challenging than hot electron collection, given the relatively short mean-free path (l_{mfp} ~ 5-10 nm) of hot holes 1-2 eV below the E_F compared to hot electrons 1-2 eV above the E_F (l_{mfp} ~20 nm).[8-11] There are also far fewer wide band gap p-type semiconductors available for sensitization than n-type semiconductors. Although p-type nickel oxide (p-NiO) has been shown to serve as a carrier-selective contact for hot-hole collection from photoexcited Au nanoparticles,[43,44] the absence of a suitable Schottky barrier at the Au-NiO interface permits the collection of holes from the metal Fermi level (E_F) down to the photon energy ($E_F - hv$). Such a system is therefore incapable of selectively probing the population of "hot" holes generated deep below the metal Fermi level upon plasmon excitation. As a result, the energy distribution and associated prevalence of hot holes in metal nanostructures upon photoexcitation is not well understood.

Here, we employ p-type gallium nitride (p-GaN) as a semiconductor support for photoelectrochemical studies of hot-hole collection from Au nanoparticles. As a wide band gap (E_g ~3.4 eV) semiconductor that exhibits p-type conductivity, p-GaN is an ideal semiconductor support for investigating hot-hole collection above the interband threshold of a plasmonic nanoantenna. Importantly, the sizable Schottky barrier ($\Phi_B > 1$ eV) established across the Au/p-GaN interface provides a suitable platform for probing the existence of very hot holes deep below the metal Fermi level upon photoexcitation of Au nanoparticles. Our photoelectrochemical studies show that plasmonic Au/p-GaN photocathodes indeed support cathodic photocurrents consistent with the collection of plasmon-induced holes that are more than 1 eV below the Au Fermi level and the measured action spectrum faithfully follows the surface plasmon resonance of the Au nanoparticles. Significantly, open-circuit voltage measurements demonstrate a sustained plasmonic photovoltage across the metal-semiconductor heterojunction whose sign is consistent with the injection of hot holes into the p-GaN support. We further used these Au/p-GaN photocathodes for plasmon-driven CO_2 reduction, demonstrating the utility of these plasmonic photocathodes for artificial photosynthesis. These results demonstrate the feasibility of harvesting hot holes from plasmonic-metal nanostructures and open a route for the design of plasmonic photocathodes that can capture visible light to drive photochemistry.

5.2 Fabrication and characterization of Au/p-GaN

Plasmonic Au/p-GaN photocathodes were constructed via evaporation of Au thin-films onto commercial p-type GaN/sapphire substrates (c-axis 0001 orientation) (5 μm thick GaN) (Pam-Xiamen). Immediately before Au deposition, the p-GaN substrates were first pre-treated with dilute NH_4OH solution (0.02% v/v%) for 30 s to remove native oxide, followed by 30 s of copious washing in Nanopure water. It was empirically found that such surface treatments were critical for achieving good device performance. The p-GaN/sapphire substrate was then blown dry with N_2 gas and loaded into the vacuum chamber. A 1.5 nm-thick film of Au was then deposited onto the p-GaN surface using electron-beam physical vapor deposition at a base pressure of ca. 1×10^{-7} torr and a deposition rate of 1.0 Å s^{-1}. The Au/p-GaN films were then annealed in ambient air at 300 °C for 1 h to ensure coalescence of the discontinuous Au thin-film into Au nanoparticles and achieve good adhesion with the underlying p-GaN surface. The bare GaN-on-sapphire substrate is optically transparent and displays a direct optical band gap of ca. 3.35 eV (Figure 5.2), consistent with the 3.4 eV band gap expected for GaN.[45-48] The wide band gap of p-GaN ensures that any visible-light response observed at photon energies below 3.4 eV from the Au/p-GaN device can be attributed to hot-hole injection from the Au nanoparticles. Scanning electron microscopy (SEM) shows Au nanoparticles of diameter, $d = 8.2 \pm 1.6$ nm uniformly distributed across the p-type GaN surface after briefly annealing in ambient air at 300 °C for 1 h (Figure 5.3a,b). The absence of stabilizing surfactants and molecular linkers is advantageous for establishing direct physical contact at the Au/p-GaN interface while also exposing a clean Au surface for catalysis. It is further noted that no adhesion layer is required to construct the metal-semiconductor heterojunction, excluding any possible contribution from interfacial metal layers on the device operation. The Au/p-GaN substrate adopts a purple color and exhibits a prominent absorption peak in the visible region at ca. 570 nm, attributable to the surface plasmon resonance of Au nanoparticles (Figure 5.3c, red curve). The fringes present in both absorption spectra are due to Fabry-Pérot interferences within the high-index GaN layer.

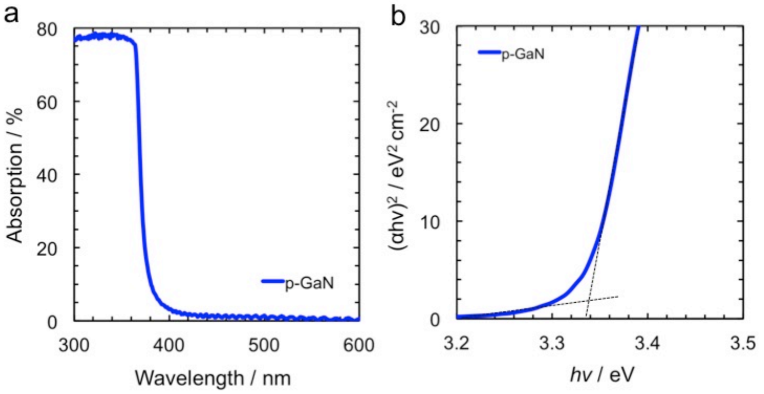

Figure 5.2: *Optical properties of p-type GaN (p-GaN) substrate. (a) Absorption of p-GaN substrate, demonstrating strong absorption in the UV region with no significant features across the visible regime. Thus, any visible-light features observed from the Au/p-GaN system can be attributed to the surface plasmon resonance of the Au nanoparticles. (b) Tauc plot of p-GaN indicates an optical band gap of* $E_G = 3.35$ *eV, consistent with the expected* E_G *of 3.4 eV for GaN.*

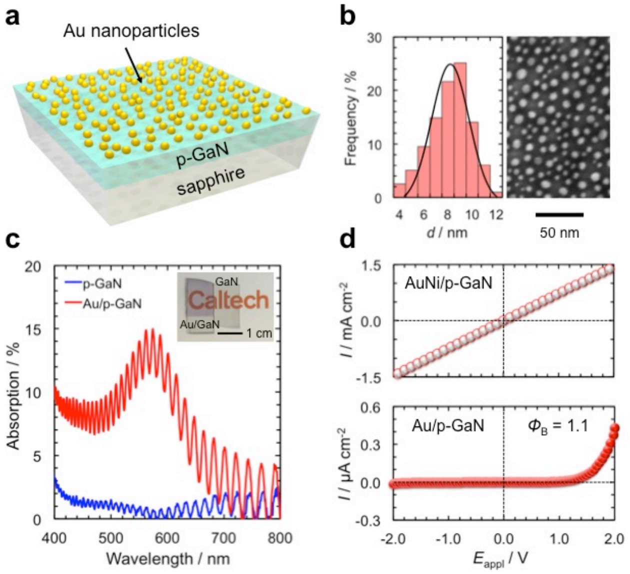

Figure 5.3: *Plasmonic Au/p-GaN photocathode device structure. (a) Schematic of Au/p-GaN photocathode on sapphire substrate. (b) SEM image with corresponding size-distribution histogram of Au nanoparticles (mean diameter,* $d = 8.2 \pm 1.6$ *nm) on p-GaN substrate. (c) Absorption spectra of plasmonic Au/p-GaN photocathode (red curve) compared to bare p-GaN substrate (blue curve). The plasmonic device shows a prominent surface plasmon resonance feature due to the Au nanoparticles at ca. 570 nm. Inset shows a digital photograph of the colorless p-GaN substrate and the purple Au/p-GaN device. (d) Solid-state*

current-voltage (I-E_{appl}) behavior from Au/p-GaN heterostructures. Ohmic contact to the p-GaN substrate was achieved through deposition of a thin-film Au/Ni alloy (top panel). In contrast, a metal-semiconductor Schottky diode was obtained across the Au/p-GaN heterojunction (bottom panel). Fitting of these data yields a Schottky barrier height of $\Phi_B = 1.1$ *eV across the Au/p-GaN interface.*

Solid-state electrical measurements were conducted to verify that a Schottky barrier (Φ_B) was established across the Au/p-GaN interface. Ohmic contacts to the p-GaN substrate were fabricated according to previous literature protocols[49,50] via co-deposition of a 10 nm-thick Ni/Au (50/50 atomic %) alloy followed by annealing in ambient air for 1 h at 500 °C. A metal-semiconductor Schottky junction was then constructed from 100 nm-thick Au contacts. Electrical measurements were conducted under an optical microscope using piezoelectric microprobes (Imina Technologies, miBots™) to electrically address the contact pads on the p-GaN substrate. As shown in Figure5.3d (top panel), Ohmic behavior was observed when both probes were electrically connected to the Ni/Au alloy contacts. In contrast, rectifying device characteristics were observed when one of the microprobes was moved onto the Au contact pad (Figure 5.3d, bottom panel). Fitting of these data to the diode equation yields a Schottky barrier height of $\Phi_B = 1.1$ eV across the Au/p-GaN heterojunction, similar to the 1.2 eV barrier previously observed for Au/p-GaN contacts.[51] The Au/p-GaN photocathode therefore provides a suitable photoelectrochemical platform to probe the production of hot holes with energies in excess of 1 eV in Au nanoparticles.

5.3 Electrochemical studies of Au/p-GaN

Photoelectrochemical studies were performed using a potentiostat in a three-electrode configuration with the Au/p-GaN photocathode as working electrode, a platinum wire mesh counter electrode, and a saturated calomel electrode (SCE) as the reference electrode. The electrolyte (50 mM K_2CO_3) was sparged with N_2 gas for 30 min prior to experiments, which were performed under a N_2 blanket. All electrochemical potentials are reported with respect to the reversible hydrogen electrode (RHE). Mott-Schottky analysis of electrochemical impedance data obtained at 2 kHz confirms the p-type conductivity of the bare GaN films (Figure 5.4). From a linear fit of the data we obtained a carrier concentration of ca. 1 x 10^{19} cm^{-3}, similar to the acceptor doping level of $N_A = 3–7 \times 10^{18}$ cm^{-3} specified by the manufacturer. The flat-band potential (E_{fb}) is ca. 2.0 V_{RHE} (V vs. RHE), consistent with prior reports.[45-47] We estimate the width of the depletion region (W_d) within the p-GaN substrate to be ca. 11–20 nm, implying that hot-hole tunneling through the barrier can be neglected. Any hot holes collected by the underlying p-GaN support upon plasmon excitation must therefore possess sufficient energy to surmount the ~1 eV Schottky barrier at the metal-semiconductor interface.

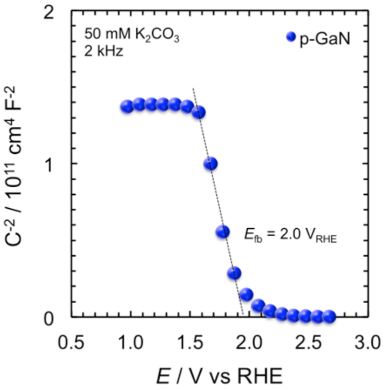

Figure 5.4: *Mott-Schottky plot of electrochemical impedance data obtained from bare p-GaN photocathodes obtained at 2 kHz. The negative slope confirms the p-type character of the GaN substrates used herein. From a linear fit of the data we obtain a carrier concentration of ca. 1 × 10^{19} cm^{-3}, similar to the acceptor doping level of N_A = 3–7 × 10^{18} cm^{-3} specified by the manufacturer, and a flat-band potential (E_{fb}) of ca. 2.0 V_{RHE} (V vs. RHE).*

The potential-current (*E*-*J*) behavior of the plasmonic photocathode was assessed via linear sweep voltammetry under periodic (0.5 Hz), visible-light excitation (λ > 495 nm) at a scan rate of 10 mV s^{-1} to simultaneously monitor the dark current (*J*) and the photocurrent (J_{ph}). As shown in Figure 5.5a (red curve), the Au/p-GaN device displayed cathodic photocurrents (J_{ph}) along the potential sweep consistent with the collection of hot holes across the metal-semiconductor heterojunction. The Au/p-GaN photocathode exhibits an onset potential (E_{on}) of ca. 0.4 V_{RHE}, and attained a J_{ph} of ca. 1.8 μA cm^{-2} at −0.8 V_{RHE}. Cyclic voltammograms of bare p-GaN and Au/p-GaN photocathodes under dark and light conditions are shown in Figure 5.6. The bare p-GaN photocathode exhibits no discernable J_{ph} response under visible-light excitation across the entire potential sweep (Figure 5.5a, blue curve and Figure 5.6). Chronoamperometry *J*(*t*) experiments were then performed with the plasmonic photocathode poised at −0.4 V_{RHE}. As shown in Figure 5.5b, the plasmonic Au/p-GaN device exhibits a prompt and reproducible cathodic J_{ph} of ca. 1.3 μA cm^{-2} under periodic, visible-light illumination (λ > 495 nm). For comparison, no visible light response was observed from the bare p-GaN support under otherwise identical experimental conditions (Figure 5.5b, blue curve). As expected for a hot carrier-driven process,[52] the plasmonic photocathode exhibits a linear J_{ph} response with respect to incident light power (Figure 5.7).

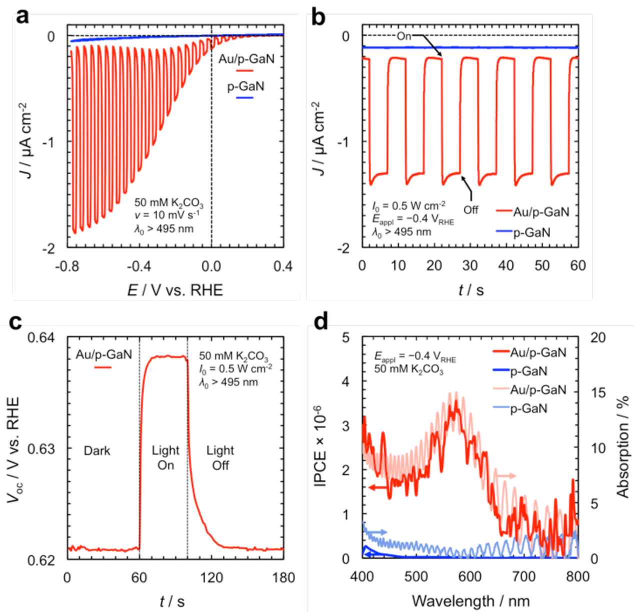

Figure 5.5: *Photoelectrochemical characterization of plasmonic Au/p-GaN photocathodes. (a) Linear sweep voltammetry of plasmonic Au/p-GaN (red) and bare p-GaN (blue) photocathodes at 10 mV s*$^{-1}$ *under periodic (0.5 Hz), visible-light irradiation (λ > 495 nm) at an incident power of* I_0 *= 600 mW cm*$^{-2}$*. (b) Chronoamperometry of plasmonic Au/p-GaN (red) and bare p-GaN (blue) photocathodes under periodic (0.5 Hz), visible-light irradiation (λ > 495 nm) while poised at a fixed applied potential of −0.4* V_{RHE}*. (c) Chronopotentiometry of the open-circuit voltage* (V_{oc}) *from plasmonic Au/p-GaN photocathodes under visible-light irradiation. (d) Incident photon-to-charge conversion efficiency (IPCE) of plasmonic Au/p-GaN (red) and bare p-GaN (blue) photocathodes immersed in 50 mM* K_2CO_3 *electrolyte while held at a fixed potential of −0.4* V_{RHE}*. The absorption spectra of each device are also plotted with the IPCE spectra to aid comparison between photoelectrochemical performance and light absorption.*

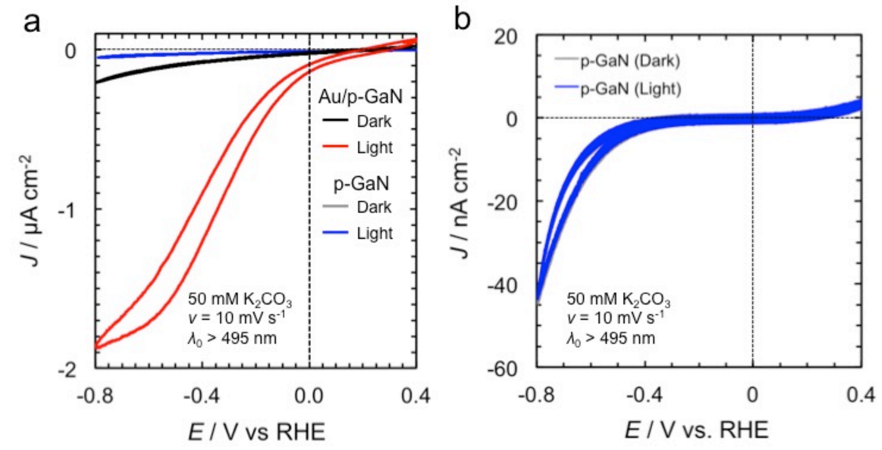

***Figure 5.6:** Cyclic voltammetry of photocathodes. (a) Cyclic voltammograms of plasmonic Au/p-GaN and bare p-GaN photocathodes under dark conditions (black and grey curves) and visible-light ($\lambda > 495$ nm) irradiation at $I_0 = 500$ mW cm^{-2} (red and blue curves). While the plasmonic Au/p-GaN device exhibits an obvious light response (red curve), no difference in current was observed for the bare p-GaN device (blue curve). (b) Close-up view of the cyclic voltammograms from bare p-GaN photocathode under dark (grey) and visible-light ($\lambda > 495$ nm) irradiation (blue) at $I_0 = 500$ mW cm^{-2}. No difference could be observed between dark (grey) and light (blue) conditions, as these two curves lay directly on top of one another, confirming that the p-GaN support does not respond to visible light. This observation is consistent with the large band gap of p-GaN (see Figure 5.2). Therefore, all visible-light responses observed from plasmonic Au/p-GaN photocathodes can be unambiguously assigned to hot-hole injection from Au to the valence band of p-GaN upon plasmon excitation.*

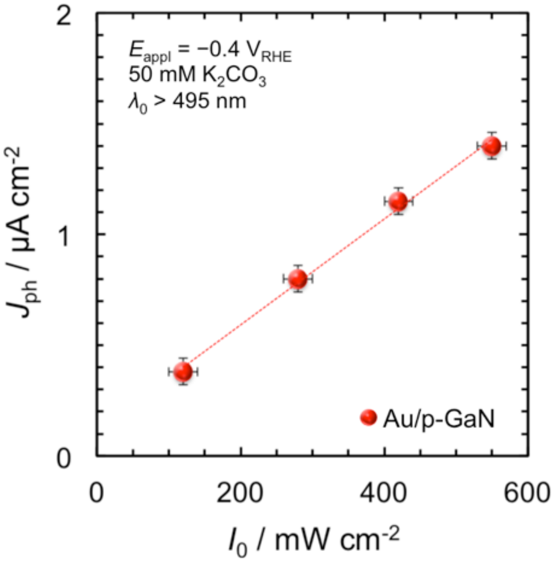

***Figure 5.7:** Photocurrent ($J_{ph} = J_{light} - J_{dark}$) response obtained from plasmonic Au/p-GaN photocathodes showing a linear trend with respect to incident light power (I_0).*

Plasmon-driven charge separation across the Au/p-GaN interface was examined by monitoring the open-circuit voltage (V_{oc}) of the device under visible-light excitation ($\lambda > 495$ nm). For a p-type semiconductor in contact with an aqueous electrolyte, Fermi level equilibration between the semiconductor (E_F) and the redox species in the electrolyte ($E_{F,Redox} = E_F$) establishes a depletion region within the semiconductor that results in downward band-bending near the surface.[47] Upon optical excitation, the electric field across the space-charge layer draws photogenerated electrons to the semiconductor-liquid junction where they are scavenged by redox species in the electrolyte (e.g. protons), leaving behind charge vacancies (i.e. holes) to accumulate within the bulk of the semiconductor. This accumulation of holes causes a downward shift of their quasi-Fermi level ($E_{F,p}$) with respect to the dark equilibrium level (E_F), driving the V_{oc} of the p-type photocathode to more positive values.[47] Indeed, band gap excitation of bare p-GaN photocathodes with UV light induces a positive shift in the V_{oc} of the device (Figure 5.8). As there are no free electrons photogenerated directly within the p-GaN conduction band upon illumination with sub-band gap visible light, any changes in the V_{oc} of the Au/p-GaN photocathode can be attributed to the injection of hot holes into the p-GaN valence band. Thus, monitoring changes in the V_{oc} of the Au/p-GaN photocathode upon plasmon excitation enables the detection of hot hole injection across the metal-semiconductor heterojunction in the absence of an applied electrical bias, E_{appl}. The Au/p-GaN photocathode was allowed to equilibrate with the electrolyte for several hours in the dark until a steady V_{oc} baseline was obtained ($V_{oc,dark} = 0.62\ V_{RHE}$). Plasmon excitation of the Au nanoparticles promptly drives the injection of hot holes into the p-GaN support (Figure 5.5c), as evidenced by the positive shift of V_{oc} upon the incidence of visible light ($V_{oc,light} = 0.64\ V_{RHE}$). A plasmonic photovoltage ($V_{ph} = V_{oc,light} - V_{oc,dark}$) of ca. 20 mV was eventually established within the photocathode and sustained over 30 s before the light was turned off. The hot holes present in the p-GaN valence band must then recombine across the Au/p-GaN interface to re-establish the equilibrium V_{oc} obtained under dark conditions. The observation of a plasmonic photovoltage demonstrates the ability to maintain charge separation across the Schottky barrier at the Au/p-GaN interface under steady-state operation.

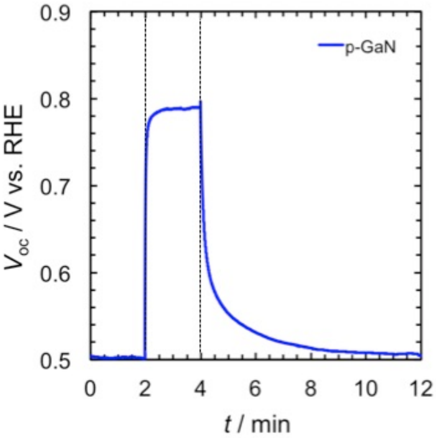

Figure 5.8: *Chronopotentiometry of the open-circuit voltage (V_{oc}) from bare p-GaN photocathodes under UV-light irradiation. The positive shift in V_{oc} upon UV light exposure confirms the p-type character of the GaN substrates used herein.*

The photoelectrochemical action spectrum, $J_{ph}(\lambda)$, was assessed via incident photon-to-current conversion efficiency (IPCE) measurements with the photocathode poised at −0.4 V_{RHE} in 50 mM K_2CO_3 electrolyte. Figure 5.5d shows that the IPCE of the plasmonic photocathode (red curve) faithfully follows the surface plasmon resonance of the Au nanoparticles (light red curve) across the visible regime. For comparison, no J_{ph} response is observed from the bare p-GaN device under otherwise identical experimental conditions

(Figure 5.5d, blue curve). Taken together, these photoelectrochemical data confirm that the visible-light response observed from the Au/p-GaN device is derived from hot-hole injection upon plasmon excitation of the Au nanoparticles. Given the considerable Schottky barrier height at the Au/p-GaN interface (Φ_B = 1.1 eV), such a result is encouraging for the design of optoelectronic devices that operate via the collection of hot holes from metal nanostructures.

5.4 Fabrication, characterization, and electrochemical studies of Au/p-NiO

The influence of interfacial barrier height on hot-hole collection from Au nanoparticles was then investigated through the construction and evaluation of a plasmonic photocathode composed of Au nanoparticles on p-type nickel oxide (p-NiO) films. Plasmonic Au/p-NiO photocathodes were constructed via evaporation of Au thin-films onto p-type NiO (p-NiO) substrates. The p-NiO films were synthesized on fluorine-doped tin oxide (FTO) glass substrates using electron-beam physical vapor deposition. Ni metal was deposited at a rate of 0.25 Å s^{-1} under flowing O_2 gas at 6 sccm. After deposition of a 20 nm-thick NiO film on the FTO substrate, a 2 nm-thick film of Au was then deposited onto the p-NiO surface using electron-beam physical vapor deposition at a base pressure of ca. 1×10^{-7} torr and a deposition rate of 1.0 Å s^{-1}. The Au/p-NiO films were then annealed in ambient air at 300 °C for 1 h to ensure coalescence of the discontinuous Au thin-film into Au nanoparticles and achieve good adhesion with the underlying p-NiO surface.

As a wide band gap semiconductor that natively exhibits p-type conductivity and forms an Ohmic contact with Au,[44] plasmonic Au/p-NiO photocathodes offer a complementary photoelectrochemical system for assessing the collection of hot holes from Au nanoparticles in the absence of an interfacial barrier (Figure S5.9a-d). Au nanoparticles of ca. 10 ± 1 nm in diameter were uniformly decorated onto the p-NiO surface in the same way as for the Au/p-GaN device (Figure 5.9e). The Au/p-NiO photocathodes exhibit a surface plasmon resonance feature at ca. 560 nm with nearly identical overall magnitude as the Au/p-GaN system (Figure 5.9f). Solid-state *I-V* measurements confirm Ohmic contact between Au nanoparticles and the p-NiO film (Figure 5.10a). Chronoamperometry of Au/p-NiO photocathodes yielded photocurrents of ca. 2.7 μA cm^{-2} at −0.4 V_{RHE} under periodic, visible-light irradiation ($\lambda > 495$ nm), while no J_{ph} response was obtained from the bare p-NiO substrate (Figure 5.10b). The incident photon-to-charge conversion efficiency (IPCE) $J_{ph}(\lambda)$ of Au/p-NiO qualitatively follows the surface plasmon resonance of the Au nanoparticles, indicating that all photocurrent is attributable to hot-hole injection from Au nanoparticles to the p-NiO support (Figure 5.10c). The striking similarity in photoelectrochemical performance between Au/p-NiO (ca. 2.7 μA cm^{-2} at −0.4 V_{RHE}) and Au/p-GaN (ca. 1.3 μA cm^{-2} at −0.4 V_{RHE}) indicates that the vast majority of hot holes generated in the Au/p-GaN device are sufficiently hot to inject above the 1.1 eV interfacial Schottky barrier at the Au/p-GaN heterojunction. This experimental result is consistent with prior theoretical predictions of the hot-hole distribution generated on Au nanoparticles upon photoexcitation above the interband threshold of the metal.[8-11] Considering the vast difference in barrier height between these two material systems (~1 eV), such a result is promising for the eventual exploitation of plasmon-derived hot holes for solar photochemistry.

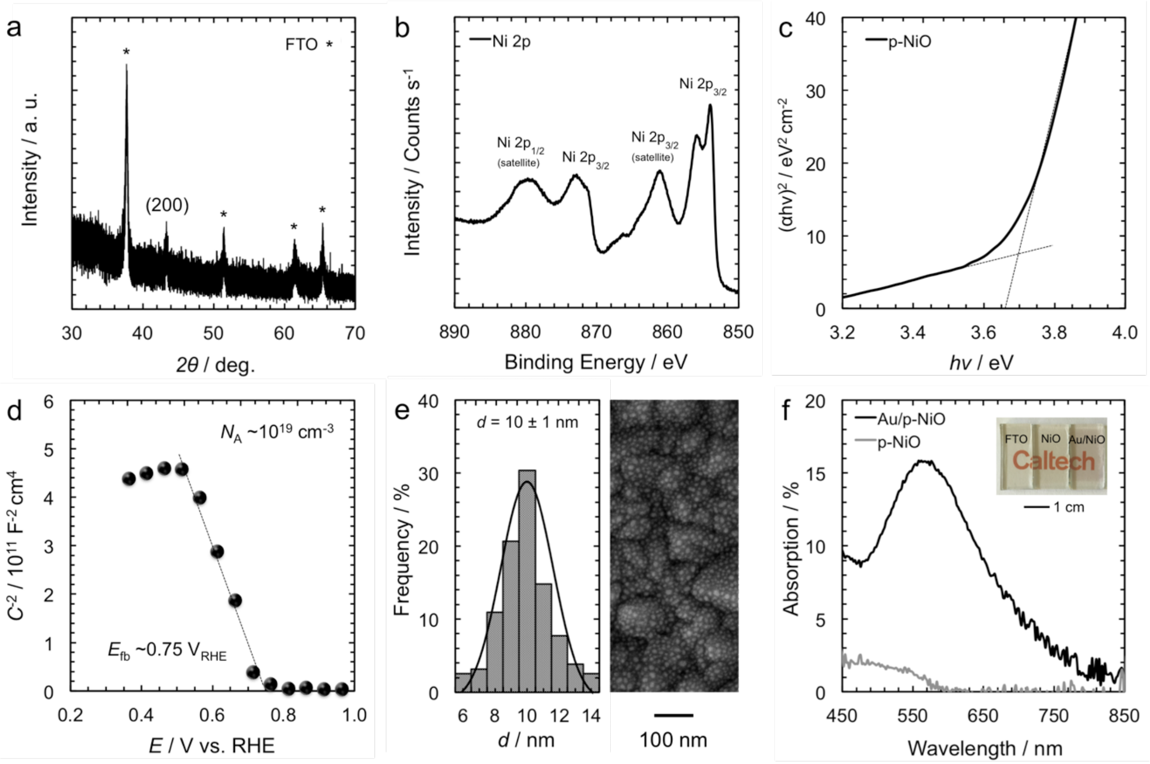

Figure 5.9: *Characterization of p-type NiO films and plasmonic Au/p-NiO films. (a) X-ray diffraction pattern from 20 nm-thick NiO films on FTO glass showing the characteristic (200) peak of NiO. (b) X-ray photoelectron spectroscopy spectrum of the Ni 2p region, showing the characteristic binding energies of NiO. (c) Tauc plot of the NiO film exhibiting a band gap of ca. 3.7 eV. (d) Mott-Schottky plot obtained from 20 nm-thick NiO films on FTO glass substrate, which shows a negative slope indicative of p-type conductivity. From these data, the flat-band potential* (E_{fb}) *is estimated to be ca. 0.75* V_{RHE} *(Volts vs. RHE) with an acceptor concentration of ca.* 1×10^{19} cm^{-3}*. All these data are consistent with previous literature reports of p-type NiO thin films.*[2] *(e) Scanning electron microscopy image of Au nanoparticles uniformly decorated on the p-NiO surface with corresponding size-distribution histogram of the Au nanoparticles, with an average Au diameter of 10 ± 1 nm. (f) Absorbance of the bare p-NiO photocathode (grey) and the plasmonic Au/p-NiO photocathode (black). A prominent surface plasmon resonance feature due to the Au nanoparticles is observed around 560 nm. Inset shows a digital image of the FTO glass substrate, p-NiO/FTO substrate, and Au/p-NiO/FTO substrate, from left to right. A faint purple color is observed from the Au/p-NiO device.*

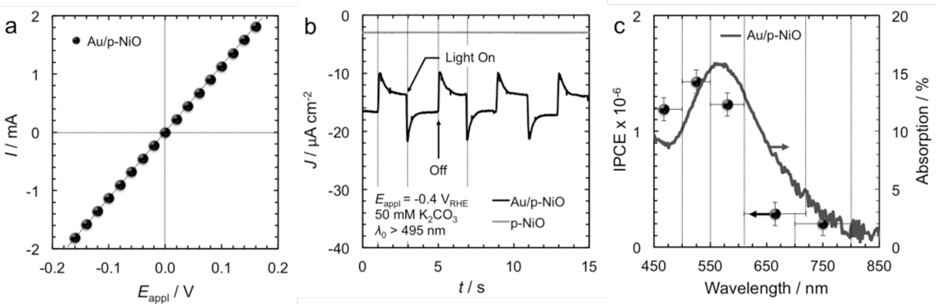

Figure 5.10: *Photoelectrochemistry of plasmonic Au/p-NiO photocathodes. (a) Solid-state current-voltage (I-E_{appl}) behavior from Au/p-NiO films exhibiting Ohmic behavior, consistent with previous literature for Au/NiO contacts. (b) Chronoamperometry from Au/p-NiO photocathodes (black) under visible-light excitation (λ > 495 nm) at 500 mW cm^{-2} while poised at −0.4 VRHE. A prompt, reproducible plasmonic photocurrent is clearly observed, indicating hot-hole collection by the p-NiO support upon plasmon excitation. For comparison, the bare p-NiO film (grey) exhibits no observable photocurrent. (c) Photoelectrochemical action spectrum obtained from Au/p-NiO device (black points), showing a clear relationship with the surface plasmon resonance of the Au nanoparticles (black curve).*

5.5 Selectivity of Au/p-GaN in light and dark conditions

To that end, Au/p-GaN photocathodes were employed for plasmon-driven carbon dioxide (CO_2) reduction in CO_2-saturated 50 mM K_2CO_3 electrolyte in a three-electrode configuration with Pt gauze as the counter electrode and a saturated calomel electrode as the reference electrode. No sacrificial reagents were used in the reaction. The photocathode was potentiostatically poised at −1.8 V_{RHE} while the reactor headspace gas was periodically sampled and analyzed via gas chromatography over a 48 h period. It has previously been reported that p-GaN nanowires, which predominantly expose m-planes, produce carbon monoxide (CO), hydrogen (H_2), and methane (CH_4) in the absence of a metal co-catalyst.[53] Under our experimental conditions, we find that the bare p-GaN substrate (c-plane) produces primarily H_2 and CO, with trace amounts of CH_4 under dark electrolysis (Figure 5.11). The bare p-GaN surface exhibits a substantial preference for proton reduction over CO_2 reduction, evolving H_2 at a rate that is ca. 3.5 times greater than CO. In contrast, the addition of Au nanoparticles substantially alters the selectivity of the device for CO_2 reduction. Under dark electrolysis, the Au/p-GaN device exhibits improved selectivity for CO_2 reduction to CO with a significant reduction in H_2 evolution relative to the bare p-GaN surface (Figure 5.12a). From these data, the Au/p-GaN device produces CO-to-H_2 at a ratio of ca. 4:1 under dark conditions. Plasmon excitation of the Au nanoparticles with visible light (λ > 495 nm) was found to increase the CO evolution rate by 20%, from ca. 4 nmol h^{-1} in the dark to ca. 5 nmol h^{-1} in the light, while exerting little influence on the rate of H_2 evolution (Figure 5.12b). Plasmonic Au/p-GaN photocathodes therefore exhibit improved selectivity for photoelectrochemical CO_2 reduction in aqueous electrolytes, producing CO-to-H_2 at a ratio of 5:1 upon plasmon excitation (Figure 5.12b). The photoelectrochemical stability of these plasmonic photocathodes is evidenced by the continuous evolution of gaseous products over 96 h of electrochemical operation. Overall, these results are consistent with recent experimental observations of improved selectivity for plasmon-driven CO_2 reduction with plasmonic-metal nanostructures[25,30] and demonstrate the utility of plasmonic photocathodes for artificial photosynthesis.

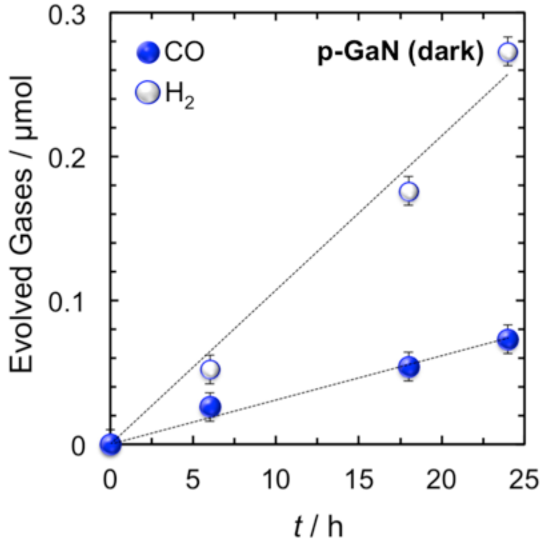

Figure 5.11: *Time-course of gas evolution from bare p-GaN photocathode under dark electrolysis conditions at −1.8* V_{RHE} *in* CO_2*-saturated 50 mM* K_2CO_3 *electrolyte.*

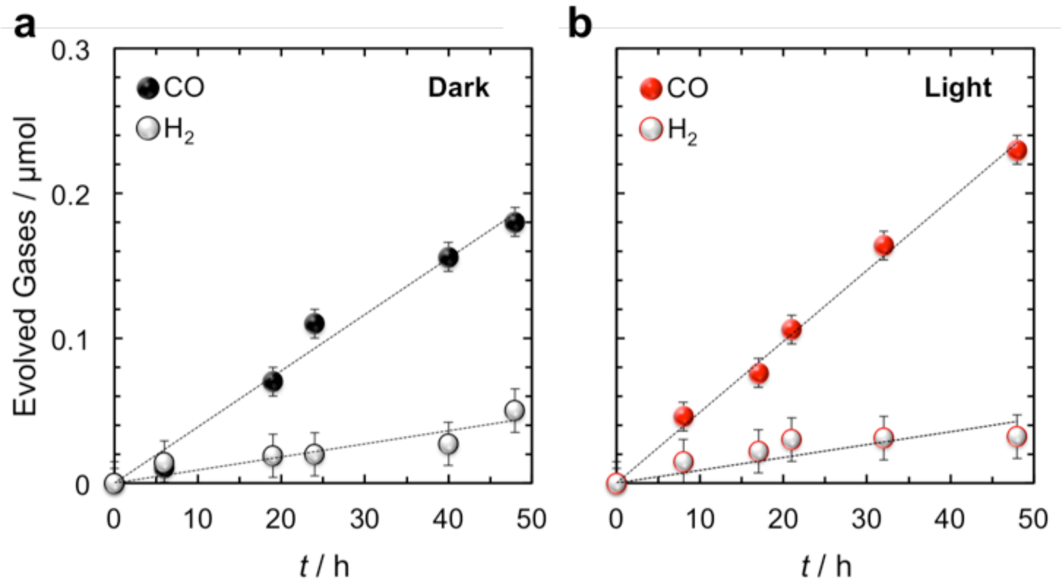

Figure 5.12: *Photoelectrochemical CO_2 reduction with plasmonic Au/p-GaN photocathodes. (a) Time-course of gas evolution from plasmonic Au/p-GaN photocathode during controlled potential electrolysis under dark conditions. (b) Time-course of gas evolution from plasmonic Au/p-GaN photocathode during controlled potential electrolysis under plasmon excitation ($\lambda > 495$ nm). All electrolysis experiments were performed at $-1.8\ V_{\mathrm{RHE}}$ in CO_2-saturated 50 mM K_2CO_3 electrolyte without sacrificial reagents.*

5.6 Conclusion

In summary, we have demonstrated the collection of plasmon-induced hot holes from Au nanoparticles via construction of an interfacial Schottky barrier with p-type GaN. Although the photocurrents reported here are relatively modest (~μA cm^{-2}), substantial enhancements in device performance may be achievable by implementing this photosensitization scheme for p-GaN nanowire arrays to dramatically increase the available surface area for light collection and catalysis.[54-57] Further improvements could also be realized through roughening the metal-semiconductor interface to relieve the momentum matching restrictions for hot hole transmission across planar metal-semiconductor Schottky junctions investigated here. More broadly, the realization of a plasmon-driven photocathode capable of collecting hot holes at least 1.1 eV below the Au Fermi level holds tantalizing prospects for plasmonic photochemistry, given the considerable oxidizing power of such carriers. These results support previous observations of plasmon-driven water oxidation with Au nanoparticles,[58-60] and suggest room for further improvements if the hot holes could be efficiently transferred to an appropriate catalyst. Further studies are needed to fully elucidate the factors governing plasmonic hot hole collection in p-type semiconductor systems along with their associated carrier dynamics. Though at an early stage, our demonstration of a plasmon-driven artificial photosynthetic system for CO_2 conversion offers promise for the eventual exploitation of both hot electrons and hot holes in fuel-forming photochemical reactions.

BIBLIOGRAPHY CHAPTER 5

1. Linic, S.; Christopher, P.; Ingram, D. B. Plasmonic-metal nanostructures for efficient conversion of solar to chemical energy. *Nat. Mater.* **2011**, *10*, 911-921.
2. Clavero, C. Plasmon-induced hot-electron generation at nanoparticle/metal-oxide interfaces for photovoltaic and photocatalytic devices. *Nat. Photon.* **2014**, *8*, 95-103.
3. Brongersma, M. L.; Halas, N. J.; Nordlander, P. Plasmon-induced hot carrier science and technology. *Nat. Nanotechnol.* **2015**, *10*, 25-34.
4. Christopher, P.; Moskovits, M. Hot Charge Carrier Transmission from Plasmonic Nanostructures. *Annu. Rev. Phys. Chem.* **2017**, *68*, 379-398.

5. Linic, S.; Aslam, U.; Boerigter, C.; Morabito, M. Photochemical transformations on plasmonic metal nanoparticles. *Nat. Mater.* **2015**, *14*, 567-576.
6. Hartland, G. V.; Besteiro, L. V.; Johns, P.; Govorov, A. O. What's so Hot about Electrons in Metal Nanoparticles? *ACS Energy Lett.* **2017**, *2*, 1641-1653.
7. Manjavacas, A.; Liu, J. G.; Kulkarni, V.; Nordlander, P. Plasmon-induced hot carriers in metallic nanoparticles. *ACS Nano* **2014**, *8*, 7630-7638.
8. Brown, A. M.; Sundararaman, R.; Narang, P.; Goddard III, W. A.; Atwater, H. A. Nonradiative Plasmon Decay and Hot Carrier Dynamics: Effects of Phonons, Surfaces, and Geometry. *ACS Nano* **2016**, *10*, 957-966.
9. Sundararaman, R.; Narang, P.; Jermyn, A. S.; Goddard III, W. A.; Atwater, H. A. Theoretical predictions for hot-carrier generation from surface plasmon decay. *Nat. Commun.* **2014**, *5*, 5788.
10. Bernardi, M.; Mustafa, J.; Neaton, J. B.; Louie, S. G. Theory and computation of hot carriers generated by surface plasmon polaritons in noble metals. *Nat. Commun.* **2015**, *6*, 7044.
11. Govorov, A. O.; Zhang, H.; Gun'ko, Y. K. Theory of Photoinjection of Hot Plasmonic Carriers from Metal Nanostructures into Semiconductors and Surface Molecules. *J. Phys. Chem. C* **2013**, *117*, 16616-16631.
12. Liu, J G.; Zhang, H.; Link, S.; Nordlander, P. Relaxation of Plasmon-Induced Hot Carriers. *ACS Photon.* **2017**, DOI: 10.1021/acsphotonics.7b00881.
13. Harutyunyan, H.; Martinson, B. F. A.; Rosenmann, D.; Khorashad, L. K.; Besteiro, L. V.; Govorov, A. O.; Wiederrecht, G. P. Anomalous ultrafast dynamics of hot plasmonic electrons in nanostructures with hot spots. *Nat. Nanotechnol.* **2015**, *10*, 770-774.
14. Hartland, G. V. Optical Studies of Dynamics in Noble Metal Nanostructures. *Chem. Rev.* **2011**, *111*, 3858-3887.
15. Brown, A. M.; Sundararaman, R.; Narang, P.; Schwartzberg, A. M.; Goddard III, W. A.; Atwater, H. A. Experimental and *Ab Initio* Ultrafast Carrier Dynamics in Plasmonic Nanoparticles. *Phys. Rev. B* **2017**, *118*, 087401.
16. Knight, M. W.; Sobhani, H.; Nordlander, P.; Halas, N. J. Photodetection with active optical antenna. *Science* **2011**, *332*, 702-704.
17. Zheng, B. Y.; Zhao, H.; Manjavacas, A.; McClain, M.; Nordlander, P.; Halas, N. J. Distinguishing between plasmon-induced and photoexcited carriers in a device geometry. *Nat. Commun.* **2015**, *6*, 7797.
18. Li, W.; Valentine, J. Metamaterial Perfect Absorber Based Hot Electron Photodetection. *Nano Lett.* **2014**, *14*, 3510-3514.
19. Goykhman, I.; Desiatov, B.; Khurgin, J.; Shappir, J.; Levy, U. Locally Oxidized Silicon Surface-Plasmon Schottky Detector for Telecom Regime. *Nano Lett.* **2011** *11*, 2219-2224.
20. Chalabi, H.; Schoen, D.; Brongersma, M. L. Hot-Electron Photodetection with a Plasmonic Nanostripe Antenn. *Nano Lett.* **2014**, *14*, 1374-1380.
21. Li, W.; Coppens, Z. J.; Besteiro, L. V.; Wang, W.; Govorov, A. O.; Valentine, J. Circularly polarized light detection with hot electrons in chiral plasmonic metamaterials. *Nat. Commun.* **2015**, *6*, 8379.
22. Mubeen, S.; Hernandez-Sosa, G.; Moses, D.; Lee, J.; Moskovits, M. Plasmonic photosensitization of a wide band gap semiconductor: converting plasmons to charge carriers. *Nano Lett.* **2011**, *11*, 5548-5552.
23. Mubeen, S.; Lee, J.; Singh, N.; Kramer, S.; Stucky, G. D.; Moskovits, M. An autonomous photosynthetic device in which all charge carriers derive from surface plasmons. *Nat. Nanotechnol.* **2013**, *8*, 247-251.
24. Mubeen, S.; Lee, J.; Liu, D.; Stucky, G. D.; Moskovits, M. Panchromatic photoproduction of H2 with surface plasmons. *Nano Lett.* **2015**, *15*, 2132-2136.
25. Robatjazi, H.; Zhao, H.; Swearer, D. F.; Hogan, N. J.; Zhou, L.; Alabastri, A.; McClain, M. J.; Nordlander, P.; Halas, N. J. Plasmon-induced selective carbon dioxide conversion on earth-abundant aluminum-cuprous oxide antenna-reactor nanoparticle. *Nat. Commun.* **2017**, 8, 27.

26. Swearer, D. F.; Zhao, H.; Zhou, L.; Zhang, C.; Robatjazi, H.; Martirez, J. M. P.; Krauter, C. M.; Yazdi, S.; McClain, M. J.; Ringe, E.; Carter, E. A.; Nordlander, P.; Halas, N. J. Plasmonic Photocatalysis of Nitrous Oxide into N2 and O2 using Aluminum-Iridium Antenna-Reactor Nanoparticles. *Proc. Natl. Acad. Sci. U. S. A.* **2016***, 113,* 8916-8920.
27. Mukherjee, S.; Zhou, L.; Goodman, A. M.; Large, N.; Ayala-Orozco, C.; Zhang, Y.; Nordlander, P.; Halas, N. J. Hot-Electron-Induced Dissociation of H_2 on Gold Nanoparticles Supported on SiO_2. *J. Am. Chem. Soc.* **2014**, *136,* 64-67.
28. Zhou, L.; Zhang, C.; McClain, M. J.; Manjavacas, A.; Krauter, C. M.; Shu, T.; Berg, F.; Everitt, H. O.; Carter, E. A.; Nordlander, P.; Halas, N. J. Aluminum Nanocrystals as a Plasmonic Photocatalyst for Hydrogen Dissociation. *Nano Lett.* **2016**, *16*, 1478-1484.
29. Zhang, C.; Zho, H.; Zhou, L.; Schlather, A. E.; Dong, L.; McClain, M. J.; Swearer, D. F.; Nordlander, P.; Halas, N. J. Al–Pd Nanodisk Heterodimers as Antenna–Reactor Photocatalysts. *Nano Lett.* **2016**, *16*, 6677-6682.
30. Zhang, X.; Li, X.; Zhang, D.; Su, N. Q.; Yang, W.; Everitt, H. O.; Liu, J. Product selectivity in plasmonic photocatalysis for carbon dioxide hydrogenation. *Nat. Commun.* **2017**, *8*, 14542.
31. Aslam, U.; Chavez, S.; Linic, S. Controlling energy flow in multimetallic nanostructures for plasmonic catalysis. *Nat. Nanotechnol.* **2017**, *12*, 1000-1005.
32. Zhong, Y.; Ueno, K.; Mori, Y.; Shi, X.; Oshikiri, T.; Murakoshi, K.; Inoue, H.; Misawa, H. Plasmon-assisted Water Splitting Using Two Sides of the Same $SrTiO_3$ Single-crystal Substrate: Conversion of Visible Light to Chemical Energy. *Angew. Chem. Int. Ed.* **2014**, *126*, 10350-10354.
33. Sá, J.; Tagliabue, G.; Friedli, P.; Szlachetko, J.; Rittmann-Frank, M. H.; Santomauro, F. G.; Milne, C. J.; Sigg, H. Direct observation of charge separation on Au localized surface plasmons. *Energy Environ. Sci.* **2013**, *6*, 3584-3588.
34. Thrall, E. S.; Steinberg, A. P.; Wu, X.; Brus, L. E. *J. Phys. Chem. C* **2013**, *117*, 26238-26247.
35. Langille, M. R.; Personick, M. L.; Mirkin, C. A. Plasmon-mediated syntheses of metallic nanostructures. *Angew. Chem. Int. Ed.* **2013**, *52*, 13910-13940.
36. Wu, X.; Redmond, P. L.; Liu, H.; Chen, Y.; Steigerwald, M.; Brus, L. Photovoltage mechanism for room light conversion of citrate stabilized silver nanocrystal seeds to large nanoprisms. *J. Am. Chem. Soc.* **2008**, *130*, 9500-9506.
37. Schlather, A. E.; Manjavacas, A.; Lauchner, A.; Marangoni, V. S.; DeSantis, C. J.; Nordlander, P.; Halas, N. J. Hot Hole Photoelectrochemistry on Au@SiO_2@Au Nanoparticles. *J. Phys. Chem. Lett.* **2017**, *8*, 2060-2067.
38. Wu, X.; Thrall, E. S.; Liu, H.; Steigerwald, M.; Brus, L. Plasmon Induced Photovoltage and Charge Separation in Citrate-Stabilized Gold Nanoparticles. *J. Phys. Chem. C* **2010**, *114*, 12896-12899.
39. Zhai, Y.; DuChene, J. S.; Wang, Y.-C.; Qiu, J.; Johnston-Peck, A. C.; You, B.; Guo, W.; DiCaccio, B.; Qian, K.; Zhao, E. W.; Ooi, F.; Hu, D.; Su, D.; Stach, E. A.; Zhu, Z.; Wei, D. W. Polyvinylpyrrolidone-induced anisotropic growth of gold nanoprisms in plasmon-driven synthesis. *Nat. Mater.* **2016**, *15*, 889-895.
40. Zhao, J.; Nguyen, S. C.; Ye, R.; Ye, B.; Weller, H.; Somorjai, G. A.; Alivisatos, A. P.; Toste, F. D. A Comparison of Photocatalytic Activities of Gold Nanoparticles Following Plasmonic and Interband Excitation and a Strategy for Harnessing Interband Hot Carriers for Solution Phase Photocatalysis**.** *ACS Cent. Sci.* **2017**, *3*, 482-488.
41. Kim, Y.; Torres, D. D.; Jain, P. K. Activation Energies of Plasmonic Catalysts. *Nano Lett.* **2016**, *16*, 3399-3407.
42. Moskovits, M. The case for plasmon-derived hot carrier devices. *Nat. Nanotechnol.* **2015**, *10*, 6-8.

43. Nakamura, K.; Oshikiri, T.; Ueno, K.; Wang, Y.; Kamata, Y.; Kotake, Y.; Misawa, H. Properties of plasmon-induced photoelectric conversion on a TiO_2/NiO p-n junction with au nanoparticles. *J. Phys. Chem. Lett.* **2016**, *7*, 1004-1009.
44. Robatjazi, H.; Bahauddin, S. M.; Doiron, C.; Thomann, I. Direct Plasmon-Driven Photoelectrocatalysis. *Nano Lett.* **2015**, *15*, 6155-6161.
45. Beach, J. D.; Collins, R. T.; Turner, J. A. *J. Electrochem. Soc.* **2003**, *7*, A899-A904.
46. Kibria, M. G.; Mi, Z. Artificial photosynthesis using metal/nonmetal-nitride semiconductors: current status, prospects, and challenges. *J. Mater. Chem. A* **2016**, *4*, 2801-2820.
47. Kamimura, J.; Bogdanoff, P.; Ramsteiner, M.; Corfdir, P.; Feix, F.; Geelhaar, L.; Riechert, H. Photoelectrochemical Properties of (In,Ga)N Nanowires for Water Splitting Investigated by in Situ Electrochemical Mass Spectroscopy. *Nano Lett.* **2017**, *17*, 1529-1537.
48. Kibria, M. G.; Chowdhury, F. A.; Zhao, S.; Al Oltaibi, B.; Trudeau, M. L.; Guo, H.; Mi, Z. Visible light-driven efficient overall water splitting using p-type metal-nitride nanowire arrays. *Nat. Commun.* **2015**, *6*, 6797.
49. Ho, J.-K.; Jong, C.-S.; Chiu, C. C.; Huang, C.-N.; Shih, K.-K. Low-resistance ohmic contacts to *p*-type GaN achieved by the oxidation of Ni/Au films. *J. Appl. Phys.* **1999**, *86*, 4491-4497.
50. Jang, H. W.; Kim, S. Y.; Lee, J.-L. Mechanism for Ohmic contact formation of oxidized NiÕAu on p-type GaN. *J. Appl. Phys.* **2003**, *94*, 1748-1752.
51. Wu, C. I.; Kahn, A. Investigation of the chemistry and electronic properties of metal/gallium nitride interfaces. *J. Vac. Sci. Technol. B* **1998**, *16*, 2218-2223.
52. Christopher, P.; Xin, H.; Linic, S. Visible-light-enhanced catalytic oxidation reactions on plasmonic silver nanostructures. *Nat. Chem.* **2011**, *3*, 467-472.
53. Al Otaibi, B.; Fan, S.; Wang, D.; Ye, J.; Mi, Z. Wafer-Level Artificial Photosynthesis for CO_2 Reduction into CH_4 and CO Using GaN Nanowires. *ACS Catal.* **2015**, *5*, 5342-5348.
54. Boettcher, S. W.; Spurgeon, J. M.; Putnam, M. C.; Warren, E. L.; Turner-Evans, D. B.; Kelzenberg, M. D.; Maiolo, J. R.; Atwater, H. A.; Lewis, N. S. Photoelectrochemical Hydrogen Evolution Using Si Microwire Arrays. *Science* **2010**, *327*, 185-187.
55. Kelzenberg, M. D.; Boettcher, S. W.; Petykiewicz, J. A.; Turner-Evans, D. B.; Putnam, M. C.; Warren, E. L.; Spurgeon, J. M.; Briggs, R. M.; Lewis, N. S.; Atwater, H. A. Enhanced absorption and carrier collection in Si wire arrays for photovoltaic applications. *Nat. Mater.* **2010**, *9*, 239-244.
56. Wang, D.; Pierre, A.; Kibria, M. G.; Cui, K.; Han, X.; Bevan, K. H.; Guo, H.; Paradis, S.; Hakima, A.-R.; Mi, Z. Wafer-level photocatalytic water splitting on GaN nanowire arrays grown by molecular beam epitaxy. *Nano Lett.* **2011**, *11*, 2353-2357.
57. Al Otaibi, B.; Nguyen, H. P. T.; Zhao, S.; Kibria, M. G.; Fan, S.; Mi, Z. Highly Stable Photoelectrochemical Water Splitting and Hydrogen Generation Using a Double-Band InGaN/GaN Core/Shell Nanowire Photoanode. *Nano Lett.* **2013**, *13*, 4356-4361.
58. Shi, X.; Ueno, K.; Takabayashi, N.; Misawa, H. Plasmon-enhanced photocurrent generation and water oxidation with a gold nanoisland-loaded titanium dioxide photoelectrode. *J. Phys. Chem. C* **2012**, *117*, 2494-2499.
59. Nishijima, Y.; Ueno, K.; Kotake, Y.; Murakoshi, K.; Inoue, H.; Misawa, H. Near-infrared plasmon-assisted water oxidation. *J. Phys. Chem. Lett.* **2012**, *3*, 1248-1252.
60. Wang, S.; Gao, Y.; Miao, S.; Liu, T.; Mu, L.; Li, R.; Fan, F.; Li, C. Positioning the Water Oxidation Reaction Sites in Plasmonic Photocatalysts. *J. Am. Chem. Soc.* **20160** *139*, 11771-11778.

Chapter 6

OPTICAL EXCITATION OF A NANOPARTICLE Cu/p-NiO PHOTOCATHODE IMPROVES REACTION SELECTIVITY FOR CO_2 REDUCTION IN AQUEOUS ELECTROLYTES

6.1 Introduction

Artificial photosynthesis seeks to mimic the catalytic machinery of natural photosynthetic systems with inorganic materials capable of converting carbon dioxide (CO_2), water (H_2O), and sunlight into useful chemicals (e.g. ethanol, ethylene, etc.).[1-6] Unfortunately, the realization of such a process is currently hindered by catalytic challenges associated with selective conversion of CO_2 into desired products without the proliferation of unwanted side reactions.[1-6] The complexity of the reaction pathway, which involve multiple proton-coupled electron transfer steps, requires a process for preferentially activating specific chemical intermediates to reliably and selectively produce a single product of interest.[1-6] The ongoing search for selectivity has inspired numerous strategies to improve the preferential conversion of CO_2 into desired products, including nanostructuring of the electrocatalyst,[7-9] elemental alloying,[10,11] engineering of the exposed catalytic surface facets[12-15] and grain boundaries,[16-18] manipulating the local solution pH,[19-21] judicious choice of chemical additives to the electrolyte itself,[22,23] or the use of ionic liquids to limit the availability of protons.[24,25]

Despite numerous examples of improved catalyst selectivity via the aforementioned approaches, to date, the use of light as a tool for guiding the selectivity of CO_2 reduction has received considerably less attention.[26-33] Given that the most commonly used metals for electrocatalytic CO_2 reduction, namely Ag, Au, and Cu, all support surface plasmon excitations, nanostructured metal catalysts offer new opportunities for exploiting their unique optical properties to shape the selectivity of chemical reactions.[26,34-39] In particular, the plasmon-driven production of energetic "hot" carriers on metal nanostructures has shown great promise for photocatalysis,[34-39] but the prompt decay ($t \sim 1$ ps) of hot carriers into phonon modes of the metal nanocrystal requires a strategy for quickly separating hot electron-hole pairs on an ultrafast timescale.[38,39] To that end, numerous studies have established the benefits of forming an interfacial Schottky barrier between a plasmonic metal and a wide band gap n-type semiconductor (e.g. Au/TiO_2) for separating hot carriers across the metal-semiconductor heterojunction.[40-49] Providing a channel for collecting hot electrons within the conduction band of the n-type semiconductor support effectively limits recombination processes and extends the lifetime of the charge-separated state to allow photochemistry to proceed.[47-49] Yet to promote plasmon-driven CO_2 reduction directly on the metal surface requires quickly extracting hot holes from below the metal Fermi level with a wide band gap p-type semiconductor so that hot electrons can accumulate on the metal and initiate reactions with adsorbed molecules. The ability to quickly collect hot holes from metal nanostructures via charge transfer to the support also obviates the need for sacrificial reagents commonly used in plasmonic photocatalysis. Indeed, we have recently demonstrated the utility of interfacing plasmonic Au nanoparticles with p-type GaN to enable photoelectrochemical CO_2 reduction with plasmonic Au/p-GaN photocathodes.[28] Unfortunately, the limited number of p-type semiconductors suitable for such studies has hindered the development of plasmonic devices capable of harvesting hot holes from metal nanostructures for applications in photocatalysis or photodetection. Our ability to manipulate and control hot carriers is currently restricted by insufficient knowledge of plasmon-induced hot holes; to date, relatively few experimental studies have been reported.[28,50-58]

Here, we employ p-type nickel oxide (p-NiO) as a wide band gap semiconductor support to harvest hot holes from photoexcited Cu nanoparticles and enable photoelectrochemical CO_2 reduction with plasmonic Cu/p-NiO photocathodes (Figure 6.1a). Nickel oxide is commonly used as a hole transport material in a variety of photovoltaic and photoelectrochemical devices due to its excellent chemical stability, high optical transparency, and suitable p-type character.[59-64] Furthermore, because p-NiO films can be deposited by a variety of low-cost methods, p-NiO may offer a more scalable option than p-type GaN as a candidate wide band gap p-type semiconductor to facilitate charge separation. In plasmonic devices, p-NiO has previously been used to collect photogenerated hot holes from Au nanoparticles, where an Ohmic contact is reportedly formed at the Au/p-NiO interface.[65-67] As a support for Cu nanoparticles, the valence band position of p-NiO (ca. −5.4 eV vs. vacuum)[60,63] relative to the Cu Fermi level (ca. −4.5 eV vs. vacuum)[68] is anticipated to establish a modest Schottky barrier (Φ_B) at the Cu/p-NiO interface that facilitates charge separation by selectively collecting plasmon-induced hot holes from the metal (Figure 6.1b). The large band gap of p-NiO (~3.7 eV)[63,64] ensures that any visible light incident upon the Cu/p-NiO device is incapable of directly exciting charge carriers within the p-NiO film, and it therefore serves solely to collect hot holes from the Cu nanoparticles. Furthermore, the conduction band edge of p-NiO (ca. −1.7 eV vs. vacuum)[60] relative to the Cu Fermi level provides rectification across the Cu/p-NiO interface by presenting a sizable energy barrier (~ 3 eV) to hot electron transfer at the metal-semiconductor heterojunction (Figure 6.1b). This plasmonic Cu/p-NiO device structure thereby limits recombination processes by providing a pathway for hot hole collection within the underlying p-NiO film while allowing for the accumulation of hot electrons on the Cu nanoparticles to drive CO_2 reduction.

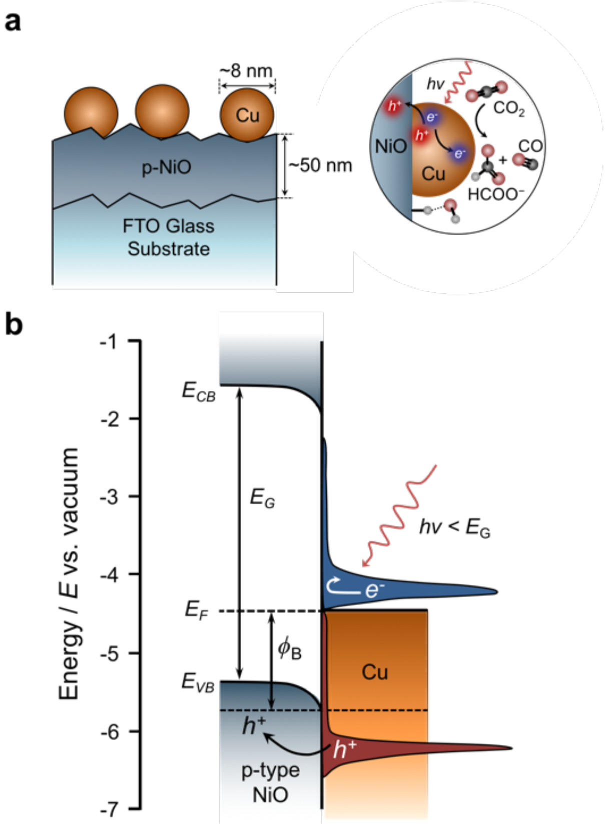

Figure 6.1: *Plasmonic Cu/p-NiO photocathode device structure. (a) Schematic of Cu/p-NiO photocathode on fluorine-doped tin oxide (FTO) glass showing the approximate dimensions of the Cu nanoparticles (~8 nm in diameter) and the p-NiO layer (~60 nm thick) on the FTO glass substrate. (b) Quantitative energy level diagram showing the relative positions of the p-NiO valence band (*E_{VB}*) and conduction band (*E_{CB}*) relative to the Cu Fermi level (*E_F*). The difference in energy between the p-NiO valence band and the Cu Fermi level is expected to allow the formation of an interfacial Schottky barrier (*Φ_B*) to hot hole injection at the Cu/p-NiO interface of around 1 eV. Photoexcitation of Cu nanoparticles with photon energy (hv) below the band gap (*E_G*) of the p-NiO support generates hot electrons and hot holes on the Cu surface. The p-NiO support facilitates charge separation across the metal-semiconductor interface by allowing the collection of hot holes from the metal while also confining the hot electrons on the Cu surface to drive *CO_2* reduction (inset).*

Photoelectrochemical studies of plasmonic Cu/p-NiO photocathodes confirm that visible-light excitation of Cu nanoparticles induces hot hole injection to the p-NiO valence band along with hot electron transfer to adsorbed molecules in the supporting electrolyte. The incidence of visible light was found to exert a significant influence over the selectivity of Cu nanoparticles for CO_2 reduction. Specifically, we observed that optical excitation of the Cu nanoparticles preferentially promoted the production of both carbon monoxide (CO) and formate ($HCOO^-$) while simultaneously limiting the evolution of hydrogen (H_2) in aqueous electrolytes. These results suggest that optical excitation of the metal alters the electrochemical reaction mechanism occurring on the Cu surface, with implications for the design of plasmonic photocatalysts that exhibit improved selectivity for CO_2 reduction. Overall, our studies demonstrate the utility of p-type semiconductors for the development of plasmonic photocathodes capable of artificial photosynthesis and open new possibilities for manipulating and controlling photochemistry at the nanoscale with plasmonic-metal nanostructures.

6.2 Fabrication and characterization of electrode

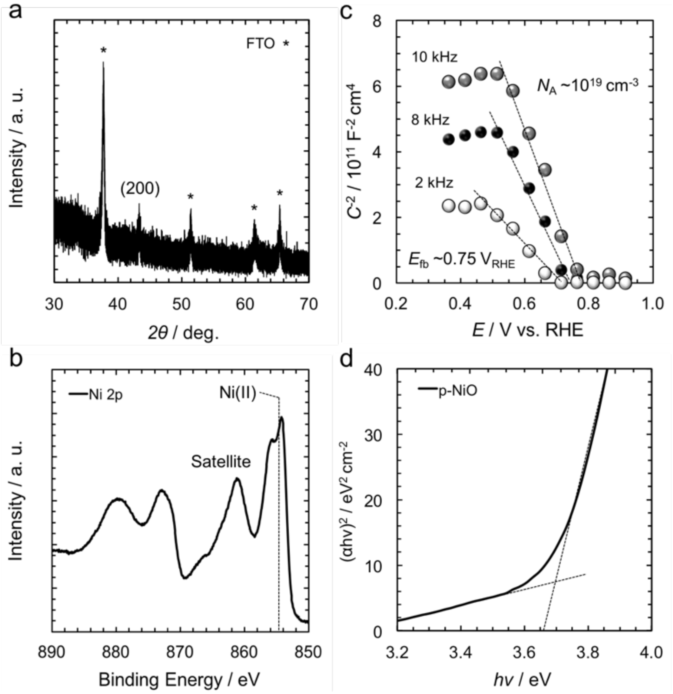

Figure 6.2: *Materials characterization of p-type NiO films. (a) X-ray diffraction pattern from NiO film on FTO glass showing the characteristic (200) peak of NiO. All other peaks can be attributed to the underlying FTO substrate. (b) X-ray photoelectron spectroscopy high-resolution scan of the Ni 2p region, showing the characteristic binding energies and satellite features of NiO. (c) Mott-Schottky plot obtained from NiO films on FTO glass substrate, which shows a negative slope indicative of p-type conductivity. From a linear fit of these data, the flat-band potential (E_{fb}) is estimated to be ca. 0.75 V_{RHE} (Volts vs. RHE) with an acceptor concentration of ca. 1×10^{19} cm^{-3}. (d) Tauc plot of the NiO film showing a band gap of around 3.7 eV. All these data indicate material properties consistent with previous literature reports of p-type NiO thin films.*

Plasmonic Cu/p-NiO photocathodes were constructed via electron beam physical vapor deposition. The p-type NiO (p-NiO) films were first synthesized on fluorine-doped tin oxide (FTO) glass substrates by depositing Ni metal at a rate of 0.25 Å s^{-1} under flowing O_2 gas at 6 sccm. After deposition of a 60 nm-thick NiO film on the FTO substrate, the film was annealed in ambient air at 300 °C for 1 h to ensure complete conversion to the desired p-NiO phase, (see Figure 6.2). Mott-Schottky analysis of the p-NiO film confirms that they exhibit p-type conductivity with a flat-band potential (E_{fb}) of around 0.75 V_{RHE} (V vs. RHE) and a carrier density of around 2 x 10^{19} cm^{-3} (Figure 6.2c). We note that these material properties of the as-synthesized p-NiO films are consistent with previous reports.[61,63] After the heat treatment, 3 nm of Cu was then deposited onto the p-NiO surface using electron-beam physical vapor deposition at a base pressure of ca. 1 x 10-7 torr and a deposition rate of 1.0 Å s^{-1}. No interfacial adhesion layer was used at the Cu/p-NiO heterojunction. Free from stabilizing surfactants required in colloidal nanoparticle synthesis, our approach ensures direct physical contact at the Cu/p-NiO interface while also exposing a clean Cu surface for catalysis. Scanning electron microscopy (SEM) imaging of the Cu/p-NiO device shows Cu nanoparticles distributed across the p-type NiO surface with a mean diameter d of 8 ± 2 nm (Figure 6.3a). Analysis of the Cu oxidation state by X-ray photoelectron spectroscopy (XPS) indicates that the as-deposited Cu nanoparticles likely oxidize to a mix of both Cu(I) and Cu(II) oxidation states[69] upon exposure to ambient air (Figure 6.3b). This interpretation is further supported by the optical properties of the Cu/p-NiO films, which appear dark grey in color and display a broad peak in the visible region spanning from around 600 nm to 800 nm (Figure 6.3c, yellow curve). This optical response is similar to that previously observed in CuO nanoparticles.[70,71] In contrast, the bare p-NiO films are nearly transparent across the visible spectrum (Figure 6.3c, blue curve) and exhibit a wide band gap E_G of around 3.7 eV (Figure 6.2d).

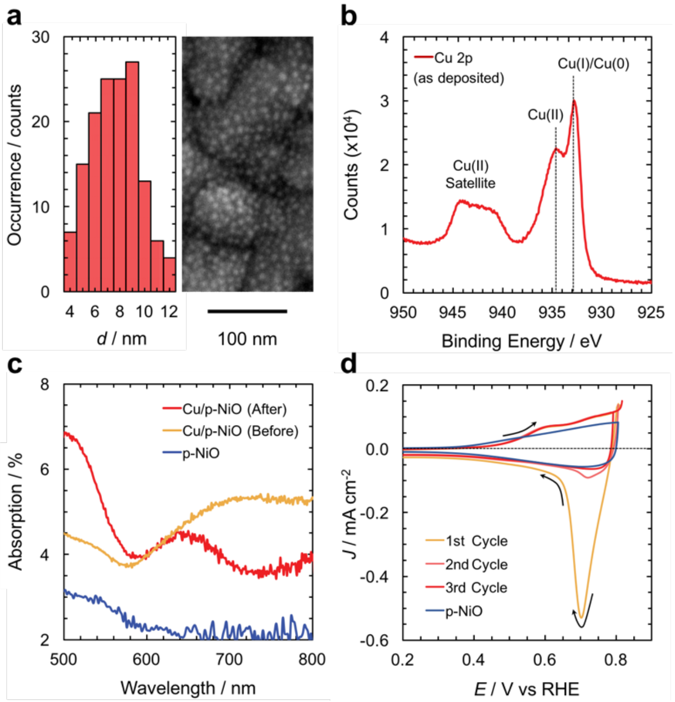

Figure 6.3: *Materials characterization of the plasmonic Cu/p-NiO photocathode. (a) SEM image with corresponding size-distribution histogram of Cu nanoparticles (mean diameter, d = 8 ± 2 nm) on a 60 nm thick p-NiO film supported on FTO glass. (b) X-ray photoelectron spectroscopy high-resolution scan of the Cu 2p region from as-synthesized Cu/p-NiO photocathodes. (c) Absorption spectra of the plasmonic Cu/p-NiO photocathode before (yellow curve) and after (red curve) electrochemical reduction via three successive cyclic voltammetry scans. The spectrum of the bare p-NiO film (blue curve) is also shown for comparison. (d) Cyclic voltammograms from plasmonic Cu/p-NiO photocathode (yellow to red curves) and bare p-NiO films (blue curve) at a scan rate of 50* $mV\ s^{-1}$*. Black arrows indicate the scan direction. The reduction of Cu oxides into metallic Cu is evidenced by the progressively smaller cathodic wave around 0.7* V_{RHE} *(yellow curve) that eventually disappears after the third successive scan (red curve). A representative voltammogram from bare p-NiO films (blue curve) is shown for reference.*

6.3 Photoelectrochemical studies

Photoelectrochemical studies were performed in a three-electrode configuration with the Cu/p-NiO photocathode as the working electrode, a platinum wire mesh counter electrode, and a saturated calomel electrode (SCE) as the reference electrode. The aqueous electrolyte (50 mM K_2CO_3) was sparged with CO_2 gas for 30 min prior to all electrochemical experiments, which were performed under a CO_2 blanket to prevent the ingress of atmospheric O_2 into the supporting electrolyte. All electrochemical potentials are reported with respect to the reversible hydrogen electrode (RHE). As shown in Figure 6.3d (yellow curve), cyclic voltammetry of the Cu/p-NiO device indicates that surface oxides formed on the Cu nanoparticles upon exposure to ambient air are successfully reduced into metallic $Cu^{(0)}$ at applied potentials more negative than 0.6 V_{RHE}. The absence of such features from bare p-NiO films (Figure 6.3d, blue curve) confirms that these cathodic and anodic waves are attributable to the redox features of the Cu nanoparticles. Subsequent cyclic voltammetry scans across the potential window from 0.8 V_{RHE} to 0.2 V_{RHE} indicate that any residual cupric/cuprous oxides are fully converted into metallic Cu, as evidenced by the progressively smaller reduction wave around 0.6 V_{RHE} that eventually disappears upon the third successive scan (Figure 6.2d, red curve). This electrochemical observation is consistent with recent *in operando* spectroscopic evidence of the electrocatalytically active phase of Cu-based cathodes.[72] We also note that a change in the optical absorption was observed for these Cu/p-NiO films immediately after cyclic voltammetry was performed. The freshly cycled Cu/p-NiO photocathodes exhibit a new spectral feature located around 630 nm that we attribute to the surface plasmon resonance of metallic Cu nanoparticles (Figure 6.3c, red curve). Collectively, these results strongly suggest that the oxide formed on the Cu nanoparticles upon exposure to ambient air is successfully reduced back into the metallic state under CO_2 reduction conditions.

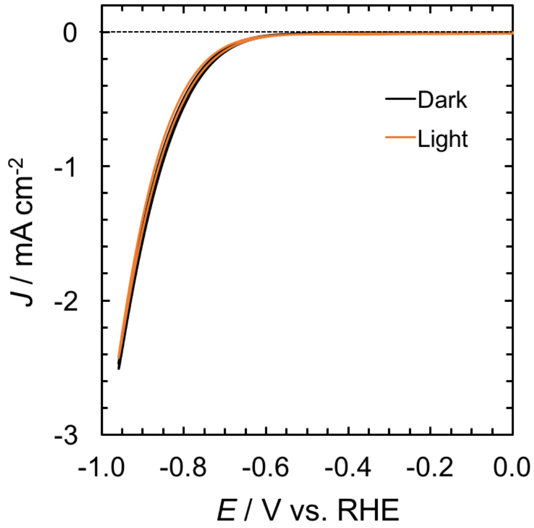

***Figure 6.4:** Cyclic voltammetry of bare p-NiO cathodes under dark (black curve) and visible light (orange curve) showing that bare p-NiO film exhibits no measurable light response across the potential sweep. This observation is consistent with the large band gap of p-NiO. Therefore, all visible-light responses observed from plasmonic Cu/p-NiO photocathodes can be unambiguously assigned to hot-hole injection from Cu to the valence band of p-NiO upon optical excitation of the Cu nanoparticles.*

The current-potential (*J*-*E*) behavior of the plasmonic Cu/p-NiO photocathode was assessed via linear sweep voltammetry at a scan rate of 20 mV s^{-1} under both dark conditions and visible-light excitation (λ = 560 ± 40 nm FWHM) with a high-power LED (I_0 = 160 mW cm^{-2}). As shown in Figure 6.5a (dotted black curve), the Cu/p-NiO device displayed a cathodic current (*J*) along the potential (*E*) sweep from 0 V_{RHE} to −1.0 V_{RHE}. The incidence of visible light (Figure 6.5a, solid red curve) imparts increased cathodic photocurrent (J_{ph}) relative to that observed in the dark and reduces the potential required for the onset of the Faradaic current from around −0.4 V_{RHE} in the dark to around −0.3 V_{RHE} in the light (see inset of Figure 6.5a). For comparison, the bare p-NiO photocathode exhibits no change in current density under visible-light excitation (Figure 6.4). Chronoamperometry *J*(*t*) experiments demonstrate that the plasmonic Cu/p-NiO device exhibits a prompt and reproducible cathodic photocurrent J_{ph} under periodic, visible-light illumination (λ = 560 ± 40 nm) while held potentiostatically at −0.2 V_{RHE} (Figure 6.5b, red curve). For comparison, no visible light response was observed from bare p-NiO supports under otherwise identical experimental conditions (Figure 6.5b, blue curve). The plasmonic Cu/p-NiO photocathode displays a linear J_{ph} response with respect to the incident light power and reaches a maximum J_{ph} of around 5 μA cm^{-2} (Figure 6.5c). Chronopotentiometry $V_{oc}(t)$ experiments were then performed to examine plasmon-driven charge separation across the metal-semiconductor heterojunction.[28] Hot hole injection from photo-excited Cu nanoparticles into the p-NiO film under open-circuit conditions leads to the accumulation of holes within the valence band of p-NiO, causing a shift in the V_{oc} of the Cu/p-NiO photocathode to more positive potentials relative to the equilibrium V_{oc} observed under dark conditions. Therefore, plasmon-induced hot hole transfer across the metal-semiconductor heterojunction can be observed by monitoring the influence of light on the V_{oc} of the device. Indeed, the plasmonic Cu/p-NiO device exhibits an increase in V_{oc} upon exposure to visible-light irradiation and eventually establishes a plasmonic photovoltage V_{ph} ($V_{ph} = V_{oc,light} - V_{oc,dark}$) of around 15 mV (Figure 6.5d, red curve). No V_{ph} response was observed from bare p-NiO films (Figure 6.5d, blue curve). Taken together, these data are consistent with plasmon-induced hot hole injection into the p-NiO valence band along with photoelectrochemical reduction of molecular species in the supporting electrolyte.

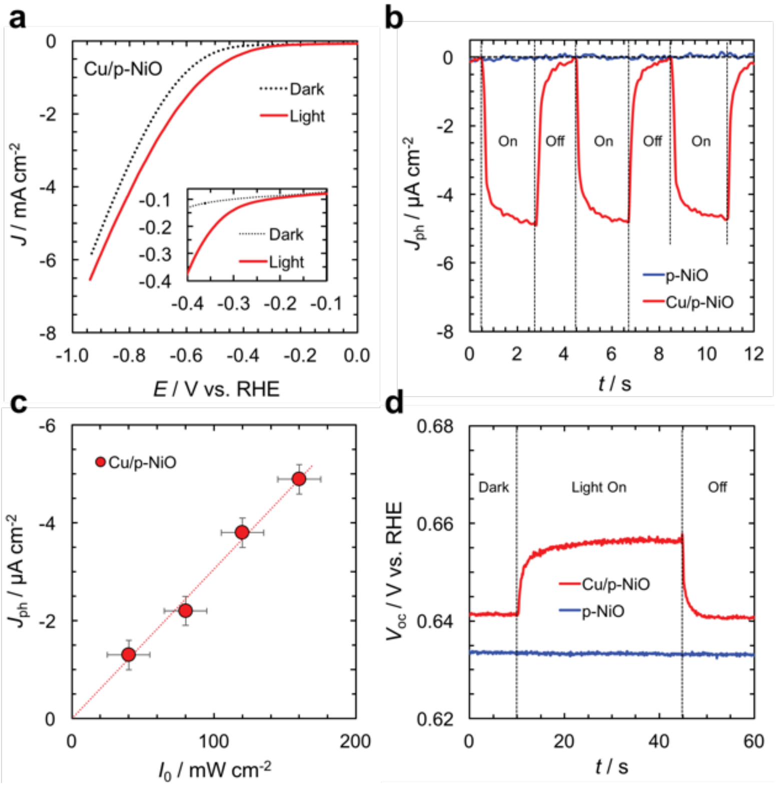

Figure 6.5: *Photoelectrochemical characterization of plasmonic Cu/p-NiO photocathodes. (a) Linear sweep voltammetry J(E) of plasmonic Cu/p-NiO photocathode at a scan rate of 20 mV* s^{-1} *under dark conditions (dotted black curve) and under visible-light irradiation* ($\lambda = 560 \pm 40$ *nm) (solid red curve). (b) Chronoamperometry J(t) of the photocurrent* ($J_{ph} = J_{light} - J_{dark}$) *obtained from plasmonic Cu/p-NiO (red) and bare p-NiO (blue) photocathodes under periodic, visible-light irradiation* ($\lambda = 560 \pm 40$ *nm) while potentiostatically poised at an applied potential of* $E = -0.2$ V_{RHE}*. (c) Power-dependence of the photocurrent* $J_{ph}(I_0)$ *obtained from the plasmonic Cu/p-NiO photocathode. (d) Chronopotentiometry V(t) of the open-circuit voltage* (V_{oc}) *obtained from the plasmonic Cu/p-NiO photocathode (red curve) and the bare p-NiO cathode (blue curve) under visible-light irradiation* ($\lambda = 560 \pm 40$ *nm).*

The influence of plasmon excitation on the selectivity of plasmonic Cu/p-NiO photocathodes for the CO_2 reduction reaction (CO_2RR) was then studied in a two-compartment compression cell specifically designed to enable photoelectrochemical operation.[73] The CO_2 reduction reaction (CO_2RR) was conducted in a three-electrode configuration with Cu/p-NiO or bare p-NiO cathode as the working electrode, Pt wire gauze as the counter electrode, and a saturated calomel electrode (SCE) as the reference electrode. All photoelectrochemical experiments were conducted within a custom-built, airtight cell equipped with a quartz window. The photoelectrochemical experiments were performed in K_2CO_3 electrolyte (pH 7) that was fully saturated with CO_2 by vigorous bubbling of the cathode and anode compartments for 1 h before commencing with the experiment. We note that photoelectrochemical collection of hot holes from the Cu nanoparticles via the underlying p-NiO film obviates the need for sacrificial reagents commonly used in plasmonic photocatalysis. The photocathode was potentiostatically poised at a given potential from −0.7 V_{RHE} to −0.9 V_{RHE} for 2 h to collect multiple data points. The potential window available for plasmon-driven CO_2 reduction studies is restricted by the limited stability of the oxide support during electrochemical operation at applied potentials more negative than −0.9 V_{RHE}. Visible-light irradiation ($\lambda = 560 \pm 40$ nm FWHM) with a high-power LED was incident on the sample through the quartz window at an incident power of $I_0 = 160$ mW cm^{-2} (measured at the quartz window). The photo(electro)catalysis experiments were performed under continuous flow conditions in a flow-cell device with periodic sampling of the reactor headspace every 15 min over the course of the 2 h reaction with a gas chromatograph. The gas chromatograph (SRI-8610) was equipped with a Hayesep D column and a Molsieve 5A column using N_2 as carrier gas. The gaseous products were detected using a thermal conductivity detector (TCD) and flame ionization detector (FID) equipped with a methanizer. Quantitative analysis of gaseous products was based on calibration with several gas standards over many orders of magnitude in concentration. Liquid products were collected from the cathode and anode compartments at the end of the 2 h electrolysis experiment and analyzed by high-pressure liquid chromatography (Thermo Fischer Dionex UltiMate 3000). All catalytic experiments at a given potential were repeated in triplicate.

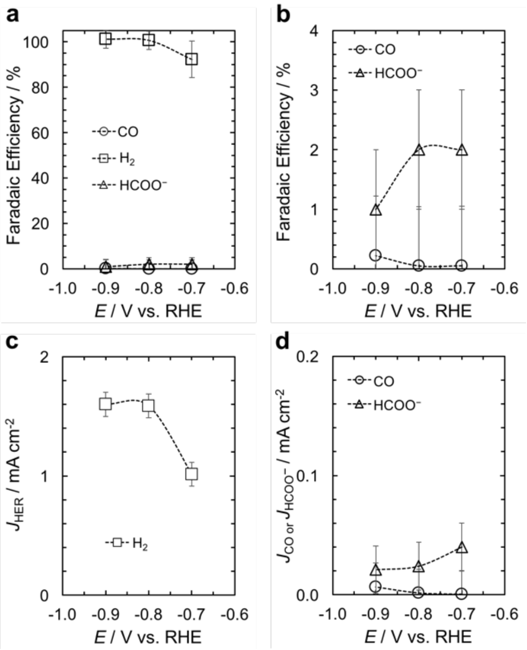

Figure 6.6: *CO_2 reduction with bare p-NiO cathodes under dark conditions. (a-b) Faradaic efficiency for H_2 (squares), CO (circles), and $HCOO^-$ (triangles) with (c-d) corresponding partial current density J for the hydrogen evolution reaction (J_{HER}, squares),*

carbon monoxide (J_{CO}, circles), and formate (J_{HCOO^-}, triangles). Electrolysis was performed under dark conditions in a CO_2-saturated 50 mM K_2CO_3 electrolyte. The device was held potentiostatically at each applied potential for 2 h while the gas products were sampled every 15 min and analyzed by gas chromatography. Liquid products were collected and analyzed by HPLC at the end of each run. Each data point represents the average of three independent trials and the error bar indicates the standard deviation.

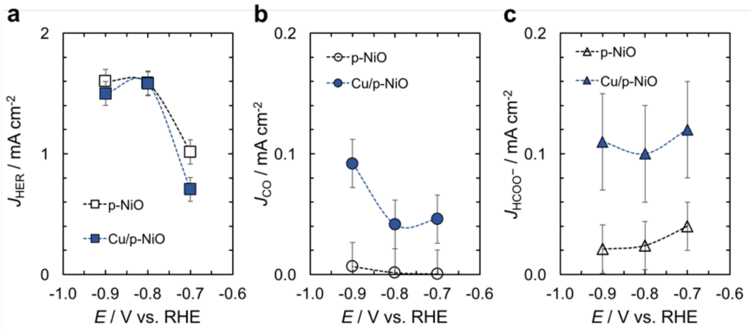

Figure 6.7: *Comparison of the partial current densities (J) obtained from bare p-NiO (open data points) and Cu/p-NiO cathodes (filled data points) under dark conditions. (a) Partial current density for the hydrogen evolution reaction (J_{HER}) from p-NiO (open squares) relative to Cu/p-NiO (filled squares). (b) Partial current density for carbon monoxide (J_{CO}) from p-NiO (open circles) relative to Cu/p-NiO (filled circles). (c) Partial current density for formate (J_{HCOO^-}) from p-NiO (open triangles) relative to Cu/p-NiO (filled triangles). Each data point represents the average of three independent trials and the error bar indicates the standard deviation. We observed a significant increase in the partial current densities for CO_2 reduction products CO and $HCOO^-$ with the addition of Cu nanoparticles, while almost no change in the amount of H_2 that was evolved. We therefore attribute the significant amount of H_2 that is evolved from the plasmonic Cu/p-NiO device to the activity of the underlying p-NiO film, which almost exclusively produces H_2 under CO_2 reduction conditions.*

As shown in Figure 6.8, the observed product distributions obtained under dark electrocatalysis are dependent on the applied electrochemical potential (E). The reported Faradaic efficiency for each chemical product represents the average value obtained from three independent trials and the error bars indicate the standard deviation. At an applied potential of $E = -0.7$ V_{RHE}, the Cu/p-NiO photocathode evolves primarily hydrogen (H_2) along with carbon monoxide (CO) and formate ($HCOO^-$) as minor products. At more negative applied potentials ($E = -0.9$ V_{RHE}), CO and $HCOO^-$ begin to comprise a more significant fraction of the total Faradaic efficiency (~40%) under dark conditions (Figure 6.8b-c). We emphasize that our cyclic voltammetry results (Figure 6.5d), together with the observed changes in the optical properties of the device (Figure 6.5c), indicate that the oxidation state of the Cu nanoparticles under these applied potentials is metallic $Cu^{(0)}$. This conclusion is also supported by recent *in operando* spectroscopic evidence.[72] Although a significant fraction of the products evolved from the Cu/p-NiO device consist of H_2 under dark conditions (Figure 6.8a, blue points), this product is largely attributable to the activity of the underlying p-NiO film that remains exposed to the electrolyte. Indeed, the bare p-NiO substrate produces almost exclusively H_2 with ~98% Faradaic efficiency across the entire potential window from −0.7 V_{RHE} to −0.9 V_{RHE} (Figure 6.6). The product distribution observed for the bare p-NiO control sample under CO_2RR conditions is consistent with a prior study of NiO-based cathodes.[62] We therefore assign nearly all CO_2RR products observed from the plasmonic Cu/p-NiO photocathodes to the catalytic activity of the Cu nanoparticles (Figure 6.7).

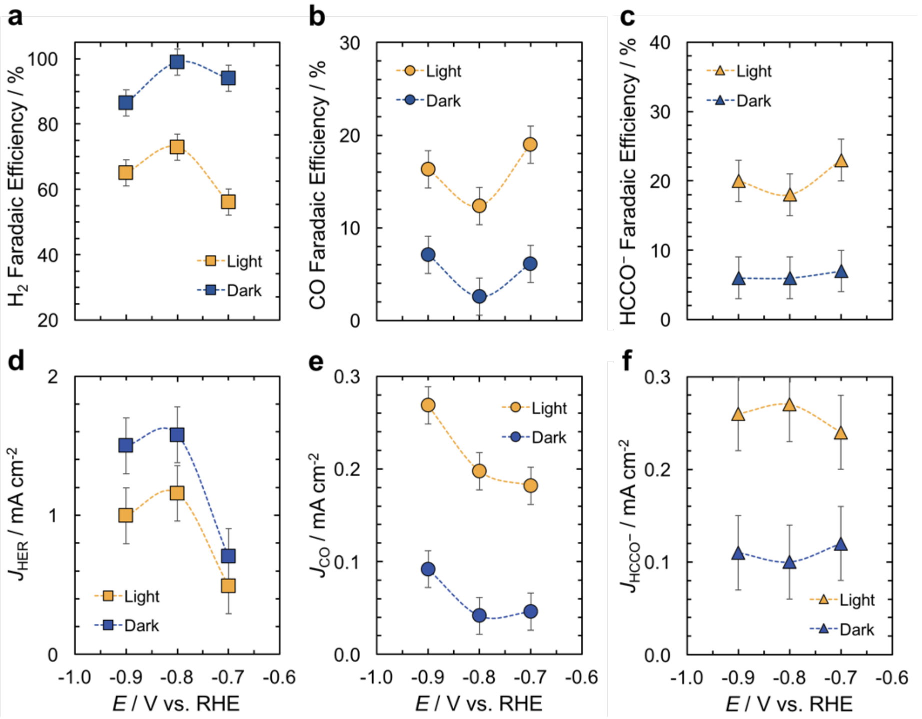

Figure 6.8: *Distribution of CO_2 reduction products obtained from plasmonic Cu/p-NiO photocathodes as a function of the applied electrochemical potential (E). Faradaic efficiency (a–c) and associated partial current density (d–f) for the production of (a,d) hydrogen (H_2) (squares), (b,e) carbon monoxide (CO) (circles), and (c,f) formate ($HCOO^-$) (triangles) during controlled potential electrolysis under dark conditions (blue symbols) and under visible-light irradiation (yellow symbols). Plasmon excitation was performed with λ = 560 ± 40 nm at an incident power of 160 mW cm^{-2}. Data points and error bars represent the average value and standard deviation, respectively, obtained from three independent trials.*

As shown in Figure 6.8, optical excitation of the plasmonic Cu/p-NiO photocathodes with 565 ± 40 nm light from a high-power LED (I_0 = 160 mW cm^{-2}) induces a marked change in the distribution of chemical products compared to that observed during dark electrocatalysis. Specifically, we observed a reduction in the Faradaic efficiency for H_2 evolution (Figure 6.8a, squares) concomitantly with an increase in the Faradaic efficiency for both carbon monoxide (Figure 6.8b, circles) and formate (Figure 6.8c, triangles) at all applied potentials. The biggest change in selectively was observed at -0.7 V_{RHE}, where the Faradaic efficiency for H_2 falls from nearly 94% in the dark to around 58% in the light (Figure 6.8a). This substantial reduction in HER activity was accompanied by a sizable improvement in the selectivity for CO_2 reduction: the Faradaic efficiency for both CO and $HCOO^-$ increased by three times relative to that observed in the dark and begin to account for nearly 50% of the total Faradaic efficiency from the device. The partial current densities associated with the H_2 evolution reaction (J_{HER}), the production of CO (J_{CO}), and the production of formate (J_{HCOO^-}) are shown in Figure 6.8d-f, respectively. At an applied potential of $E = -0.7$ V_{RHE}, we observed little change in J_{HER} between dark and light conditions (Figure 6.8d), but a notable increase in both J_{CO} and J_{HCOO^-} was observed (Figure 6.8e-f). As we moved to more negative applied potentials, the proportion of J_{CO} and J_{HCOO^-} continued to increase along with a sizable reduction in J_{HER} relative to that observed during dark electrocatalysis. At the most negative potential studied ($E = -0.9$ V_{RHE}), the J_{HER} was reduced by nearly 33% from around 1.5 mA cm^{-2} in the dark to around 1 mA cm^{-2} in the light, while both J_{CO} and J_{HCOO^-} are nearly three times greater than they were in the dark. Overall, these results indicate that optical excitation of the Cu nanoparticles increases their selectivity for the CO_2RR relative to the HER at all applied potentials. We exclude the possibility that such changes in CO_2RR selectivity arise solely due to plasmonic heating of the electrocatalytic surface, as it has previously been shown that increased electrolyte temperatures promote H_2 evolution while reducing the selectivity for CO_2 reduction.[73] Such heating-induced trends in electrocatalytic selectivity are clearly opposite to those observed here. We note that these results are interesting in light of previous observations of plasmon-enhanced selectivity involving gas-phase photocatalysis conducted at elevated temperatures, in which the conversion of CO_2 and H_2 to carbon monoxide (CO) or methane (CH_4) was enhanced with optical excitation of the plasmonic photocatalyst.[29,33]

6.4 Discussion of mechanisms

There are several possible mechanisms by which plasmon excitation of Cu nanoparticles may alter the distribution of CO_2 reduction products obtained from the plasmonic Cu/p-NiO photocathode. Here, we consider three distinct plasmon-induced processes that could account for our observed photoelectrochemical results. Photo-induced hot hole injection into the p-NiO valence band leads to increased electron density on the Cu nanoparticles, which could potentially influence the reaction mechanism in a variety of ways. Hot electrons may be selectively injected into available molecular orbitals of adsorbed species at the metal-electrolyte interface. If such a process were to occur preferentially on adsorbed CO_2, hot electrons would selectively activate CO_2 to aid in formation of the CO_2^- species on the Cu surface. The generation of hot electrons on the Cu nanoparticles via plasmon excitation may therefore help initiate the catalytic cascade on the Cu surface by activating adsorbed CO_2 molecules.

Alternatively, it is conceivable that plasmon excitation of the Cu nanoparticles serves to reduce the evolution of H_2 from the Cu surface through a process known as desorption induced by electronic transitions (DIET).[36,37] In this mechanism, preferential hot-electron transfer to adsorbed H_2 or H_2-evolving species (i.e. protons, hydroxide ions, water) may destabilize surface bound molecules by populating anti-bonding orbitals of the adsorbate and causing the molecule to dissociate on the Cu surface. Indeed, it has previously been reported that plasmon-induced hot electrons can initiate photo-dissociation of H_2 molecules.[74-76] As an additional consequence of molecular H_2 dissociation, surface-bound hydrogen atoms would be available to protonate nearby CO_2^- molecules and facilitate CO_2 reduction. Such a process may be responsible for the suppression of H_2 observed upon optical excitation of the plasmonic Cu/p-NiO photocathode.

Finally, it is possible that plasmon-induced hot hole injection to the p-NiO support modifies the molecular interactions with the Cu surface by altering the electronic structure of the Cu nanoparticles. It is well known that the electronic structure of the metal *d*-bands plays the dominant mechanism in determining molecular adsorption at a metal surface.[77,78] Although a distribution of hot holes spanning the *sp*-band down to the *d*-bands are created within the Cu nanoparticles upon visble-light excitation, direct transitions (*d*-band to *sp*-band) are the dominate mechanism for hot-hole generation when irradiated above the interband threshold of Cu (~1.6 – 1.8 eV).[79,80] Thus, optical excitation of the Cu nanoparticles with 560 nm light ($h\nu$ = 2.2 eV) preferentially excites hot holes within the metal *d*-bands[77,78] that can then transfer to the underlying p-NiO film. Injection of hot holes into the p-NiO valence band thereby alters the occupation of states below the Cu Fermi level, which could thereby modify the molecular surface interactions by tuning the extent of hybridization between the metal *d*-bands and the frontier orbitals of the adsorbate. This change in electronic structure of the metal via plasmon-induced hot hole transfer to the p-NiO support offers an alternative pathway towards shaping the selectivity of Cu nanoparticles.

Although the production of hydrogen (H_2), carbon monoxide (CO), and formate ($HCOO^-$) are all thought to involve two proton-coupled electron-transfer steps, these three products originate from different reactive intermediates formed on the Cu surface under reaction conditions.[1,3] It therefore seems unlikely that hot electron transfer is occurring preferentially to a short-lived CO_2RR intermediate formed on the Cu surface *in operando*, since the Faradaic efficiencies for both CO and $HCOO^-$ were observed to increase with light excitation. Instead, we suspect that plasmon-induced hot electrons on the Cu nanoparticles likely play a key role in improving the selectivity for the CO_2RR by preferentially activating CO_2 to form the CO_2^- anion. Furthermore, if a fraction of the electrochemically-derived H_2 molecules were photo-dissociated on the Cu surface by hot electrons via DIET, the surface-bound hydrogen atoms would be readily available for protonation of activated CO_2^- molecules. We also hypothesize that the injection of hot holes into the p-NiO film changes the intrinsic binding affinity of the metal surface for reactant molecules by altering the *d*-band structure of the Cu nanoparticles. In tandem, these processes could synergistically shape the selectivity of the plasmonic Cu/p-NiO photocathode in favor of the CO_2RR relative to the HER. As several reduction reactions are occurring simultaneously on the plasmonic photocathode, and both the Cu nanoparticles and the underlying p-NiO film are exposed to the electrolyte, advanced *in operando* spectroscopic studies are needed to conclusively distinguish between these possible reaction mechanisms. At present, it remains unclear if plasmon-induced hot electrons are transferred directly to adsorbed molecules on timescales commensurate with electron-electron scattering processes ($t \sim$ 10–100 fs) or if charge transfer occurs after establishing an excited-state Fermi-Dirac distribution at an elevated electronic temperature ($t >$ 1 ps). Nevertheless, these initial photoelectrochemical observations indicate that optical excitation of the Cu nanoparticles alters the selectivity of CO_2 reduction relative to traditional electrochemical reduction performed under dark conditions.

6.5 Conclusion

In summary, we have demonstrated the benefits of using p-type NiO as a wide band gap support for harvesting hot holes from Cu nanoparticles to allow the accumulation of hot electrons on the metal surface and drive CO_2 reduction with plasmonic Cu/p-NiO photocathodes. The collection of hot holes from the Cu nanoparticles via injection to the p-NiO support also removes the requirements for sacrificial reagents commonly employed in plasmon-induced photochemical reactions. The Cu-wide band gap p-type semiconductor Schottky junction design therefore represents a path forward for the realization of plasmon-driven photocathodes capable of harnessing surface plasmon excitations to steer the selectivity of Cu surfaces for photoelectrochemical CO_2 reduction in aqueous media. We observed that plasmon excitation of the Cu nanoparticles modulates the chemical selectivity for CO_2 reduction products, increasing CO evolution and $HCOO^-$ production while simultaneously suppressing H_2 evolution. Several possible reaction mechanisms are proposed to account for the observed influence of light on the selectivity of photoelectrochemical CO_2 reduction. Although a conclusive assignment of the reaction mechanism requires *in operando* spectroscopy to observe the molecular details of the reaction occurring on the plasmonic photocathode, we speculate that plasmon-induced hot electrons likely play a key role in altering the selectivity of the reaction. Overall, our photoelectrochemical results illustrate a promising strategy towards optically manipulating the catalytic selectivity of Cu surfaces for CO_2 conversion.

BIBLIOGRAPHY CHAPTER 6

1. Montoya, J. H.; Seitz, L. C.; Chakthranont, P.; Vojvodic, A.; Jaramillo, T. F.; Nørskov, J. K. Materials for Solar Fuels and Chemicals. *Nat. Mater.* **2017**, 16, 70−81.
2. Nitopi, S.; Bertheussen, E.; Scott, S. B.; Liu, X.; Engstfeld, A. K.; Horch, S.; Seger, B.; Stephens, I. E. L.; Chan, K.; Hahn, C.; Nørskov, J. K.; Jaramillo, T. F.; Chorkendorff, I. Progress and Perspectives of Electrochemical CO_2 Reduction on Copper in Aqueous Electrolyte. *Chem. Rev.* **2019**, 119, 7610−7672.
3. Birdja,Y.Y.;Peŕez-Gallent,E.;Figueiredo,M.C.;Go̎ttle,A.J.; Calle-Vallejo, F.; Koper, M. T. M. Advances and Challenges in Understanding the Electrocatalytic Conversion of Carbon Dioxide to Fuels. *Nat. Energy* **2019**, 4, 732−745.
4. Todorova, T. K.; Schreiber, M. W.; Fontecave, M. Mechanistic Understanding of CO_2 Reduction Reaction (CO2RR) Toward Multicarbon Products by Heterogeneous Copper-Based Catalysts. *ACS Catal.* **2020**, 10, 1754−1768.
5. Xu, S.; Carter, E. A. Theoretical Insights into Heterogeneous (Photo)electrochemical CO_2 Reduction. *Chem. Rev.* **2019**, 119, 6631−6669.
6. White, J. L.; Baruch, M. F.; Pander, J. E., III; Hu, Y.; Fortmeyer, I. C.; Park, J. E.; Zhang, T.; Liao, K.; Gu, J.; Yan, Y.; Shaw, T. W.; Ebelev, E.; Bocarsly, A. B. Light-Driven Heterogeneous Reduction of Carbon Dioxide: Photocatalysts and Photoelectrodes. *Chem. Rev.* **2015**, 115, 12888−12935.
7. Liu, M.; Pang, Y.; Zhang, B.; De Luna, P.; Voznyy, O.; Xu, J.; Zheng, X.; Dinh, C.-T.; Fan, F.; Cao, C.; García de Arquer, F. P.; Safaei, T. S.; Mepham, A.; Klinkova, A.; Kumacheva, E.; Filleter, T.; Sinton, D.; Kelley, S. O.; Sargent, E. H. Enhanced Electrocatalytic CO_2 Reduction via Field-Induced Reagent Concentration. *Nature* **2016**, 537, 382−386.
8. Saberi Safaei, T.; Mepham, A.; Zheng, X.; Pang, Y.; Dinh, C.-T.; Liu, M.; Sinton, D.; Kelley, S. O.; Sargent, E. H. High-Density Nanosharp Microstructures Enable Efficient CO_2 Electroreduction. *Nano Lett.* **2016**, 16, 7224−7228.
9. De Luna, P.; Quintero-Bermudez, R.; Dinh, C.-T.; Ross, M. B.; Bushuyev, O. S.; Todorovic, P.; Regier, T.; Kelly, S. O.; Yang, P.; Sargent, E. H. Catalyst Electro-Redeposition Controls Morphology and Oxidation State for Selective Carbon Dioxide Reduction. *Nat. Catal.* **2018**, 1, 103−110.
10. Kim, D.; Resasco, J.; Yu, Y.; Asiri, A. M.; Yang, P. Synergistic Geometric and Electronic Effects for Electrochemical Reduction of Carbon Dioxide Using Gold-Copper Bimetallic Nanoparticles. *Nat. Commun.* **2014**, 5, 4948.
11. Kim, D.; Xie, C.; Becknell, N.; Yu, Y.; Karamad, M.; Chan, K.; Crumin, E. J.; Nørskov, J. K.; Yang, P. Electrochemical Activation of CO_2 through Atomic Ordering Transformations of AuCu Nano-particles. *J. Am. Chem. Soc.* **2017**, 139, 8329−8336.
12. Hahn, C.; Hatsukade, T.; Kim, Y.-G.; Vailionis, A.; Baricuatro, J. H.; Higgins, D. C.; Nitopi, S. A.; Soriaga, M. P.; Jaramillo, T. F. Engineering Cu Surfaces for the Electrocatalytic Conversion of CO_2: Controlling Selectivity Toward Oxygenates and Hydrocarbons. *Proc. Natl. Acad. Sci. U. S. A.* **2017**, 114, 5918−5923.
13. Lu, Q.; Rosen, J.; Zhou, Y.; Hutchings, G. S.; Kimmel, Y. C.; Chen, J. G.; Jiao, F. A Selective and Efficient Electrocatalyst for Carbon Dioxide Reduction. *Nat. Commun.* **2014**, 5, 3242.
14. Zhu, W.; Zhang, Y.-J.; Zhang, H.; Lv, H.; Li, Q.; Michalsky, R.; Peterson, A. A.; Sun, S. Active and Selective Conversion of CO_2 to CO on Ultrathin Au Nanowires. *J. Am. Chem. Soc.* **2014**, 136, 16132−16135.

15. Zhu, W.; Michalsky, R.; Metin, Ö.; Lv, H.; Guo, S.; Wright, C. J.; Sun, X.; Peterson, A. A.; Sun, S. Monodisperse Au Nanoparticles for Selective Electrocatalytic Reduction of CO_2 to CO. *J. Am. Chem. Soc.* **2013**, 135, 16833−16836.
16. Mariano, R. G.; McKelvey, K.; White, H. S.; Kanan, M. W. Selective Increase in CO_2 Electroreduction Activity at Grain- Boundary Surface Terminations. *Science* **2017**, 358, 1187−1192.
17. Feng, X.; Jiang, K.; Fan, S.; Kanan, M. W. A Direct Grain- Boundary-Activity Correlation for CO Electroreduction on Cu Nanoparticles. *ACS Cent. Sci.* **2016**, 2, 169−174.
18. Feng, X.; Jiang, K.; Fan, S.; Kanan, M. W. Grain-Boundary- Dependent CO_2 Electroreduction Activity. *J. Am. Chem. Soc.* **2015**, 137, 4606−4609.
19. Hall, A. S.; Yoon, Y.; Wuttig, A.; Surendranath, Y. Mesostructure-Induced Selectivity in CO_2 Reduction Catalysis. *J. Am. Chem. Soc.* **2015**, 137, 14834−14837.
20. Yoon, Y.; Hall, A. S.; Surendranath, Y. Tuning of Silver Catalyst Mesostructure Promotes Selective Carbon Dioxide Conversion into Fuels. *Angew. Chem., Int. Ed.* **2016**, 55, 15282−15286.
21. Welch, A. J.; DuChene, J. S.; Tagliabue, G.; Davoyan, A.; Cheng, W.-H.; Atwater, H. A. Nanoporous Gold as a Highly Selective and Active Carbon Dioxide Reduction Catalyst. *ACS Appl. Energy Lett.* **2019**, 2, 164−170.
22. Cao, Z.; Kim, D.; Hong, D.; Yu, Y.; Xu, J.; Lin, S.; Wen, X.; Nichols, E. M.; Jeong, K.; Reimer, J. A.; Yang, P.; Chang, C. J. A Molecular Surface Functionalization Approach to Tuning Nano- particle Electrocatalysts for Carbon Dioxide Reduction. *J. Am. Chem. Soc.* **2016**, 138, 8120−8125.
23. Han, Z.; Kortlever, R.; Chen, H.-Y.; Peters, J. C.; Agapie, T. CO_2 Reduction Selective for $C_{\geq 2}$ Products on Polycrystalline Copper with N-Substituted Pyridinium Additives. ACS Cent. Sci. **2017**, 3, 853−859.
24. Rosen, B. A.; Salehi-Khojin, A.; Thorson, M. R.; Zhu, W.; Whipple, D. T.; Kenis, P. J. A.; Masel, R. I. Ionic Liquid-Mediated Selective Conversion of CO_2 to CO at Low Overpotentials. *Science* **2011**, 334, 643−644.
25. Asadi, M.; Ki, K.; Liu, C.; Addepalli, A. V.; Abbasi, P.; Yasaei, P.; Phillips, P.; Behranginia, A.; Cerrato, J. M.; Haasch, R.; Zapol, P.; Kumar, B.; Klie, R. F.; Abiade, J.; Curtiss, L. A.; Salehi-Khojin, A. Nanostructured Transition Metal Dichalcogenide Electrocatalysts for CO_2 Reduction in Ionic Liquid. *Science* **2016**, 353, 467−470.
26. Yu, S.; Wilson, A. J.; Kumari, G.; Zhang, X.; Jain, P. K. Opportunities and Challenges of Solar-Energy-Driven Carbon Dioxide to Fuel Conversion with Plasmonic Catalysts. *ACS Energy Lett.* **2017**, 2, 2058−2070.
27. Creel, E. B.; Corson, E. R.; Eichhorn, J.; Kostecki, R.; Urban, J. J.; McCloskey, B. D. Directing Selectivity of Electrochemical Carbon Dioxide Reduction Using Plasmonics. *ACS Energy Lett.* **2019**, 4, 1098−1105.
28. DuChene, J. S.; Tagliabue, G.; Welch, A. J.; Cheng, W.-H.; Atwater, H. A. Hot Hole Collection and Photoelectrochemical CO_2 Reduction with Plasmonic Au/p-GaN Photocathodes. *Nano Lett.* **2018**, 18, 2545−2550.
29. Zhang, X.; Li, X.; Zhang, D.; Su, N. Q.; Yang, W.; Everitt, H. O.; Liu, J. Product Selectivity in Plasmonic Photocatalysis for Carbon Dioxide Hydrogenation. *Nat. Commun.* **2017**, 8, 14542.
30. Yu, S.; Jain, P. K. Plasmonic Photosynthesis of C_1-C_3 Hydrocarbons from Carbon Dioxide Assisted by an Ionic Liquid. *Nat. Commun.* **2019**, 10, 2022.
31. Yu, S.; Wilson, A. J.; Heo, J.; Jain, P. K. Plasmonic Control of Multi-Electron Transfer and C-C Coupling in Visible-Light-Driven CO_2 Reduction on Au Nanoparticles. *Nano Lett.* **2018**, 18, 2189−2194.
32. Yu, S.; Jain, P. K. Selective Branching of Plasmonic Photosynthesis into Hydrocarbon Production and Hydrogen Generation. *ACS Energy Lett.* **2019**, 4, 2295−2300.

33. Robatjazi, H.; Zhao, H.; Swearer, D. F.; Hogan, N. J.; Zhou, L.; Alabastri, A.; McClain, M. J.; Nordlander, P.; Halas, N. J. Plasmon- Induced Selective Carbon Dioxide Conversion on Earth-Abundant Aluminum-Cuprous Oxide Antenna-Reactor Nanoparticles. *Nat. Commun.* **2017**, 8, 27.
34. Linic, S.; Christopher, P.; Ingram, D. B. Plasmonic-Metal Nanostructures for Efficient Conversion of Solar to Chemical Energy. *Nat. Mater.* **2011**, 10, 911−921.
35. Brongersma, M. L.; Halas, N. J.; Nordlander, P. Plasmon- Induced Hot Carrier Science and Technology. *Nat. Nanotechnol.* **2015**, 10, 25−34.
36. Christopher, P.; Moskovits, M. Hot Charge Carrier Trans- mission from Plasmonic Nanostructures. *Annu. Rev. Phys. Chem.* **2017**, 68, 379−398.
37. Linic, S.; Aslam, U.; Boerigter, C.; Morabito, M. Photochemical Transformations on Plasmonic Metal Nanoparticles. *Nat. Mater.* **2015**, 14, 567−576.
38. Hartland, G. V.; Besteiro, L. V.; Johns, P.; Govorov, A. O. What's so Hot about Electrons in Metal Nanoparticles? *ACS Energy Lett.* **2017**, 2, 1641−1653.
39. Zhang, Y.; He, S.; Guo, W.; Huang, J.; Mulcahy, J. R.; Wei, W. D. Surface-Plasmon-Driven Hot Electron Photochemistry. *Chem. Rev.* **2018**, 118, 2927−2954.
40. Knight, M. W.; Sobhani, H.; Nordlander, P.; Halas, N. J. Photodetection with Active Optical Antennas. *Science* **2011**, 332, 702−704.
41. Zheng, B. Y.; Zhao, H.; Manjavacas, A.; McClain, M.; Nordlander, P.; Halas, N. J. Distinguishing Between Plasmon-Induced and Photoexcited Carriers in a Device Geometry. *Nat. Commun.* **2015**, 6, 7797.
42. Li, W.; Valentine, J. Metamaterial Perfect Absorber Based Hot Electron Photodetection. *Nano Lett.* **2014**, 14, 3510−3514.
43. Tagliabue, G.; Jermyn, A. S.; Sundararaman, R.; Welch, A. J.; DuChene, J. S.; Pala, R.; Davoyan, A. R.; Narang, P.; Atwater, H. A. Quantifying the Role of Surface Plasmon Excitation and Hot Carrier Transport in Plasmonic Devices. *Nat. Commun.* **2018**, 9, 3394.
44. Mubeen, S.; Lee, J.; Singh, N.; Kramer, S.; Stucky, G. D.; Moskovits, M. An Autonomous Photosynthetic Device in Which All Charge Carriers Derive from Surface Plasmons. *Nat. Nanotechnol.* **2013**, 8, 247−251.
45. Mubeen, S.; Lee, J.; Liu, D.; Stucky, G. D.; Moskovits, M. Panchromatic Photoproduction of H_2 with Surface Plasmons. *Nano Lett.* **2015**, 15, 2132−2136.
46. Tian, Y.; Tatsuma, T. Mechanisms and Applications of Plasmon-Induced Charge Separation at TiO_2 Films Loaded with Gold Nanoparticles. *J. Am. Chem. Soc.* **2005**, 127, 7632−7637.
47. DuChene, J. S.; Sweeny, B. C.; Johnston-Peck, A. C.; Su, D.; Stach, E. A.; Wei, W. D. Prolonged Hot Electron Dynamics in Plasmonic-Metal/Semiconductor Heterostructures with Implications for Solar Photocatalysis. *Angew. Chem., Int. Ed.* **2014**, 53, 7887−7891.
48. Pu, Y.-C.; Wang, G.; Chang, K.-D.; Ling, Y.; Lin, Y.-K.; Fitzmorris, B. C.; Liu, C.-M.; Lu, X.; Tong, Y.; Zhang, J. Z.; Hsu, Y.-J.; Li, Y. Au Nanostructure-Decorated TiO_2 Nanowires Exhibiting Photoactivity Across Entire UV-visible Region for Photoelectrochemical Water Splitting. *Nano Lett.* **2013**, 13, 3817−3823.
49. Qian, K.; Sweeny, B. C.; Johnston-Peck, A. C.; Niu, W.; Graham, J. O.; DuChene, D. J.; Qiu, J.; Wang, Y.-C.; Engelhard, M. E.; Su, D.; Stach, E. A.; Wei, W. D. Surface Plasmon-Driven Water Reduction: Gold Nanoparticle Size Matters. *J. Am. Chem. Soc.* **2014**, 136, 9842−9845.
50. Schlather, A. E.; Manjavacas, A.; Lauchner, A.; Marangoni, V. S.; DeSantis, C. J.; Nordlander, P.; Halas, N. J. Hot Hole Photoelectrochemistry on Au@SiO_2@Au Nanoparticles. *J. Phys. Chem. Lett.* **2017**, 8, 2060−2067.
51. Zhao, J.; Nguyen, S. C.; Ye, R.; Ye, B.; Weller, H.; Somorjai, G. A.; Alivisatos, A. P.; Toste, F. D. A Comparison of Photocatalytic Activities of Gold Nanoparticles Following Plasmonic and Interband

Excitation and a Strategy for Harnessing Interband Hot Carriers for Solution Phase Photocatalysis. *ACS Cent. Sci.* **2017**,3,482−488.

52. Al-Zubeidi, A.; Hoener, B. S.; Collins, S. S. E.; Wang, W. Kirchner, S. R.; Jebeli, S. A. H.; Joplin, A.; Chang, W.-S.; Link, S.; Landes, C. F. Hot Holes Assist Plasmonic Nanoelectrode Dissolution. *Nano Lett.* **2019**, 19, 1301−1306.
53. Yu, W.; Wijesekara, K. D.; Xi, X.; Willets, K. A. Quantifying Wavelength-Dependent Plasmonic Hot Carrier Energy Distributions at Metal/Semiconductor Interfaces. *ACS Nano* **2019**, 13, 3629−3637.
54. Pensa, E.; Garguilo, J.; Lauir, A.; Schlucker, S.; Cortes, A.; Maier, S. A. Spectral Screening of the Energy of Hot Holes over a Particle Plasmon Resonance. *Nano Lett.* **2019**, 19, 1867−1874.
55. Matsui, T.; Li, Y.; Hsu, M.-H. M.; Merckling, C.; Oulton, R. F.; Cohen, L. F.; Maier, S. A. Highly Stable Plasmon Induced Hot Hole Transfer into Silicon via a $SrTiO_3$ Passivation Interface. *Adv. Funct. Mater.* **2018**, 28, 1705829.
56. Gusken, N. A.; Lauri, A.; Li, Y.; Matsui, T.; Doiron, B.; Bower, R.; Regoutz, A.; Mihai, A.; Petrov, P. K.; Oulton, R. F.; Cohen, L. F.; Maier, S. A. TiO_{2-x} - Enhanced IR Hot Carrier Based Photodetection in Metal Thin Film-Si Junctions. *ACS Photonics* **2019**, 6, 953−960.
57. Tanzid, M.; Ahmadivand, A.; Zhang, R.; Cerjan, B.; Sobhani, A.; Yazdi, S.; Nordlander, P.; Halas, N. J. Combining Plasmonic Hot Carrier Generation with Free Carrier Absorption for High-Perform- ance Near-Infrared Silicon-Based Photodetection. *ACS Photonics* **2018**, 5, 3472−3477.
58. Cai, Y.-Y.; Collings, S. S. E.; Gallagher, M. J.; Bhattacharjee, U.; Zhang, R.; Chow, T. H.; Ahmadivand, A.; Ostovar, B.; Al-Zubeidi, A.; Wang, J.; Nordlander, P.; Landes, C. F.; Link, S. Single-Particle Emission Spectroscopy Resolves d-Hole Relaxation in Copper Nanocubes. *ACS Energy Lett.* **2019**, 4, 2458−2465.
59. He, J.; Lindström, E.; Hagfeldt, A.; Lindquist, S.-E. Dye- Sensitized Nanostructured p-Type Nickel Oxide Film as a Photo- cathode for a Solar Cell. *J. Phys. Chem. B* **1999**, 103, 8940−8943.
60. Irwin, M. D.; Buchholz, D. B.; Hains, A. W.; Chang, R. P. H.; Marks, T. J. p-Type Semiconducting Nickel Oxide as an Efficiency- Enhancing Anode Interfacial Layer in Polymer Bulk-Heterojunction Solar Cells. *Proc. Natl. Acad. Sci. U. S. A.* **2008**, 105, 2783−2787.
61. Seo, S.; Park, I. J.; Kim, M.; Lee, S.; B, C.; Jung, H. S.; Park, N.- G.; Kim, J. Y.; Shin, H. An Ultra-Thin, Un-Doped NiO Hole Transporting Layer of Highly Efficient (16.4%) Organic-Inorganic Hybrid Perovskite Solar Cells. *Nanoscale* **2016**, 8, 11403.
62. Kamata, R.; Kumagai, H.; Yamazaki, Y.; Sahara, G.; Ishitani, O. Photoelectrochemical CO2 Reduction Using a Ru(II)-Re(I) Supra- molecular Photocatalyst Connected to a Vinyl Polymer on a NiO Electrode. *ACS Appl. Mater. Interfaces* **2019**, 11, 5632−5641.
63. Thimsen, E.; Martinson, A. B. F.; Elam, J. W.; Pellin, M. J. Energy Levels, Electronic Properties, and Rectification in Ultrathin p-NiO Films Synthesized by Atomic Layer Deposition. *J. Phys. Chem. C* **2012**, 116, 16830−16840.
64. Sai Gautam, G.; Senftle, T. P.; Alidoust, N.; Carter, E. A. Novel Solar Cell Materials: Insights from First-Principles. *J. Phys. Chem. C* **2018**, 122, 27107−27126.
65. Robatjazi, H.; Bahauddin, S. M.; Doiron, C.; Thomann, I. Direct Plasmon-Driven Photoelectrocatalysis. *Nano Lett.* **2015**, 15, 6155−6161.
66. Nakamura, K.; Oshikiri, T.; Ueno, K.; Wang, Y.; Kamta, Y.; Kotake, Y.; Misawa, H. Plasmon-Enhanced Photocurrent Generation and Water Oxidation with a Gold Nanoisland-Loaded Titanium Dioxide Photoelectrode. *J. Phys. Chem. Lett.* **2016**, 7, 1004−1009.
67. Kao, K.-C.; Kuroiwa, Y.; Nishi, H.; Tatsuma, T. Hydrogen Evolution from Water Based on Plasmon-Induced Charge Separation at a TiO_2/Au/NiO/Pt System. *Phys. Chem. Chem. Phys.* **2017**, 19, 31429−31435.
68. Anderson, P. A. The Work Function of Copper. *Phys. Rev.* **1949**, 76, 388−390.

69. Dabera, G. D. M. R.; Walker, M.; Sanchez, A. M.; Pereira, H. J.; Beanland, R.; Hatton, R. A. Retarding Oxidation of Copper Nanoparticles Without Electrical IIsolation and the Size Dependence of Work Function. *Nat. Commun.* **2017**, *8*, 1894.
70. Mendez-Medrarno, M. G.; Kowalska, E.; Lehoux, A.; Herriisan, A.; Othani, B.; Bahena, D.; Briois, V.; Colbeau-Justin, C.; Rodríguez- Lopez, J. L.; Remita, H. Surface Modification of TiO_2 with Ag Nanoparticles and CuO Nanoclusters for Application in Photo- catalysis. *J. Phys. Chem. C* **2016**, 120, 5143−5154.
71. Yu, J.; Zhuang, S.; Xu, X.; Zhu, W.; Feng, B.; Hu, J. Photogenerated Electron Reservoir in Hetero-p-n CuO-ZnO Nano-composite Device for Visible-Light-Driven Photocatalytic Reduction of Aqueous Cr(VI). *J. Mater. Chem. A* **2015**, 3, 1199−1207.
72. Scott, S. B.; Hogg, T. V.; Landers, A. T.; Maagaard, T.; Bertheussen, E.; Lin, J. C.; Davis, R. C.; Beeman, J. W.; Higgins, D.; Drisdell, W. S.; Hahn, C.; Mehta, A.; Seger, B.; Jaramillo, T. F.; Chorkendorff, I. Absence of Oxidized Phases in Cu under CO Reduction Conditions. *ACS Energy Lett.* **2019**, 4, 803−804.
73. Corson, E. R.; Creel, E. B.; Kim, Y.; Urban, J. J.; Kostecki, R.; McCloskey, B. D. A Temperature-Controlled Photoelectrochemical Cell for Quantitative Product Analysis. *Rev. Sci. Instrum.* **2018**, 89, 055112.
74. Mukherjee, S.; Zhou, L.; Goodman, A. M.; Large, N.; Ayala- Orozco, C.; Zhang, Y.; Nordlander, P.; Halas, N. J. Hot-Electron- Induced Dissociation of H_2 on Gold Nanoparticles Supported on SiO_2. *J. Am. Chem. Soc.* **2014**, 136, 64−67.
75. Zhou, L.; Zhang, C.; McClain, M. J.; Manjavacas, A.; Krauter, C. M.; Shu, T.; Berg, F.; Everitt, H. O.; Carter, E. A.; Nordlander, P.; Halas, N. J. Aluminum Nanocrystals as a Plasmonic Photocatalyst for Hydrogen Dissociation. *Nano Lett.* **2016**, 16, 1478−1484.
76. Zhang, C.; Zhao, H.; Zhou, L.; Schlather, A. E.; Dong, L.; McClain, M. J.; Swearer, D. F.; Nordlander, P.; Halas, N. J. Al-Pd Nanodisk Heterodimers as Antenna-Reactor Photocatalysts. *Nano Lett.* **2016**, 16, 6677−6682.
77. Nørskov, J. K.; Abild-Pedersen, F.; Studt, F.; Bligaard, T. Density Functional Theory in Surface Chemistry and Catalysis. *Proc. Natl. Acad. Sci. U. S. A.* **2011**, 108, 937−943.
78. Hammer, B.; Nørskov, J. K. Theoretical Surface Science and Catalysis Calculations and Concepts. *Adv. Catal.* **2000**, 45, 71−129.
79. Sundararaman, R.; Narang, P.; Jermyn, A. S.; Goddard, W. A., III; Atwater, H. A. Theoretical Predictions for Hot-Carrier Generation from Surface Plasmon Decay. *Nat. Commun.* **2014**, 5, 5788.
80. Brown, A. M.; Sundararaman, R.; Narang, P.; Goddard, W. A., III; Atwater, H. A. Nonradiative Plasmon Decay and Hot Carrier Dynamics: Effects of Phonons, Surfaces, and Geometry. *ACS Nano* **2016**, 10, 957−966.
81. Wuttig, A.; Yaguchi, M.; Motobayashi, K.; Osawa, M.; Surendranath, Y. Inhibited Proton Transfer Enhances Au-Catalyzed CO_2-to-Fuels Selectivity. *Proc. Natl. Acad. Sci. U. S. A.* **2016**, 113, E4585−E4593.
82. Christopher, P.; Xin, H.; Marimuthu, A.; Linic, S. Singular Characteristics and Unique Chemical Bond Activation Mechanisms of Photocatalytic Reactions on Plasmonic Nanostructures. *Nat. Mater.* **2012**, 11, 1044−1050.
83. Boerigter, C.; Campana, R.; Morabito, M.; Linic, S. Evidence and Implications of Direct Charge Excitation as the Dominant Mechanism in Plasmon-Mediated Photocatalysis. *Nat. Commun.* **2016**, 7, 10545.
84. Boerigter, C.; Aslam, U.; Linic, S. Mechanism of Charge Transfer from Plasmonic Nanostructures to Chemically Attached Materials. *ACS Nano* **2016**, 10, 6108−6115.

85. Rao, V. G.; Aslam, U.; Linic, S. Chemical Requirement for Extracting Energetic Charge Carriers from Plasmonic Metal Nano- particles to Perform Electron-Transfer Reactions. *J. Am. Chem. Soc.* **2019**, 141, 643−647.
86. Aslam, U.; Rao, V. G.; Chavez, S.; Linic, S. Catalytic Conversion of Solar to Chemical Energy on Plasmonic Metal Nanostructures. *Nat. Catal.* **2018**, 1, 656−665.
87. Wu, K.; Chen, J.; McBride, J. R.; Lian, T. Efficient Hot-Electron Transfer by a Plasmon-Induced Interfacial Charge-Transfer Transition. *Science* **2015**, 349, 632−635.
88. Tan, S.; Argondizzo, A.; Ren, J.; Liu, L.; Zhao, J.; Petek, H. Plasmonic Coupling at a Metal/Semiconductor Interface. *Nat. Photonics* **2017**, 11, 806−812.
89. Kumar, P. V.; Rossi, T. P.; Marti-Dafcik, D.; Reichmuth, D.; Kuisma, M.; Erhart, P.; Puska, M. J.; Norris, D. J. Plasmon-Induced Direct Hot-Carrier Transfer at Metal-Acceptor Interfaces. *ACS Nano* **2019**, 13, 3188−3195.
90. Zhang, Y.; Nelson, T.; Tretiak, S.; Guo, H.; Schatz, G. C. Plasmonic Hot-Carrier-Mediated Tunable Photochemical Reactions. *ACS Nano* **2018**, 12, 8415−8422.

Chapter 7

BICARBONATE OR CARBONATE PROCESSES FOR COUPLING CARBON DIOXIDE CAPTURE AND ELECTROCHEMICAL CONVERSION

7.1 Introduction

Designing a scalable system to capture CO_2 from the air and convert it into valuable chemicals, fuels, and materials could be transformational for mitigating climate change.[1–3] Climate models predict that negative greenhouse gas emissions will be required by the year 2050 in order to stay below a 2 °C change in global temperature.[4] The processes of CO_2 capture, CO_2 conversion, and finally product separation all require significant energy inputs; devising a system that simultaneously minimizes the energy required for all steps is an important challenge. To date, a variety of prototype or pilot-level CO_2 capture and/or conversion systems have been designed and built targeting the individual objectives of either capture or conversion. One approach has focused on CO_2 removal from the atmosphere and storage of pure pressurized CO_2.[5,6] Other efforts have concentrated on CO_2 conversion processes, such as electrochemical reduction[7–10] or fermentation.[10,11] Only a few concepts or analyses have been developed for complete end-to-end processes that perform both CO_2 capture and transformation.[12,13]

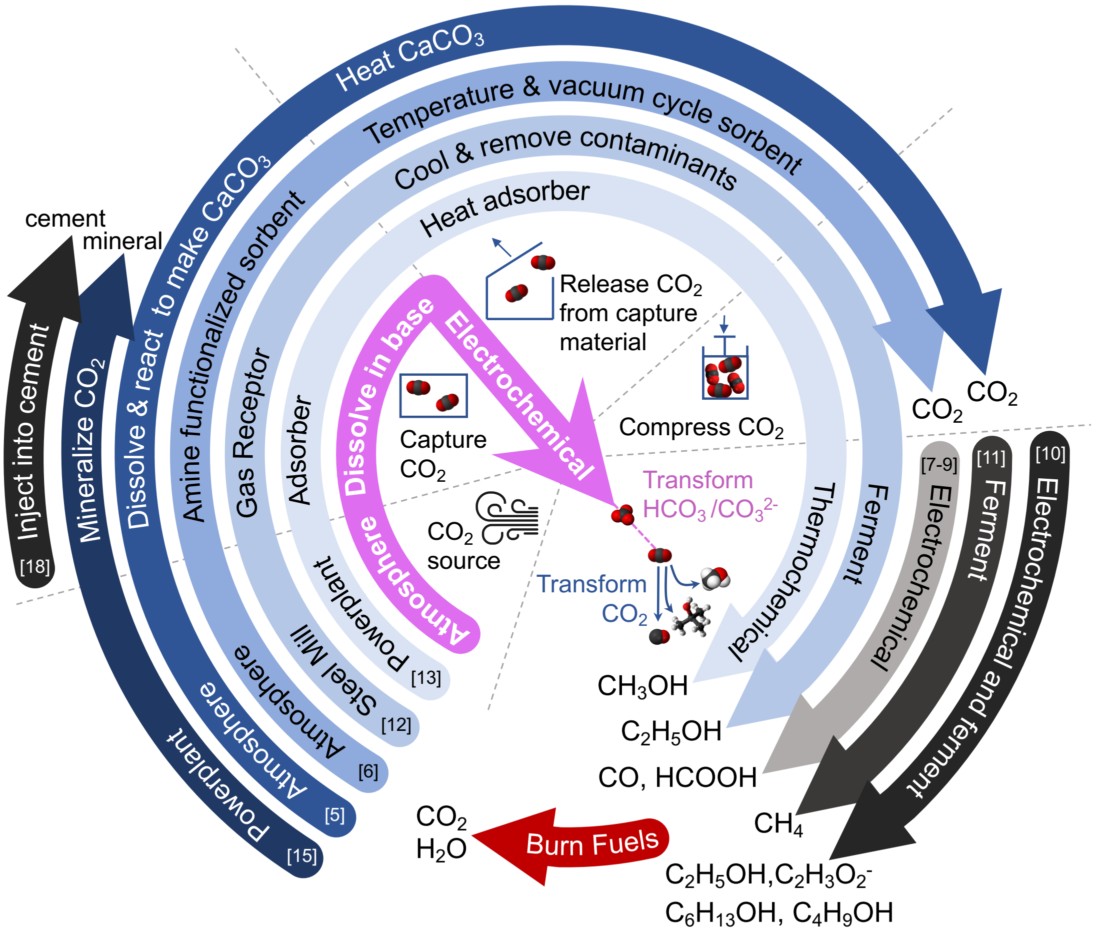

Figure 7.1: *Schematic representation of the steps for various prototype systems designed to capture CO_2 and/or convert it to either concentrated and pressurized CO_2 or to a value-added product. The blue arrows represent prototype processes that capture and convert CO_2, grey arrows represent prototype processes that only focus on CO_2 conversion, and the pink arrow represents the process that we propose. The numbers in brackets correspond to references for the various processes [5-13,15,18].*

Here we explore an approach for the design of a CO_2 capture and conversion system - (i) formation of bicarbonate or carbonate ((bi)carbonate) through dissolution of CO_2 into basic solution, followed by (ii) electrochemical reduction to syngas or formate, and finally (iii) transformation into useful chemicals, fuels, and materials. Unlike traditional electrochemical systems, in which gaseous CO_2 is the primary chemical feedstock that is converted into products, our analysis focuses on the transformation of CO_2 carried by (bi)carbonate solutions (Figure 7.1). This approach offers several advantages for coupling CO_2 capture with conversion. First, capturing CO_2 from the atmosphere does not require an energy-intensive heating step to recover gaseous CO_2 from a capture medium for later conversion. Second, by transforming the CO_2 carried by (bi)carbonate ions, the process avoids the energy-intensive compression of gaseous CO_2 and allows for significantly higher conversion efficiency per mol of captured CO_2. We outline the energy requirements for various steps in this (bi)carbonate feedstock route and compare it to systems with conventional CO_2 capture and conversion processes.

7.2 CO_2 capture and conversion steps

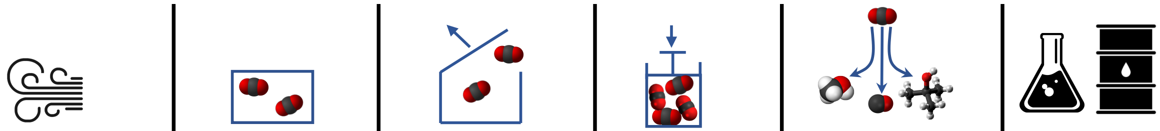

CO_2 Source	Capture CO_2	Release from capture material	Compress CO_2	Transform CO_2	Products
Environment - Air - Seawater Point Source - Petrochemical Industry - e.g. ethylene - Iron and Steel - Cement production - Natural gas sweetening - Fossil fuels or Minerals - e.g. coal	Absorption - e.g. amines Adsorption - e.g. zeolites Membranes - e.g. fibers Biological - e.g. algae Other - e.g. mineralization	Heat Vacuum cycle	~15 PSIA for fermentation ~15-50 PSIA for electrochemical processes ~250-1450 PSIA for thermo-chemical processes	Electrochemical Fermentation Photo-electrochemical Photocatalysis Thermocatalytic Thermolysis Industrial Processes	$C_xH_yO_z$ C_xH_{2x} C_xH_{2x+1} C_xH_{2x+2} Diesel Syngas Ethylene Butanol Hexanol Propanol Ethanol Plastics

Figure 7.2: *Synopsis of the various steps involved in capturing CO_2 and transforming it into valuable chemicals.*

There are many possible configurations for CO_2 capture and conversion systems, but five steps are integral to every conventional design (Figure 7.2): (i) a CO_2 source, (ii) a capture medium, (iii) a process to release CO_2 from the capture medium, (iv) CO_2 compression into a concentrated gas stream, and (v) conversion of CO_2 into fuels, chemicals, and/or materials (e.g. hydrocarbons). The design of an energy-efficient integrated system for capture and conversion requires careful consideration of the CO_2 source. Whether it is a point source with a mixed-process gas stream (i.e. flue gas from a coal-fired power plant) or a relatively dilute source (i.e. atmosphere) will dictate the CO_2 concentration in the feedstock and therefore the type of capture media that is most appropriate to use. There are a variety of options for CO_2 capture media, ranging from polymer membranes to organic and inorganic liquid adsorbers.[14] After collection by the capture media, the release of CO_2 is usually accomplished by heating the capture media itself. The collected CO_2 must then be compressed to a suitable pressure for flow and injection into a conversion system. As will be shown below, these two processes related to CO_2 capture and compression potentially constitute a major energy input that must be considered when designing a complete system for mitigating global atmospheric CO_2.

To better facilitate an end-to-end comparison of complete systems, we analyze CO_2 capture and conversion systems that have been realized to date at a pilot-plant level. We divide them into three categories:

systems that (i) perform direct air capture, (ii) use a concentrated CO_2 source for conversion, and (iii) only focus on the conversion of CO_2. The steps for each pilot-plant and prototype are shown in Figure 7.1, and a more detailed schematic is given in the Appendix A: Figures A1-A2. We compare the pilot processes using the metric of energy required to remove/transform one mole of CO_2 from the atmosphere because this metric directly affects the operational expenses of the plant. However, it should be noted that this metric does not account for other expenses (labor, maintenance, materials, etc.) needed to operate the plant, or the construction capital expense and amortization period. Due to these considerations, we have therefore chosen to not compare fermentation processes to electrochemical or thermocatalytic processes. Fermentation is an interesting CO_2 conversion technique that shows significant promise because of its high selectivity for products like ethanol and other multiple carbon products.[10–12] Fermenters also operate near room temperature, making the energy requirements per mole of CO_2 transformed low (Appendix A:1G-H).[10,11] However, fermentation processes require labor to operate and maintain the system, reaction times can be long, and fermenters are typically operated as a batch reactor rather than in a continuous chemical process. These considerations make it difficult to directly compare electrochemical and fermentation processes using only energy required per mole of CO_2 captured/transformed as a metric. In this perspective, we are proposing an electrochemical process and will therefore focus our attention on comparing it to similar systems.

Pilot-plants that remove CO_2 from the atmosphere and produce concentrated and pressurized CO_2 streams have been designed using a capture medium of potassium hydroxide (Carbon Engineering)[5] or polyamines (ClimeWorks).[6] The potassium hydroxide process requires ~0.28 MJ per mole of CO_2 (kJ/mol CO_2) removed from the atmosphere (Appendix A:1A)[5] while the polyamine process requires 0.58 MJ/mol CO_2.[6] For both of these atmospheric CO_2 capture processes, the enthalpy required to release the CO_2 from the capture medium and subsequent pressurization of the gaseous CO_2 dominates the total energy requirements of the system.

Other pilot-scale processes have been developed that capture CO_2 from concentrated sources. For instance, CO_2 emitted from a geothermal power plant is dissolved into a potassium hydroxide solution, which is then pumped underground to react with naturally occurring basalt rock (CarbFix).[15] By taking advantage of location-specific geology for CO_2 transformation, the system only requires 0.13 MJ/mol CO_2 (Appendix A:1B).[16] Another process captures CO_2 from a geothermal power plant, then pressurizes and heats the CO_2 in the presence of H_2 generated via water electrolysis to create methanol and water (Carbon Recycling International). This process requires 1.53 MJ/mol CO_2 (Appendix A:1C), but it also produces a chemical fuel in the form of methanol.[13] As expected, this process requires more energy than the other systems described because it incorporates a CO_2 conversion process.

Pilot-scale CO_2 conversion systems have also received extensive attention.[7–11,17] A pilot-scale CO_2 electrolyzer was shown to create CO and O_2 using an energy input of 0.81 MJ/mol CO_2 (Appendix A:1D).[9] Other pilot-scale CO_2 electrolyzers have been demonstrated to make CO[7] or formic acid[8], requiring 0.61 MJ/mol CO_2 or 0.75 MJ/mol CO_2, respectively (Appendix A:1E). Finally, an approach for carbon sequestration uses a process that injects CO_2 into cement during production, allowing cement producers to use less binder and offset their CO_2 emissions in the process; using this method, 25 lbs of CO_2 can be stored per cubic yard of cement (Appendix A:1H).[17] Notably, none of the these transformation processes account for the energy required to capture the CO_2 from the atmosphere or a concentrated point source. As mentioned above, procuring a pressurized CO_2 source in suitable purity does not represent a trivial amount of energy.

In order to construct an alternative process with a modest energy consumption alternative, we seek to evaluate the energy intensive steps of each process. Energy consumption varies greatly depending on the source of CO_2 and the desired products. While the process of CO_2 conversion requires significantly greater energy than CO_2 capture, conversion schemes discussed above have yet to report their conversion efficiency. Based on our calculations, all reported devices have CO_2 conversion efficiencies less than 40% (Appendix A:3A-H) with the majority having conversion efficiencies less than 10%.[18] For many electrolysis processes the energy required per mole of CO_2 would at minimum double unless the unused CO_2 is recycled through the system. To decrease the overall energy requirements for CO_2 capture and conversion, it is interesting to consider a system that converts nearly 100% of the captured CO_2.

7.3 Direct (bi)carbonate conversion

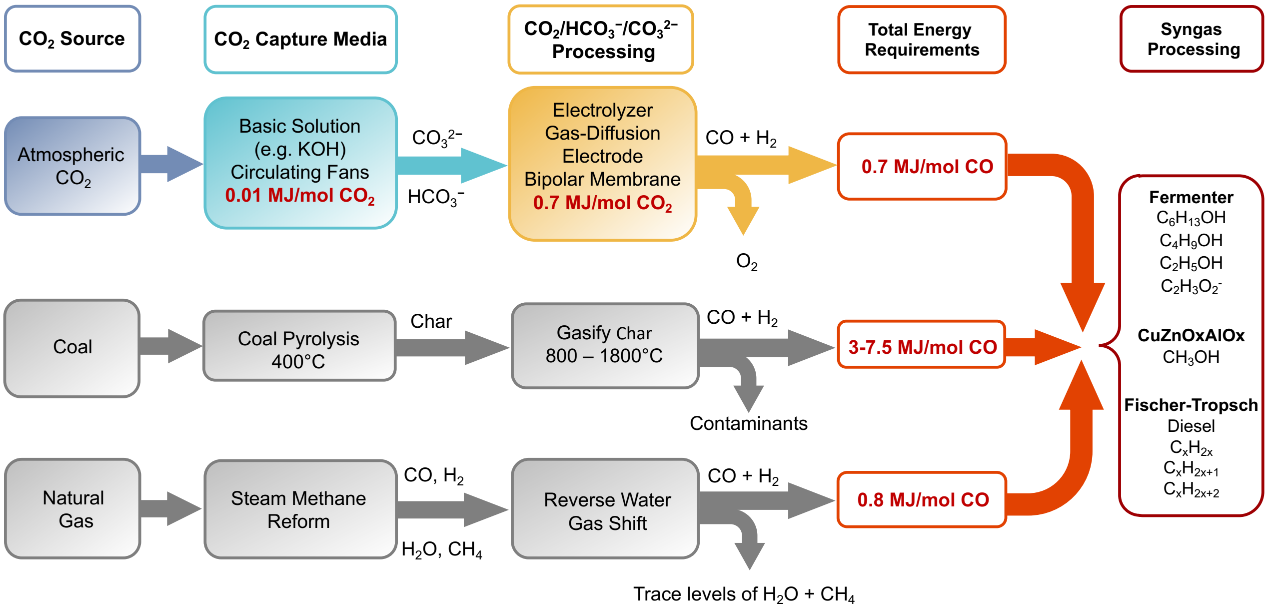

Figure 7.3: *Schematic representation of processes and energy requirements for various proposed schemes that capture CO_2 and*

transform it to value-added products. The bottom rows show the commercial syngas synthesis process, with either a feed stock of coal or of natural gas. The energy needed to produce 1 mol of CO while related to the cost needed to operate the plant does not encompass the full picture of expenses such as materials, maintenance, and labor.

Electrochemically reducing CO_2 carried by (bi)carbonate instead of pressurized CO_2 bypasses energy intensive processes necessary for concentration and compression of gaseous CO_2 (see Figure 7.3 and Figure 7.4 for schematics of the overall process designs). This change in the carbon-bearing feedstock molecule allows us to avoid energy-intensive processes, such as heating or vacuum cycling of a sorbent material to release the captured CO_2, along with the subsequent compression of the captured CO_2 into a sufficient pressure that can adequately supply a CO_2 conversion system, such as a gas-diffusion electrolyzer. Furthermore, transforming the CO_2 carried by a (bi)carbonate ion allows for high conversion efficiency per mol of captured CO_2, unlike many other electrolysis devices operating with gaseous CO_2 as the carbon input (Appendix A:3A-H).

An example schematic system could combine (bi)carbonate formation with syngas production (Figure 7.3), which can then be flexibly converted to valuable chemicals, fuels, and materials. Assuming the first step of CO_2 capture uses an already demonstrated air contactor design[5], ~0.01 MJ/mol CO_2 would be required (Appendix A:2A), depending on the alkalinity of the solution. The solution of (bi)carbonate could then be fed into an electrolyzer where it is converted to syngas (CO and H_2). Recent reports of gas-diffusion electrodes using a silver catalyst at the cathode and a bipolar membrane have shown that CO_2 can be generated locally near the catalyst from a (bi)carbonate electrolyte, which can then be converted to syngas.[19,20] Importantly, no CO_2 was observed in the output stream of chemical products,[19] thus eliminating the need to separate the syngas from the unconverted CO_2 stream. These reported prototype devices[19,20] required between ~0.7 MJ/mol CO_2 and achieved a desirable syngas ratio of between 3:1 and 2:1 (H_2:CO) (Appendix A:2B and Appendix A:2C). In all of the electrolysis processes discussed above, the oxygen evolution reaction (OER) occurs at the counter electrode. It should also be noted that the base does not need to be replenished as long as the rate of CO_2 capture is matched to the rate of CO production. To create a plant that could capture and transform 1 metric ton of CO_2 per day would require a capture system of approximately 16.6 m^2, an electrode area of 0.4 m^2, and an array of solar panels covering an area of 4,571 m^2 (Appendix A:2D). Additional space for solar energy storage and syngas processing would also be required, but would be negligible compared to the area needed for the photovoltaic system generating the electricity. If this system were to be used to capture all CO_2 emitted globally daily, approximately 100 million tons of CO_2, the system would need to be around 460,000 km^2. This is slightly larger than the area of California (~424,000 km^2), and only around 0.09% of the area of the earth.

Notably, the total energy requirement of the (bi)carbonate conversion system is 0.7 MJ/mol CO to make syngas, while commercial processes to make syngas from coal require 3-7.5 MJ/mol CO (Appendix A:2E).[21] To make syngas from natural gas requires 0.8 MJ/mol CO (Appendix A:2F-G).[22] It should be noted, however, that the energies listed for these conventional industrial processes do not account for the energy required to extract the coal or natural gas feedstocks. The (bi)carbonate process we have outlined compares favorably on an energetic basis to current commercial processes, and unlike typical gasification systems, it also produces a syngas stream without any contaminants. As is well known, syngas is a versatile feedstock for further generation of a variety of useful chemicals and fuels. For example, butanol, hexanol, acetate, and ethanol can be synthesized from syngas by using a fermenter.[10,12] Another option is to synthesize methanol by heating and pressurizing syngas in the presence of a CuZnOxAlOx catalyst.[23] A third option would be to use Fischer-Tropsch processes to make longer-chain hydrocarbons, such as diesel fuel, which can be synthesized at 240 °C and 25 bar in the presence of a cobalt catalyst.[24]

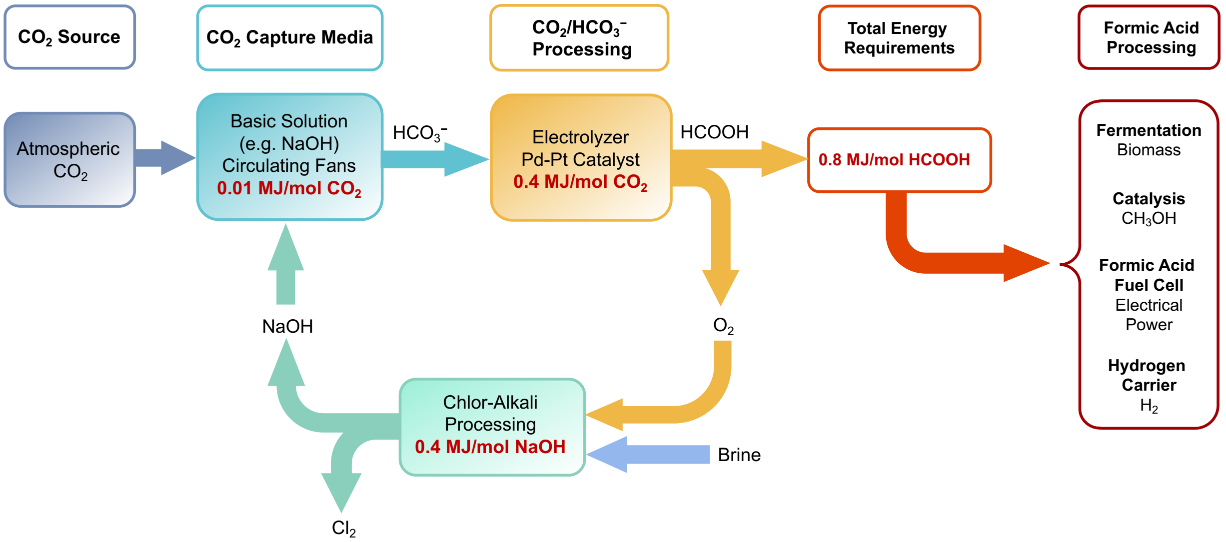

Figure 7.4: *Schematic representation of processes and energy requirements for various proposed schemes that capture CO_2 and transform into formic acid.*

Syngas is not the only chemical product that can be electrochemically synthesized from CO_2-bearing bicarbonate solutions. Several studies have shown that bicarbonate solutions can also be electrochemically reduced to formate at low overpotentials (Appendix A:2H).[25–28] The global market for formic acid is relatively small (currently ~570 million USD) but expected to grow significantly in the coming years because of the increased use of formic acid in the rubber industry.[29] The energy required to electrochemically synthesize formate from bicarbonate via atmospheric CO_2 capture is 0.8 MJ/mol CO_2 (Figure 7.4). Not only is formic acid a useful chemical in and of itself, but formic acid can also be transformed into valuable chemicals such as methanol by either molecular catalysts,[30–33] thermocatalysis,[34–36] or fermentation processes.[37] Although the heat of combustion is modest (0.25 MJ/mol), formic acid could conceivably be used to generate power either directly in a formic acid fuel cell[38–41] or as a hydrogen carrier[42–45] for a hydrogen fuel cell.

7.4 Conclusion

This system-level design approach for CO_2 capture and conversion highlights the favorable characteristics of processes that use a (bi)carbonate solution as the carbon-bearing feedstock. Instead of reducing CO_2 directly from a pressurized gas stream, CO_2 molecules contained in (bi)carbonate solutions are electrochemically reduced to form value-added chemicals, thus removing energy intensive steps, and with a potential for a near-unity conversion rate of the captured CO_2 molecules. While we have focused on syngas production in our analyses, the main advantage of the proposed process involves changing the starting feedstock from gaseous CO_2 to aqueous CO_2 carrying (bi)carbonate solutions, whose advantage is enhanced when coupled with a direct-air capture system to remove atmospheric CO_2.

BIBLIOGRAPHY CHAPTER 7

1. Figueres, C.; et al. Emissions are still rising: ramp up the cuts. *Nature* **2018**, 564, 27−30.
2. Huntingford, C.; Mercado, L. M. High chance that current atmospheric greenhouse concentrations commit to warmings greater than 1.5°C over land. *Sci. Rep.* **2016**, 6, 1−7.
3. Jackson, R. B. Global energy growth is outpacing decarbonization. *Environ. Res. Lett.* **2018**, 13, 120401.
4. Le Quere, C. et al. Global carbon budget 2018; **2018**.
5. Keith, D. W.; Angelo, D. St; Holmes, G.; Heidel, K. A process for capturing CO_2 from the atmosphere. *Joule* **2018**, 2, 1573−1594.
6. Wurzbacher, J. A.; Gebald, C.; Piatkowski, N.; Steinfeld, A. Concurrent separation of CO_2 and H_2O from air by a temperature- vacuum swing adsorption/desorption cycle. *Environ. Sci. Technol.* **2012**, 46, 9191−9198.
7. Dioxide Materials. Dioxide Materials: Electrolyzer to convert carbon dioxide to carbon monoxide. https://dioxidematerials.com/ technology/co2-electrolysis/ (accessed 2020-02-10)
8. Dioxide Materials. Dioxide Materials: Electrolyzer to transform carbon dioxide into formic acid. https://dioxidematerials.com/ technology/formic-acid/(accessed 2020-02-10)
9. Flanders, N.; Kuhl, K.; Cave, E. Opus 12 − Recycling carbon dioxide back into fuels and chemicals; **2016**.
10. Haas, T.; Krause, R.; Weber, R.; Demler, M.; Schmid, G. Technical photosynthesis involving CO_2 electrolysis and fermentation. *Nat. Catal.* **2018**, 1, 32−39.
11. Electrochaea. Applications of Electrochaea's BioCat biomethanation technology; **2018**, http://www.electrochaea.com/wp-content/ uploads/2018/03/201803_Data-Sheet_BioCat-Plant.pdf.
12. LanzaTech. Technical background on the LanzaTech Process; **2013**, http://www.arpae-summit.com/paperclip/exhibitor_docs/ 14AE/LanzaTech_Inc._131.pdf.
13. Kauw, M.; Benders, R. M. J.; Visser, C. Green methanol from hydrogen and carbon dioxide using geothermal energy and/or hydropower in Iceland or excess renewable electricity in Germany. *Energy* **2015**, 90, 208−217.
14. Li, B.; Duan, Y.; Luebke, D.; Morreale, B. Advances in CO_2 capture technology: A patent review. *Appl. Energy* **2013**, 102, 1439− 1447.

15. Matter, J. M.; et al. Rapid carbon mineralization for permanent disposal of anthropogenic carbon dioxide emissions. Science (Washington, DC, U. S.) 2016, 352, 1312.
16. Ragnheidardottir, E.; Sigurdardottir, H.; Kristjansdottir, H.; Harvey, W. Opportunities and challenges for CarbFix: An evaluation of capacities and costs for the pilot scale mineralization sequestration project at Hellisheidi, Iceland and beyond. *Int. J. Greenhouse Gas Control* **2011**, 5, 1065−1072.
17. Monkman, S.; MacDonal, M. Ready mixed technology case study CO_2 utilization in concrete mix design optimization; 2016, http://info. carboncure.com/hubfs/Downloads/ CarbonCure%20Ready%20Mixed%20Technology%20Case%20Study. pdf?hsCtaTracking=3acd2ed8-631d-4960-a516- eb14990ee747%7Cf4c138bf-0589-4751-a2c8-576a17dd4453.
18. Weng, L. C.; Bell, A. T.; Weber, A. Z. Towards membrane- electrode assembly systems for CO_2 reduction: A modeling study. *Energy Environ. Sci.* **2019**, 12, 1950−1968.
19. Li, Y. C.; et al. CO2 electroreduction from carbonate electrolyte. *ACS Energy Lett.* **2019**, 4, 1427−1431.
20. Li, T.; et al. Electrolytic conversion of bicarbonate into CO in a flow cell. *Joule* **2019**, 3, 1487−1497.
21. Energy Technology Systems Analysis Programme. Syngas production from coal; **2010**, http://large.stanford.edu/courses/2013/ ph241/kallman1/docs/estap.pdf.
22. Baltrusaitis, J.; Luyben, W. L. Methane conversion to syngas for gas-to-liquids (GTL): is sustainable CO_2 reuse via dry methane reforming (DMR) cost competitive with SMR and ATR processes? *ACS Sustainable Chem. Eng.* **2015**, 3, 2100−2111.
23. Tountas, A. A. Towards solar methanol: past, present, and future. *Adv. Sci.* **2019**, 6, 1970048.
24. Samavati, M.; Santarelli, M.; Martin, A.; Nemanova, V. Production of synthetic Fischer−Tropsch diesel from renewables: thermoeconomic and environmental analysis. *Energy Fuels* **2018**, 32, 1744−1753.
25. Chatterjee, D.; Jaiswal, N.; Banerjee, P. Electrochemical conversion of bicarbonate to formate mediated by the complex Ru III (edta) (edta^{4-} = ethylenediaminetetraacetate). *Eur. J. Inorg. Chem.* **2014**, 2014, 5856−5859.
26. Stalder, C. J.; Chao, S.; Wrighton, M. S. Electrochemical reduction of aqueous bicarbonate to formate with high current efficiency near the thermodynamic potential at chemically derivatized electrodes. *J. Am. Chem. Soc.* **1984**, 106, 3673−3675.
27. Kortlever, R.; Peters, I.; Koper, S.; Koper, M. T. M. Electrochemical CO_2 Reduction to Formic Acid at Low Over- potential and with High Faradaic Efficiency on Carbon-Supported Bimetallic Pd-Pt Nanoparticles. *ACS Catal.* **2015**, 5, 3916−3923.
28. Kortlever, R.; Balemans, C.; Kwon, Y.; Koper, M. T. M. Electrochemical CO2 reduction to formic acid on a Pd-based formic acid oxidation catalyst. *Catal. Today* **2015**, 244, 58−62.
29. Sawant, A. Global Formic Acid Market; Market Research Future, 2018.
30. De, S.; Gevers, L.; Emwas, A. H.; Gascon, J. Conversion of Formic Acid into Methanol Using a Bipyridine-Functionalized Molecular Heterogeneous Catalyst. *ACS Sustainable Chem. Eng.* **2019**, 7, 3933−3939.
31. Miller, A. J. M.; Heinekey, D. M.; Mayer, J. M.; Goldberg, K. I. Catalytic disproportionation of formic acid to generate methanol. *Angew. Chem., Int. Ed.* **2013**, 52, 3981−3984.
32. Savourey, S.; et al. Efficient disproportionation of formic acid to methanol using molecular ruthenium catalysts. *Angew. Chem., Int. Ed.* **2014**, 53, 10466−10470.
33. Sasayama, A. F.; Moore, C. E.; Kubiak, C. P. Electronic effects on the catalytic disproportionation of formic acid to methanol by [Cp*IrIII(R-bpy)Cl]Cl complexes. *Dalt. Trans.* **2016**, 45, 2436− 2439.
34. Sordakis, K.; et al. Aqueous phase homogeneous formic acid disproportionation into methanol. Green Chem. **2017**, 19, 2371−2378.
35. Tsurusaki, A.; et al. Investigation of Hydrogenation of Formic Acid to Methanol using H_2 or Formic Acid as a Hydrogen Source. *ACS Catal.* **2017**, 7, 1123−1131.

36. Sordakis, K.; et al. Carbon Dioxide to Methanol: The Aqueous Catalytic Way at Room Temperature. *Chem. Eur. J.* **2016**, 22, 15605−15608.
37. Gleizer, S.; et al. Conversion of escherichia coli to generate all biomass carbon from CO_2. *Cell* **2019**, 179, 1255−1263.e12.
38. Rice, C.; Ha, S.; Masel, R. I.; Wieckowski, A. Catalysts for direct formic acid fuel cells. *J. Power Sources* **2003**, 115, 229−235.
39. Yu, X.; Pickup, P. G. Recent advances in direct formic acid fuel cells (DFAFC). *J. Power Sources* **2008**, 182, 124−132.
40. Rice, C.; et al. Direct formic acid fuel cells. *J. Power Sources* **2002**, 111, 83−89.
41. Ji, X.; et al. Nanocrystalline intermetallics on mesoporous carbon for direct formic acid fuel cell anodes. *Nat. Chem.* **2010**, 2, 286−293.
42. Muller, K.; Brooks, K.; Autrey, T. Hydrogen storage in formic acid: a comparison of process options. *Energy Fuels* **2017**, 31, 12603− 12611.
43. Bavykina, A. V.; Goesten, M. G.; Kapteijn, F.; Makkee, M.; Gascon, J. Efficient production of hydrogen from formic acid using a covalent triazine framework supported molecular catalyst. *ChemSusChem* **2015**, 8, 809−812.
44. Joó, F. Breakthroughs in Hydrogen Storage — Formic Acid as a Sustainable Storage Material for Hydrogen. *ChemSusChem* **2008**, 1, 805−808.
45. Bi, Q.; et al. An aqueous rechargeable formate-based hydrogen battery driven by heterogeneous Pd catalysis. *Angew. Chem.*, *Int. Ed.* **2014**, 53, 13583.

Chapter 8

COMPARATIVE TECHNO-ECONOMIC ANALYSIS OF RENEWABLE GENERATION OF METHANE USING SUNLIGHT, WATER, AND CARBON DIOXIDE

8.1 Introduction

Thirty-one percent of the primary energy consumed in the United States comes from the burning of natural gas, 70-90% of which is comprised of methane (CH_4).[1] Natural gas is recovered from onshore and offshore natural gas and oil wells, and from coal beds. Currently, the United States has enough supply of dry natural gas to sustain current consumption for 92 years.[2] Meanwhile, California consumes 2.14 MMcf (43.2 million ton) of natural gas per year,[2] over a quarter of which is used to generate electric power[3] and which provides approximately 40% of electrical energy in the state.[4] Since an extensive nationwide storage and distribution network already exists for natural gas, the development of renewable methane could enable rapid and widespread distribution of zero-carbon energy services. Thus for California to meet its renewable portfolio standard, e.g., 60% renewable energy for electricity generation by 2030,[5] and to conserve a limited resource, it is imperative to assess how to develop and deploy technologies for renewable generation of CH_4 in the next few decades.

While an increasing number of power to gas (PtG) projects for CH_4 generation or H_2 generation are being planned globally,[6] the largest source of renewable CH_4 currently being produced in the United States comes from anaerobic digesters that convert cow manure into natural gas. There are currently over 250 such systems in operation with more under construction.[7] In addition to generating CH_4 renewably, these anaerobic digesters also prevent the release of CH_4 – one of the most potent greenhouse gases – into the atmosphere. However, co-location of dairy farms and anaerobic digesters alone will not yield enough renewable methane to replace the current energy demand met by natural gas.[8] For example, the residential natural gas demand in

California is ~25,000 ton/day,[4] while an average dairy farm can only produce ~5 ton/day of natural gas from anaerobic digesters.[7,9] If all potential biogas in California was realized it could power 180,000 homes or 435,000 vehicles, which represents approximately 1.2% of all homes or 3% of all registered vehicles in the state.[8] While these anaerobic digesters co-located with dairy farms may seem to have small production capacity, they are among the largest sources of renewable CH_4 generation in the world.[6] Therefore, it is important to evaluate other more readily scalable technology pathways for renewable generation of CH_4.

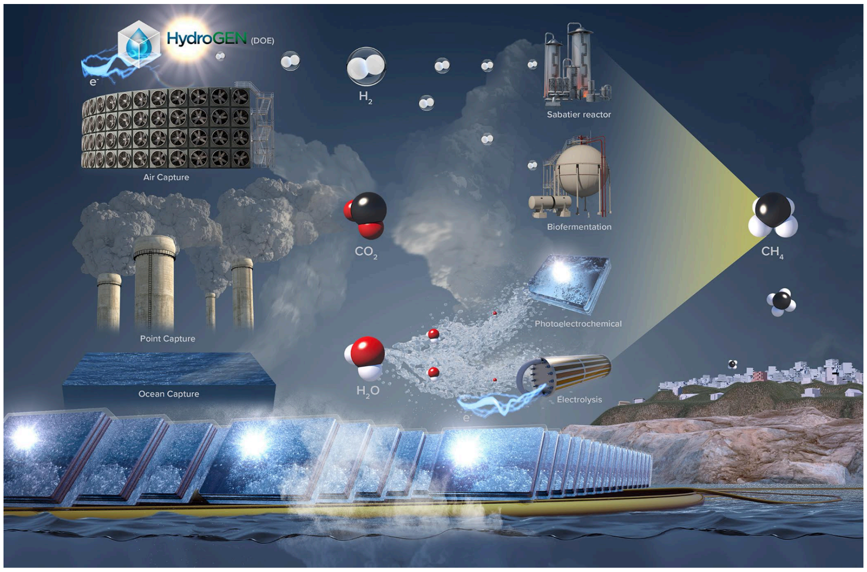

Figure 8.1*: Schematic of various pathways to capture CO_2, generate H_2, and generate CH_4 from sunlight, H_2O, and sunlight.*

Here we outline multiple technology routes for renewable generation of CH_4 from sunlight, water (H_2O), and carbon dioxide (CO_2) (Figure 8.1 and Figure 8.2). We evaluate the technology readiness level (TRL), the demonstrated scale of these candidate technologies, the cost for CH_4 generation, as well as the cost required to provide the necessary feedstocks – H_2O, CO_2, and H_2. We investigate and compare four main CO_2 methanation pathways: thermochemical (via the Sabatier reaction), biochemical, photo-electrochemical, and electrochemical (Figure 8.2). By applying a standard discounted cash flow method to each technology, we assess the current status, future opportunities and compare different technology pathways side-by-side.

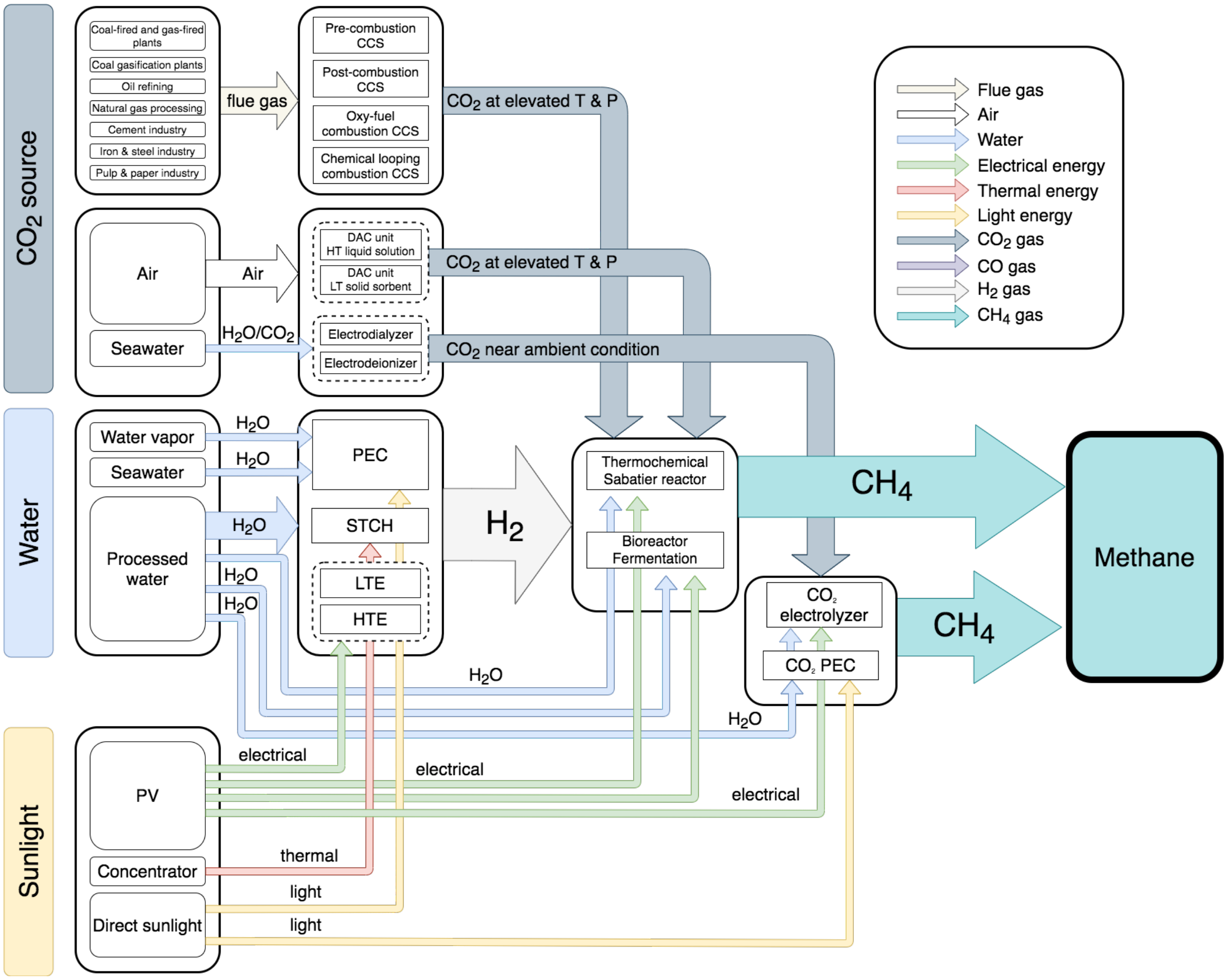

Figure 8.2: *Schematic representation of various technology pathways for sustainable generation of methane from sunlight, water, and carbon dioxide.*

The detailed assumptions for the TEA of technologies evaluated in this study are included in the Supporting Information and the database files used for arriving at detailed cost values are also included in the Supporting Information. The baseline CH_4 production was assumed to be at a scale of 30 kton CH_4 per year (1,500 Mcf per year), or 81 tons CH_4 per day (4 Mcf per day). We calculate the CO_2 capture, H_2 production and water generation rates needed to match this production rate, e.g., H_2 production rate of 40 ton/day, CO_2 capture rate of 245 ton/day and water generation rate of 365 ton/day. No carbon credits were accounted for in this study. The electricity price for all current systems was assumed to be $49/MWh based on the 2018 data from solar utility PV in California.[10] The TRL is evaluated from 1 to 9, where TRL 1-2 corresponds to the observation of basic principles in the academic development, TRL 3-4 to proof-of-concept development at lab scale, TRL 5-6 to process development and system integration from lab to pre-pilot scale, TRL 7-8 to optimization and pre-commercialization scale and TRL 8-9 to commercial operation at scale.[11]

	Method	**Current Cost $/ton**	**TRL**	**Current demonstrated Scale**
CO_2 Capture	Point Source	60-70[81]	8-9	~20,000 ton/day[19]
	Air	277 (115 in future)	7-8	~1 ton/day[14]
	Ocean Water	416 (118 in future)	3-4	~1 kg/day[31]
Water Source	Utility	<0.0003[32]	8-9	~1.6 million ton/day[33]
	Desalination	1.62[35]	8-9	~0.19 million ton/day[35]
	Membrane	150	8-9	~120 ton/day[41]
	Condensation	339	5-6	~6 kg/day[46]
H_2 Generation	Low Temperature Electrolysis (LTE)	3518	8-9	~2.6 ton/day[6,51]
	Photoelectrochemical (PEC)	5294	5-6	<1 kg/day[58]
	High Temperature Electrolysis (HTE)	3956	7-8	~1 ton/day[56]
	Solar Thermo-chemical (STCH)	3706	5-6	<1 kg/day[61]
CH_4 Generation	Electrochemical	(2,500-10,000 with feedstock)	3-4	<1 kg/day[72]
	Photoelectrochemical	(1,500-17,000 with feedstock)	3-4	<1 kg/day[75]
	Thermochemical	199 without feedstock, 2,797 with feedstock	7-8	~5 ton/day[69]
	Biochemical	189 without feedstock, 2,830 with feedstock	7-8	~4 ton/day[65]

Table 8.1: *Summary of cost, TRLs, and demonstrated scale of different technological pathways for renewable generation of methane. The cost of methane generation in the thermochemical and biochemical routes assumed water from utility, CO_2 from direct air capture, and H_2 from LTE as the feedstock.*

The technological pathways considered in this study also included the traditional PtG routes, in which H_2 is produced via electrolysis followed by CH_4 synthesis.[12] In addition, while many reports [13–16] have focused on individual components of a renewable methane system, this work used the state-of-the-art performance metrics from specific technologies, including four advanced water-splitting technologies, CO_2 capture from air and oceanwater, (photo)electrochemical CO_2 reduction into CH_4 and thermo-chemical and biochemical methanation from H_2 and CO_2, so that different technological pathways can be directly compared. Table 8.1 summarized the cost estimate from this study, TRLs and demonstrated scale for each technology, derived from literature reports of renewable generation of CH_4.

8.2 Carbon dioxide capture

Carbon dioxide can be captured from point sources of emission, atmospheric air, or oceanwater. The location of capture often dictates where CH_4 generation can occur. CO_2 capture from point sources, such as oil refineries and the cement industry, is primarily based on chemical absorption and desorption of flue gas with amine solutions.[17,18] Point source CO_2 capture has been demonstrated at a rate of 20,000 ton/day by the Century NG plant in Texas in 2010.[19] For a typical coal fired power plant, a CO_2 capture rate of ~5,000 ton/day provides a CO_2 emission reduction of ~10%.[20] Point source CO_2 capture utilizes relatively mature technology and has been validated by large industrial scale demonstrations at multiple locations, at an average TRL of 8-9. However, point source CO_2 capture is not compatible for a negative CO_2 emission future. A typical carbon capture system for a coal fired power plant reduces the plant energy efficiency, consuming 16% of the generated energy from the plant.[21] Since point source capture has been deployed at large scale in multiple geographical locations, the estimated cost has converged to a narrow cost range of ~\$60-70/ton of CO_2 from reported literature.[22,23]

Carbon dioxide can also be captured from the environment in a dilute form from either atmospheric air or from ocean water. Direct air capture (DAC) has been demonstrated at an early commercial scale.[14,24] The operating principle of DAC from Carbon Engineering includes two sequential loops. In the first loop, CO_2 is captured from the atmosphere using capturing solvents, such as aqueous alkaline solutions, to form aqueous carbonate solutions. The second loop precipitates the carbonate using Ca^{2+}, regenerates the alkaline solution, and releases CO_2 by calcination.[14] The largest system that is currently built based on this technology is capable of capturing roughly 1 ton CO_2/day, which corresponds to a TRL of 7-8.[14] Assuming 803 kWh/ton CO_2 to power calciner, compressor, pumps, etc. with the largest single line item being the air contactor, our TEA model predicts a cost of \$277/ton of CO_2 at a plant capacity of 240 tons/day (Appendix B: Table B2). This is in good agreement with reported values.[14] Assuming an energy input of 555 kWh/ton CO_2, , and cost of electricity of \$10/MWh, we further estimate that the future cost for DAC can be reduced to \$115/ton, upon scaling to a plant capacity of 2,400 ton/day (Appendix B: Table B3).

Capturing CO_2 from oceanwater is an attractive alternative to DAC because the concentration of CO_2 is 140 times higher in oceanwater than it is in the air.[16] The operating principle for oceanwater capture is to shift the CO_2/bicarbonate equilibrium toward dissolved CO_2 by acidifying oceanwater, achieved via a process which lowers pH of oceanwater, such as electrodialysis. The acidified stream is then passed through a liquid–gas membrane contactor, which captures the gaseous CO_2 from the dissolved CO_2 in the aqueous stream. However, oceanwater intake, pre-treatment, and pumping from an offshore site to an onshore capture plant accounts for a major portion of the cost of capturing CO_2 from oceanwater.[16] By either co-locating, with a desalination or electric power plant, or creating an onshore floating system, this cost can be significantly reduced.[25,26] Electrochemical systems for the extraction of CO_2 from oceanwater have been reported previously.[16,27–30] Assuming current density of 100 mA/cm^2, voltage of 1.2V, we estimate the cost to be \$416/ton of CO_2 for a floating CO_2 capture from ocean water system via electrodialysis with shallow intake and a plant capacity of 240 ton/day (Appendix B: Table B4). In the future, by assuming an increased system scale with throughput of 2,700 ton/day, electrodialyzer current density of 1 A/cm^2, and an electrodialyzer voltage of 1.6V, the cost of the system can be reduced to ~ \$118/ton CO_2 (Appendix B: Table B5). Our calculated current cost of \$402/ton of CO_2 for a floating ocean capture system is similar to the value reported by Eisaman et. al.[16] for a system that is co-located with a water desalination plant. Differences in assumptions made for electricity price, electrodialysis performance, pre-treatment processes, and other economic assumptions account for the differences. While this technology appears to be promising, it is in its nascent phase, corresponding to a TRL of 5-6 for oceanwater

CO_2 capture given that the largest system realized to date operates with a throughput of ~1 kg/day in a lab environment.[31]

Encouragingly, the costs for CO_2 capture from either air or oceanwater via the most compelling processes may be able to reach <$100/ton in the future. As CO_2 capture from dilute sources reaches this cost range, large scale CO_2 utilization or storage will not be limited by the physical location of point sources of CO_2 emission. This will mark the transition to an infrastructure that can effectively offset CO_2 emissions from sources that are very difficult to address with a point-of-emission capture approach, such as consumer appliances and vehicles.

8.3 Water generation

Regardless of the methanation technology used, water is required as a feedstock for the hydrogen content in CH_4. A small total amount of water is needed and its cost is low, as compared to other steps in the process; thus the choice of water generation method is largely dependent on the system location. Water can either be purchased at a utility scale, from a desalination plant, captured from the air with a membrane, or condensed out of the air by engineering desired thermal properties of the material.

Utility scale water is the cheapest option due to its scale and government subsidy. The price of ground water depends on the pumping depth, energy source, cost of energy, and the amount of water available. Prices in 2010, according to the Organization for Economic Cooperation and Development (OECD), range from $0.000195/ton in California to $0.00023/ton in Arizona.[32] For our analysis, we used the water cost in California. One of the largest water suppliers is the Los Angeles Department of Water and Power (LADWP), which supplied 632 billion liters of water in 2014.[33] Another water generation option is desalination, in which ocean water is processed with a pretreatment filter to remove large particles, and is then forced under high pressure through a membrane to perform reverse osmosis. The fresh water is then treated for drinking and the brine is discharged to the ocean.[34] Large scale desalination has only been demonstrated at a tenth the scale of utility water sources. For example, in 2015 San Diego deployed a desalination plant that produces 68.9 billion liters of fresh water per year at a cost of \$1.62/ton.[35] While more expensive, water supply from desalination is preferable in locations near the ocean with minimal rainfall. Both of these technologies are assigned a TRL of 8-9 due to their large scale and multiple plant locations.

Alternative routes for water generation involve extraction from atmospheric air. While these methods are more expensive and have lower TRLs, they remove location restrictions for CH_4 production systems. One way to extract water from the air is via a membrane or mesh, which provides a surface upon which water vapor in the atmosphere can condense. These droplets are harvested into a collection area under the influence of gravity drop.[36] This has been shown in numerous studies[37–39] and demonstrated on a larger scale at 12 ton/day.[40] We assign a TRL of 8-9 for the membrane water capturing technology.[41] The cost of water obtained from membrane capture is estimated to be \$60 /ton at a plant capacity of 365 ton/day (Appendix B: Table B6). Another way to remove water from the air is by using radiatively cooled surfaces to condense water out of the air.[42–45] In these systems, materials are designed to maximize infrared emission properties and allow the surface to be cooler than ambient temperature. This change in temperature between surface and ambient promotes the condensation of atmospheric water on the surface which can then be harvested.[36] Currently, condensation via radiative cooling is the most expensive option among those we considered, due to the high capital expense for purchase of the materials to capture water at a relevant scale. The largest demonstration to date is by OPUR (International Organization for the Utilization of Dew), which has shown a system that can generate 0.006 ton/day, which we assign a TRL of 5-6.[45,46] We estimate the cost of water using radiative cooling to be \$339/ton at a scale of 365 ton/day (Appendix B: Table B7).

Despite the significant cost differences between various water generation strategies, the cost of water remains lower than other costs of a renewable methanation system. For low temperature electrolysis if water produced via membrane air capture is used rather than utility water the cost of hydrogen increases from \$3.48/kg to \$4.53/kg. It is notable that no matter where a methane system is deployed, near a utility water source, ocean, or desert that generating water is likely not to be a limiting factor.

8.4 Hydrogen generation

CO_2 and water are the main raw feedstocks for direct methanation pathways (electrochemical and photoelectrochemical); however, indirect methanation pathways (thermochemical and bio-methanation) (Figure 8.2) rely on reaction between CO_2 and H_2. It is therefore appropriate to assess the technology options for renewable H_2 generation from water. The renewable generation of H_2 is also the most critical step in all the PtG studies.[6,12,47–49] We focus on four H_2 generation technologies, including low temperature electrolysis (LTE), photoelectrochemical (PEC), high temperature electrolysis (HTE), and solar thermo-chemical (STCH). We used H2A analyses guidelines and applied the DOE financial and operational assumptions that are adjusted to our case studies to calculate the cost of hydrogen generated using these technologies.[50] All technologies are evaluated at a design capacity of 40-45 ton H_2/day. This average production will therefore maintain the 81 tons CH_4 per day (4 Mcf CH_4 per day) production required by our baseline assumptions.

The largest scale demonstrated for LTE thus far is 10 MW, corresponding to ~2.6 ton/day generation rate.[51] MW scale LTE systems were also deployed world-wide, at an average TRL of 8-9.[52] In LTE, H_2 is produced at the cathode and O_2 at the anode electrochemically under a voltage bias. The cathode and anode are separated by a membrane separator.[53] Three types of LTE systems have been developed including alkaline water electrolysis, proton exchange membrane based water electrolysis and hydroxide exchange membrane based water electrolysis.[54] State of the art proton exchange membrane (PEM) cells operate at ~2 A cm^{-2} and ~2 V with a stack level efficiency of 55 kWh/kg of H_2.[54] We assume on operating voltage of 1.9 V/cell, current density of 2 A/cm^2, stack life of 7 years.[15,50] From this we estimate the current cost of a PEM system at a design capacity of 40 ton/day is \$3,518/ton (Appendix B: Table B8). The values that we calculated are similar to those calculated previously, but significantly lower than those calculated by the DOE case study.[15] The discrepancy was largely due to the higher cost of electricity assumed by the DOE of \$87/MWh and the higher after-tax real IRR of 8%.[50,53] A sensitivity analysis (Appendix B: Figure B1) for the impact of electricity cost, energy efficiency, capital expenditures and after-tax real IRR on the cost of hydrogen indicates that presentably the electricity cost was the largest levers among those variables.

High temperature electrolysis (HTE) is another H_2 production method using electricity. The operating principle for HTE is very similar to LTE. High temperature electrolysis cells include a cathode for water reduction, an anode for oxygen generation and a solid ceramic material, which is used as the electrolyte to selectively conduct oxygen ions (O^{2-}) at ~700°–800°C.[55] It has been demonstrated at a scale of 2.6 MW, corresponding to ~1 ton H_2/day.[56] Assuming an energy usage of 51 kWh/kg H_2,[52] we estimate the cost of HTE system to be $3956 /ton H_2 (Appendix B: Table B9), which was similarly less than the value calculated by the DOE, $4660/ton.[50] Both LTE and HTE use electricity for H_2 generation, as a result, the electricity price has a large influence on the cost of H_2 from both technologies. For instance, at a scale of 40 ton H_2/day, LTE system will produce H_2 at $2410/ton with an electricity price of $30/MWh, whereas at an electricity price of $60/MWh, the cost of H_2 is $4160/ton.

Photoelectrochemical (PEC) and solar thermochemical processes (STCH) produce H_2 from sunlight and water. Photoelectrochemical water-splitting cells integrate multiple functional materials and couple water oxidation and hydrogen evolution reactions to produce molecular hydrogen and oxygen. Key PEC processes include light absorption, photo-generated carrier transport, electrocatalysis, ionic transport and product separation.[57] Photoelectrochemical devices operate at much lower current densities, typically in the range of ~10-100 mA cm^{-2}, relative to LTE or HTE, since the production rate is matched to the solar flux. State of the art PEC devices have exhibited a solar to hydrogen conversion efficiency of 19.3%.[58] Currently PEC devices have only been demonstrated at a laboratory scale <1 kg/day H_2, giving it a TRL of 5-6.[13] Assuming a solar to hydrogen (STH) efficiency of 10%, photovoltaic (PV) efficiency of 19.1%, cost per unit area of $161/m^2 (which includes the cost of PV cells, catalyst, membrane, chassis, water processing, gas processing, power electronics, and control system),[13] the current cost of H_2 from PEC is estimated to be $5294/ton (Appendix B: Table B10). However, the projected price drops of photovoltaic materials, dramatic improvements in membrane costs, and increases in solar to fuel efficiency are projected to lead to a significantly reduced cost for H_2. For example, with an STH efficiency of 20%, PV efficiency of 25%, cost per unit area of \$119/m^2 (which includes the cost of PV cells, catalyst, membrane, chassis, water processing, gas processing, power electronics, and control system), we estimate the cost of PEC H_2 can reach \$1775/ton in future (Appendix B: Figure B2, Appendix B: Table B11). The estimated value is lower than values calculated by Shaner, et al.,[13] due to a higher assumed solar capacity factor of 28.4% (for California) in our case study, as opposed to 20%, and more up to date value of \$0.37/W[59] for the cost/Watt of photovoltaic panels (See Supporting Information).

Solar thermochemical (STCH) cycles use the heat from the sunlight to produce hydrogen and oxygen from water. STCH uses two-step redox active metal oxide thermochemical cycles to produce H_2 and O_2 sequentially in two different chemical reactions.[60] STCH has been demonstrated at ~1 kg/day, giving it a TRL of 5-6.[61] Using an economic model adapted from the U.S. DOE H2A analysis,[50,62] assuming an STH efficiency of 20%, plant capacity factor of 90%, we estimated H_2 cost from STCH to be \$3706/ton for a system with a design capacity of 45 ton H_2/day (Appendix B: Table B12).

H_2 generation is the largest cost driver for indirect renewable CH_4 generation and is expected to play a critical role in a broader setting in future energy systems. However, it is important to realize that presently the largest demonstrated H_2 generation project even with the highest TRL technology, e.g., low temperature electrolysis, is limited at < 3 ton of H_2 per day. Note that a single digester co-located with a dairy farm produces on average ~5 ton of CH_4 per day, which translates to ~2.5 ton of H_2 per day required based on the CO_2 methanation reaction. Hence, it is not surprising to note that large electrolysis projects for renewable generation of H_2, such as a 156 ton H_2/day system in France,[63] have been planned in the near future.[6] However, converting H_2 to CH_4 has its own advantages. CH_4 has ~3.5 times higher storage capacity that H_2, and H_2 is significantly more difficult to store since it is corrosive and leads to embrittlement of container materials.[64] Considering this last point, many costly modifications and component replacements would be needed in the legacy gas piping, storage, and distribution infrastructure to make it compatible with H_2 distribution rather than methane distribution. These infrastructure utilization considerations represent a strong argument in favor of renewable methane as an alternative to H_2, as a gas energy carrier for widespread distribution.

8.5 Methane generation

Having surveyed pathways to generate the raw feedstocks needed for renewable methane synthesis, we now analyze and compare different methanation pathways. We separate these into two main categories: i) indirect CO_2 to CH_4 conversion via thermochemical and bio-methanation methods, and ii) direct CO_2 to methane conversion via electrochemical and PEC methods.

The two indirect methane conversion methods that we focus on are thermochemical methanation via the Sabatier reaction and biochemical methanation. Biochemical methanation has been demonstrated at 5MW scale, or ~4.3 ton/day from Electrochaea.[65] We assign a TRL of 7-8 for this technology. The basic technology relies on anaerobic microorganisms called methanogenic archaea that are able under certain conditions to produce CH_4 from H_2 and CO_2 with high selectivity.[66] These organisms exist naturally in the environment and have been selectively evolved for higher selectivity in these reactors. In this process, the archaea are heated up to 60 °C and pressurized to ~10 bar and then fed CO_2 and H_2.[65] The organisms can then self-sustain the heat and highly selectively convert the CO_2 and H_2 to CH_4. Assuming a 99% efficient biological methanation reactor[65], biochemically produced CH_4 is estimated to have a cost of $189/ton without the feedstock cost, and $2830/ton (Appendix B: Table B13), assuming that the H_2 is generated via LTE and the CO_2 is captured from air.[67]

We focus on the Sabatier reaction as a method for thermochemical methanation. Similar to the biomethanation route, CO_2 is reacted with H_2; however instead of using a micro-organism the reactor is heated to ~350 °C in the presence of a catalyst (i.e. Ni). The CO_2 and H_2 then react exothermically to produce CH_4.[68] The largest Sabatier reactor built thus far is a 6MW reactor by Audi at their Audi e-gas facility in germany.[69] We estimate a TRL of 7-8 for this technology. Assuming a conversion efficiency of 93%, we calculate the cost of thermochemical methanation to be $193/ton CH_4 without the feedstock cost, and $2791/ton CH_4 (Appendix B: Table B14), using H_2 generated via LTE and CO_2 captured from air.

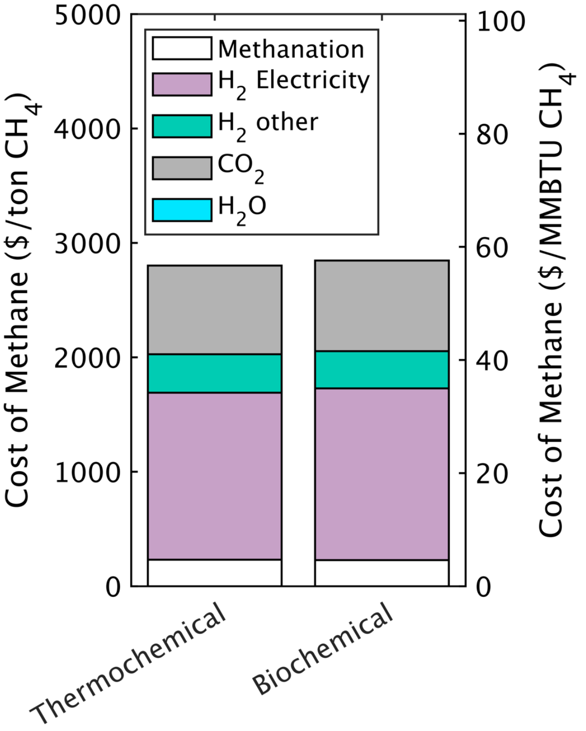

Figure 8.3*: The cost breakdown of the green methane from thermochemical and biochemical processes. The feedstock of the thermochemical and biochemical process assumed water from utility, CO_2 from direct air capture, and H_2 from LTE with an electricity price of \$49/MWh.*

Figure 8.3 shows cost breakdown for the indirect methanation methods, assuming H_2 generated via PEM electrolysis, CO_2 captured from the atmosphere and H_2O from a utility source. The cost for CO_2 capture and the methanation process (both thermochemical and biochemical) are small, and it is clear that the cost of renewable H_2 generation is the largest cost component for the indirect methanation pathways. As shown in Figure 8.3 and Appendix B: Figure B1, the cost of electricity remains the largest cost and largest lever for renewable H_2 generation via LTE, which is consistent with recent DOE reports.[62]

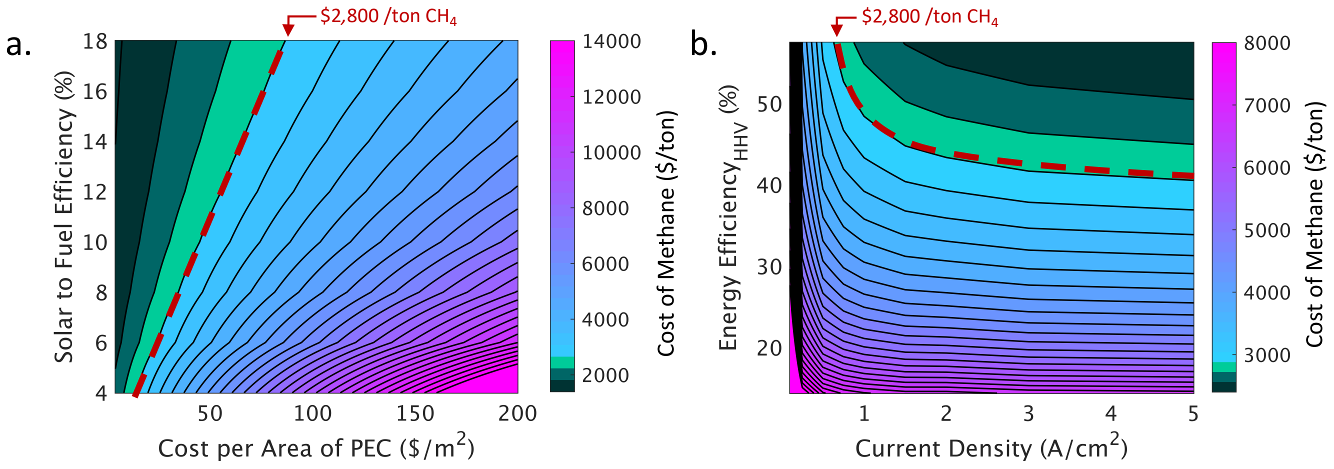

***Figure 8.4**: Cost of methane from (a) photoelectrochemical (PEC) and (b) electrochemical methanation processes as a function of key performance metrics in those technologies. (a) The cost of PEC methanation as a function of the STF conversion efficiency and the cost per area of PEC material. (b) The cost of electrochemical methanation as a function of the energy efficiency of the device and the operating current density. The green region in both plots shows where the cost is equal to or less than thermochemical or biochemical methanation. For all systems compared the cost of CO_2 is assumed to be $278/ton and the electricity price is $49/MWh.*

For the direct methane conversion methods, we first consider an electrochemical system powered by grid electricity at a high-capacity factor, similar to LTE H_2 electrolysis. The main differences between an H_2 electrolysis and a CO_2 electrochemical system comes from the consideration of charge transfer in electrocatalysis, which requires 8 electrons per CH_4 molecule from CO_2 as opposed to the 2 electrons needed for generation of an H_2 molecule. Currently, the multi-electron and proton reaction still faces significant challenges in selectivity, activity and durability.[70,71] One of the highest performing electrolysis systems developed, exhibited a Faradaic Efficiency (FE) of 85% for CH_4 generation with an overpotential of 2.8 V at ~25 mA/cm^2.[72] Electrochemical CO_2 conversion devices have also exhibited high operating current densities up to 700 mA/cm^2 in other reduction products such as CO and ethylene.[73,74] The cost for direct electrochemical methanation process as a function of the operating current density and the energy efficiency of cell was illustrated in Figure 8.4a. A range of operating current density from 10 mA/cm^2 to 5 A/cm^2 and a range of Faradaic efficiency from 50 to 100%

were considered for the direct electrochemical CH_4 generation. Note that the overall cell efficiency is a combination of the Faradaic efficiency of the reaction and the operating cell voltage. At an operating current density of 100 mA/cm^2, and an energy efficiency of 15%, the cost of CH_4 was estimated to be $10,700/ton CH_4 (Appendix B: Table B15), assuming $278/ton CO_2 captured from the atmosphere, and a plant size of 81 ton/day. If we assume a more optimistic device performance of 5 A/cm^2, and an energy efficiency of 56%, the cost of CH_4 was estimated to be $2,420/ton CH_4 (Appendix B: Table B15), assuming $278/ton CO_2 captured from the atmosphere, and a plant size of 81 ton/day. Based on the demonstrated current density and energy efficiency in the literature, the electrochemical methanation is not competitive with indirect methanation techniques. It would require very significant advancement in materials and device development to be cost competitive to the indirect methanation processes.

Photoelectrochemical (PEC) methanation operates using the similar mechanisms as PEC H_2 generation except that the electrons are reducing CO_2 instead of H_2O. Both PEC H_2 and PEC methanation use water as the proton source. Photoelectrochemical (PEC) methanation also faces similar challenges as the electrochemical methanation, specifically the fact that producing methane requires 8 electrons, and since PEC devices are limited by the solar flux, this limits the rate of methanation. A PEC methanation device has been realized with a solar to fuel efficiency (STF) of 0.1%.[75] While PEC methanation has significant challenges in the activity and selectivity, other PEC CO_2 reduction devices, such as CO_2 reduction to CO or formate, have reached STF conversion efficiency of >10%.[76] The cost for direct PEC methanation pathway as a function of the cost per area and the STF conversion efficiency was illustrated in Figure 8.4b. A range of STF conversion efficiency from 4 to 18% was considered for direct PEC CH_4 generation. At an STF of 4% for the PEC methanation device, and a $200/m^2 constructed in a PEC type 3 configuration,[13] we estimate the cost of CH_4 to be to be $16,930/ton (Appendix B: Table B16). If we assume more optimistic device metrics of an STF of 18% for the PEC methanation device, and a $10/m^2 constructed in a PEC type 3 configuration,[13] we estimate the cost of CH_4 to be to be $1,500/ton (Appendix B: Table B16). As shown in Figure 8.3b, for PEC methanation to be competitive with indirect methanation, the cost of the system per square meter must be significantly reduced as well as improvements in efficiency.

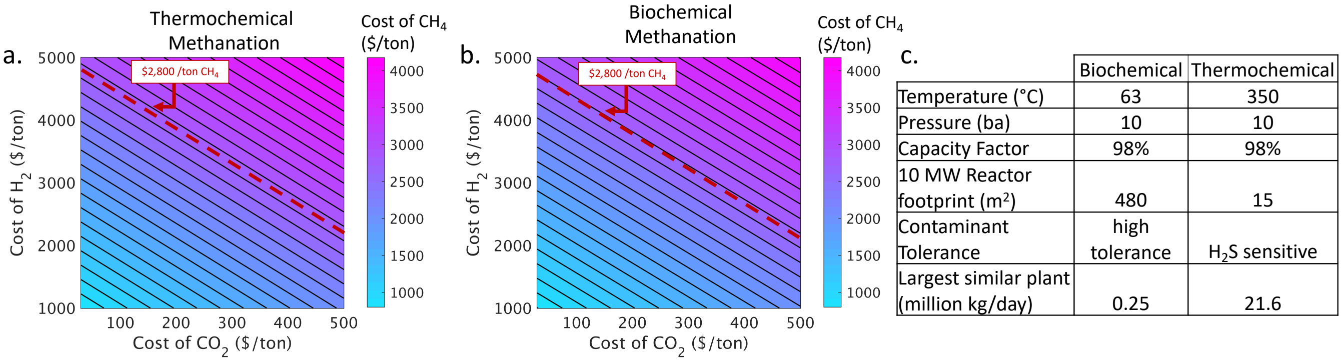

	Biochemical	Thermochemical
Temperature (°C)	63	350
Pressure (ba)	10	10
Capacity Factor	98%	98%
10 MW Reactor footprint (m²)	480	15
Contaminant Tolerance	high tolerance	H_2S sensitive
Largest similar plant (million kg/day)	0.25	21.6

***Figure 8.5**: Cost of the (a) thermochemical and (b) biochemical methanation processes as a function of H_2 cost and CO_2 cost. (c) A side-by-side comparison between the biochemical methanation process and the thermochemical methanation process.*

Figures 8.5a-b show how the cost of thermochemical and biochemical methanation is affected by the cost of the feedstocks. The cost of both approaches is very close, due to the similarity of their CapEx's and that the CapEx makes up 75% of the methanation cost. The CapEx's are similar because much of the equipment required for both systems is the same, items such as compressors, reactor, pumps, piping, etc. The heterogeneous catalysts in the thermochemical methanation and the anaerobic microorganisms in the biochemical methanation were not the main cost driver for methanation. Other factors to consider are listed in Figurer 8.5c. One advantage of biochemical methanation is its high tolerance for contaminants, whereas catalysts for the Sabatier reaction are highly sensitive to H_2S.[48,77] This advantage is most important when the CO_2 is being captured from point sources, however CO_2 captured from the air or oceanwater environment is likely to result in a very pure CO_2 stream, making this difference less important. Another advantage of biochemical methanation is the lower operating temperature, making it possibly more suitable for small scale reactors.[65,78] However, thermochemical methanation may be favorable when considering scaling of methanation to a large capacity. First, the required areal footprint of the reactor is significantly smaller.[49,67,79] Second, examination of scales of similar processes via bio- vs. thermochemical processes such as Fischer Tropsch via thermochemical or bio ethanol for biochemical methanation, there is nearly a 100x difference in scale at which these processes have been demonstrated, suggesting it may be significantly easier to scale up thermochemical methanation than biochemical methanation.

8.6 Conclusion

In summary, thermochemical or biochemical methane generation using CO_2 captured from point sources and H_2 produced from low temperature electrolysis powered by renewables turned out to be the most cost competitive pathway in the short term. The cost of renewable H_2 is found to be the dominant cost component of renewable methane synthesized by indirect methanation. We also found that the cost of CO_2 from dilute sources (air or oceanwater) is likely to be competitive with CO_2 from point sources as the technology advances, and the cost of CO_2 will not be a cost driver for CH_4 generation. The largest demonstrated scale for direct CO_2 capture from air (~1 ton of CO_2 per day), the renewable H_2 generation via low temperature electrolysis (~2.6 ton of H_2 per day), the thermo-chemical methanation (~5 ton of CH_4 per day) and the biochemical methanation (~4 ton of CH_4 per day) are all very small, and are dwarfed by a single anaerobic digester co-located with a dairy farm. As cost of the renewable electricity continued to decrease, at an electricity price of $10/MWh, we estimated that an overall optimistic cost of $983/ton of CH_4 in the future, which is then cost competitive to the market CH_4 price in certain regions of the world,[80] can be achieved. In the long term, significant improvements of key performance metrics in electrochemical and photoelectrochemical methanation can provide unique alternatives to the short-term pathway winners with more energy resilience and ultimately achieve CH_4 production cost of < $1000/ton.

BIBLIOGRAPHY CHAPTER 8

1. U.S. Energy Information Administration. *August 2020, Monthly Energy Review. United States Energy Information Administration Monthly Review* 0035, (2020).
2. United States Energy Information Administration. *EIA Annual Energy Outlook 2020. Annual Energy Outlook* (2020).

3. U.S. Energy Information Administration. *Natural Gas Consumption by End Use.* (2020).
4. United States Energy Information Administration. *California State Energy Profile. U.S. Energy Information Administration* (2020).
5. *California Renewables Portfolio Standard Program. California Legislative Information* (2018).
6. Thema, M., Bauer, F. & Sterner, M. Power-to-Gas: Electrolysis and methanation status review. *Renew. Sustain. Energy Rev.* **2019**, 112, 775–787.
7. AgSTAR. *Livestock Anaerobic Digester Database.* (2020).
8. American Biogas Council. *Biogas State Profile: California.* (2015).
9. GMI. *Successful Applications of Anaerobic Digestion From Across the World. Global Methane Initiative (GMI)* (2013).
10. National Renewable Energy Laboratory. *2018 Annual Technology Baseline.* (2018).
11. NASA. Technology readiness levels introduction. (2004). Available at: https://web.archive.org/web/20051206035043/http://as.nasa.gov/aboutus/trl-introduction.html. (Accessed: 24th January 2021)
12. Peters, R., Baltruweit, M., Grube, T., Samsun, R. C. & Stolten, D. A techno economic analysis of the power to gas route. *J. CO_2 Util.* **2019**, 34, 616–634.
13. Shaner, M. R., Atwater, H. A., Lewis, N. S. & McFarland, E. W. A comparative technoeconomic analysis of renewable hydrogen production using solar energy. *Energy Environ. Sci.* **2016**, 9, 2354–2371.
14. Keith, D. W., Angelo, D. St., Holmes, G. & Heidel, K. A process for capturing CO_2 from the atmosphere. *Joule* **2018**, 2, 1573–1594.
15. Glenk, G. & Reichelstein, S. Economics of converting renewable power to hydrogen. *Nat. Energy* **2019**, 4, 216–222.
16. Eisaman, M. D. *et al.* Indirect ocean capture of atmospheric CO_2: Part II. Understanding the cost of negative emissions. *Int. J. Greenh. Gas Control* **2018**, 70, 254–261.
17. Sang Sefidi, V. & Luis, P. Advanced Amino Acid-Based Technologies for CO_2 Capture: A Review. *Ind. Eng. Chem. Res.* **2019**, 58, 20181–20194.
18. Hu, X. *et al.* Toward Solvent Development for Industrial CO_2 Capture by Optimizing the Catalyst-Amine Formulation for Lower Energy Consumption in the Solvent Regeneration Process. *Energy and Fuels* (2019). doi:10.1021/acs.energyfuels.9b02874
19. Carbon Capture and Sequestration Technologies @ MIT. Century Plant Fact Sheet: Commercial EOR using Anthropogenic Carbon Dioxide. (2019). Available at: http://18.9.60.74/tools/projects/century_plant.html#:~:text=Comments%3A Century plant is the,projects in the Permian Basin. (Accessed: 30th October 2020)
20. Evans, S. Around the world in 22 carbon capture projects. *Carbon Brief* (2014). Available at: https://www.carbonbrief.org/around-the-world-in-22-carbon-capture-projects. (Accessed: 20th October 2020)
21. Hammond, G. P. & Spargo, J. The prospects for coal-fired power plants with carbon capture and storage: A UK perspective. *Energy Convers. Manag.* **2014**, 86, 476–489.
22. Chou, V., Iyengar, A. K. S., Shah, V. & Woods, M. *Cost and performance baseline for fossil energy plants: Report Number DOE/NETL-2007/1281.* (2015).
23. Fout, T. *et al. Cost and Performance Baseline for Fossil Energy Plants Volume 1a: Bituminous Coal (PC) and Natural Gas to Electricity Revision 3. National Energy Technology Laboratory (NETL)* (2015).
24. Wurzbacher, J. A., Gebald, C., Piatkowski, N. & Steinfeld, A. Concurrent separation of CO_2 and H_2O from air by a temperature-vacuum swing adsorption/desorption cycle. *Environ. Sci. Technol.* **2012**, 46, 9191–9198.
25. Eisaman, M. D. Negative Emissions Technologies: The Tradeoffs of Air-Capture Economics. *Joule* **2020**, 4, 516–520.
26. Patterson, B. D. *et al.* Renewable CO_2 recycling and synthetic fuel production in a marine environment. *Proc. Natl. Acad. Sci. U. S. A.* **2019**, 116, 12212–12219.

27. Eisaman, M. D. *et al.* CO_2 extraction from seawater using bipolar membrane electrodialysis. *Energy Environ. Sci.* **2012**, 5, 7346–7352.
28. de Lannoy, C. F. *et al.* Indirect ocean capture of atmospheric CO_2: Part I. Prototype of a negative emissions technology. *Int. J. Greenh. Gas Control* **2018**, 70, 243–253.
29. Willauer, H. D., Dimascio, F., Hardy, D. R. & Williams, F. W. Feasibility of CO_2 extraction from seawater and simultaneous hydrogen gas generation using a novel and robust electrolytic cation exchange module based on continuous electrodeionization technology. *Ind. Eng. Chem. Res.* **2014**, 53, 12192–12200.
30. Willauer, H. D., DiMascio, F., Hardy, D. R. & Williams, F. W. Development of an Electrolytic Cation Exchange Module for the Simultaneous Extraction of Carbon Dioxide and Hydrogen Gas from Natural Seawater. *Energy and Fuels* **2017**, 31, 1723–1730.
31. Digdaya, I. A. *et al.* A direct coupled electrochemical system for capture and conversion of CO_2 from oceanwater. *Nat. Commun.* **2020**, 11, 1–10.
32. Wichelns, D. *Agricultural Water Pricing : United States*. (2010).
33. LADWP. *Briefing Book 2018-19*. (2019).
34. Water Corporation. *Water Forever, towards climate resilience*. (2009).
35. San Diego County Water Authority. *Seawater Desalination*. (2015). doi:10.1002/9780470276280.ch3
36. Jarimi, H., Powell, R. & Riffat, S. Review of sustainable methods for atmospheric water harvesting. *Int. J. Low-Carbon Technol.* **2020**, 15, 253–276.
37. Kim, Hyunho, Yang, S. *et al.* Water harvesting from air with metal-organic frameworks powered by natural sunlight. *Science* **2017**, 434, 430–434.
38. Schemenauer, R. S. & Cereceda, P. A proposed standard fog collector for use in high-elevation regions. (1387).
39. Klemm, O. *et al.* Fog as a fresh-water resource: Overview and perspectives. *Ambio* **2012**, 41, 221–234.
40. Drupps Electric. The Value of Water. (2020). Available at: https://www.drupps.com/web/content/2197/. (Accessed: 3rd November 2020)
41. Drupps Electric. An Adaptable Solution to Water Security. (2020). Available at: https://www.drupps.com/products. (Accessed: 1st October 2020)
42. Maestre-Valero, J. F., Ragab, R., Martínez-Alvarez, V. & Baille, A. Estimation of dew yield from radiative condensers by means of an energy balance model. *J. Hydrol.* **2012**, 460–461, 103–109.
43. Muselli, M., Beysens, D. & Milimouk, I. A comparative study of two large radiative dew water condensers. *J. Arid Environ.* **2006**, 64, 54–76.
44. Khalil, B. *et al.* A review: dew water collection from radiative passive collectors to recent developments of active collectors. *Sustain. Water Resour. Manag.* **2016**, 2, 71–86.
45. Zhou, M. *et al.* Accelerating vapor condensation with daytime radiative cooling. *arxiv* 6 (2019). doi:10.1117/12.2525125
46. International Organization for Dew Utilization. Condensers for sale. (2019). Available at: https://www.opur.fr/angl/noscondenseurs_ang.htm. (Accessed: 3rd November 2020)
47. Kauw, M., Benders, R. M. J. & Visser, C. Green methanol from hydrogen and carbon dioxide using geothermal energy and/or hydropower in Iceland or excess renewable electricity in Germany. *Energy* **2015**, 90, 208–217.
48. Becker, W. L., Penev, M. & Braun, R. J. Production of synthetic natural gas from carbon dioxide and renewably generated hydrogen: A techno-economic analysis of a power-to-gas strategy. *J. Energy Resour. Technol.* **2019**, 141.
49. Rönsch, S. *et al.* Review on methanation - From fundamentals to current projects. *Fuel* **2016**, 166, 276–296.
50. NREL. *H2A: Hydrogen Analysis Production Models*. (2018).
51. FuelCellsWorks. World's Largest Hydrogen Plant Opens in Fukushima. (2020).

52. James, B. D., Colella, W. G. & Moton, J. M. *Techno-Economic Analysis of Hydrogen Production Pathways. Stategic Analysis* (2013).
53. James, B., Colella, W. & Moton, J. *PEM Electrolysis H2A Production Case Study Documentation*. (2013).
54. Shiva Kumar, S. & Himabindu, V. Hydrogen production by PEM water electrolysis – A review. *Mater. Sci. Energy Technol.* **2019**, 2, 442–454.
55. Elder, R., Cumming, D. & Mogensen, M. B. *High Temperature Electrolysis. Carbon Dioxide Utilisation: Closing the Carbon Cycle: First Edition* (Elsevier B.V., 2015). doi:10.1016/B978-0-444-62746-9.00011-6
56. Lonis, F., Tola, V., Cascetta, M., Arena, S. & Cau, G. Performance evaluation of an integrated energy system for the production and use of renewable methanol via water electrolysis and carbon dioxide hydrogenation. in *AIP Conference Proceedings* **2019**, 2191.
57. Joy, J., Mathew, J. & George, S. C. Nanomaterials for photoelectrochemical water splitting – review. *Int. J. Hydrogen Energy* **2018**, 43, 4804–4817.
58. Cheng, W. H. *et al.* Monolithic Photoelectrochemical Device for Direct Water Splitting with 19% Efficiency. *ACS Energy Lett.* **2018**, 3, 1795–1800.
59. Woodhouse, M., Smith, B., Ramdas, A. & Robert Margolis. *Crystalline Silicon Photovoltaic Module Manufacturing Costs and Sustainable Pricing: 1H 2018 Benchmark and Cost Reduction Roadmap. National Renewable Energy Laboratory* (2020).
60. Steinfeld, A. Solar thermochemical production of hydrogen - A review. *Sol. Energy* **2005**, 78, 603–615.
61. Mcdaniel, A. *et al. High Efficiency Solar Thermochemical Reactor for Hydrogen Production*. (2017).
62. Peterson, D. & Miller, E. *Hydrogen and Fuel Cells Program Record - Hydrogen Production Cost from Solid Oxide Electrolysis. Hydrogen and Fuel Cells Program Record - Hydrogen Production Cost from Solid Oxide Electrolysis* (2016).
63. Business Portal Norwegen. Nel ASA:Framework agreement for six hydrogen plants in France. 2019, (2017).
64. Amos, W. A. *Cost of Storing and Transporting Hydrogen. NREL* (1998).
65. Electrochaea. *Applications of Electrochaea's BioCat biomethanation technology*. (2018).
66. Thauer, R. K., Kaster, A. K., Seedorf, H., Buckel, W. & Hedderich, R. Methanogenic archaea: Ecologically relevant differences in energy conservation. *Nat. Rev. Microbiol.* **2008**, 6, 579–591.
67. Electrochaea. *Power-to-Gas via Biological Catalysis (P2G-Biocat)*. (2017).
68. Veselovskaya, J. V., Parunin, P. D. & Okunev, A. G. Catalytic process for methane production from atmospheric carbon dioxide utilizing renewable energy. *Catal. Today* **2017**, 298, 117–123.
69. Strategieplattform Power to Gas. Audi e-gas project. (2014).
70. Luna, P. De, Hahn, C., Higgins, D. & Jaffer, S. A. What would it take for renewably powered electrosynthesis to displace petrochemical processes? **2019**, 3506, 1–9.
71. Nitopi, S. *et al.* Progress and Perspectives of Electrochemical CO_2 Reduction on Copper in Aqueous Electrolyte. *Chem. Rev.* **2019**, 119, 7610–7672.
72. Qiu, Y. L. *et al.* Copper Electrode Fabricated via Pulse Electrodeposition: Toward High Methane Selectivity and Activity for CO_2 Electroreduction. *ACS Catal.* **2017**, 7, 6302–6310.
73. García de Arquer, F. P. *et al.* CO_2 electrolysis to multicarbon products at activities greater than 1 A cm^{-2}. *Science* **2020**, 367, 661–666.
74. De Luna, P. *et al.* What would it take for renewably powered electrosynthesis to displace petrochemical processes? *Science* **2019**, 364.
75. Fu, Q. *et al.* Hybrid solar-to-methane conversion system with a Faradaic efficiency of up to 96%. *Nano Energy* **2018**, 53, 232–239.
76. Cheng, W. H. *et al.* CO_2 Reduction to CO with 19% Efficiency in a Solar-Driven Gas Diffusion Electrode Flow Cell under Outdoor Solar Illumination. *ACS Energy Lett.* **2020**, 470–476.
77. Spath, P. *et al. Biomass to Hydrogen Production Detailed Design and Economics Utilizing the Battele Columbus Laboratory Indirectly-Heated Gasifier.* (2005).
78. Ghaib, K. & Ben-Fares, F. Z. Power-to-Methane: A state-of-the-art review. *Renew. Sustain. Energy Rev.*

2018, 81, 433–446.

79. Martin, M. R., Fornero, J. J., Stark, R., Mets, L. & Angenent, L. T. A single-culture bioprocess of methanothermobacter thermautotrophicus to upgrade digester biogas by CO_2-to-CH_4 conversion with H2. *Archaea* 2013, (2013).
80. US Energy Information Administration. *United Statets Nattural Gas Industrial Price.* (2020).
81. Matsumiya, N., Teramoto, M., Kitada, S. & Matsuyama, H. Evaluation of energy consumption for separation of CO_2 in flue gas by hollow fiber facilitated transport membrane module with permeation of amine solution. *Sep. Purif. Technol.* **2005**, 46, 26–32.

Chapter 9

CONCLUSIONS

9.1 Conclusion

Throughout this thesis we have explored a variety of different ways to control and enhance the CO_2 reduction reaction, as well as analyzed systems that synergies between different CO_2 capture and conversion technologies.

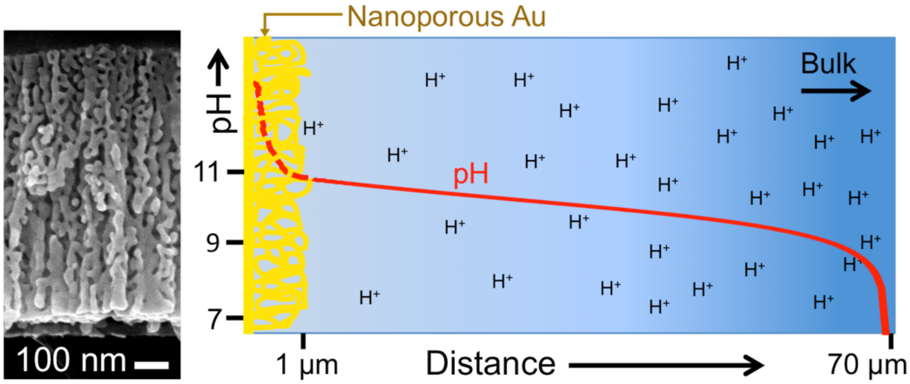

Figure 9.1: *shows an SEM and a schematic of a nanoporous gold catalyst. On the left is a cross sectional SEM of a 25% gold nanoporous gold sample. On the right is a schematic of the nanoporous gold during electroreduction conditions. The red curve represents the pH in solution as a function of distance from the electrode surface. The solid part of the red curve has been calculated based on experimental conditions and the dashed portion of the red line is an assumed pH inside of the nanoporous gold.*

In Chapter 2 we discussed how nanoporous gold (np-Au) films, with pore sizes ranging from 10 nm to 30 nm, represent promising electrocatalytic architectures for the CO_2 reduction reaction due to their large electrochemically active surface area, relative abundance of grain boundaries, and ability to support pH gradients inside the nanoporous network. Electrochemical studies show that np-Au films support partial current densities for the conversion of CO_2 to CO in excess of 6 mA cm^{-2} at a Faradaic efficiency of ~99% in aqueous electrolytes (50 mM K_2CO_3 saturated with CO_2). Moreover, np-Au films are able to maintain Faradaic efficiency greater than 80% for CO production over prolonged periods of continuous operation (110 h). Electrocatalytic experiments at different electrolyte concentrations demonstrate that the pore diameter of nanoporous cathodes represents a critical parameter for creating and controlling local pH gradients inside the porous network of metal ligaments (Figure 9.1). These results demonstrate the merits of nanoporous metal films for the CO_2 reduction reaction and offer an interesting architecture for highly selective electrocatalysis capable of sustaining high catalytic currents over prolonged periods.

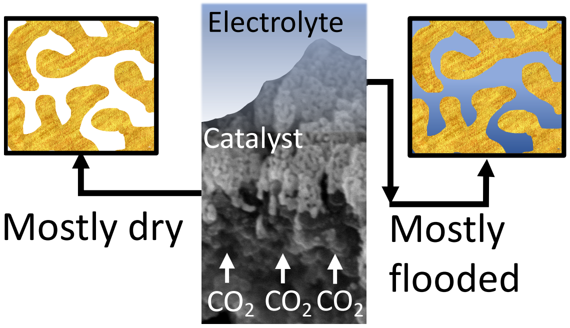

Figure 9.2: *shows an SEM and a schematic of a nanoporous gold gas diffusion electrode system with arrows indicating which regions of the catalyst are mostly dry or mostly flooded*

Then in Chapter 3 we built on this catalyst by transforming it into a gas diffusion electrode. This unique catalyst structure allowed us to achieve Faradaic efficiencies for CO greater than 95% and a maximum partial current density for CO of -168 mA cm^{-2}. In addition, through a combination of secondary ion mass spectroscopy and copper underpotential deposition we showed that approximately half of the catalyst is not in contact with the electrolyte during operation and that the majority of this dry region exists in the bottom half of the catalyst.

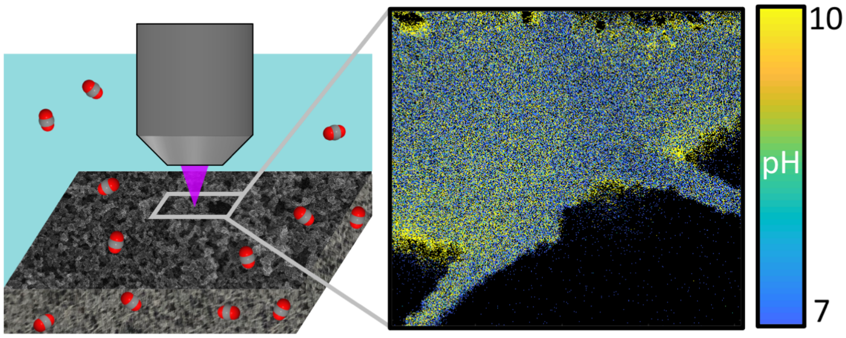

Figure 9.3: *shows a schematic of the confocal fluorescent microscopy experimental set up. On the left we see the water immersion objective scanning the surface of a CO_2 reduction gas diffusion electrode. On the right is an example of a pH map, for more details see Chapter 4.*

After exploring how local pH can impact catalyst performance in Chapter 2, we dive more deeply into trying to understand the pH in Chapter 4. Here, confocal fluorescent microscopy was used to map the electrolyte pH near a copper gas diffusion electrode during CO_2 reduction with micron spatial resolution in three dimensions (Figure 9.3). We observed that the local pH increased from pH 6.8 to greater than pH 10 as the current density was increased from 0 to 28 mA/cm^2 in a 100 mM $KHCO_3$ electrolyte. Variations in the pH across the surface indicate areas of locally increased activity. Within deep trenches of the active layer, the local pH increases as trench width decreases. Computational models confirm these experimental results and also showed that catalyst found within narrow trenches is more active than that found at the surface of the electrode. This study suggests that the overpotential required to perform selective CO_2 reduction can be reduced by increasing the density of narrow trench regions in the microporous layer.

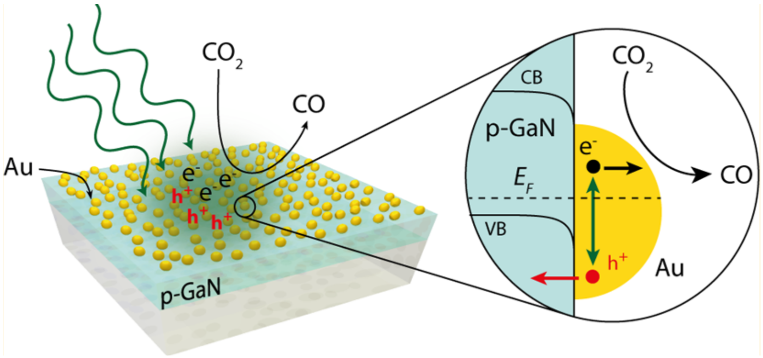

Figure 9.4: *shows a schematic of the illuminated gold nanoparticles on p-type GaN. The circle on the right shows the band diagram of the p-GaN and the Au nanoparticles, showing the energy that the hot holes need to be injected into the semiconductor.*

In Chapter 5 and 6 we then explored harvesting non-equilibrium hot carriers from plasmonic-metal nanostructures offers unique opportunities for driving photochemical reactions at the nanoscale. Despite numerous examples of hot electron-driven processes, the realization of plasmonic systems capable of harvesting hot holes from metal nanostructures has eluded the nascent field of plasmonic photocatalysis. In Chapter 5 (Figure 9.4), we fabricate gold/p-type gallium nitride (Au/p-GaN) Schottky junctions tailored for photoelectrochemical studies of plasmon-induced hot-hole capture and conversion. Despite the presence of an interfacial Schottky barrier to hot-hole injection of more than 1 eV across the Au/p-GaN heterojunction, plasmonic Au/p-GaN photocathodes exhibit photoelectrochemical properties consistent with the injection of hot holes from Au nanoparticles into p-GaN upon plasmon excitation. The photocurrent action spectrum of the plasmonic photocathodes faithfully follows the surface plasmon resonance absorption spectrum of the Au nanoparticles and open-circuit voltage studies demonstrate a sustained photovoltage during plasmon excitation. Comparison with Ohmic Au/p-NiO heterojunctions confirms that the vast majority of hot holes generated via interband transitions in Au are sufficiently hot to inject above the 1.1 eV interfacial Schottky barrier at the Au/p-GaN heterojunction. We further investigated plasmon-driven photoelectrochemical CO_2 reduction with the Au/p-GaN photocathodes, and observed improved selectivity for CO production over H_2 evolution in aqueous electrolytes. Taken together, our results offer experimental validation of photoexcited hot holes more than 1 eV below the Au Fermi level and demonstrate a photoelectrochemical platform for harvesting hot carriers to drive solar-to-fuel energy conversion. Then in Chapter 6 (Figure 9.5) we report the light-induced modification of catalytic selectivity for photoelectrochemical CO_2 reduction in aqueous media using copper nanoparticles dispersed onto p-type nickel oxide photocathodes. Optical excitation of Cu nanoparticles generates hot electrons available for driving CO_2 reduction on the Cu surface while charge separation is accomplished by hot hole injection from the Cu nanoparticles into the underlying p-NiO support. Photoelectrochemical studies demonstrate that optical excitation of plasmonic Cu/p-NiO photocathodes imparts increased selectivity for CO_2 reduction over hydrogen evolution in aqueous electrolytes. Specifically, we observed that plasmon-driven CO_2 reduction increased the production of carbon monoxide and formate, while simultaneously reducing the evolution of hydrogen. Our results demonstrate an optical route towards steering the selectivity of artificial photosynthetic systems with plasmon-driven photocathodes for photoelectrochemical CO_2 reduction in aqueous media.

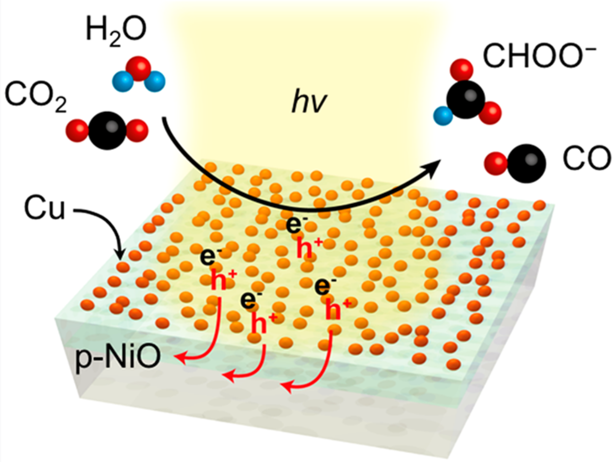

Figure 9.5: *shows a schematic of illuminated copper nanoparticles on p-type NiO.*

After exploring the specific science of how to convert CO_2 into chemical products, in Chapters 7 and 8 we turned our focus to how to design CO_2 capture and conversion systems that work together. In typical CO_2 capture and conversion systems there are five components: (i) a CO_2 source, (ii) a medium to capture the CO_2, (iii) the release of the CO_2 from the capture material, (iv) compression of the released CO_2, and (v) conversion of the CO_2. In Chapter 7, we evaluate the energy requirements of current prototypes and pilot scale plants for CO_2 capture and conversion. We point out an alternative pathway which uses bicarbonate or carbonate as a chemical feedstock rather than gaseous CO_2. The use of bicarbonate or carbonate removes the need to release CO_2 from the capture medium or compress it while also offering opportunities for higher conversion efficiencies. Bicarbonate and carbonate can be electrochemically converted into syngas or formate and subsequently into valuable chemicals and fuels using existing industrial processes. We suggest that moving to a bicarbonate or carbonate feedstock will reduce the energy required to capture and convert atmospheric CO_2. Then in Chapter 8 we give a technical and economic perspective for the generation of renewable CH_4 from sunlight, H_2O, and CO_2. We evaluate the technology readiness level (TRL), the demonstrated scale of these candidate technologies, the cost for CH_4 generation, as well as the cost required to provide the necessary feedstocks – H_2O, CO_2, and H_2. We investigate and compare four main CO_2 methanation pathways: thermochemical (via the Sabatier reaction), biochemical, photo-electrochemical, and electrochemical. A unified technoeconomic framework allows for side-by-side comparison of different pathways for sustainable CH_4 generation. Based on the state-of-the-art materials and processes, we find that the indirect methanation processes: thermochemical or biochemical are significantly more economic than that of the direct methanation processes: electrochemical or photoelectrochemical routes. We also provide quantitative key metrics for electrochemical or photoelectrochemical processes to become cost competitive with the indirect methanation processes.

Through the process of evaluating different carbon capture and conversion systems (Chapter 7 and 8) we have shown that the conversion process is a critical parameter. Since CO_2 conversion is so critical and the least understood part of the system, we have tried to bring further understanding to how to optimize these devices. We have shown that illumination can be used to suppress hydrogen evolution reaction as well as enhance CO_2 reduction reaction rates. We have also shown through the nanoporous gold catalyst and the confocal fluorescent microscopy experiments that by increasing the local pH the activity and selectivity of the catalyst are increased. Finally, we have shown that by nanostructuring a catalyst to increase its surface area and undercoordinated sites the activity and selectivity can be enhanced. We hope that this thesis will provide critical insight for the design of future electrochemical CO_2 reduction devices.

9.2 Outlook

This thesis begins to probe some fundamental questions facing the CO_2 reduction community; particularly, where is the reaction actually occurring in the catalyst. Chapter 3 uses copper underpotential deposition (Cu UPD) and secondary ion mass spectroscopy (SIMS) to probe this, and chapter 4 dives even deeper by imaging the local pH during operation using confocal fluorescent microscopy. The open questions that remain from Chapter 3 is what the 'wetted' layer actually looks like. Is it a thin layer of water coating the catalyst as was proposed, or does it look more like a channel of electrolyte going through the pores. SIMS and Cu UPD are not able to provide the necessary insight to answer this question, therefore I propose that future work should be done using either Auger spectroscopy or cryogenic scanning electron microscopy (CSEM). Auger is a promising technique because of its very high resolution which could allow us to see precisely where the copper atoms are. (Copper is a proxy for the electrolyte because copper can only plated where the catalyst is in contact with the electrolyte.) CSEM is also intriguing because the electrode could be frozen during CO_2 reduction and then the water could be directly imaged. The more we understand about the interaction between the water and the catalyst the better electrodes we will be able to design, and in addition this experimental knowledge will also allow us to create more accurate models of the system.

The next phase of experiments for the confocal fluorescent microscopy will be to find dyes that are not sensitive to pH, but are sensitive to CO_2 reduction products or hydrogen. This will allow us to create maps showing which part of the catalyst is producing what product. Then we can match which catalyst site under what conditions is producing what product which would be very exciting. This type of data can also help to improve models and allow us to create electrodes that are more selective for a single product.

While my work has begun answering these fundamental questions about catalyst environment and activity, there is still much that is left to be explored. I am excited to see how future researchers continue to probe these questions and build on this work.

Appendix A:

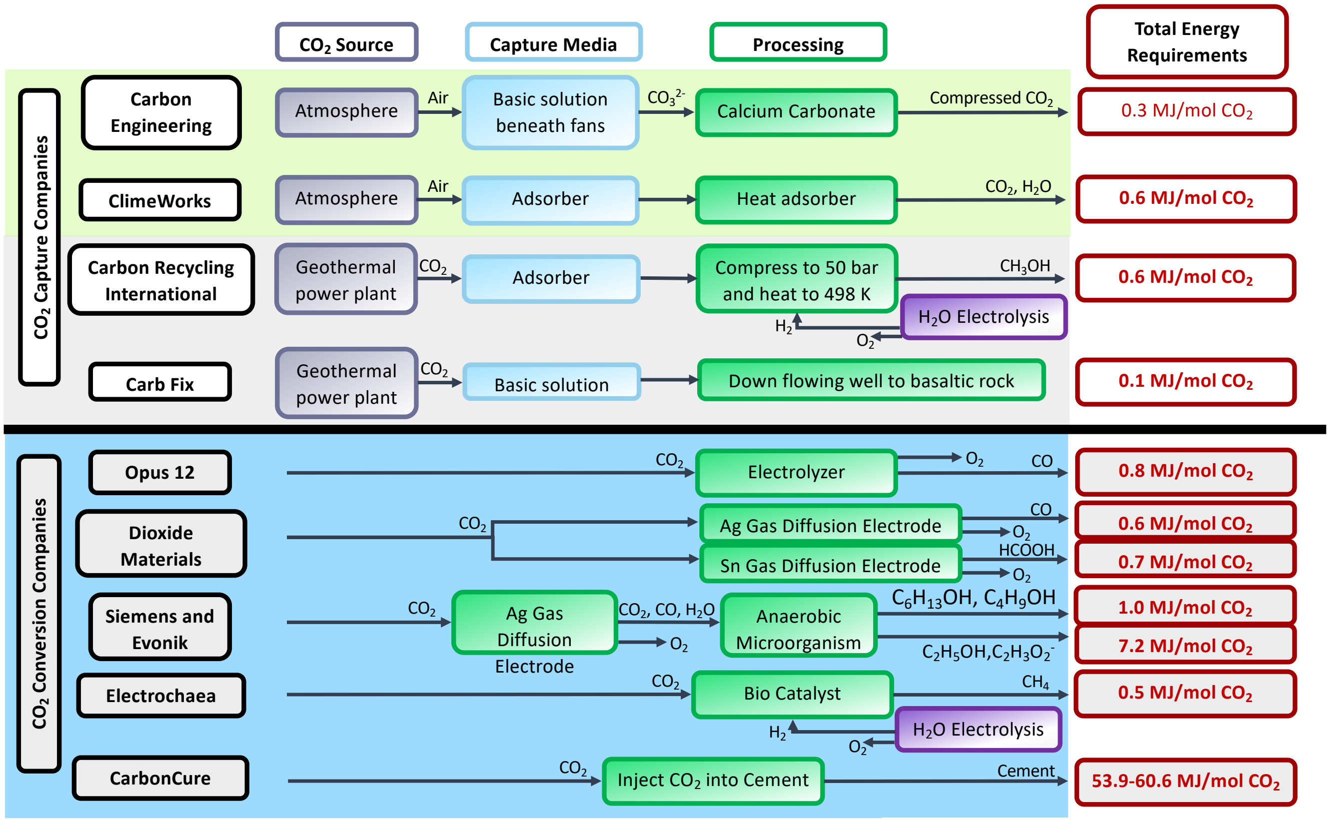

Figure A1: *Schematic representation of various pilot plants that capture CO_2 and/or transform it to either concentrated and pressurized CO_2 or to a value-added product. The companies in the light blue region capture CO_2 from the atmosphere. The companies in the mid-blue region capture CO_2 from concentrated sources. The companies in the dark blue region focus only on transforming already captured CO_2. The energies reported for these companies does not include the energy required to capture the CO_2. The energy reported for the electrolyzer systems assume 100% conversion efficiency of CO_2 which is not realistic, so there would be additional energy costs for a recirculating system.*

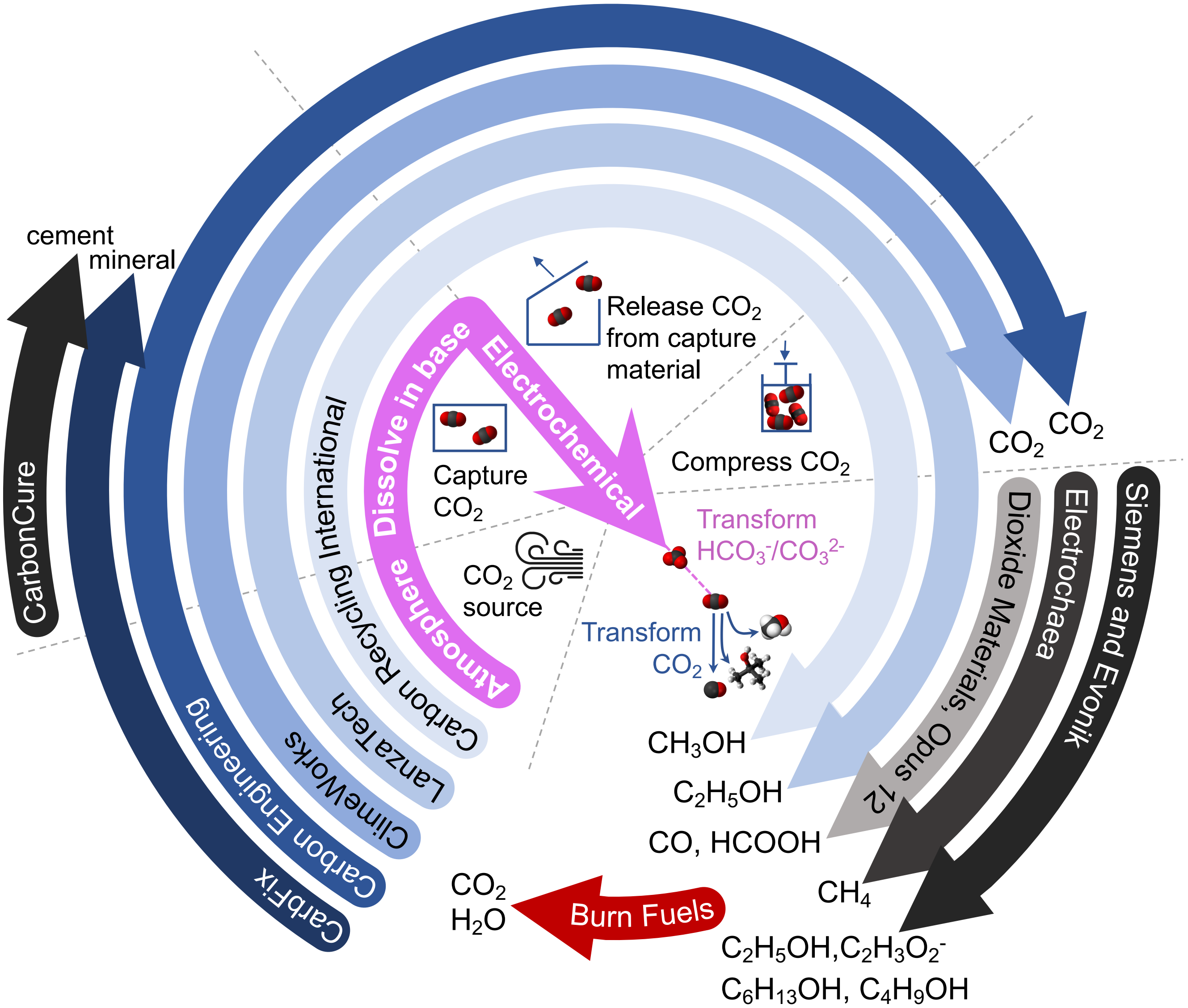

Figure A2: *Schematic representation of the steps for various prototype systems designed to capture CO_2 and/or convert it to either concentrated and pressurized CO_2 or to a value-added product. The blue arrows represent prototype processes that capture and convert CO_2, grey arrows represent prototype processes that only focus on CO_2 conversion, and the pink arrow represents the process that we propose.*

Section I: Energy Input Calculations for CO_2 Capture and Conversion Processes

A: Carbon Engineering

Carbon Engineering uses fans to contact air with a basic solution, thus dissolving CO_2 and transforming it into carbonate.[1] The carbonate reacts with $Ca(OH)_2$ to form $CaCO_3$, which is then heated to release pure CO_2 for compression and storage. Carbon Engineering reports that their process for capturing CO_2 from the air requires 8.81 GJ per 1.3-1.5 metric tons of pure and compressed CO_2 produced. Below we convert this value to kJ/mol CO_2 so that the value can be readily compared to other processes reported.

$$Energy = \frac{8.81\ GJ}{1.3 - 1.5\ t\ pure\ CO_2} \times \frac{1\ t\ pure\ CO_2}{1000 kg} \times \frac{1 kg}{1000 g} \times \frac{44.01\ g}{1\ mol\ CO_2} \times \frac{1000000\ kJ}{1\ GJ}$$
$$= \frac{259\ to\ 298\ kJ}{mol\ CO_2}$$

We would like to note that Carbon Engineering has now reported that they have also developed a process to make liquid fuels with their captured CO_2. They estimate the cost will be \$1/L once the process is scaled up.[2] However, they do not report any details on how they do this, what specific fuel they synthesize, or the energy requirements of the process, so we will not discuss this process further.

B: CarbFix

Ragnheidardottier, E., et al.[3] reports that the power requirement for the CarbFix pilot plant is 200 kW and it stores 2099 metric tons of CO_2 annually. Below we use these values to convert to kJ/mol CO_2 so that the value can be readily compared to other processes reported.

$$Energy = \frac{200\ kJ}{s} \times \frac{3600\ sec}{1\ hr} \times \frac{24\ hrs}{1\ day} \times \frac{365\ days}{1\ yr} \times \frac{1\ yr}{2099\ tCO_2} \times \frac{1\ t\ CO_2}{1000 kg} \times \frac{1 kg}{1000 g}$$
$$\times \frac{44.01\ g}{1\ mol\ CO_2} = \frac{132\ kJ}{mol\ CO_2}$$

C: Carbon Recycling International

Kauw, M. et al.[4] report that the Carbon Recycling International 5M plant consumes 47.9 MJ/kg methanol. Below we convert this value to kJ/mol CO_2 so that the value can be readily compared to other processes reported.

$$Energy = \frac{47.9\ MJ}{kg\ methanol} \times \frac{1000\ kJ}{1\ MJ} \times \frac{1\ kg}{1000\ g} \times \frac{32.04\ g}{1\ mole\ methanol} \times \frac{1\ mol\ methanol}{1\ mole\ CO_2}$$
$$= \frac{1535\ kJ}{mol\ CO_2}$$

D: Opus12

Opus 12 reports that their pilot device uses 5kW and produces 15kg of CO per day, and the input is concentrated CO_2.[5] We assume for these devices that the conversion percentage of CO_2 is 100%. Below we convert these values to kJ/mol CO_2 so that the value can be readily compared to other processes reported.

$$Energy = \frac{1\ day}{15000g\ CO} \times \frac{24\ hrs}{1\ day} \times \frac{3600\ sec}{1\ hr} \times \frac{5\ kJ}{1\ sec} \times \frac{28.01\ g}{1\ mol\ CO} \times \frac{1\ mol\ CO}{1\ mole\ CO_2} = \frac{807\ kJ}{mol\ CO_2}$$

E: Dioxide Materials

Dioxide Materials provides information on the voltage at which to run their devices, the Faradaic efficiency, and the stability of the devices.[6,7] The electrolyzer that takes CO_2 to CO runs at $500 mA/cm^2$ at 3V full cell potential with a FE of 95%. The cathode is made of a Ag catalyst and the membrane is made of Sustanion, leading to a device stability of over 3000 hours.[7] The electrolyzer that takes CO_2 to formic acid runs at $160 mA/cm^2$ at 3.5V full cell potential with a FE of 90%. The cathode is made of an Sn nanoparticle catalyst, the membrane is made of Sustanion, and the counter is IrO_2.[6] We assume for these devices that the conversion percentage of CO_2 is 100%. We take this information and calculate the energy in kJ/mol CO_2.

For CO_2 to CO electrolyzer

$$Energy = \frac{UzF}{FE} = \frac{(3\ V)(2\ mole\ electrons)(96485\ \mathrm{C\ mol^{-1}})}{.95} \times \frac{1\ kJ}{1000\ J} = \frac{609\ kJ}{mol\ CO_2}$$

For CO_2 to Formic Acid electrolyzer

$$Energy = \frac{UzF}{FE} = \frac{(3.5\ V)(2\ mole\ electrons)(96485\ \mathrm{C\ mol^{-1}})}{.90} \times \frac{1\ kJ}{1000\ J} = \frac{750\ kJ}{mol\ CO_2}$$

F: Cement production

World Coal Association reports that it requires 200kg of coal to produce 1 metric ton of cement.[8] The higher heating value of coal is approximately 28.8-32.4 MJ/kg of coal according to the European Nuclear Society.[9] Carbon Cure can store 25 lbs of CO_2 per cubic yard of cement.[10] From these values we were able to calculate the amount of energy required per mol of CO_2 stored in the cement.

$$Energy \cong \frac{200\ kg\ coal}{1\ tonne\ cement} \times \frac{28.8\ to\ 32.4\ MJ}{1\ kg\ coal} \times \frac{1000\ kJ}{1\ MJ} \times \frac{1\ tonne}{1000\ kg} \times \frac{1\ kg}{1000\ g} \times \frac{3.15\ \ g\ cement}{1\ cm^3} \times \frac{764555cm^3}{1\ yd^3} \times \frac{1\ yd^3}{25\ lb\ CO_2} \times \frac{1lb}{453.6\ g} \times \frac{44.01\ g\ CO_2}{1\ mol\ CO_2} = \frac{53{,}837\ to\ 60{,}567\ kJ}{mol\ CO_2}$$

G: Siemens and Evonik

Haas, T., et al.[11] report a system designed in collaboration between Siemens in Evonik.[11] This system uses a CO_2 electrolyzer to make syngas which is then fermented in the presence of bacteria. Depending on the type of bacteria, operating conditions, and ratio of CO to H_2, the fermenters either produce a 1:1 mixture of hexanol and butanol or a combination of acetate and ethanol. For the hexanol and butanol they report that this process requires 22kWh/kg of alcohol and then an additional 0.6 kWh/kg hexanol to separate the alcohols. For the acetate and ethanol process they apply 4.94V over the whole CO_2 electrolyzer. The fermenter is put at 36°C.[11] We assume that the fermenter has a specific heat capacity of water to calculate the energy required to heat it. We then add the energy for the electrolyzer to the energy of the fermenter to obtain a final energy, this energy does not include the energy required to separate the products. In a practical system there would also be energy costs for pumps, feeding the bacteria, capturing the CO_2, etc. which we have not taken into account here.

For CO_2 to hexanol and butanol

$$Energy = \frac{22.6\ kWh}{kg\ alcohol} \times \frac{3600\ sec}{1\ hr} \times \frac{1\ \ kg\ alcohol}{1000\ g} \times \frac{.5\ (74.12 + 102.17)\ g}{1\ mol\ alcohol} = \frac{7{,}171\ kJ}{mol\ alcohol}$$

For CO_2 to acetate and ethanol

$$Energy = \frac{UzF}{FE} = \frac{(4.94\ V)(2\ mole\ electrons)(96485\ \mathrm{C\ mol^{-1}})}{1} \times \frac{1\ kJ}{1000\ J} = \frac{953\ kJ}{mol}$$

$$Q\ water = mc\Delta T = \left(2\ L\ H_2O \times \frac{1\ mole}{22.4L}\right) \times \frac{18.02\ g}{1\ mole\ H_2O} \times \frac{1\ kg}{1000\ g} \times \left(\frac{4.181\ kJ}{kg\ K}\right)(309 - 293K)$$
$$= \frac{0.11\ kJ}{mol\ H_2O}$$

H: Electrochaea[12]

For a BioCat 10 reaction the reported installed power is 220kW, the input of CO_2 is 500 Nm^3/h, the input of H_2 is 2000 Nm^3/h. The output is 500 Nm^3/h CH_4.[12]

$$Energy = \frac{220\ kJ}{1s} \times \frac{3600s}{1\ h} \times \frac{1h}{500\ Nm^3 CO_2} \times \frac{1\ Nm^3}{1000L} \times \frac{22.4L}{1\ mol\ CO_2} = \frac{36\ kJ}{mol\ CO_2}$$

We assume use of an NEL H_2O electrolyzer to produce the H_2.[4]

$$Energy = \frac{52\ kWh}{1\ kg\ H_2} \times \frac{3600s}{1\ h} \times \frac{.002\ kg\ H_2}{1\ mol\ H_2} = \frac{374\ kJ}{mol\ H_2}$$

Section 2: Energy Input Calculations for Bicarbonate or Carbonate Feedstock Systems

A: Energy required to dissolve CO_2 in solutions of various alkalinity

Keith, D., et al.[13] report an air contactor that requires 61 kWh/tCO_2 for the fan which is 70% efficient and 21 kWh/tCO_2 for the fan which is 82% efficient.[13] In the air contactor described in this paper they have a basic solution comprised of 2M K^+, 0.45M CO_3^{2-} , 1.1M OH^-.[13] We have calculated the energy in kJ/mol CO_2 assuming this solution concentration and for a solution comprised of 2.24M K^+, 2.24M HCO_3^- , $10^{-4.78}$M OH^-.

Energy to dissolve CO_2 in solution to make carbonate

Solution: 2M K^+, 0.45M CO_3^{2-} , 1.1M OH^-

$$\frac{61\ kWh + 21\ kWh}{1\ tCO_2} \times \frac{3600\ sec}{1\ hr} \times \frac{1\ tCO_2}{1000\ kg} \times \frac{1\ kg}{1000\ g} \times \frac{44.01\ g\ CO_2}{1\ mol} = \frac{13\ kJ}{mol\ CO_2}$$

Energy to dissolve CO_2 in solution to make bicarbonate

Solution: 2.24M K^+, 2.24M HCO_3^- , $10^{-4.78}$M OH^-

$$\frac{61kWh}{1\ t\ CO_2}+\frac{21kWh}{1\ t\ CO_2}\times\frac{0.45M\ CO_3^{-2}}{2.24\ M\ HCO_3^-}=\frac{65\ kJ}{mol\ CO_2}$$

$$\frac{65\ kWh}{1\ t\ CO_2}\times\frac{3600\ sec}{1\ hr}\times\frac{1\ t\ CO_2}{1000\ kg}\times\frac{1\ kg}{1000\ g}\times\frac{44.01\ g\ CO_2}{1\ mol}=\frac{10\ kJ}{mol\ CO_2}$$

B: Bipolar membrane with Ag catalyst cathode and Ni foam anode

Sargent, E., et al.[14] reports a carbonate electrolyzer that uses a Ag catalyst cathode and a Ni foam anode separated by a bipolar membrane. The catholyte is a carbonate solution and the anolyte is a potassium hydroxide solution. The device is tested at various potentials; for our calculations we choose to look at when the applied a full cell potential of 3.8V, which gives the appropriate ratio of CO to H_2.[14]

$$Energy=\frac{UzF}{FE}=\frac{(\ 3.8V)(2\ mole\ electrons)(96485.33212\ \mathrm{C\ mol^{-1}})}{1}\times\frac{1\ kJ}{1000\ J}=\frac{733\ kJ}{mol\ CO_2}$$

This energy does not take into account the energy of the pumps or other practical considerations that would be needed for a functional system.

C: Bipolar membrane with Ag catalyst cathode and Ni anode

Li, T., et al.[15] reports an electrolyzer that uses a Ag catalyst at the cathode and a Ni anode to transform a solution of bicarbonate into syngas. When 3.5V is applied over the full cell the appropriate ratio of H_2 and CO are produced. Below we calculate the energy this corresponds to.[15]

$$Energy=\frac{UzF}{FE}=\frac{(3.5\ V)(2\ mole\ electrons)(96485\ \mathrm{C\ mol^{-1}})}{1}\times\frac{1\ kJ}{1000\ J}=\frac{675\ kJ}{mol\ CO_2}$$

This energy does not take into account the energy of the pumps or other practical considerations that would be needed for a functional system.

D: Area required of electrolyzer, capture system, and solar cells

We calculate the area required for a plant able to process 1 metric ton of CO_2 per day (t-CO_2/day) and how much would area would be needed to convert the 37.1 gigatons of CO_2 emitted globally annually.[16] We also assume that the plant is operates continuously for 24 hours, all power needs are generated on site via solar energy, and that there is sufficient battery storage to power the capture and conversion system continuously. We assume that the capture system is designed in the same way as Carbon Engineering's air contactor. They report that their air contactor processes 22 t-CO_2/m^2/year and that the plant they describe in their report can capture 1 t-CO_2/day.[13] For the electrolyzer we assume that the metrics from the electrolyzer reported by Sargent, et al. – 200 mA/cm^2 at 3.8 V.[17] For the solar system we assume a 350 W solar panels with an area of 2.03 m^2.[18] The average capacity factor in the united states is approximately 25%.[19]

Calculate area of capture system to capture 1 t-CO_2 per day

$$Total\ Area = \frac{1\ t - CO_2}{day} \times \frac{365\ day}{1\ year} \times \frac{m^2 * year}{22\ t - CO_2} = 16.6\ m^2$$

Calculate area of electrolyzer to convert 1 t-CO_2 per day

$$\begin{aligned} Total\ Area = {} & \frac{0.2\ C}{cm^2 * sec} \times \frac{10000\ cm^2}{1\ m^2} \times \frac{1\ mol\ CO_2}{3\ mol\ syngas} \times \frac{60\ sec}{1 min} \times \frac{60\ min}{1\ hr} \times \frac{24\ hr}{1\ day} \\ & \times \frac{1\ electron}{1.6 * 10^{-19} C} \times \frac{1\ CO_2 molecule\ converted}{2\ electron} \times \frac{1\ mole\ CO_2}{6.022 * 10^{23} CO_2 molecule} \\ & \times \frac{.04401\ kg}{1\ mol\ CO_2} \times \frac{1\ ton}{1000\ kg} = \frac{2.36\ ton\ CO_2}{m^2 * day} = \frac{1\ ton\ CO_2}{0.38\ m^2 * day} \end{aligned}$$

Calculate area of photovoltaic system needed to power plant that processes 1 t-CO_2 per day

$$Power\ density = \frac{350\ W}{2.03\ m^2} \times 0.25 \times 24\ hr = \frac{1.03\ kWh}{1\ m^2}$$

$$\begin{aligned} Total\ Area = {} & \frac{746\ kJ}{mol\ CO_2} \times \frac{1\ mol\ CO_2}{.04401\ kg} \times \frac{1000\ kg}{1\ ton} \times \frac{0.0002778\ kWh}{1\ kJ} \times \frac{1\ m^2}{1.03\ \frac{kWh}{day} solar\ panel} \\ = {} & \frac{4571\ m^2}{tCO_2/day} \sim \frac{0.005\ km^2}{tCO_2/day} \end{aligned}$$

Calculate area of whole system needed to process CO_2 emitted globally daily

$$\begin{aligned} Total\ area = {} & \frac{37.1 * 10^9 tons\ CO_2}{1 yr} \times \frac{1\ yr}{365\ days} \times \frac{4571\ m^2}{tCO_2/day} \times \frac{1\ km^2}{(1000\ m)^2} \\ = {} & \ 464{,}614\ km^2 \sim\ 460{,}000\ km^2 \end{aligned}$$

E: Energy required to make syngas from coal

Energy Technology Systems Analysis Programme reports that the process of synthesizing syngas from coal is roughly 74.7% efficient.[20] Syngas has roughly half of the energy density of natural gas. From this we can estimate the energy required to make syngas.

$$E = 0.5 \times \frac{33.4 - 82.7\ MJ}{1\ m^3\ natural\ gas} \times \frac{1 m^3}{1000 L} \times \frac{22.4 L}{1\ mol\ syngas} \times \frac{3\ mol\ syngas}{1\ mol\ CO} \times \frac{100}{74.7} = \frac{1.5 - 3.7\ MJ}{mol\ CO}$$

F: Energy required to make syngas from natural gas using steam reforming and the reverse water gas shift with CO_2 capture

For the process of steam reforming natural gas and then performing the reverse water gas shift to obtain the proper ratio of CO to H_2 there are many steps involved. Baltrusaitis, J. and W. Luyben[21] report that the energy for the preheater is 10.47 MW, vaporizer is 202.9 MW, steam methane reforming is 536.6 MW, the furnace for the reverse water gas shift is 121.2 MW, heat exchanger two is 219.8 MW, heat exchanger is 46 MW, the steam methane reforming cooler is 177.2 MW, the reboiler is 75.2 MW, the feed effluent heat exchanger is 53.2 MW, the condenser is 30.2 MW, the compressor is 9.83 MW, the intercoolers are 10.76 MW, and the stripper cooler is 40.86 MW. There are also some additional smaller energies that total 400MW. This system produces 15,013 kmol/h H_2, 7500 kmol/h CO, 271 kmol/h CH_4, and 94 kmol/h H_2O. From this we can calculate the energy needed to make the syngas.

$$\begin{aligned} Total\ power &= 10.47MW + 202.9MW + 536.6MW + 121.2MW + 46MW + 177.2MW + 75.2MW \\ &\quad + 53.2\ MW + 30.2\ MW + 9.83\ MW + 10.76\ MW + 40.86MW + 400MW \\ &= 1{,}314.4\ MW \end{aligned}$$

$$E = \frac{1714.4\ MJ}{1s} \times \frac{60s}{1min} \times \frac{60\ min}{1hr} \times \frac{1hr}{7500\ kmol\ CO} \times \frac{1kmol}{1000mol} = \frac{0.8\ MJ}{mol\ CO}$$

G: Energy required to make syngas from natural gas using steam reforming and the reverse water gas shift

For the process of steam reforming natural gas and then performing the reverse water gas shift to obtain the proper ratio of CO to H_2 there are many steps involved. Baltrusaitis, J. and W. Luyben[21] report that the energy for the preheater is 10.47 MW, vaporizer is 202.9 MW, steam methane reforming is 536.6 MW, the furnace for the reverse water gas shift is 121.2 MW, heat exchanger two is 219.8 MW, heat exchanger 3 is 46 MW, compressor is 9.83MW, and the steam methane reforming cooler is 177.2 MW here are also some additional smaller energies that total 400MW. This system produces 15,013 kmol/h H_2, 7500 kmol/h CO, 272 kmol/h CH_4, and 75 kmol/h H_2O. From this we can calculate the energy needed to make the syngas.

$$\begin{aligned} Total\ power &= 10.47MW + 202.9MW + 536.6MW + 121.2MW + 46MW + 177.2MW \\ &\quad + 9.83\ MW + 400MW = 1{,}504.2\ MW \end{aligned}$$

$$E = \frac{1314.4\ MJ}{1s} \times \frac{60s}{1min} \times \frac{60\ min}{1hr} \times \frac{1hr}{7500\ kmol\ CO} \times \frac{1kmol}{1000mol} = \frac{0.7\ MJ}{mol\ CO}$$

H: Pd-Pt cathode with Pt anode to reduce bicarbonate to formate

Kortlever, R., et al. reports an electrochemical cell that reduces bicarbonate to formate at low overpotentials using a Pd-Pt cathode and Pt anode. A potential of -0.4V vs the reversible hydrogen electrode (RHE) is applied to the cathode, which corresponds to ~90% faradaic efficiency for formate.[22] We assume a full cell potential of 2V, since the cell has some resistance and the anode is performing OER which has a standard potential of 1.23V. We have calculated the energy used by the cell below, the calculation does not include the energy that would be required for pumps or other practical considerations.

$$Energy = \frac{UzF}{FE} = \frac{(2\ V)(2\ mole\ electrons)(96485\ \mathrm{C\ mol^{-1}})}{.90} \times \frac{1\ kJ}{1000\ J} = \frac{429\ kJ}{mol\ CO_2}$$

H: Production of Sodium Hydroxide

The Office of Energy Efficiency and Renewable Energy of the U.S. Department of Energy report that when a zero-gap membrane chlor-alkali cell with an oxygen-depolarized cathode is used for the chlor-alkali process, sodium hydroxide can be produced for 2,500 kWh/ton.[23]

$$Energy = \frac{2{,}500\ kWh}{1\ ton\ NaOH} * \frac{3600\ kJ}{1\ kWh} \times \frac{1\ ton}{1000\ kg} \times \frac{1\ kg}{1000\ g} \times \frac{39.997\ g\ NaPH}{1\ mol\ NaOH} = \frac{360\ kJ}{mol\ NaOH}$$

Section 3: CO_2 Electrolyzer Conversion Efficiencies

For all calculations in this section we assume that the CO_2 is at standard temperature and pressure.

A: Gewirth, A., et al CO_2 to electrolyzer[24]

$$Mols\ of\ CO_2\ per\ second = \left(\frac{7\ ml\ CO_2}{1\ min}\right)\left(\frac{1\ min}{60s}\right)\left(\frac{22{,}400\ ml\ CO_2}{1\ mol\ CO_2}\right) = \frac{5.2 * 10^{-6}\ mol\ CO_2}{1s}$$

$$Mols\ of\ ethylene\ per\ second = \left(\frac{.17\ C}{1s}\right)\left(\frac{1\ mol\ e-}{96485\ C}\right)\left(\frac{1\ mol\ ethylene}{12\ mol\ e-}\right) = \frac{1.5 * 10^{-10}\ mol\ CO}{1s}$$

$$Mols\ of\ ethanol\ per\ second = \left(\frac{.09\ C}{1s}\right)\left(\frac{1\ mol\ e-}{96485\ C}\right)\left(\frac{1\ mol\ ethanol}{12\ mol\ e-}\right) = \frac{7.8 * 10^{-11}\ mol\ CO}{1s}$$

$$Conversion\ Percentage = \frac{2.2 * 10^{-10}\ mol\ C2}{1s} * \frac{1s}{5.2 * 10^{-6}\ mol\ CO_2} = 0.004\%$$

B: Siemens and Evonik CO_2 electrolyzer[11]

$$Mols\ of\ CO_2\ per\ second = \left(\frac{90\ ml\ CO_2}{1\ min}\right)\left(\frac{1\ min}{60s}\right)\left(\frac{22{,}400\ ml\ CO_2}{1\ mol\ CO_2}\right) = \frac{6.7 * 10^{-5}\ mol\ CO_2}{1s}$$

$$Mols\ of\ Formate\ per\ second = \left(\frac{.3\ C}{1s}\right)\left(\frac{1\ mol\ e-}{96485\ C}\right)\left(\frac{1\ mol\ CO}{2\ mol\ e-}\right) * .7 = \frac{1.1 * 10^{-6}\ mol\ CO}{1s}$$

$$Conversion\ Percentage = \frac{1.1 * 10^{-6}\ mol\ CO}{1s} * \frac{1s}{6.7 * 10^{-5}\ mol\ CO_2} = 1.6\%$$

C: Sargent, E., et al CO_2 electrolyzer[25]

$$Mols\ of\ CO_2\ per\ second = \left(\frac{30\ ml\ CO_2}{1\ min}\right)\left(\frac{1\ min}{60s}\right)\left(\frac{22{,}400\ ml\ CO_2}{1\ mol\ CO_2}\right) = \frac{2.2 * 10^{-5}\ mol\ CO_2}{1s}$$

$$Mols\ of\ Acetic\ acid\ per\ second = \left(\frac{.75\ C}{1s}\right)\left(\frac{1\ mol\ e-}{96485\ C}\right)\left(\frac{1\ mol\ acetic\ acid}{8\ mol\ e-}\right) * .05 = \frac{4.8 * 10^{-8}\ mol\ acetic\ acid}{1s}$$

$$Mols\ of\ ethylene\ per\ second = \left(\frac{.75\ C}{1s}\right)\left(\frac{1\ mol\ e-}{96485\ C}\right)\left(\frac{1\ mol\ ethylene}{12\ mol\ e-}\right) * .65$$
$$= \frac{4.2 * 10^{-7}\ mol\ CO}{1s}$$

$$Mols\ of\ ethanol\ per\ second = \left(\frac{.75\ C}{1s}\right)\left(\frac{1\ mol\ e-}{96485\ C}\right)\left(\frac{1\ mol\ ethanol}{12\ mol\ e-}\right) * .1 = \frac{6.4 * 10^{-8}\ mol\ CO}{1s}$$

$$Conversion\ Percentage = \frac{5.3 * 10^{-7}\ mol\ C2}{1s} * \frac{1s}{2.2 * 10^{-5}\ mol\ CO_2} = 2.4\%$$

D: Kenis, P., et al CO_2 electrolyzer[26]

$$Mols\ of\ CO_2\ per\ second = \left(\frac{7\ ml\ CO_2}{1\ min}\right)\left(\frac{1\ min}{60s}\right)\left(\frac{22{,}400\ ml\ CO_2}{1\ mol\ CO_2}\right) = \frac{5.2 * 10^{-6}\ mol\ CO_2}{1s}$$

$$Mols\ of\ CO\ per\ second = \left(\frac{.275\ C}{1s}\right)\left(\frac{1\ mol\ e-}{96485\ C}\right)\left(\frac{1\ mol\ CO}{2\ mol\ e-}\right) *= \frac{1.4 * 10^{-6}\ mol\ CO}{1s}$$

$$Conversion\ Percentage = \frac{5.3 * 10^{-7}\ mol\ CO}{1s} * \frac{1s}{2.2 * 10^{-5}\ mol\ CO_2} = 27.3\%$$

E: Kenis, P., et al CO_2 electrolyzer[27]

$$Mols\ of\ CO_2\ per\ second = \left(\frac{7\ ml\ CO_2}{1\ min}\right)\left(\frac{1\ min}{60s}\right)\left(\frac{22{,}400\ ml\ CO_2}{1\ mol\ CO_2}\right) = \frac{5.2 * 10^{-6}\ mol\ CO_2}{1s}$$

$$Mols\ of\ CO\ per\ second = \left(\frac{.375\ C}{1s}\right)\left(\frac{1\ mol\ e-}{96485\ C}\right)\left(\frac{1\ mol\ CO}{2\ mol\ e-}\right) = \frac{1.8 * 10^{-6}\ mol\ CO}{1s}$$

$$Conversion\ Percentage = \frac{5.3 * 10^{-7}\ mol\ CO}{1s} * \frac{1s}{2.2 * 10^{-5}\ mol\ CO_2} = 34.8\%$$

F: Xuan, J., et al CO_2 electrolyzer[28]

$$Mols\ of\ CO_2\ per\ second = \left(\frac{50\ ml\ CO_2}{1\ min}\right)\left(\frac{1\ min}{60s}\right)\left(\frac{22{,}400\ ml\ CO_2}{1\ mol\ CO_2}\right) = \frac{3.7 * 10^{-5}\ mol\ CO_2}{1s}$$

$$Mols\ of\ formate\ per\ second = \left(\frac{.350\ C}{1s}\right)\left(\frac{1\ mol\ e-}{96485\ C}\right)\left(\frac{1\ mol\ HCOO^-}{2\ mol\ e-}\right) = \frac{1.8 * 10^{-6}\ mol\ HCOO^-}{1s}$$

$$Conversion\ Percentage = \frac{1.8 * 10^{-6}\ mol\ HCOO^{-}}{1s} * \frac{1s}{3.7 * 10^{-5}\ mol\ CO_2} = 4.9\%$$

G: Lv, J. J., et al CO_2 electrolyzer[29]

$$Mols\ of\ CO_2\ per\ second = \left(\frac{10\ ml\ CO_2}{1\ min}\right)\left(\frac{1\ min}{60s}\right)\left(\frac{22{,}400\ ml\ CO_2}{1\ mol\ CO_2}\right) = \frac{7.4 * 10^{-6}\ mol\ CO_2}{1s}$$

$$Mols\ of\ ethylene\ per\ second = \left(\frac{.255\ C}{1s}\right)\left(\frac{1\ mol\ e-}{96485\ C}\right)\left(\frac{1\ mol\ C_2H_4}{12\ mol\ e-}\right) = \frac{2.2 * 10^{-7}\ mol\ C_2H_4}{1s}$$

$$Conversion\ Percentage = \frac{2.2 * 10^{-7}\ mol\ C_2H_4}{1s} * \frac{1s}{7.4 * 10^{-6}\ mol\ CO_2} = 2.9\%$$

H: Verma, S., et al CO_2 electrolyzer[30]

$$Mols\ of\ CO_2\ per\ second = \left(\frac{10\ ml\ CO_2}{1\ min}\right)\left(\frac{1\ min}{60s}\right)\left(\frac{22{,}400\ ml\ CO_2}{1\ mol\ CO_2}\right) = \frac{1.3 * 10^{-5}\ mol\ CO_2}{1s}$$

$$Mols\ of\ CO\ per\ second = \left(\frac{.255\ C}{1s}\right)\left(\frac{1\ mol\ e-}{96485\ C}\right)\left(\frac{1\ mol\ CO}{2\ mol\ e-}\right) = \frac{8.3 * 10^{-7}\ mol\ CO}{1s}$$

$$Conversion\ Percentage = \frac{2.2 * 10^{-7}\ mol\ CO}{1s} * \frac{1s}{7.4 * 10^{-6}\ mol\ CO_2} = 6.6\%$$

BIBLIOGRAPHY: APPENDIX A

1. Singh, M. R., Clark, E. L. & Bell, A. T. Effects of electrolyte, catalyst, and membrane composition and operating conditions on the performance of solar-driven electrochemical reduction of carbon dioxide. *Phys. Chem. Chem. Phys.* **2015**, 17, 18924–18936.
2. Carbon Engineering. Air to fuels. (2019). Available at: https://carbonengineering.com/about-a2f/. (Accessed: 18th October 2019)
3. Ragnheidardottir, E., Sigurdardottir, H., Kristjansdottir, H. & Harvey, W. Opportunities and challenges for CarbFix: An evaluation of capacities and costs for the pilot scale mineralization sequestration project at Hellisheidi, Iceland and beyond. *Int. J. Greenh. Gas Control* **2011**, 5, 1065–1072.
4. Benders, M. J., Visser, C. & Kauw, M. Green methanol from hydrogen and carbon dioxide using geothermal energy and/or hydropower in Iceland or excess renewable electricity in Germany. *Energy* **2015**, 1–10.
5. Flanders, N., Kuhl, K. & Cave, E. *Opus 12 – Recycling carbon dioxide back into fuels and chemicals.* (2016).
6. Dioxide Materials. Dioxide Materials: Electrolyzer to transform carbon dioxide into formic acid. Available at: https://dioxidematerials.com/technology/formic-acid/. (Accessed: 10th February 2020)
7. Dioxide Materials. Dioxide Materials: Electrolyzer to convert carbon dioxide to carbon monoxide. Available at: https://dioxidematerials.com/technology/co2-electrolysis/. (Accessed: 10th February

2020)

8. What is cement? *World Coal Association* 1–4 (2019). Available at: https://www.worldcoal.org/coal/uses-coal/coal-cement. (Accessed: 10th February 2020)
9. European Nuclear Society. Fuel comparison. (2014). Available at: http://www.euronuclear.org/info/encyclopedia/f/fuelcomparison.htm. (Accessed: 10th February 2020)
10. Monkman, S. & MacDonal, M. *Ready mixed technology case study CO2 utilization in concrete mix design optimization*. (2016).
11. Haas, T., Krause, R., Weber, R., Demler, M. & Schmid, G. Technical photosynthesis involving CO_2 electrolysis and fermentation. *Nat. Catal.* **2018**, 1, 32–39.
12. Electrochaea. *Applications of Electrochaea's BioCat biomethanation technology*. (2018).
13. Keith, D. W., Angelo, D. St., Holmes, G. & Heidel, K. A process for capturing CO_2 from the atmosphere. *Joule* **2018**, 2, 1573–1594.
14. Li, Y. C. *et al.* CO_2 electroreduction from carbonate electrolyte. *ACS Energy Lett.* **2019**, 4, 1427–1431.
15. Li, T. *et al.* Electrolytic conversion of bicarbonate into CO in a flow cell. *Joule* **2019**, 3, 1487–1497.
16. Le Quere, C. *et al. Global carbon budget 2018*. (2018).
17. Li, Y. C. *et al.* CO_2 electroreduction from carbonate electrolyte. *ACS Energy Lett.* **2019**, 4, 1427–1431.
18. Trina Solar. *The Tallmax framed 144 half cell module*. (2019).
19. US Energy Information Administration. *Electric Power Monthly with Data for September 2012*. (2012).
20. Energy Technology Systems Analysis Programme. *Syngas production from coal*. (2010).
21. Baltrusaitis, J. & Luyben, W. L. Methane conversion to syngas for gas-to-liquids (GTL): is sustainable CO_2 reuse via dry methane reforming (DMR) cost competitive with SMR and ATR processes? *ACS Sustain. Chem. Eng.* **2015**, 3, 2100–2111.
22. Kortlever, R., Balemans, C., Kwon, Y. & Koper, M. T. M. Electrochemical CO_2 reduction to formic acid on a Pd-based formic acid oxidation catalyst. *Catal. Today* **2015**, 244, 58–62.
23. U.S. Department of Energy. *Advanced Chlor-Alkali Technology (CPS #1797). Industrial Technologies Program* (2004).
24. Hoang, T. T. H. *et al.* Nanoporous copper-silver alloys by additive-controlled electrodeposition for the selective electroreduction of CO_2 to ethylene and ethanol. *J. Am. Chem. Soc.* **2018**, 140, 5791–5797.
25. Dinh, C. *et al.* CO_2 electroreduction to ethylene via hydroxide-mediated copper catalysis at an abrupt interface. *Science* **2018**, 360, 783–787.
26. Kim, B., Hillman, F., Ariyoshi, M., Fujikawa, S. & Kenis, P. J. A. Effects of composition of the microporous layer and the substrate on performance in the electrochemical reduction of CO_2 to CO. *J. Power Sources* **2016**, 312, 192–198.
27. Ma, S. *et al.* Carbon nanotube containing Ag catalyst layers for efficient and selective reduction of carbon dioxide. *J. Mater. Chem. A* **2016**, 4, 8573–8578.
28. Lu, X., Leung, D. Y. C., Wang, H. & Xuan, J. A high performance dual electrolyte microfluidic reactor for the utilization of CO_2. *Appl. Energy* **2017**, 194, 549–559.
29. Lv, J. J. *et al.* A highly porous copper electrocatalyst for carbon dioxide reduction. *Adv. Mater.* **2018**, 30, 1–8.
30. Verma, S. *et al.* Insights into the low overpotential electroreduction of CO_2 to CO on a supported gold catalyst in an alkaline flow electrolyzer. *ACS Energy Lett.* **2017**, 3, 193–198.

Appendix B:

Analytical basis

Relevant process assumption and cost information for direct air capture (DAC),[1] low-temperature electrolysis (LTE),[2,3] high-temperature electrolysis (HTE),[3,4] solar thermochemical hydrogen (STCH), and thermochemical methanation[5] were solicited from available reports. Various sources were adopted to develop process and cost estimates for ocean capture,[6–10] photoelectrochemical (PEC) hydrogen generation,[11,12] grid electrolysis methanation,[3,4] PEC methanation,[11,12] and biochemical methanation.[13,14] The plant design capacity was assumed to be 240 ton/day for CO_2 capture, 45 ton/day for H_2 generation, 81 ton/day for CH_4 production.

In some cases where cost information were already available in a certain plant capacity, the costs of similar items of different sizes were approximated to our specific design capacity using exponential scaling factor, as follows:

$$C_\mathrm{D} = C_\mathrm{B}\left(\frac{S_D}{S_B}\right)^N \tag{B.1}$$

where C_D is the cost at design capacity, C_B is the cost at known baseline capacity, S_D is the design capacity, S_B is the known baseline capacity, and N is the scaling factor exponent that varies from 0.1 to unity. Unless otherwise specified, an average value of 0.6 was as used for N.

All equipment capital costs reported in the past were adjusted to 2019 dollars by multiplying the reported base cost from an earlier year by the ratio of a cost index (I) in 2019 to a base cost index (I_base) that corresponds to the year of which the cost information was obtained:[10]

$$C_{2019} = C_\mathrm{R}\frac{I_{2019}}{I_\mathrm{R}} \tag{B.2}$$

where C_{2019} is the equipment purchase cost in 2019, C_R is the equipment purchase cost in reference year, I_{2019} is the Chemical Engineering Plant Cost Index (CEPCI) in 2019 and I_R is CEPCI in reference year.

The calculated results of the levelized product costs were adjusted to 2020 dollars using inflation rate of 1.9%:

$$LCP_{2020} = LCP_{2019}\,(1 + 1.9\%)^{2020-2019} \tag{B.3}$$

where LCP_{2020} and LCP_{2019} are the levelized cost of product in 2020 dollars and in 2019 dollars, respectively.

Table B1: The default H2A hydrogen production economic model and its financial values were applied to all systems studied.

Financial Parameters	Assumptions
Length of Construction Period (years)	1
Year of analysis	2020
% of Capital Spent in 1st Year of Construction	100%
Start-up Time (years)	1
Plant life (years)	40
Analysis period (years)	40
Depreciation Schedule Length (years)	20
Depreciation Type	MACRS
% Debt Financing	60%
% Equity Financing	40%
Interest rate on debt (%)	3.70%
Debt period (years)	Constant debt
% of Fixed Operating Costs During Start-up (%)	75%
% of Revenues During Start-up (%)	50%
% of Variable Operating Costs During Start-up (%)	75%
Decommissioning costs (% of depreciable capital investment)	10%
Salvage value (% of total capital investment)	10%
Inflation rate (%)	1.9%
State Taxes (%)	6.0%
Federal Taxes (%)	21.0%
Total Tax Rate (%)	25.74%
Working capital (% of yearly change in operating costs)	15%
After-tax real IRR	6%
After-tax nominal IRR	8.01%

Table B2: Assumptions for calculating the cost of direct air capture of CO_2 currently. For further information see excel sheet titled "Direct Air Capture of CO2 (current)".

Process Assumptions		
Design capacity	244444.44	kg CO_2/day
Average production	220000	kg CO_2/day
Capacity factor	0.9	
Baseline capacity	2684931.507	kg CO_2/day
Scale ratio	0.09	
Fan energy	61	kWh/t-CO_2
Fluid pumping energy	21	kWh/t-CO_2
Fluid pumping energy	27	kWh/t-CO_2
Power produced from slaking heat	-77	kWh/t-CO_2
Energy consumption	32	kWh/t-CO_2
ASU power usage	238	kWh/t-CO_2
Compressor power usage	132	kWh/t-CO_2
Calciner	369	kWh/t-CO_2
Water consumption	4.7	t-water/t-CO_2
Water price	0.69307362	$/t-water
Industrial electricity	0.049	$/kWh
Natural gas price	3.5	$/GJ

Baseline system cost	Baseline installed cost in startup year dollars	Installation cost factor	Combined plant scaling	Installed cost
Air contactor	$135,867,821	1.86	0.09	$22,984,912
Pellet reactor	$91,490,678	1.70	0.09	$14,167,891
Calciner-slaker	$52,110,425	1.77	0.15	$13,591,553
Air separation unit	$45,209,958	1.43	0.24	$15,339,052
CO_2 compressor	$20,463,455	1.16	0.20	$4,777,228
Steam turbine	$7,971,229	1.12	0.19	$1,667,188
Power plant	$38,904,359	1.07	0.30	$12,564,408
Fines filter	$20,939,349	1.76	0.24	$8,728,853
Other equipment	$115,285,393	1.06	0.24	$29,039,678
Buildings	$2,974,339	2.68	0.43	$3,445,575
Transformer	$22,129,085	1.06	0.33	$7,822,927
Total				**$134,129,266**

Capital costs	
Depreciable capital costs	Value in startup year dollars
Direct capital cost	$134,129,266
Indirect capital cost	
Site preparation (2% direct capital cost)	$2,682,585
Engineering and design (10% direct capital cost)	$13,412,927
Project contingency (15% direct capital cost)	$20,119,390
Upfront permitting cost (legal and contractors fees) (7.5% direct capital cost)	$10,059,695
Total capital cost	**$180,403,863**

Fixed operating costs	Value in startup year
Labor cost ($50/FTE) ($/year) (11 FTE)	$1,282,289
G&A ($/year) (20% labor cost)	$256,458
Property taxes and insurance ($/year) (2% total capital cost)	$3,608,077
Production maintenance and repairs ($/year) (2.9% direct capital cost)	$3,889,749
Total fixed operating costs ($/year)	$9,036,573

Variable operating costs	Value in startup year
Energy utilities costs	$17,823,995
Non energy utilities costs	$3,032,682
Total variable operating costs ($/year)	**$20,856,677**

Replacements	Value in startup year
Unplanned replacement capital cost (0.5% of total direct capital costs/year)	$670,646

Table B3: Assumptions for calculating the cost of direct air capture of CO_2 in the future. For further information see excel sheet titled "Direct Air Capture of CO2 (future)".

Process Assumptions		
Design capacity	2684931.51	kg CO_2/day
Average production	2550684.932	kg CO_2/day
Capacity factor	0.95	
Baseline capacity	2684931.507	kg CO_2/day
Scale ratio	1	
Scaling factor exponent	0.6	
Electricity equivalent gas input	478.3333333	kWh/t-CO_2
Electricity input	77	kWh/t-CO_2
Water consumption	4.7	t-water/t-CO_2
Water price	0.69307362	$/t-water
Industrial electricity	0.01	$/kWh
Natural gas price	3.5	$/GJ

Baseline system cost	Uninstalled cost in startup year dollars	Installation cost factor	Installed cost
Air contactor	$157,996,906	1.00	$157,996,906
Pellet reactor	$112,786,948	1.00	$112,786,948
Calciner-slaker	$75,667,193	1.00	$75,667,193
Air separation unit	$55,560,659	1.00	$55,560,659
CO_2 compressor	$18,440,904	1.00	$18,440,904
Steam turbine	$6,900,467	1.00	$6,900,467
Power plant	$31,765,944	1.00	$31,765,944
Fines filter	$29,505,446	1.00	$29,505,446
Other equipment	$91,609,652	1.00	$91,609,652
Buildings	$6,900,467	1.00	$6,900,467
Transformer	$19,868,587	1.00	$19,868,587
Total			**$607,003,173**

Capital costs	
Depreciable capital costs	Value in startup year dollars
Direct capital cost	$607,003,173
Indirect capital cost	
Site preparation (2% direct capital cost)	$12,140,063
Engineering and design (10% direct capital cost)	$60,700,317
Project contingency (15% direct capital cost)	$91,050,476
Upfront permitting cost (legal and contractors fees) (7.5% direct capital cost)	$45,525,238
Total capital cost	**$816,419,268**

Fixed operating costs	Value in startup year dollars
Labor cost ($50/FTE) ($/year) (46.34 FTE)	$5,402,081
G&A ($/year) (20% labor cost)	$1,080,416
Property taxes and insurance ($/year) (2% total capital cost)	$16,328,385
Production maintenance and repairs ($/year) (2.9% direct capital cost)	$17,603,092
Total fixed operating costs ($/year)	$40,413,974

Variable operating costs	Value in startup year dollars
Energy utilities costs	$17,823,995
Non energy utilities costs	$3,032,682
Total variable operating costs ($/year)	**$20,856,677**

Replacements	Value in startup year dollars
Unplanned replacement capital cost (0.5% of total direct capital costs/year)	$670,646

Table B4: Assumptions for calculating the cost of ocean CO_2 capture currently. For further information see excel sheet titled "Ocean CO2 Capture (current)".

Process Assumptions		
Design capacity	246575.34	kg CO_2/day
Average production rate	221917.8082	kg CO_2/day
Capacity factor	0.9	
Extraction efficiency	0.9	
Electrodialysis acidified stream target pH	0.40	
Oceanwater target pH	4	
Current density	100	mA/cm^2
Voltage	1.2	V
Electrodialysis energy at oceanwater target pH	0.97736927	kWh/kg CO_2
CO2 stripping energy	0.072994345	kWh/kg CO_2
Intake energy (0.5 bar, 5 m intake)	0.206827333	kWh/kg CO_2
Pre-treatment energy (3 bar ultrafiltration, 7.6 bar nanofiltration, 0.5 bar electrodialyzer)	0.04804125	kWh/kg CO_2
Pump energy (0.5 bar membrane contactor)	0.206827333	kWh/kg CO_2
Industrial electricity	0.049	$/kWh

Baseline system cost	Uninstalled cost in startup year dollars	Installation cost factor	Installed cost
Electrodialyzer	$15,133,812	1.20	$18,160,574
Pre-treatment	$6,657,344	1.20	$7,988,813
Gas stripping	$21,691,109	1.20	$26,029,331
Intake	$6,717,271	1.20	$8,060,725
Screening	$22,973,169	1.20	$27,567,802
Pumping	$3,747,976	1.20	$4,497,572
Total			**$92,304,818**

Capital costs	
Depreciable capital costs	Value in startup year dollars
Direct capital cost	$92,304,818
Indirect capital cost	
Site preparation (2% direct capital cost)	$1,846,096
Engineering and design (10% direct capital cost)	$9,230,482
Project contingency (15% direct capital cost)	$13,845,723
Upfront permitting cost (legal and contractors fees) (7.5% direct capital cost)	$6,922,861
Total capital cost	**$124,149,981**

Fixed operating costs	Value in startup year dollars
Labor cost ($50/FTE) ($/year) (34.95 FTE)	$4,074,146
G&A ($/year) (20% labor cost)	$814,829
Property taxes and insurance ($/year) (2% total capital cost)	$2,483,000
Production maintenance and repairs ($/year) (2.9% direct capital cost)	$2,769,145
Total fixed operating costs ($/year)	**$10,141,120**

Variable operating costs	Value in startup year
Energy utilities costs	$6,001,364
Non energy utilities costs	$0
Total variable operating costs ($/year)	**$6,001,364**

Replacements	Value in startup year dollars
Unplanned replacement capital cost (0.5% of total direct capital costs/year)	$461,524.09
Replacement costs (15% of depreciable capital cost/5year)	$18,622,497.08
Specified replacement cost (electrodialyzer/5year)	$18,160,574.35
Specified replacement cost (60% pre-treatment/5year)	$4,793,288.03
Specified replacement cost (gas stripping/10year)	$26,029,331.20

Table B5: Assumptions for calculating the cost of ocean CO_2 capture in the future. For further information see excel sheet titled "Ocean CO2 Capture (future)".

Process Assumptions		
Design capacity	2739726.03	kg CO_2/day
Average production rate	2602739.726	kg CO_2/day
Capacity factor	0.95	
Extraction efficiency	0.98	
Electrodialysis acidified stream target pH	0.40	
Oceanwater target pH	4	
Current density	1000	mA/cm^2
Voltage	1.6	V
Electrodialysis energy at oceanwater target pH	1.196778698	kWh/kg CO_2
CO2 stripping energy	0.072994345	kWh/kg CO_2
Intake energy (0.5 bar, 5 m intake)	0.189943469	kWh/kg CO_2
Pre-treatment energy (3 bar ultrafiltration, 7.6 bar nanofiltration, 0.5 bar electrodialyzer)	0.044119516	kWh/kg CO_2
Pump energy (0.5 bar membrane contactor)	0.189943469	kWh/kg CO_2
Industrial electricity	0.01	$/kWh

Baseline system cost	Uninstalled cost in startup year dollars	Installation cost factor	Installed cost
Electrodialyzer	$7,721,333	1.00	$7,721,333
Pre-treatment	$25,033,436	1.00	$25,033,436
Gas stripping	$73,347,986	1.00	$73,347,986
Intake	$68,543,583	1.00	$68,543,583
Screening	$234,420,087	1.00	$234,420,087
Pumping	$38,244,657	1.00	$38,244,657
Total			**$447,311,082**

Capital costs	
Depreciable capital costs	Value in startup year dollars
Direct capital cost	$447,311,082
Indirect capital cost	
Site preparation (2% direct capital cost)	$8,946,222
Engineering and design (10% direct capital cost)	$44,731,108
Project contingency (15% direct capital cost)	$67,096,662
Upfront permitting cost (legal and contractors fees) (7.5% direct capital cost)	$33,548,331
Total capital cost	**$601,633,406**

Fixed operating costs	Value in startup year dollars
Labor cost ($50/FTE) ($/year) (126.79 FTE)	$14,780,298
G&A ($/year) (20% labor cost)	$2,956,060
Property taxes and insurance ($/year) (2% total capital cost)	$12,032,668
Production maintenance and repairs ($/year) (2.9% direct capital cost)	$13,419,332
Total fixed operating costs ($/year)	**$43,188,359**

Variable operating costs	Value in startup year
Energy utilities costs	$16,090,905
Non energy utilities costs	$0
Total variable operating costs ($/year)	**$16,090,905**

Replacements	Value in startup year dollars
Unplanned replacement capital cost (0.5% of total direct capital costs/year)	$2,236,555
Replacement costs (15% of depreciable capital cost/5year)	$60,163,341
Specified replacement cost (electrodialyzer/5year)	$7,721,333
Specified replacement cost (60% pre-treatment/5year)	$25,033,436
Specified replacement cost (gas stripping/10year)	$73,347,986

Table B6: Assumptions for calculating the cost of membrane water capture. For further information see excel sheet titled "Membrane Water Capture".

Process Assumptions		
Design capacity	365000	kg H_2O/day
Average production rate	357700	kg H_2O/day
Capacity factor	98%	

System cost	Uninstalled cost in startup year dollars	Installation cost factor	Installed cost
Equipment cost	$52,581,424	1.00	$52,581,424
Total			**$52,581,424**

Capital costs	Value in startup year dollars
Depreciable capital costs	
Direct capital cost	$52,581,424
Indirect capital cost	
Site preparation (2% direct capital cost)	$761,944
Engineering and design (10% direct capital cost)	$3,809,721
Project contingency (15% direct capital cost)	$5,714,581
Upfront permitting cost (legal and contractors fees) (15% direct capital cost)	$5,714,581
Total capital cost	**$68,582,251**

Fixed operating costs	Value in startup year dollars
Labor cost ($50/FTE) ($/year) (3 FTE)	$362,980
G&A ($/year) (20% labor cost)	$67,339
Property taxes and insurance ($/year) (2% total capital cost)	$1,371,645
Production maintenance and repairs ($/year) (3% direct capital cost)	$1,577,443
Total fixed operating costs ($/year)	**$3,379,407**

Variable operating costs	Value in startup year dollars
Total variable operating costs ($/year)	**$321,067**

Replacements	Value in startup year dollars
Unplanned replacement capital cost (1% of total direct capital costs/year)	$525,814

Table B7: Assumptions for calculating the cost of condensation water capture. For further information see excel sheet titled "Condensation Water Capture".

Process Assumptions		
Design capacity	365000	kg H_2O/day
Average production rate	357700	kg H_2O/day
Capacity factor	98%	

System cost	Uninstalled cost in startup year dollars	Installation cost factor	Installed cost
OPUR structure	$19,993,088	1.00	$19,993,088
Pumps	$214,000	1.00	$214,000
Total			**$1,273,210,134**

Capital costs	Value in startup year dollars
Depreciable capital costs	
Direct capital cost	$327,803,864
Indirect capital cost	
Site preparation (2% direct capital cost)	$4,750,123
Engineering and design (10% direct capital cost)	$23,750,615
Project contingency (15% direct capital cost)	$35,625,923
Upfront permitting cost (legal and contractors fees) (15% direct capital cost)	$35,625,923
Total capital cost	**$427,556,448**

Fixed operating costs	Value in startup year dollars
Labor cost ($50/FTE) ($/year) (3 FTE)	$362,980
G&A ($/year) (20% labor cost)	$67,339
Property taxes and insurance ($/year) (2% total capital cost)	$8,551,129
Production maintenance and repairs ($/year) (3% direct capital cost)	$9,834,116
Total fixed operating costs ($/year)	**$18,815,564**

Variable operating costs	Value in startup year dollars
Total variable operating costs ($/year)	**$0**

Replacements	Value in startup year dollars
Unplanned replacement capital cost (1% of total direct capital costs/year)	$3,278,039

Table B8: Assumptions for calculating the cost of low temperature electrolysis for H_2 production. For further information see excel sheet titled "Low Temperature Electrolysis H2".

Process Assumptions		
Design capacity	40000	kg H_2/day
Current Density	2	A/cm^2
Voltage	1.9	V/cell
Baseline design capacity	50000	kg H_2/day
Degradation Rate	1.5	mV/1000 hrs
Cell/stack	150	
Stack Life	7	years
Hours per stack life	59480.4	hrs/life
Degradation Rate	89.2206	V/life
Stack oversize due to degradation	0.13	
Peak production rate	45200	kg H_2/day
Capacity factor	0.97	
Average production	43844	kg H_2/day
Total Active Area	2212	m^2
Total Active Area (with degradation)	2499	m^2
Total System Electrical Usage	55.5	kWh/kg H_2
Stack Electrical Usage	50.4	kWh/kg H_2
BoP Electrical Usage	5.1	kWh/kg H_2
Total System Input Power (Peak)	104.525	MW
Stack Input Power (peak)	94.92	MW
Process Water Flow Rate	3.78	gal/kg H_2
Total System Cost	460	$/kW
Stack System Cost	1.3	$/cm^2
Mechanical BoP	76.00	$/(kg H_2/day)
Electrical BoP	82	$/kW
Industrial electricity	0.049	$/kWh
Processed water	0.00263368	$(2016)/gal

Baseline system cost	Uninstalled cost in startup year dollars	Installation cost factor	Installed cost
Stack capital cost	$38,650,945	1.12	$43,289,058
Mechanical BoP	$4,086,980	1.00	$4,086,980
Electrical BoP	$9,260,237	1.12	$10,371,465
Total			**$57,747,504**

Capital costs	
Depreciable capital costs	
Direct capital cost	$57,747,504
Indirect capital cost	
Site preparation (2% direct capital cost)	$1,154,950
Engineering and design (10% direct capital cost)	$5,774,750
Project contingency (15% direct capital cost)	$8,662,126
Upfront permitting cost (legal and contractors fees) (15% direct capital cost)	$8,662,126
Non depreciable capital costs	
Cost of land (5 acre, $50,000/acre) (2016 dollars)	$245,459
Total capital cost	**$82,246,914**

Fixed operating costs	
Labor cost ($50/FTE) ($/year) (8.75 FTE)	$1,019,641
G&A ($/year) (20% labor cost)	$203,928
Property taxes and insurance ($/year) (2% total capital cost)	$1,644,938
Production maintenance and repairs ($/year) (3% direct capital cost)	$1,732,425
Total fixed operating costs ($/year)	**$4,600,932**

Variable operating costs	
Energy utilities costs	$43,520,322
Non energy utilities costs	$176,671
Total variable operating costs ($/year)	**$43,696,993**

Replacements	
Unplanned replacement capital cost (0.5% of total direct capital costs/year)	$410,007
Replacement costs (15% of depreciable capital cost/7year)	$8,662,126

Table B9: Assumptions for calculating the cost of high temperature electrolysis for H_2 production. For further information see excel sheet titled "High Temperature Electrolysis H2".

Process Assumptions		
Design capacity	40000	kg H_2/day
Capacity factor	0.8244	
Average production	32976	kg H_2/day
Total System Electrical Usage	50.9	kWh/kg H_2
Electrical usage	36.8	kWh/kg H_2
Heat usage	14.1	kWh/kg H_2
Heat usage	0.05613	mmBtu/kg H_2
Process Water Flow Rate	2.384702106	gal/kg H_2
Total System Cost	820	$/kW
Stack Cost (% of uninst. SOEC Sys Cost)	0.35	
BoP Cost (% of uninst. SOEC Sys Cost)	0.65	
Industrial natural gas	3.733674814	$/mmbtu
Industrial electricity	0.049	$/kWh
Processed water	0.00263368	$(2016)/gal

Baseline system cost	Uninstalled cost in startup year dollars	Installation cost factor	Installed cost
Stack capital cost	$38,650,945	1.12	$23,455,624
BoP	$4,086,980	1.12	$43,560,445
Total			**$67,016,069**

Capital costs	Value in startup year dollars
Depreciable capital costs	
Direct capital cost	$67,016,069
Indirect capital cost	
Site preparation (2% direct capital cost)	$1,340,321
Engineering and design (10% direct capital cost)	$6,701,607
Project contingency (15% direct capital cost)	$10,052,410
Upfront permitting cost (legal and contractors fees) (15% direct capital cost)	$10,052,410
Non depreciable capital costs	
Cost of land (1 acre, $50,000/acre) (2016 dollars)	$49,092
Total capital cost	**$95,211,910**

Fixed operating costs	Value in startup year dollars
Labor cost ($50/FTE) ($/year) 13.12 FTE)	$1,529,461
G&A ($/year) (20% labor cost)	$305,892
Property taxes and insurance ($/year) (2% total capital cost)	$1,904,238
Production maintenance and repairs ($/year) (3% direct capital cost)	$2,010,482
Total fixed operating costs ($/year)	**$5,750,074**

Variable operating costs	Value in startup year
Energy utilities costs	$25,633,493
Non energy utilities costs	$83,829
Total variable operating costs ($/year)	**$25,717,323**

Replacements	Value in startup year dollars
Unplanned replacement capital cost (1% of total direct capital costs/year)	$951,628
Specified replacement costs (27.3% of stack cost/year)	$6,403,385
Specified replacement costs (100% of BoP cost/15 year)	$43,560,445

Table B10: Assumptions for calculating the cost of photoelectrochemical H_2 production currently. For further information see excel sheet titled "Photoelectrochemical H2 (current)".

Process Assumptions		
Design capacity	40000	kg H_2/day
Average production rate	40000	kg H_2/day
Location	California	
PV efficiency	19.1%	
STH efficiency	10%	
Solar power	1000	W/m^2
Solar capacity factor	28.4%	
PV module	0.37	$/W
Solar capture area for stack only	1914218	m^2
Solar capture area for BoP (10% of stack)	191421.8	m^2
Total solar capture area	2105639.8	m^2
PV cells	70.67	$/$m^2$
Catalyst	8	$/$m^2$
Membrane	30	$/$m^2$
Chassis	37.74869216	$/$m^2$
Water processing	0.76	$/$m^2$
Gas processing	6.599227784	$/$m^2$
Power electronics and control system	7.908190728	$/$m^2$
Process Water Flow Rate	3.78	gal/kg H_2
Processed water	0.00263368	$(2016)/gal

Baseline system cost	Uninstalled cost in startup year dollars	Installation cost factor	Installed cost
PV capital cost	$148,805,565	1.30	$193,447,234
Stack capital cost	$159,499,461	1.12	$178,639,396
Mechanical BoP	$15,487,230	1.00	$15,487,230
Electrical BoP	$16,651,801	1.12	$18,650,017
Total			**$406,223,878**

Capital costs	Value in startup year dollars
Depreciable capital costs	
Direct capital cost	$406,223,878
Indirect capital cost	
Site preparation (2% direct capital cost)	$8,124,478
Engineering and design (10% direct capital cost)	$40,622,388
Project contingency (15% direct capital cost)	$60,933,582
Upfront permitting cost (legal and contractors fees) (15% direct capital cost)	$60,933,582
Non depreciable capital costs	
Cost of land (520 acre, $50,000/acre) (2016 dollars)	$26,015,706
Total capital cost	**$602,853,613**

Fixed operating costs	Value in startup year dollars
Labor cost ($50/FTE) ($/year) (20.67 FTE)	$2,409,559
G&A ($/year) (20% labor cost)	$481,912
Property taxes and insurance ($/year) (2% total capital cost)	$12,057,072
Production maintenance and repairs ($/year) (3% direct capital cost)	$12,186,716
Total fixed operating costs ($/year)	**$27,135,260**

Variable operating costs	Value in startup year
Energy utilities costs	$0
Non energy utilities costs	$145,348
Total variable operating costs ($/year)	**$145,348**

Replacements	Value in startup year dollars
Unplanned replacement capital cost (0.5% of total direct capital costs/year)	$2,031,119
Replacement costs (15% of depreciable capital cost/7year)	$86,525,686
Specified replacement cost (PV stack cost/20 year)	$193,447,234

Table B11: Assumptions for calculating the cost of photoelectrochemical H_2 production in the future. For further information see excel sheet titled "Photoelectrochemical H2 (future)".

Process Assumptions			
Design capacity		40000	kg H_2/day
Average production rate		40000	kg H_2/day
Location	California		
PV efficiency		19.1%	
STH efficiency		10.0%	
Solar power		1000	W/m^2
Solar capacity factor		28.40%	
PV module		0.24	$/W
Solar capture area for stack only		957109	m^2
Solar capture area for BoP (10% of stack)		95710.9	m^2
Total solar capture area		1052819.9	m^2
PV cells		70.67	$/$m^2$
Catalyst		8	$/$m^2$
Membrane		30	$/$m^2$
Chassis		37.74869216	$/$m^2$
Water processing		0.76	$/$m^2$
Gas processing		6.599227784	$/$m^2$
Power electronics and control system		7.908190728	$/$m^2$
Process Water Flow Rate		3.78	gal/kg H_2
Processed water		0.00263368	$(2016)/gal

Baseline system cost	Uninstalled cost in startup year dollars	Installation cost factor	Installed cost
PV capital cost	$148,805,565	1.30	$193,447,234
Stack capital cost	$159,499,461	1.12	$178,639,396
Mechanical BoP	$15,487,230	1.00	$15,487,230
Electrical BoP	$16,651,801	1.12	$18,650,017
Total			**$406,223,878**

Capital costs	Value in startup year dollars
Depreciable capital costs	
Direct capital cost	$406,223,878
Indirect capital cost	
Site preparation (2% direct capital cost)	$8,124,478
Engineering and design (10% direct capital cost)	$40,622,388
Project contingency (15% direct capital cost)	$60,933,582
Upfront permitting cost (legal and contractors fees) (15% direct capital cost)	$60,933,582
Non depreciable capital costs	
Cost of land (520 acre, $50,000/acre) (2016 dollars)	$26,015,706
Total capital cost	**$602,853,613**

Fixed operating costs	Value in startup year dollars
Labor cost ($50/FTE) ($/year) (20.67 FTE)	$2,409,559
G&A ($/year) (20% labor cost)	$481,912
Property taxes and insurance ($/year) (2% total capital cost)	$12,057,072
Production maintenance and repairs ($/year) (3% direct capital cost)	$12,186,716
Total fixed operating costs ($/year)	**$27,135,260**

Variable operating costs	Value in startup year
Energy utilities costs	$0
Non energy utilities costs	$145,348
Total variable operating costs ($/year)	**$145,348**

Replacements	Value in startup year dollars
Unplanned replacement capital cost (0.5% of total direct capital costs/year)	$2,031,119
Replacement costs (15% of depreciable capital cost/7year)	$86,525,686
Specified replacement cost (PV stack cost/20 year)	$193,447,234

Table B12: Assumptions for calculating the cost of solar thermochemical H_2. For further information see excel sheet titled "Solar Thermochemical H2".

Process Assumptions		
Plant design capacity	45000	kg H_2/day
Baseline design capacity	100000	kg H_2/day
Plant capacity factor	90.00%	
Average production rate	40500	kg H_2/day
STH efficiency	20%	
Process Water Flow Rate	2.378	gal/kg H_2
Scale ratio	0.45	
Scaling factor exponent	0.78	
Lower limit for scaling capacity	20000	kg H_2/day
Upper limit for scaling capacity	200000	kg H_2/day
Processed water price	0.00263368	$(2016)/gal

System cost	Baseline uninstalled cost in reference year dollars	Scaled uninstalled cost in reference year dollars	Scaled uninstalled cost in startup year dollars	Installation cost factor	Scaled installed cost
ZrO2	$50,604	$27,145	$32,296	1	$32,296
Compression System	$36,614,848	$19,640,973	$23,367,567	1	$23,367,567
Solar Reactors	$27,852,508	$14,940,670	$17,775,449	3.17	$56,348,173
Vacuum Pumps	$4,850,000	$2,601,642	$3,095,266	3.3	$10,214,379
Water Pumps	$97,785	$52,454	$62,406	3.3	$205,940
Turbine	$693,223	$371,860	$442,415	2.15	$951,191
Heat Exchangers	$378,081	$202,811	$241,291	3.17	$764,893
Heliostats	$193,334,841	$103,708,866	$123,386,145	1	$123,386,145
Secondary Concentrators	$738,859	$396,340	$471,539	1	$471,539
Towers	$72,990,255	$39,153,505	$46,582,324	1	$46,582,324
Ferrite	$50,999,508	$27,357,206	$32,547,846	1	$32,547,846
Total	**$388,600,513**				**$294,872,293**

Capital costs	Value in startup year dollars
Depreciable capital costs	
Direct capital cost	$294,872,293
Indirect capital cost	
Site preparation (2% direct capital cost)	$7,016,402
Engineering and design (17.8% solar subsystem cost)	$36,094,585
Project contingency (16.8% solar and 18% chemical system cost)	$60,714,276
Upfront permitting cost (legal and contractors fees) (7.5% direct capital cost)	$26,311,508
Non depreciable capital costs	
Cost of land (374.44 acre, $50,000/acre) (2016 dollars)	$1,842,960
Total capital cost	**$426,852,024**

Fixed operating costs	Value in startup year dollars
Labor cost ($50/FTE) ($/year) (239.07 FTE)	$4,554,227
G&A ($/year) (20% labor cost)	$910,845
Property taxes and insurance ($/year) (2% total capital cost)	$8,537,040
Production maintenance and repairs ($/year) (0.5% solar + 6% nonsolar)	$8,318,137
Total fixed operating costs ($/year)	**$22,320,251**

Variable operating costs	
Energy utilities costs	$0
Non energy utilities costs	$92,581
Environmental surcharges	$1,208,144
Total variable operating costs ($/year)	**$1,300,725**

Replacements	Value in startup year dollars
Unplanned replacement capital cost (0.5% of total direct capital costs/year)	$2,125,045
Specified replacement costs (ZrO_2 and Ferrite/5 year)	$32,580,141

Table B13: Assumptions for calculating the cost of biochemical methanation. For further information see excel sheet titled "Biochemical Methanation".

Process Assumptions		
Design capacity	85714	kg SNG/day
Average production	84000	kg SNG/day
Capacity factor	98%	
H_2 input rate	42857	kg/day
CO_2 input rate	235714	kg/day
H_2 price (LTE H_2)	3.50	$/kg
CO_2 price (DAC CO_2)	0.28	$/kg

System cost	Uninstalled cost in reference year dollars	Uninstalled cost in startup year dollars	Installation cost factor	Installed cost
Compressor	$5,299,039	$6,061,570	1.00	$6,061,570
Methanation	$15,799,014	$18,072,489	1.00	$18,072,489
Piping installation				$4,826,812
Total				**$28,960,870**

Capital costs	Value in startup year dollars
Depreciable capital costs	
Direct capital cost	$28,960,870
Indirect capital cost	
Site preparation (2% direct capital cost)	$506,353
Engineering and design (10% direct capital cost)	$2,531,766
Project contingency (15% direct capital cost)	$3,797,650
Upfront permitting cost (legal and contractors fees) (15% direct capital cost)	$3,797,650
Total capital cost	**$39,594,290**

Fixed operating costs	Value in startup year dollars
Labor cost ($50/FTE) ($/year) (12 FTE)	$1,449,927
G&A ($/year) (20% labor cost)	$268,985
Property taxes and insurance ($/year) (2% total capital cost)	$791,886
Production maintenance and repairs ($/year) (3% direct capital cost)	$868,826
Total fixed operating costs ($/year)	**$3,379,624**

Variable operating costs	Value in startup year dollars
Energy utilities costs	$0
H_2 cost	$53,596,721
CO_2 cost	$23,448,298
Total variable operating costs ($/year)	**$53,596,721**

Replacements	Value in startup year dollars
Unplanned replacement capital cost (1% of total direct capital costs/year)	$289,609

Table B14: Assumptions for calculating the cost of thermochemical methanation. For further information see excel sheet titled “Thermochemical Methanation”.

Process Assumptions		
Design capacity	81100	kg SNG/day
Average production	79478	kg SNG/day
Capacity factor	98%	
H_2 input rate	40000	kg/day
CO_2 input rate	218200	kg/day
H_2 price (LTE H_2)	3.50	\$/kg
CO_2 price (DAC CO_2)	0.28	\$/kg

System cost	Uninstalled cost in reference year dollars	Uninstalled cost in startup year dollars	Installation cost factor	Installed cost
Heat exchangers	1957000	2701033.858	1	2701033.858
Reactors	2919000	4028777.635	1	4028777.635
Catalyst (Ni supported)	318000	438900.7496	1	438900.7496
Compressors	5126000	7074859.252	1	7074859.252
MDEA unit	1049000	1447820.397	2.47	3576116.381
Membrane unit	263000	362990.2426	2.47	896585.8991
Organic Rankine Cycle Unit	1100000	1518210.14	2.47	3749979.046
Pumps	\$214,000	\$295,361	1.00	\$295,361
Cooling tower	\$555,000	\$766,006	1.00	\$766,006
Piping installation				\$4,705,524
Total				**\$28,233,144**

Capital costs	Values in startup year dollars
Depreciable capital costs	
Direct capital cost	\$28,233,144
Indirect capital cost	
Site preparation (2% direct capital cost)	\$564,663
Engineering and design (10% direct capital cost)	\$2,823,314
Project contingency (15% direct capital cost)	\$4,234,972
Upfront permitting cost (legal and contractors fees) (15% direct capital cost)	\$4,234,972
Total capital cost	**\$40,091,064**

Fixed operating costs	Values in startup year dollars
Labor cost (\$50/FTE) (\$/year) (12 FTE)	\$1,398,861
G&A (\$/year) (20% labor cost)	\$279,772
Property taxes and insurance (\$/year) (2% total capital cost)	\$801,821
Production maintenance and repairs (\$/year) (3% direct capital cost)	\$846,994
Total fixed operating costs (\$/year)	**\$3,327,448**

Variable operating costs	Values in startup year
Energy utilities costs	\$0
H_2 cost	\$50,023,606
CO_2 cost	\$21,706,018
Total variable operating costs (\$/year)	**\$71,729,624**

Replacements	Values in startup year dollars
Unplanned replacement capital cost (1% of total direct capital costs/year)	\$282,331

Table B15: Assumptions for calculating the cost of electrochemical methanation. For further information see excel sheet titled "Low Temperature electrochemical CH4".

Process Assumptions		
Design capacity	81000	kg CH_4/day
Current Density	0.5	A/cm^2
Voltage	4	V/cell
Cell/stack	150	
Degradation Rate	0.5	mV/1000 hrs
Stack Life	7	years
Degradation Rate	30.66	V/life
Stack oversize due to degradation	0.045	
Peak production rate	84645	kg CH_4/day
Capacity factor	0.97	
Average production	82105.65	kg CH_4/day
Total Active Area	10642	m^2
Total Active Area (with degradation)	11121	m^2
Total System Electrical Usage	65.61	kWh/kg CH_4
Stack Electrical Usage	63.06	kWh/kg CH_4
BoP Electrical Usage	2.55	kWh/kg CH_4
Total System Input Power (Peak)	231.41	MW
Stack Input Power (peak)	222.41	MW
Utilization	100%	
Process Water Flow Rate	1.89	gal/kg H_4
Process CO_2 Flow Rate	2.75	kg/kg H_4
Total System Cost	460	\$/kW
Stack System Cost	1.3	\$/cm^2
Mechanical BoP	38.00	\$/(kg CH_4/day)
Electrical BoP	82	\$/kW
Industrial electricity	0.049	\$/kWh
Processed water	0.00263368	\$(2016)/gal
CO_2 (DAC)	0.28	\$/kg CH_4

System cost	Uninstalled cost in startup year dollars	Installation cost factor	Installed cost
Stack capital cost	\$172,003,665	1.12	\$192,644,104
Mechanical BoP	\$3,826,797	1.00	\$3,826,797
Electrical BoP	\$21,698,172	1.12	\$24,301,952
Total			**\$220,772,854**

Capital costs	
Depreciable capital costs	
Direct capital cost	\$220,772,854
Indirect capital cost	
Site preparation (2% direct capital cost)	\$4,415,457
Engineering and design (10% direct capital cost)	\$22,077,285
Project contingency (15% direct capital cost)	\$33,115,928
Upfront permitting cost (legal and contractors fees) (15% direct capital cost)	\$33,115,928
Non depreciable capital costs	\$313,497,452
Cost of land (4.4 acre, \$50,000/acre) (2016 dollars)	\$247,296
Total capital cost	**\$313,744,748**

Fixed operating costs	
Labor cost (\$50/FTE) (\$/year) (8.81 FTE)	\$1,027,269
G&A (\$/year) (20% labor cost)	\$205,454
Property taxes and insurance (\$/year) (2% total capital cost)	\$6,274,895
Production maintenance and repairs (\$/year) (3% direct capital cost)	\$6,623,186
Total fixed operating costs (\$/year)	**\$14,130,803**

Variable operating costs	
Energy utilities costs	\$96,348,776
CO_2 cost	\$22,919,497
H_2O cost	\$165,424
Total variable operating costs (\$/year)	**\$119,433,698**

Replacements	
Unplanned replacement capital cost (0.5% of total direct capital costs/year)	\$1,567,487
Replacement costs (15% of depreciable capital cost/7year + unplanned cost)	\$33,115,928

Table B16: Assumptions for calculating the cost of photoelectrochemical methanation. For further information see excel sheet titled "Photoelectrochemical CH4".

Process Assumptions			
Design capacity		81000	kg CH_4/day
Average production rate		81000	kg CH_4/day
Location	California		
PV efficiency		19.1%	
STH efficiency		6.0%	
Solar power		1000	W/m^2
Solar capacity factor		28.40%	
PV module		0.37	$/W
Solar capture area for stack only		6460484	m^2
Solar capture area for BoP (10% of stack)		646048.4	m^2
Total solar capture area		7106532.4	m^2
PV cells		70.67	$\$/m^2$
Catalyst		8	$\$/m^2$
Membrane		30	$\$/m^2$
Chassis		37.75	$\$/m^2$
Water processing		0.23	$\$/m^2$
Gas processing		1.71	$\$/m^2$
Power electronics and control system		0.46	$\$/m^2$
Utilization		100%	
Process CO_2 Flow Rate		2.75	kg CO_2/kg CH_4
Process Water Flow Rate		3.78	gal/kg CH_4
Processed water		0.00263368	$(2016)/gal
CO_2 (DAC)		0.28	$(2016)/gal

System cost	Uninstalled cost in startup year dollars	Installation cost factor	Installed cost
PV capital cost	$502,218,645	1.30	$652,884,238
Stack capital cost	$538,310,535	1.12	$602,907,799
Mechanical BoP	$13,790,861	1.00	$13,790,861
Electrical BoP	$3,238,603	1.12	$3,627,235
Total			**$1,273,210,134**

Capital costs	
Depreciable capital costs	
Direct capital cost	$1,273,210,134
Indirect capital cost	
Site preparation (2% direct capital cost)	$25,464,203
Engineering and design (10% direct capital cost)	$127,321,013
Project contingency (15% direct capital cost)	$190,981,520
Upfront permitting cost (legal and contractors fees) (15% direct capital cost)	$190,981,520
Non depreciable capital costs	
Cost of land (520 acre, $50,000/acre) (2016 dollars)	$87,802,984
Total capital cost	**$1,895,761,374**

Fixed operating costs	
Labor cost ($50/FTE) ($/year) (20.67 FTE)	$12,803,772
G&A ($/year) (20% labor cost)	$2,560,754
Property taxes and insurance ($/year) (2% total capital cost)	$37,915,227
Production maintenance and repairs ($/year) (3% direct capital cost)	$38,196,304
Total fixed operating costs ($/year)	**$91,476,057**

Variable operating costs	
Energy utilities costs	$0
CO_2 cost	$22,610,859
H_2O cost	$147,164
Total variable operating costs ($/year)	**$22,758,023**

Replacements	
Unplanned replacement capital cost (0.5% of total direct capital costs/year)	$6,366,051
Replacement costs (15% of depreciable capital cost/7year)	$271,193,758
Specified replacement cost (PV stack cost/20 year)	$652,884,238

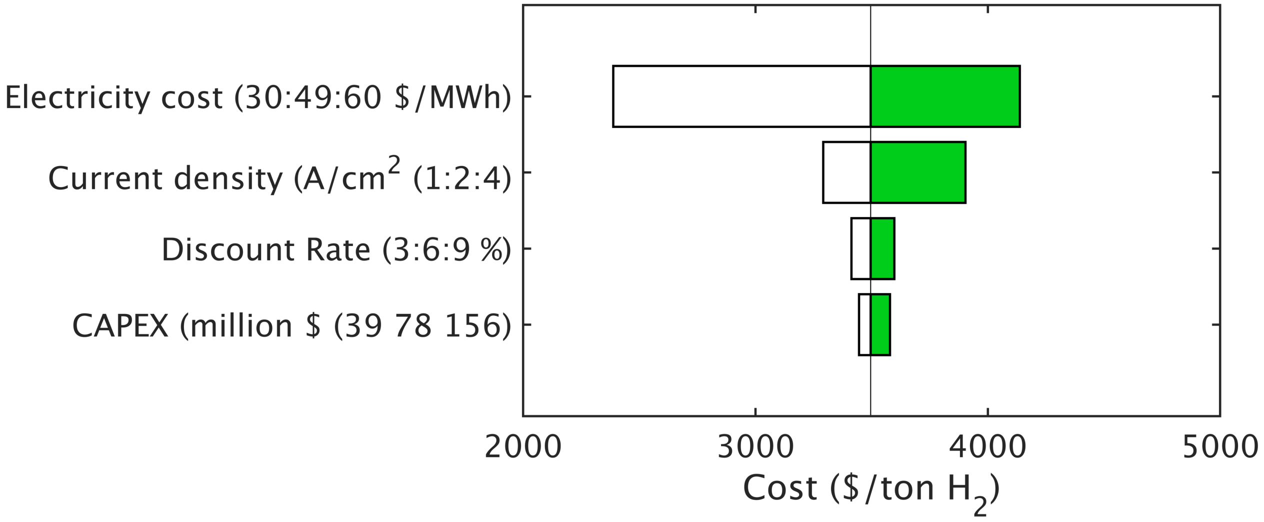

Figure B1: *Sensitivity analysis of low temperature electrolysis processes.*

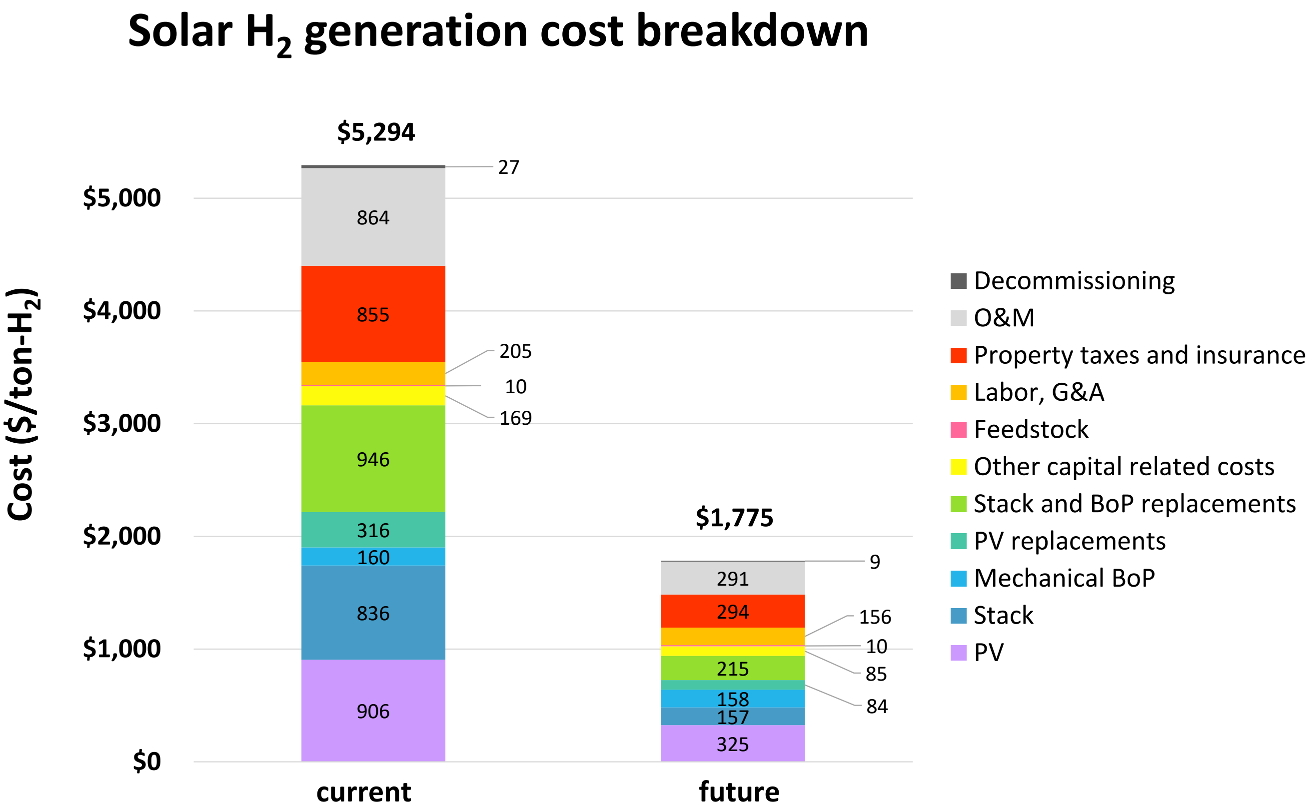

Figure B2: *Cost breakdown for current and future cost of photoelectrochemical water splitting.*

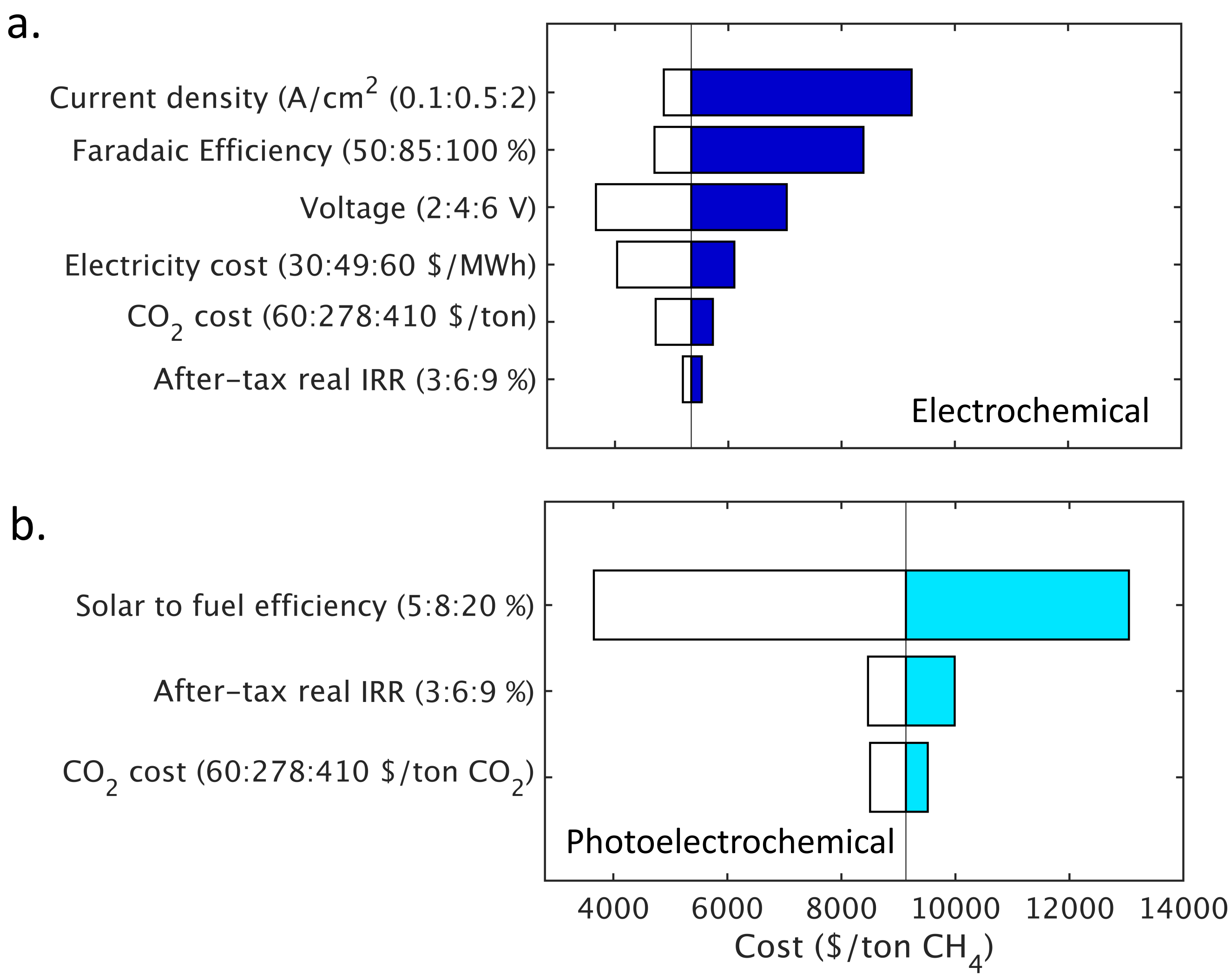

Figure B3: *Sensitivity analysis of (a) electrochemical and (b) photoelectrochemical methanation processes. The base case for the methanation processes assumes* CO_2 *captured from the atmosphere and* H_2 *generated via low temperature electrolysis.*

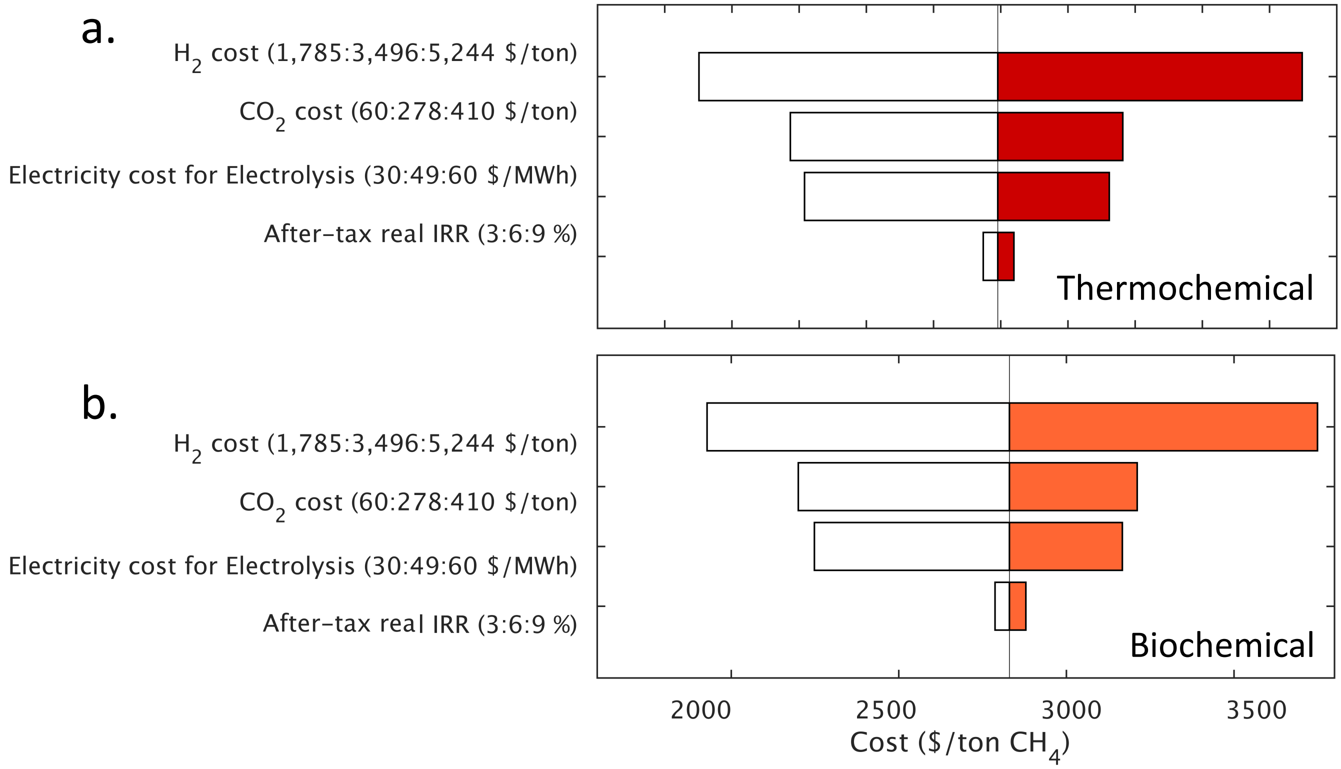

Figure B4: *Sensitivity analysis of (a) thermochemical and (b) biochemical methanation processes. The base case for the methanation processes assumes CO_2 captured from the atmosphere and H_2 generated via low temperature electrolysis.*

BIBLIOGRAPHY: APPENDIX B

1. Keith, D. W., Angelo, D. St., Holmes, G. & Heidel, K. A process for capturing CO_2 from the atmosphere. *Joule* **2018**, 2, 1573–1594.
2. James, B. D., Colella, W. G. & Moton, J. M. *Techno-Economic Analysis of Hydrogen Production Pathways. Stategic Analysis* (2013).
3. NREL. *H2A: Hydrogen Analysis Production Models.* (2018).
4. Peterson, D. & Miller, E. *Hydrogen and Fuel Cells Program Record - Hydrogen Production Cost from Solid Oxide Electrolysis. Hydrogen and Fuel Cells Program Record - Hydrogen Production Cost from Solid Oxide Electrolysis* (2016).
5. Becker, W. L., Penev, M. & Braun, R. J. Production of synthetic natural gas from carbon dioxide and renewably generated hydrogen: A techno-economic analysis of a power-to-gas strategy. *J. Energy Resour. Technol.* **2019**, 141.
6. de Lannoy, C. F. *et al.* Indirect ocean capture of atmospheric CO_2: Part I. Prototype of a negative emissions technology. *Int. J. Greenh. Gas Control* **2018**, 70, 243–253.
7. Eisaman, M. D. *et al.* Indirect ocean capture of atmospheric CO_2: Part II. Understanding the cost of negative emissions. *Int. J. Greenh. Gas Control* **2018**, 70, 254–261.
8. Matsumiya, N., Teramoto, M., Kitada, S. & Matsuyama, H. Evaluation of energy consumption for separation of CO2 in flue gas by hollow fiber facilitated transport membrane module with permeation of amine solution. *Sep. Purif. Technol.* **2005**, 46, 26–32.
9. Voutchkov, N. *Desaliniation Engineering Planning and Design.* (McGraw-Hill Companies, Inc, 2013).
10. Seider, W. D., Seader, J. D., Lewin, D. R. & Widagdo, S. *Product and Process Design.* (John Wiley & Sons, 2009).
11. Shaner, M. R., Atwater, H. A., Lewis, N. S. & McFarland, E. W. A comparative technoeconomic analysis of renewable hydrogen production using solar energy. *Energy Environ. Sci.* **2016**, 9, 2354–2371.
12. James, B. D., Baum, G. N., Perez, J. & Baum, K. N. *Discovery of viable methanotrophic bacteria in permafrost sediments of northeast Siberia.* (2009).
13. Electrochaea. *Power-to-Gas via Biological Catalysis (P2G-Biocat).* (2017).
14. Electrochaea. *Applications of Electrochaea's BioCat biomethanation technology.* (2018).